ulm university universität ulm

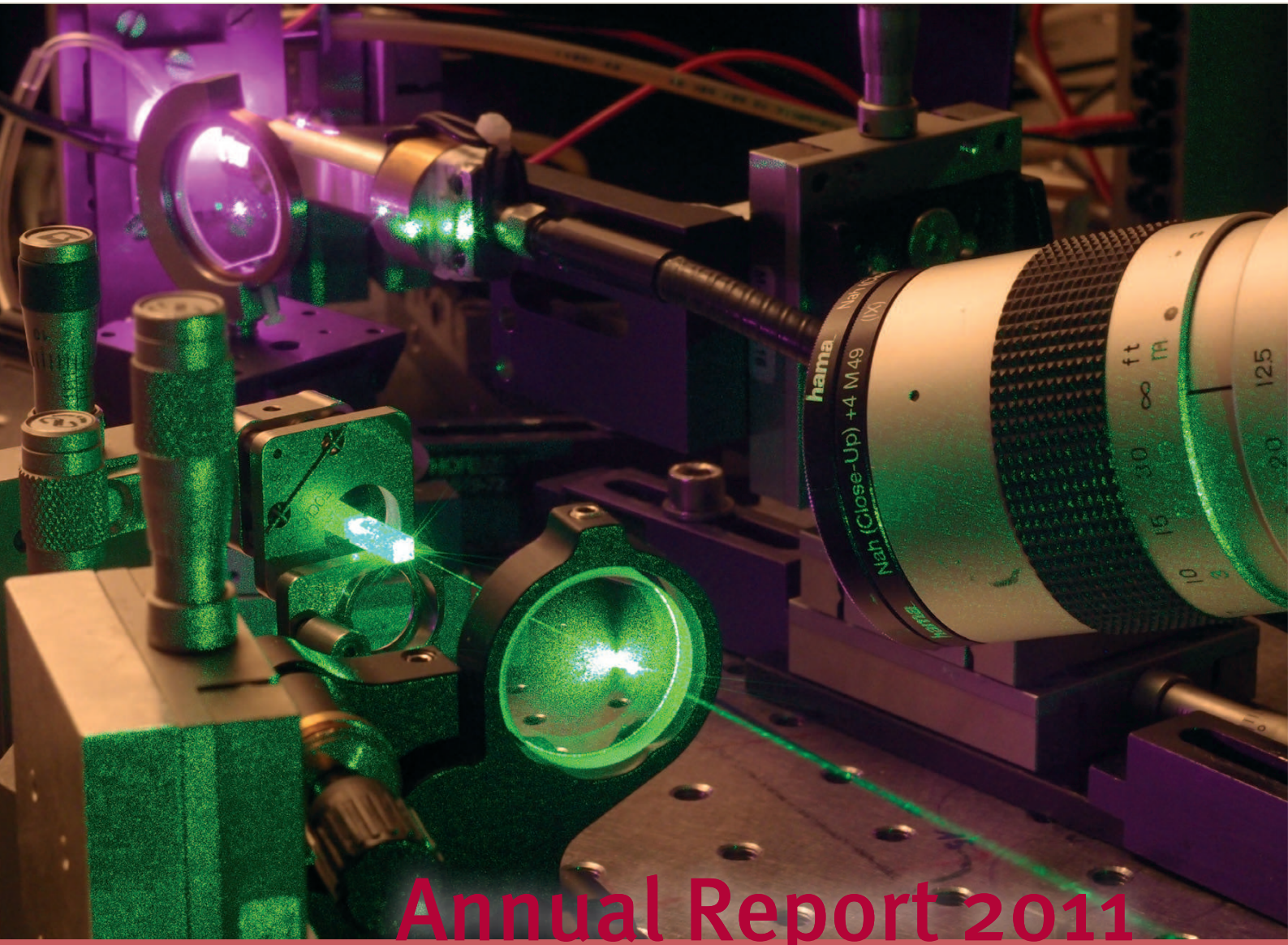

Annual Report 2011

Institute of Optoelectronics

Cover photo:
Frequency-doubled semiconductor disk laser system emitting up to 7.2 W of green light at a wavelength of 520 nm (see article on page 69). The laser system has a folded resonator setup including a nonlinear lithium triborate (LBO) crystal for second-harmonic generation of the fundamental emission at 1040 nm and a birefringent filter for polarization and frequency stabilization. The disk laser is optically pumped by a fiber-coupled broad-area diode laser bar at a wavelength of 808 nm. The pump light appears in magenta color due to the sensitivity of the CCD camera sensor at this wavelength.

Contents

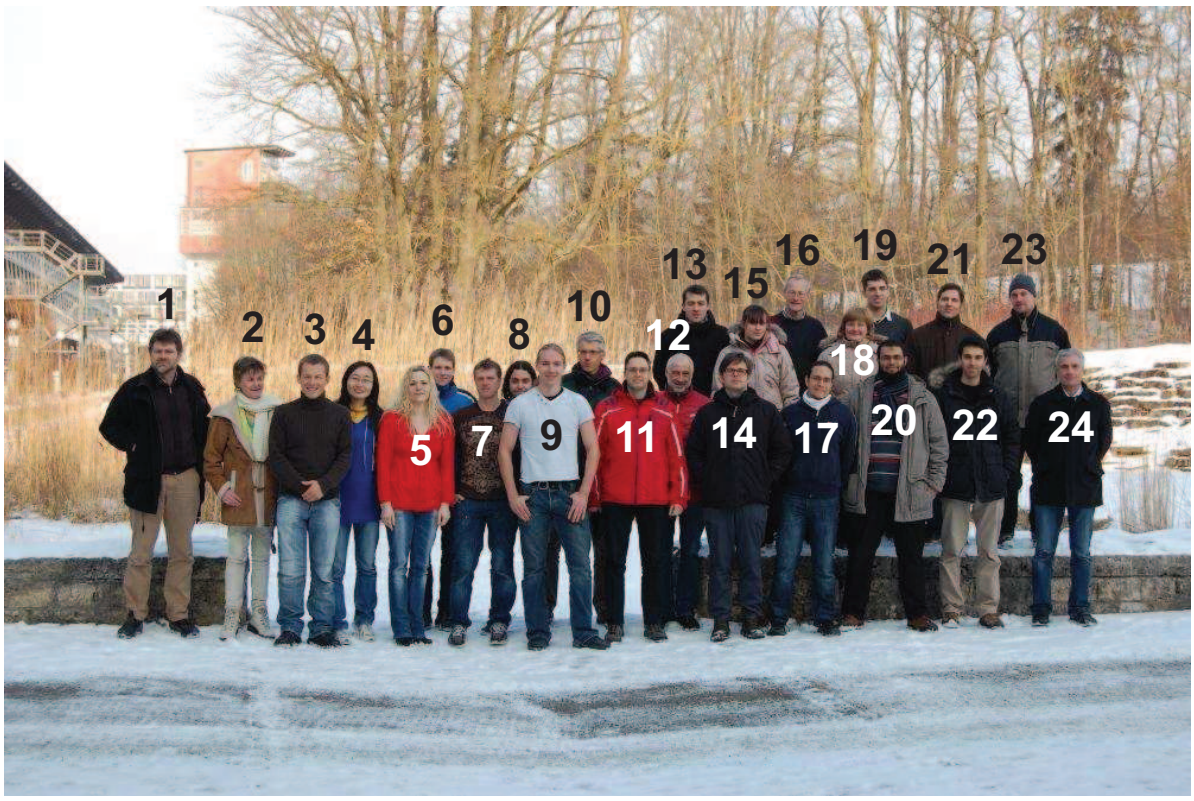

1: Peter Unger
2: Christine Bunk
3: Alexander Kern
4: Junjun Wang
5: Ilona Schwaiger
6: Marcel Sattler
7: Rainer Blood
8: Tobias Meisch
9: Robert Leute
10: Rainer Michalzik
11: Dietmar Wahl
12: Rudolf Rösch
13: Alexander Hein
14: Frank Demaria
15: Anna Bergmann
16: Jürgen Mähnß
17: Mohamed Fikry
18: Hildegard Mack
19: Dominik Heinz
20: Ahmed Al-Samaneh
21: Benedikt Westenfelder
22: Kamran Forghani
23: Martin Klein
24: Ferdinand Scholz

Missing in the picture:

Karl Joachim Ebeling, Sükran Kilic, Frank Lipski,
Gerlinde Meixner, Susanne Menzel, Eva Nüßle

Ulm University
Institute of Optoelectronics

Albert-Einstein-Allee 45, 89081 Ulm, Germany
URL: http://www.uni-ulm.de/opto
Fax: +49–731/50–2 60 49
Phone: +49–731/50–

Head of Institute

Prof. Dr.	Peter Unger	–2 60 54	peter.unger@uni-ulm.de

Deputy Head

Prof. Dr.	Ferdinand Scholz	–2 60 52	ferdinand.scholz@uni-ulm.de

President of Ulm University

Prof. Dr.	Karl Joachim Ebeling	–2 20 00	karl.ebeling@uni-ulm.de

Group Leader

apl. Prof. Dr.-Ing.	Rainer Michalzik	–2 60 48	rainer.michalzik@uni-ulm.de

Cleanroom Management

Dr.-Ing.	Jürgen Mähnß	–2 60 53	juergen.maehnss@uni-ulm.de

Secretaries

	Christine Bunk	–2 60 51	christine.bunk@uni-ulm.de
	Sükran Kilic	–2 60 59	suekran.kilic@uni-ulm.de
	Hildegard Mack	–2 60 60	hildegard.mack@uni-ulm.de
	Eva Nüßle	–2 60 50	eva.nuessle@uni-ulm.de

Research Staff

M.Sc.	Ahmed Al-Samaneh	–2 60 37	ahmed.al-samaneh@uni-ulm.de
Dipl.-Ing.	Anna Bergmann	–2 60 38	anna.bergmann@uni-ulm.de
Dr.-Ing.	Frank Demaria*	–2 60 46	frank.demaria@uni-ulm.de
M.Sc.	Mohamed Fikry	–2 61 95	mohamed.fikry@uni-ulm.de
M.Sc.	Kamran Forghani*	–2 60 39	kamran.forghani@uni-ulm.de
Dipl.-Ing.	Alexander Hein	–2 60 46	alexander.hein@uni-ulm.de
Dipl.-Phys.	Dominik Heinz	–2 64 53	dominik.heinz@uni-ulm.de
Dipl.-Ing.	Alexander Kern	–2 60 37	alexander.kern@uni-ulm.de
Dipl.-Ing.	Martin Klein	–2 60 44	martin.klein@uni-ulm.de
M.Sc.	Fabian Krapp*	–2 60 35	fabian.krapp@uni-ulm.de
Dipl.-Phys.	Robert Leute	–2 60 56	robert.leute@uni-ulm.de
Dipl.-Phys.	Frank Lipski*	–2 60 39	frank.lipski@uni-ulm.de
Dipl.-Phys.	Tobias Meisch	–2 60 56	tobias.meisch@uni-ulm.de
Dipl.-Inf.	Marcel Sattler	–2 60 35	marcel.sattler@uni-ulm.de
Dipl.-Ing.	Wolfgang Schwarz*	–2 60 38	wolfgang.schwarz@uni-ulm.de
Dipl.-Phys.	Dietmar Wahl	–2 60 37	dietmar.wahl@uni-ulm.de
M.Sc.	Junjun Wang	–2 61 95	junjun.wang@uni-ulm.de
Dipl.-Phys.	Benedikt Westenfelder	–2 64 54	benedikt.westenfelder@uni-ulm.de

Technical Staff

Ilona Schwaiger	–2 60 56	ilona.schwaiger@uni-ulm.de
Rainer Blood	–2 60 44	rainer.blood@uni-ulm.de
Gerlinde Meixner	–2 60 41	gerlinde.meixner@uni-ulm.de
Susanne Menzel	–2 60 41	susanne.menzel@uni-ulm.de
Rudolf Rösch	–2 60 57	rudolf.roesch@uni-ulm.de

* Member has left the institute meanwhile

Preface

The year 2011 was full of success for the Institute of Optoelectronics. Research concentrated on vertical-cavity surface-emitting lasers (VCSELs), optical interconnect systems, GaN-based electronic and optoelectronic devices, and semiconductor disk lasers.

The VCSELs and Optical Interconnects Group has continued its work on vertical-cavity laser-based systems for optical data communications, optical sensing, as well as biophotonics. For the first time, true bidirectional data transmission over multimode fiber at 10 Gbit/s could be demonstrated with monolithically integrated VCSEL–PIN photodiode chips.

During 2011, the GaN Group could slightly increase its activities towards semipolar GaN heterostructures as a part of our transregional research group *PolarCoN*. In particular, work on sub-micrometer laser interference lithography opened new possibilities, which may be also of great interest for highly efficient green LEDs, which are addressed in another research project. Also on the other side of the spectral range, we achieved quite remarkable results by demonstrating excellent structures for UV-LEDs. 4-point probe measurements performed on graphene sheets in-situ in a transmission electron microscope demonstrated the great advantages of combining optical lithography engineering with electron microscopy studies.

In the High-Power Semiconductor Laser Group, a frequency-doubled optically-pumped semiconductor disk laser system has been realized which emits up to 7.2 W of green light at a wavelength of 520 nm and shows an overall power conversion efficiency of 20 %. The laser system has a folded resonator setup including a nonlinear lithium triborate (LBO) crystal for second-harmonic generation of the fundamental emission at 1040 nm and a birefringent filter for polarization and frequency stabilization.

In July 2011, Andreas Strodl's Diploma Thesis on quantum dot-based laser structures was awarded by the VDI. In March 2012, Rainer Michalzik was appointed apl. Prof. at the Institute. He has served as the editor of a new VCSEL book by Springer-Verlag which is introduced in one of the articles of this Annual Report.

Rainer Michalzik
Ferdinand Scholz
Peter Unger

Ulm, March 2012

Coaxial InGaN Epitaxy Around GaN Nano-tubes: Tracing the Signs

Mohamed Fikry

This work focuses on investigations of the luminescence properties of coaxial InGaN layers around single GaN nano-tubes on top of GaN micro-pyramids. The nano-tube structure was formed after the controlled desorption of ZnO nano-pillar templates during the coaxial GaN epitaxy. An intense and broad photoluminescence (PL) peak centered around 2.85 eV is attributed to transitions from a shallow donor or from the conduction band to a Zn_{Ga} acceptor level above the valence band edge. A thin layer near the area around the inner diameter of the nano-tube is believed to be heavily doped with Zn impurities. These are believed to hinder the luminescence from coaxial InGaN quantum wells (QWs) around the GaN nanotube. Comparing samples with and without QWs, where the thickness of the GaN tube wall before the QW growth was doubled, a clear indication of In incorporation in low temperature PL was observed via an intense peak around 3.1 eV. Moreover, as the temperature of the QW growth was changed from 830°C to 780°C, a shift of the peak corresponding to an increase in In incorporation from 3.5 % to 7.5 % was noticed.

1. Introduction

Nano-structures based on GaN and related group III-N alloys have been receiving significant attention in recent years as possible candidates for the development of nano-photonic devices. Moreover, due to their high surface to volume ratio, tuneable direct band gap and high chemical stability, GaN based nano-structures promise a high potential as sensing elements for biomedical applications. Developing a scalable process for the realization of these novel structures with high crystal quality is necessary as a first step towards their realization. We have reported in [1] our approach using coaxial casting of ZnO nano-pillars for the generation of high crystal quality GaN nano-tube structures after the controlled desorption of the ZnO nano-pillars (Fig. 1). Such a nano-tube structure has a larger surface to volume ratio than a GaN nano-pillar in addition to possible different optical wave-guiding properties. We have also reported in [2] about our approach for the position control of the ZnO nano-pillars on top of GaN micro-pyramids, where a high degree of scalability is achieved, thus enabling a consistent investigation of epitaxial parameters. As a further challenge, the epitaxial optimization of coaxial InGaN hetero-structures around our GaN nano-tubes was set. In addition to their non-polar characteristics with reduced Quantum Confined Stark Effect (QCSE), the afore-mentioned coaxial InGaN nano-hetero-structures could be optically interfaced to measure their luminescence response to surface conditions. An SEM picture of the afore-mentioned structure with coaxial InGaN layers is shown in Fig. 2. Due to the reduction of growth temperature to realize epitaxial InGaN

layers, the top part of the tubes was sealed by a pyramid-shape cap. In this study, we report on the challenges for generating highly luminescent coaxial InGaN layers with the help of photoluminescence and locally resolved cathodoluminescence characterization for a series of samples with and without coaxial InGaN layers of varying In content.

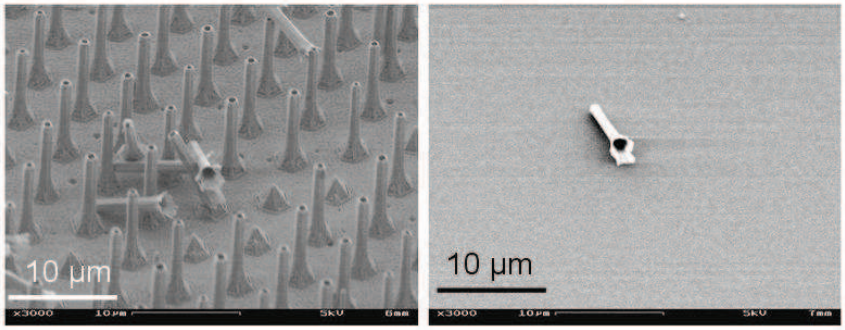

Fig. 1: SEM picture of single hollow GaN nano-tubes on top of GaN pyramids (left). Hollow GaN nano-tube separated on a sapphire substrate confirming the complete desorption of ZnO (right).

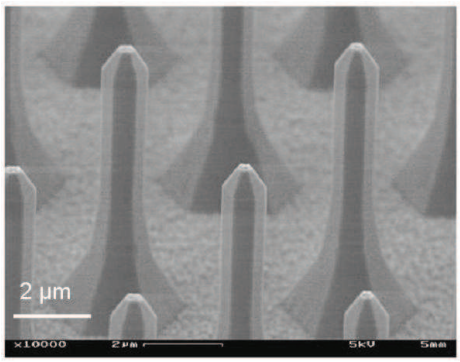

Fig. 2: SEM picture of single hollow GaN nano-tubes on top of GaN pyramids with epitaxial InGaN layers.

2. Experimental

Single ZnO nano-pillars used as templates in these studies with diameters of 150–300 nm and heights of 4–6 µm were grown using the vapor-transport on top of GaN pyramids. ZnO/carbon powder mixture and oxygen were used as precursors in a three heating zones furnace [3]. The GaN pyramids were patterned and subsequently grown using optical lithography and selective area epitaxy, respectively, in our AIXTRON AIX 200 RF low pressure MOVPE system with a SiO_2 mask of 5 µm openings [2]. Trimethylgallium (TMGa) and ammonia (NH_3) were used for the deposition of GaN layers around the well positioned ZnO pillars, whereas trimethylindium (TMIn) and triethylgallium (TEGa) have been used for the deposition of the quantum wells and the barriers. Low temperature photoluminescence measurements (around 18 K) were performed using a He-Cd laser with

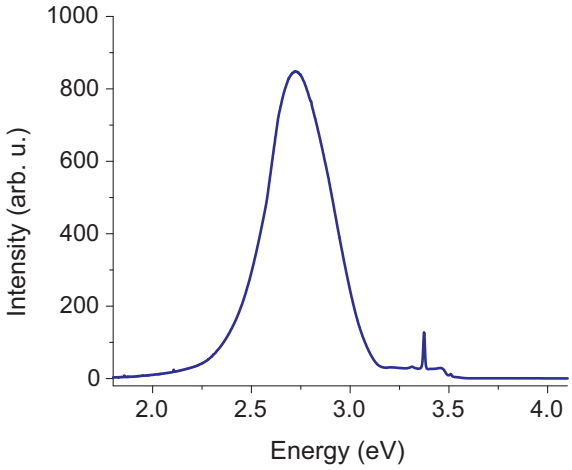

Fig. 3: Low temperature photoluminescence spectrum of a single coaxial InGaN layer around GaN nanotubes grown at 835 °C.

a wavelength of 325 nm and a spot size of around 150 µm. Locally resolved cathodoluminescence was performed at a temperature of 9 K employing excitation voltages between 2 and 5 keV and a detector window of 5 nm. The deposition of a single coaxial GaInN quantum well which was finally coated by a GaN layer was done at reduced growth temperatures ranging between 760 °C and 850 °C [2]. In order to examine the presence of InGaN layers, a series of samples epitaxially designed to have different In incorporations were developed. By mechanical contact, we were able to separate single rods on different substrates, where measuring the thickness of the tube was possible and consequently the growth rate of our GaN and InGaN layers was estimated to be 2.5 nm/min.

3. Photoluminescence and Cathodoluminescence Investigations

As reported in [4], due to the desorption of TMIn during growth, an Arrhenius plot of the indium incorporation coefficient k_{In} defined as

$$K_{\mathrm{In}} = \frac{x}{1-x} \cdot \frac{f_{\mathrm{TEGa}}}{f_{\mathrm{TMIn}}}. \tag{1}$$

is expected, where x is the In mole fraction in the InGaN layer[1], f_{TEGa} and f_{TMIn} are the molar flow rates of triethylgallium and trimethylindium, respectively. The coefficient is expected to increase with decreasing substrate temperature with an activation energy of 1.6 eV for c-plane growth [4] (Fig. 4 (left)). Although we are expecting InGaN growth on non-polar planes, we still expect a similar Arrhenius plot behavior but possibly with a different activation energy.

[1]We have evaluated the In mole fraction x by measuring the center peak position in low temperature photoluminescence where a thickness of 10 nm of InGaN layers was assumed, neglecting the piezoelectric field (since they are grown coaxially on non-polar planes) and assuming a conduction band offset of 40 %.

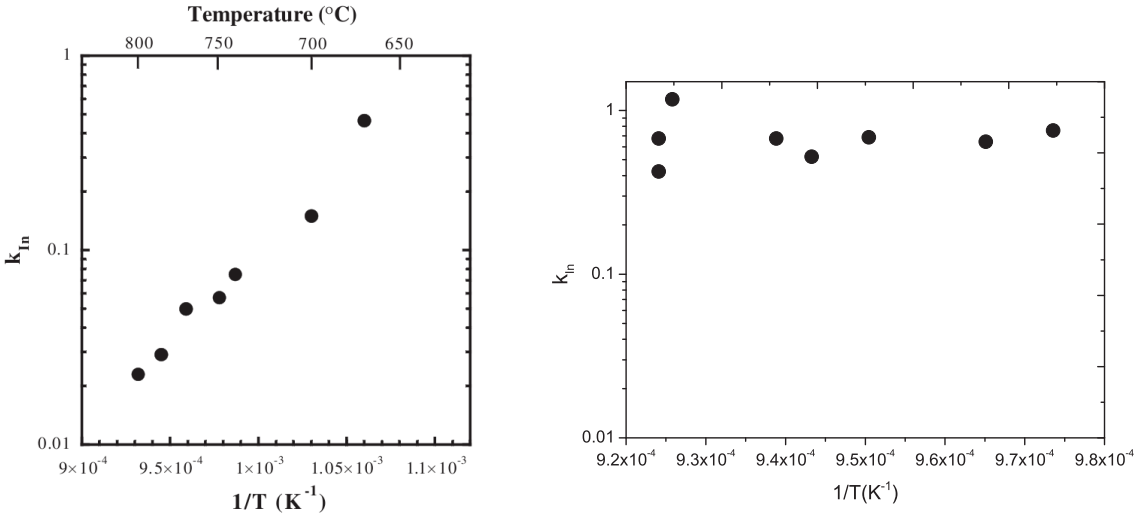

Fig. 4: Arrhenius plot of a series of InGaN layers grown at different temperatures on c-plane bulk GaN [4] (left) and a similar series of single coaxial InGaN layer around GaN nano-tubes related to a peak around 2.85 eV (right).

Figure 3 shows a PL spectrum for a coaxial InGaN layer grown at 835 °C. In order to check if the main peak at 2.85 eV is related to the InGaN layer luminescence, a series of growth temperatures and indium flows was examined. The corresponding data revealed a negligible shift with temperature (Fig. 4 (right)). This result indicated that another source of luminescence is dominant. As reported in [5] and [6], a similar peak has been always observed for Zn impurities in GaN and is attributed to transitions from a shallow donor or from the conduction band to a Zn_{Ga} acceptor level above the valence band edge. So our next approach was to examine the local luminescence distribution from single rods with and without InGaN layers by means of cathodoluminescence. We have separated single rods on TEM grids to exclude any parasitic luminescence from the substrate. The spectrum of a nano-pillar without a QW gave a similar peak at 2.85 eV with homogeneous distribution of luminescence (Fig. 5). This has confirmed that this peak is attributed to transitions to a Zn_{Ga} acceptor level of 0.4 eV above the valence band edge [6]. The luminescence at 2.85 eV for the rods with a single QW was less homogeneous and a new peak around 3.3 eV gave more localized luminescence near the top and bottom of the rod (Fig. 6). This indicated that the epitaxial structure is clearly different. We do believe that this peak at 3.3 eV originates from the InGaN layer (also supported by experiments described in the next section), however, the question remains why does it give higher luminescence from the top or bottom of the rod. Further investigations using CL are planned using different excitation voltages for clarification.

4. Investigations of InGaN Layers Around Thicker GaN Nano-tubes

We believe that a thin layer near the inner surface of the nano-tube is heavily doped with Zn_{Ga} acceptors as compared to deeper layers along the coaxial growth direction. This

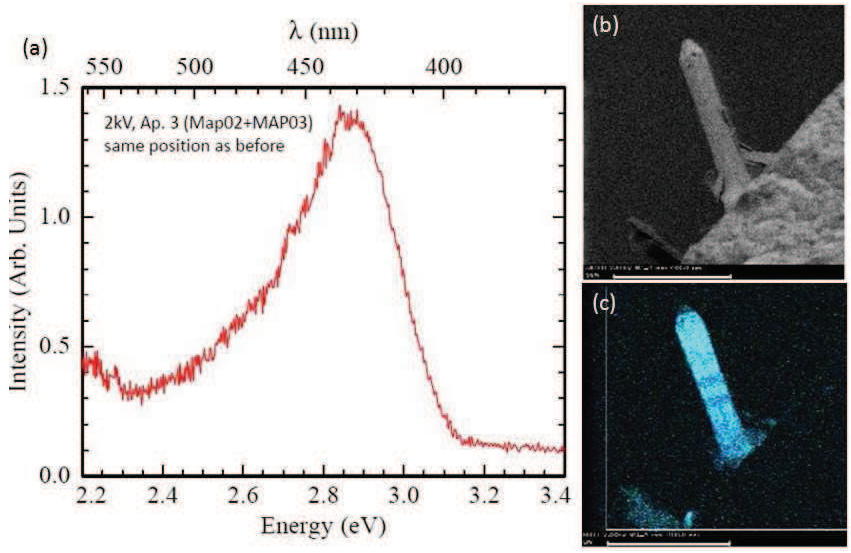

Fig. 5: Locally resolved cathodoluminescence distribution and spectrum from a single GaN nanotube without InGaN QW separated on TEM grid.

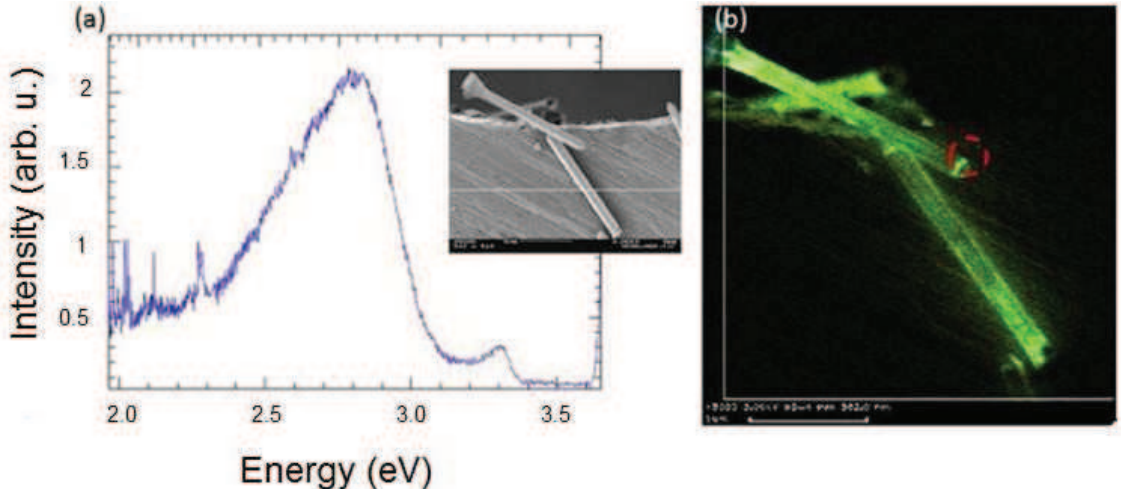

Fig. 6: Locally resolved cathodoluminescence distribution and spectrum from single GaN nanotubes with InGaN QW separated on TEM grid.

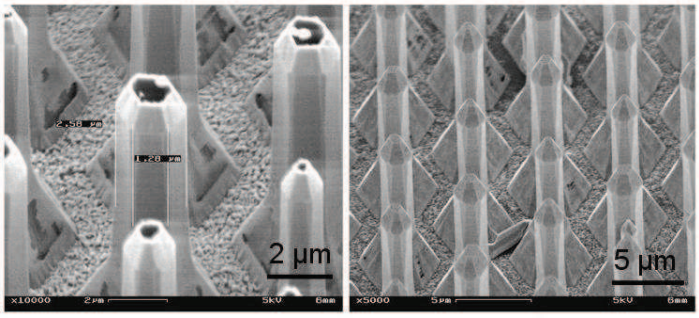

Fig. 7: SEM picture of thick hollow GaN nano-tubes on top of GaN pyramids (left). Thick GaN nano-tubes with a single QW of 10 nm (right).

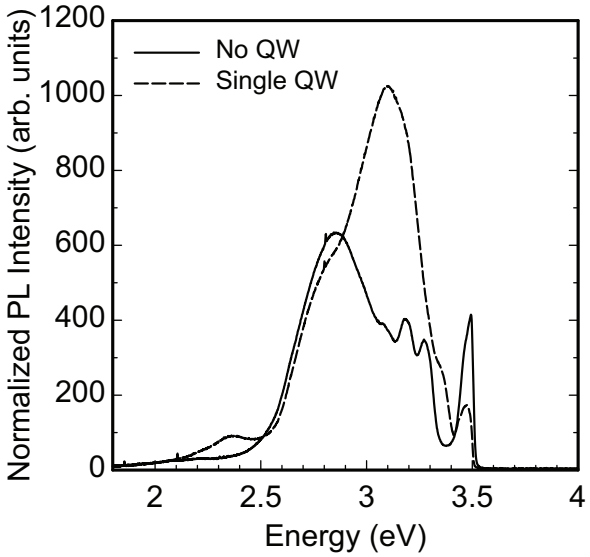

Fig. 8: Low temperature photoluminescence spectrum of thick GaN nanotubes with and without a single coaxial InGaN layer.

might be due to the fact that the growth rate of our layers is assumed to be much faster than the diffusion of Zn atoms through the material. This fact has been also reported in [7] using EDX investigation of the Zn concentration across the nano-tube structure.

As a counteract to this presumed effect, we tried to investigate thicker GaN nano-tubes where the QW is positioned further away from the inner tube surface. GaN nano-tubes with doubled wall thickness with and without a single QW were realized and compared (Fig. 7), where the same original ZnO template was used and the QW was grown at 800 °C. As shown in Fig. 8, the peak around 2.85 eV was observed in both samples whereas a highly luminescent new peak around 3.1 eV emerged for the sample with a single QW, corresponding to In incorporation of 10 %. Furthermore, another ZnO template was split into two halves and the InGaN layers were grown at 780 °C and 830 °C, respectively. The resulting PL spectrum at low temperature indicated a clear shift in the main peak with peak positions of 3.21 eV and 3.345 eV respectively (Fig. 9). This indicated an In incorporation of 7.5 % and 3.4 %, respectively. Comparing this result to the PL spectrum

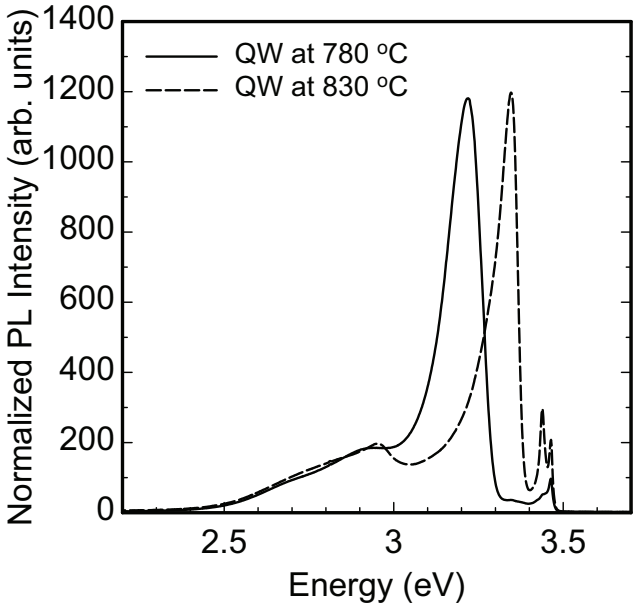

Fig. 9: Low temperature photoluminescence spectrum of thick GaN nanotubes with single coaxial InGaN layers grown at 830 °C and 780 °C.

in Fig. 7, we expected an In incorporation higher than 10 % for the sample grown at 780 °C. However, since the original ZnO template was different, we assume that the InGaN layer luminescence energy depends on the original ZnO template. These last results are to be confirmed by locally resolved cathodoluminescence measurements for single nano-pillars separated on TEM grids.

5. Conclusion

We reported about an investigation of epitaxial InGaN layers grown epitaxially around GaN nano-tubes on top of GaN micro-pyramids involving low temperature photoluminescence and locally resolved cathodoluminescence. An intense and broad peak centered around 2.85 eV is attributed to transitions from a shallow donor or from the conduction band to a Zn_{Ga} acceptor level above the valence band edge. This peak did not shift with varying InGaN layer growth temperature and TMIn flows and it had homogeneous luminescence distribution in locally resolved cathodoluminescence mapping for samples without InGaN layers. A thin layer near the inner surface of the nano-tube is believed to be heavily doped with Zn_{Ga} acceptors as compared to deeper layers along the coaxial growth direction. This layer is also assumed to prevent efficient carrier recombinations in the QW. A clear indication of In incorporation in low temperature PL was observed via an intense peak around 3.1 eV by growing double GaN layer thicknesses before the QW growth. Furthermore, a shift of a similar peak by growing at different InGaN layer growth temperatures from 3.34 eV to 3.21 eV supported the argument of In incorporation into the coaxial layers.

Acknowledgment

We like to thank Zhe Ren for his scientific contributions and investigations of the samples in this work throughout his master thesis, Manfred Madel for growing the ZnO nanopillars used in these studies, Ingo Tischer for undertaking the cathodoluminescence measurements, S.B. Thapa for his previous work on the epitaxial growth of GaN on ZnO as well as I. Argut for her assisstance with sample processing. This work has been partly financially supported by the Helmholtz Association within the project "PINCH Photonics".

References

[1] S.B. Thapa, J. Hertkorn, T. Wunderer, F. Lipski, F. Scholz, A. Reiser, Y. Xie, M. Feneberg, K. Thonke, R. Sauer, M. Dürrschnabel, L.D. Yao, D. Gerthsen, H. Hochmuth, M. Lorenz, and M. Grundmann, "MOVPE growth of GaN around ZnO nanopillars", *J. Cryst. Growth*, vol. 310, pp. 5139–5142, 2008.

[2] M. Fikry, M. Madel, I. Tischer, K. Thonke, and F. Scholz, "Luminescence properties of epitaxially grown GaN and InGaN layers around ZnO nanopillars", *Phys. Status Solidi A*, vol. 208, pp. 1582–1585, 2011.

[3] A. Reiser, V. Raeesi, G.M. Prinz, M. Schirra, M. Feneberg, U. Röder, R. Sauer, and K. Thonke, "Growth of high-quality, uniform c-axis-oriented zinc oxide nano-wires on a-plane sapphire substrate with zinc oxide templates", *Microelectron. J.*, vol. 40, pp. 306–308, 2009.

[4] Y. Kobayashi, V. Perez-Solorzano, J. Off, B. Kuhn, H. Gräbeldinger, H. Schweizer, and F. Scholz, "Investigations of growth of self-assembled GaInN islands on SiC substrate by metalorganic vapor phase epitaxy", *J. Cryst. Growth*, vol. 243, pp. 103–107, 2002.

[5] M.A. Reshchikov, and H. Morkoc, "Luminescence properties of defects in GaN", *J. Appl. Phys.*, vol. 97, pp. 061301-1–95, 2005.

[6] M.A. Reshchikov, A.A. Kvasov, M.F. Bishop, T. McMullen, A. Usikov, V. Soukhoveev, and V.A. Dmitriev, "Tunable and abrupt thermal quenching of photoluminescence in high-resistivity Zn-doped GaN", *Phys. Rev. B*, vol. 84, pp. 075212-1–14, 2011.

[7] J. Goldberger, R.R. He, Y. Zhang, S. Lee, H. Yan, H.J. Choi, and P. Yang."Single-crystal gallium nitride nanotubes", *Nature*, vol. 422, pp. 599–602, 2003.

Investigations on the Growth of AlN Heterostructures for UV Emitting Devices

Kamran Forghani

We report on the metalorganic vapor phase epitaxial (MOVPE) growth of AlN films on sapphire substrates. The effect of precursor flow rate and nucleation layer (NL) on the film quality was investigated. The films were characterized using AFM, XRD and PL. We could realize AlN films with very smooth surfaces and narrow symmetric XRD peaks indicating low screw/mixed type dislocation densities in the films. Moreover, PL spectra showed a very strong luminescence, confirming high crystalline quality of the optimized AlN films.

1. Introduction

AlGaN as a wide band gap semiconductor material has found increasing scientific and practical interest in the last few years. This is, in large part, due to its use in UV light emitting diodes (LEDs) as well as laser diodes (LDs). A common method in realizing high quality AlGaN epilayers with high Al content is to grow on AlN epilayers—serving as a template. The AlN templates are transparent for UV-LEDs based on $Al_xGa_{1-x}N$. The goal in this work is to realize high quality AlN films—suitable for AlGaN-based UV-B and UV-C LEDs—using metalorganic vapor phase epitaxy (MOVPE).

All samples investigated in this study were grown on (0001) sapphire substrates in a low pressure horizontal reactor (Aixtron AIX-200/4 RF-S). Trimethylaluminum (TMAl) was used as group-III precursor and ammonia as group-V precursor. Moreover, the investigated films have been grown by using a TaC coated graphite susceptor. This so called *high temperature setup* is capable of reaching temperatures up to about 1400 °C in our MOVPE reactor whereas the conventional *low temperature setup*—SiC coated graphite susceptor—can reach temperatures up to about about 1200 °C.

The growth of high quality AlN is much more challenging compared to GaN. Al has a higher sticking coefficient than Ga and the parasitic pre-reactions of the precursors are stronger in the case of MOVPE of AlN. Hence, these issues result in higher dislocation densities and poorer surface properties in AlN epilayers compared to the case MOVPE of GaN, causing deficiency of emitting devices grown on top of such templates. In this work we have investigated the effect of the TMAl flow rate and NL layer deposition temperature on the AlN epilayer properties.

2. Variation of TMAl Flow Rate

A lower growth rate may result in films with higher crystal qualities. At very high growth rates, there is not enough time for ad-atoms to make a complete AlN monolayer before the next atomic layer starts to grow on top. Conversely, at sufficiently low growth rates, there is an increase of capture time of ad-atoms to find suitable points to reside within the crystal structure. According to the work of Xie et al. [1], a strong improvement of crystal quality was achieved by reducing the TMAl flow rate. Therefore, we investigated the effect of the TMAl flow rate on the growth properties of our AlN films.

Table 1: The notable growth characteristics of AlN epilayers grown with different TMAl flow rates. TMAl molar flow rates here correspond to 25, 13 and 7 sccm gas flow from a bubbler kept at 17 °C. NH_3 molar flow corresponds to 240 sccm gas flow. The last column indicates the ratio between defect luminescence and NBE luminescence.

Sample	TMAl (µmole/min)	NH_3 (mmole/min)	$T_{proces.}$ (°C)	Thickness (nm)	Def. lum./NBE lum.
T1191AbH	3	10.7	1200	500	41
T1190AbH	5	〃	〃	〃	18.3
T1166AbH	10	〃	〃	〃	18.5

Table 2: Low temperature AlN:O nucleation layer conditions for investigations of AlN epilayers growth. For oxygen doping a mixture of oxygen and nitrogen was used. The carrier gas was hydrogen.

$T_{proces.}$ (°C)	Pressure (hPa)	TMAl (µmole/min)	NH_3 (mmole/min)	$N_{99.7}O_{0.3}$ (sccm)	Thickness (nm)
805	80	2.35	5.6	10	15

Three AlN samples have been grown at a process temperature[2] of 1200 °C with a film thickness of about 500 nm (see Table 1). The reactor pressure during the growth of these AlN epilayers was chosen to be 35 hPa which is much lower than the typical reactor pressures applied to the growth of GaN films. Lower reactor pressures mean faster gas flows and hence less time for undesired parasitic reactions in the gas phase above the substrate. These AlN films (500 nm thick) have been grown on an oxygen doped AlN nucleation layer (NL) (Table 2). The growth of AlGaN on such a NL results in high quality AlGaN films [2], and therefore it may be also suitable for the growth of high quality AlN films as well. The deposition temperature of such nucleation layers was lower than that of the sequential AlN films in order to accommodate the large lattice mismatch between the sapphire and AlN film.

According to the XRD investigations, although the (002) reflections of this series of samples were very narrow—with an FWHM below 50 arcsec—the asymmetric (102) reflections

[2] $T_{proc.}$ denotes the process temperature which is the temperature measured from the back side of the rotation tray by using a pyrometry system. In other word, this does not indicate the true temperature on top side of the susceptor or wafer surface ($T_{surf.}$).

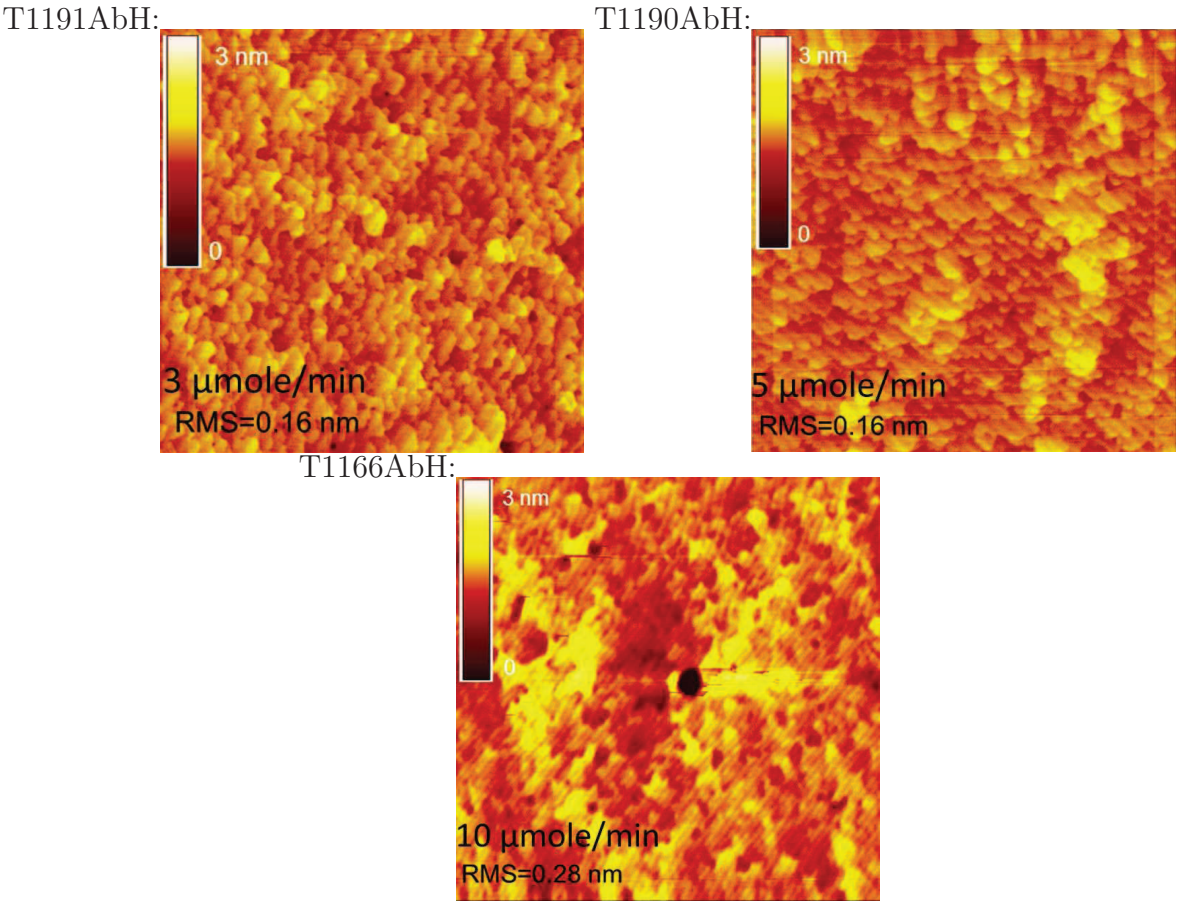

Fig. 1: $2\times2\,\mu m^2$ AFM investigations on the samples shown in Table 1 with different TMAl flow rates.

were very broad—approximately 5000 arcsec. Moreover, an intense defect related blue luminescence was visible in all samples. The sample grown with the lowest TMAl flow rate was the worst sample in this respect. The surface properties were visibly improved in the samples grown with reduced TMAl flow (T1190AbH) in which both big and small surface pits fairly disappeared (Fig. 1). In the sample with the lowest TMAl flow (T1191AbH), however, the small surface pits appeared again. The growth rate of these films show a linearly increasing trend with the increase of the TMAl flow rate as expected (see Fig. 2). Nevertheless, the growth rate is well below the predicted mass transport line which can be attributed to material loss due to gas phase pre-reactions on the heated susceptor during the growth process.

In summary, we could realize high quality AlN films based on an oxygen doped AlN nucleation layer. These AlN films have very smooth and (almost) pit-free surfaces in addition to very low level of mixed/screw type dislocations. Nonetheless, more optimization steps are necessary to reduce effectively the high level of twist and other types of crystal imperfections in our AlN films. For this purpose, we have optimized the nucleation layer deposition temperature as described in the next section.

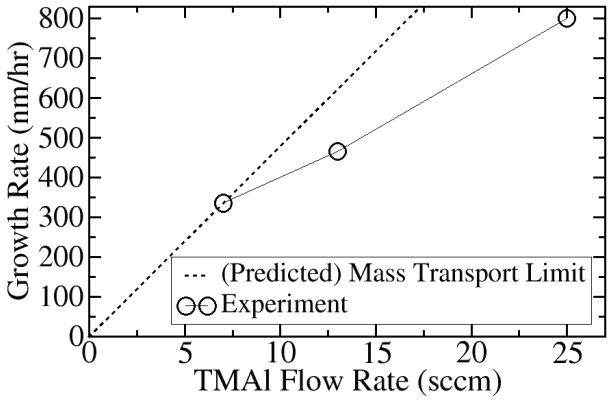

Fig. 2: Growth rate of the samples with different TMAl flow rates (Table 1).

3. Importance of the Nucleation Layer in AlN Epi-Films

It is expected that the nucleation layer (NL) plays an important role in reducing—or introducing—crystal imperfections in the epitaxial films as also observed by many groups in III-V nitrides, see e.g. [4–7]. As mentioned earlier, our NL is a thin AlN layer doped with oxygen. In this section, we tried to optimize the NL growth conditions starting from the NL deposition conditions for our high quality GaN films [3] as presented in Table 3 in order to grow AlN films. We investigated mainly the deposition temperature of the NL on the quality of AlN films. The nucleation layer deposition temperature ($T_{\text{surf.}}$) was varied between 825 and 890 °C (Table 3)[3]. About 500 nm thick AlN was grown with TMAl and ammonia molar flow rates (gas flow rates) of 10 µmole/min (25 sccm) and 10.7 mmole/min (240 sccm), respectively. The process temperature for growth of the AlN film was set to 1200 °C.

Table 3: Low temperature AlN:O nucleation layer conditions optimized for our high quality GaN to be adopted for AlN films. For oxygen doping a mixture of oxygen and nitrogen was injected into the reactor.

Pressure (hPa)	TMAl (µmole/min)	NH_3 (mmole/min)	$N_{99.7}O_{0.3}$ (sccm)	Thickness (nm)
80	4.7	11.2	10	25

We compare five samples having about 500 nm thick AlN grown on the NL as listed in Table 4. Moreover, Table 4 presents the FWHMs of the (002) and (102) reflections which were used to estimate the dislocation densities based on XRD investigations in our AlN films, as depicted in Fig. 4.

Generally, the investigated samples in this section exhibit a reduced defect luminescence to

[3]Surprisingly, despite the process temperature for both samples T1374AHa and T1249AHa was set to be 845 °C, the difference in wafer surface temperatures was 40 °C. Considering that sample T1374AHa has been grown two months after the other sample, this shows the importance of *in-situ* true surface temperature measurements in MOVPE reactors to assure the repeatability/reproducibility of the grown epilayers.

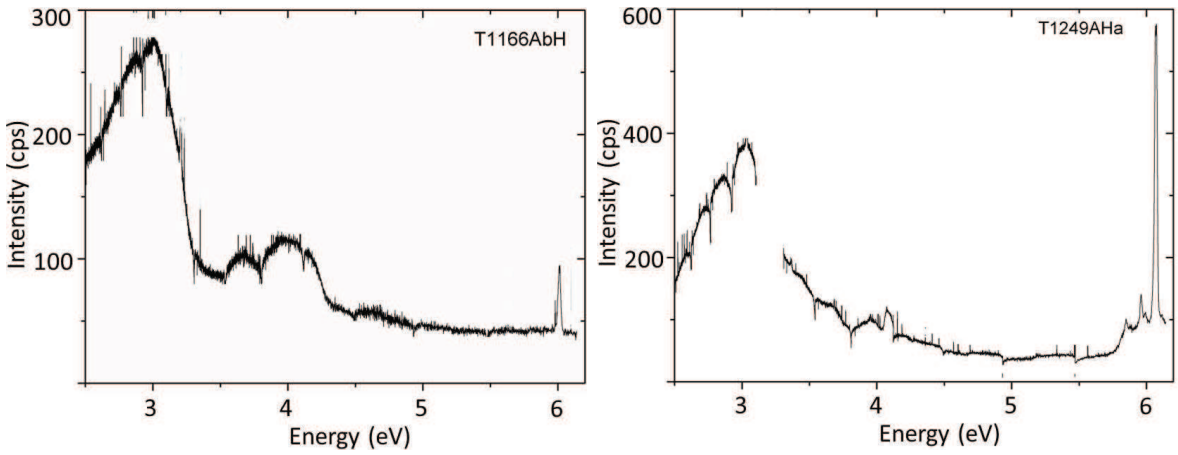

Fig. 3: PL spectra of samples T1166AbH and T1249AHa: The NBE luminescence is more intense in the sample with the NL deposited at a (process) temperature of 845 °C.

Table 4: The influence of wafer surface temperature during the NL deposition on the FWHM of (002) and (102) reflections and dominant D°X line broadening in PL of the 500 nm thick AlN films.

Sample	$T_{process}$	$T_{surface}$	(002)-FWHM	(102)-FWHM	PL-FWHM
T1346AHa	825 °C	850 °C	45”	1350”	9.2 meV
T1347AHa	845 °C	870 °C	125”	1400”	11.2 meV
T1345AHa	870 °C	895 °C	60”	1230”	8.6 meV
T1249AHa	845 °C	910 °C	60”	1600”	14.2 meV
T1354AHa	890 °C	925 °C	70”	1625”	14.6 meV

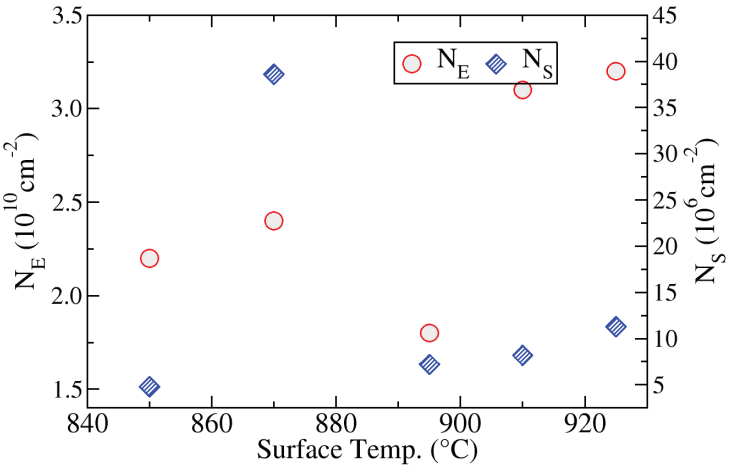

Fig. 4: The estimated screw/mix-type (N_S) and edge/mix-type (N_E) dislocation densities from XRD peak broadening, for the samples presented in Table 4.

NBE luminescence ratio compared to that of the films presented in the previous section—see Fig. 3 as an example.

The AlN epilayers with a NL deposition temperature of 895 °C (sample T1345AHa) showed the best results within this series with the narrowest (102) reflection (1230 arcsec)

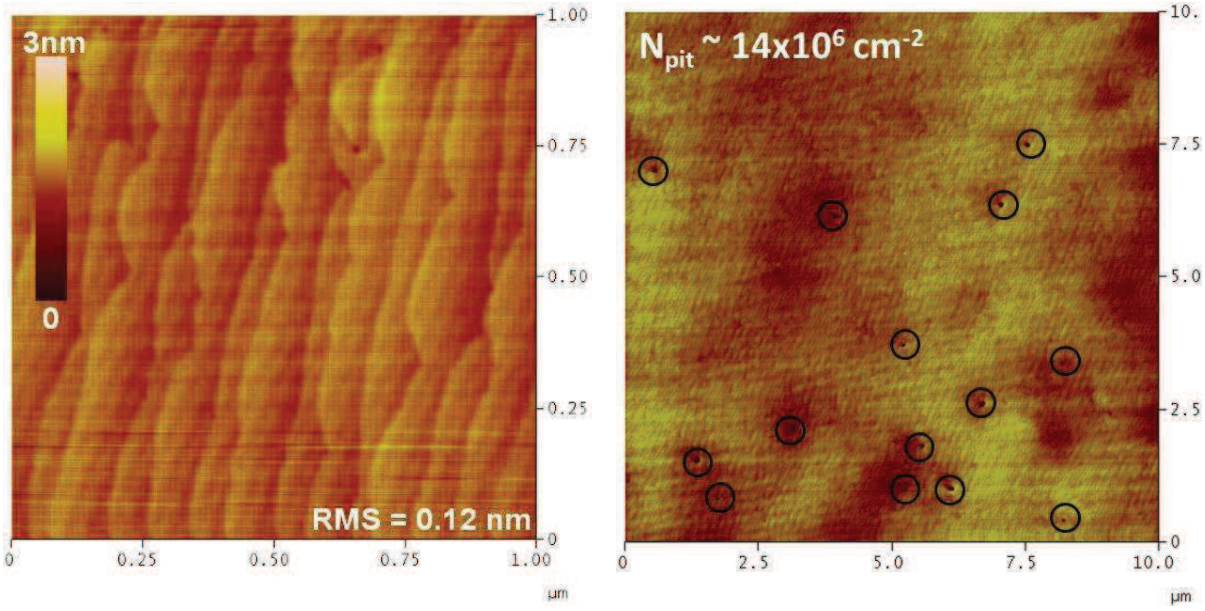

Fig. 5: $1\times1\,\mu m^2$ and $10\times10\,\mu m^2$ AFM investigations of the surface of a 500 nm thick AlN film (sample T1345AHa) grown on a NL deposited at a temperature of 895 °C.

corresponding to an estimated edge-type dislocation density of $1.8\times10^{10}\,cm^{-2}$. This sample also shows the narrowest PL peak (8.6 meV). This can be compared to 2 µm thick high quality AlN films from Onuma *et al.* [12] with an estimated edge-type dislocation density of $1\times10^{9}\,cm^{-2}$ in which the D°X line was 12 meV broad. There are several reports on recording narrower D°X lines in PL spectra of AlN films [8–11], nonetheless, those films were grown homoepitaxially (on AlN substrates) and therefore, they have much lower dislocation densities compared to our heteroepitaxial growth process. Sample T1345AHa exhibits also excellent surface properties with a surface RMS roughness of ≈ 0.1 nm (see Fig. 5). In this sample, the surface morphology is dominated by in-phase wandering steps and terraces [13]. The step heights are approximately 0.25 nm, corresponding to one mono-layer of AlN. Moreover, there are few pits visible in $10\times10\,\mu m^2$ AFM scans on the surface of this sample (Fig. 5). The pit density fits very well with the screw/mix type dislocation density in this sample (Fig. 4).

4. Conclusion

MOVPE growth of AlN was investigated in this work. We demonstrated that a low temperature AlN NL doped with oxygen is a very suitable NL to realize AlN films with very low levels of screw/mixed dislocations. By further optimizations of the NL deposition temperature, we observed a huge reduction of lattice twist corresponding to a reduction of mixed/edge-type dislocations. PL investigations showed a very intense and narrow NBE luminescence confirming the high quality of our AlN epi-films. The AlN films in our work are about 500 nm thick. Based on the work of S.B. Thapa [14], we expect that an increase of the AlN epilayer thickness results in further reduction of edge-type dislocations. Moreover, future work will include growth at higher temperatures on the NL

optimized in this work. This will certainly require lower V/III ratios to suppress parasitic gas phase reactions.

Acknowledgment

The assistance of Haoyuan Qi in characterization of the samples and respective evaluations is gratefully acknowledged. The author would like to thank B. Neuschl and K. Thonke from Institute of Quantum Matter (Semiconductor Physics Group) in University of Ulm for PL investigations. This work was financially supported by the German Federal Ministry of Education and Research (BMBF) within the framework of the "Deep UV-LED" project.

References

[1] Y.A. Xi, K.X. Chen, F. Mont, J.K. Kim, E.F. Schubert, C. Wetzel, W. Liu, X. Li, and J.A. Smart, "Optimization of high-quality AlN epitaxially grown on (0001) sapphire by metal-organic vapor phase epitaxy", *J. Electron. Mat.*, vol. 36, pp. 533–537, 2007.

[2] M. Klein, *Untersuchungen zur metallorganischen Gasphasenepitaxie von AlGaN-Heterostrukturen mit hohem Al-Gehalt*. Diploma Thesis, Ulm University, Ulm, Germany, 2009.

[3] J. Hertkorn, P. Brückner, T. Wunderer, F. Scholz, M. Feneberg, K. Thonke, R. Sauer, M. Beer, and J. Zweck, "Optimization of nucleation and buffer layer growth for improved GaN quality", *J. Cryst. Growth*, vol. 308, pp. 30–36, 2007.

[4] P. Jian-Hai, W. Xin-Qiang, C. Guang, L. Shi-Tao, F. Li, X. Fu-Jun, T. Ning, and S. Bo, "Epitaxy of an Al-droplet-free AlN layer with step-flow features by molecular beam epitaxy", *Chinese Phys. Lett.*, vol. 28, pp. 068102-1–4, 2011.

[5] D. Huantao, H. Yue, and Z. Jincheng, "Effect of nucleation layer morphology on crystal quality, surface morphology and electrical properties of AlGaN/GaN heterostructures", *J. Semicond.*, vol. 30, pp. 105002–105005, 2009.

[6] T. Nishida and N. Kobayashi, "Nucleation control in MOVPE of group III-nitrides on SiC substrate", *J. Cryst. Growth*, vol. 221, pp. 297–300, 2000.

[7] H. Amano, I. Akasaki, K. Hiramatsu, N. Koide, and N. Sawaki, "Effects of the buffer layer in metalorganic vapour phase epitaxy of GaN on sapphire substrate", *Thin Solid Films*, vol. 163, pp. 415–420, 1988.

[8] E. Silveira, J.J.A. Freitas, M. Kneissl, D.W. Treat, N.M. Johnson, G.A. Slack, and L.J. Schowalter, "Near-bandedge cathodoluminescence of an AlN homoepitaxial film", *Appl. Phys. Lett.*, vol. 84, pp. 3501–3503, 2004.

[9] M. Feneberg, R.A.R. Leute, B. Neuschl, K. Thonke, and M. Bickermann, "High-excitation and high-resolution photoluminescence spectra of bulk AlN", *Phys. Rev. B*, vol. 82, pp. 075208-1–8, 2010.

[10] B. Neuschl, K. Thonke, M. Feneberg, S. Mita, J. Xie, R. Dalmau, R. Collazo, and Z. Sitar, "Optical identification of silicon as a shallow donor in MOVPE grown homoepitaxial AlN", *Phys. Status Solidi B*, DOI 10.1002/pssb.201100381, 2012.

[11] M. Feneberg, B. Neuschl, K. Thonke, R. Collazo, A. Rice, Z. Sitar, R. Dalmau, J. Xie, S. Mita, and R. Goldhahn, "Sharp bound and free exciton lines from homoepitaxial AlN", *Phys. Status Solidi A*, vol. 208, pp. 1520–1522, 2011.

[12] T. Onuma, T. Shibata, K. Kosaka, K. Asai, S. Sumiya, M. Tanaka, T. Sota, A. Uedono, and S.F. Chichibu,"Free and bound exciton fine structures in AlN epilayers grown by low-pressure metalorganic vapor phase epitaxy", *J. Appl. Phys.*, vol. 105, pp. 023529-1–7, 2009.

[13] K. Yagi, H. Minoda, and M. Degawa, "Step bunching, step wandering and faceting: self-organization at Si surfaces", *Surf. Sci. Rep.*, vol. 43, pp. 45–126, 2001.

[14] S.B. Thapa, *Studies of AlN grown by MOVPE for Electronic and Optoelectronic Applications*. Ph.D. Thesis, Ulm University, Ulm, Germany, 2010.

Enhancing GaN Self Separation in HVPE by Use of Molybdenum

Martin Klein

We prepared 2"-GaN wafers as templates for a self separation process which is happening during cooldown after growing thick layers of GaN in our hydride vapor phase epitaxy (HVPE) reactor. Our templates process starts with GaN grown by metalorganic vapor phase epitaxy (MOVPE) directly on sapphire. These GaN layers are getting masked with 200nm of SiN that is structured by means of optical lithography. These masks are subsequently overgrown with a thin GaN layer by MOVPE. When overgrowing these templates with thick layers of GaN in HVPE, several problems occur. Because of GaN nucleation on the wafer side, the top layer is clamped to the sapphire substrate. This hinders separation during cooldown. Moreover mis-shaped material is growing at the wafer edge in very long growth runs. Both problems can be addressed by using molybdenum to locally influence the V-III ratio during growth.

1. Introduction

Becoming a more and more common material, galliumnitride (GaN) still suffers from the lack of suitable substrates. This leads to the need for heteroepitaxy in mid and low price applications. Although homoepitaxy is used for producing blue lasers, available GaN substrates are much too costly for growing LEDs and transistors. To achieve affordable homoepitaxial substrates, great efforts have been made in the field of ammonothermal growth [1]. Yet thick layers grown by HVPE are still a good candidate to provide GaN wafers for future industrial processes. Although being under research for some time, producing such layers is still not a trivial task. Differences in the thermal expansion coefficients of GaN and sapphire result in big layer curvatures and the large mismatch in lattice constants leads to strain and defects in the GaN layer. In order to cope with these problems, several methods have been developed to remove the GaN layer from the substrate such as laser-lift-off (LLO) [2], mechanical polishing [3] or growth on etchable substrates like GaAs [4] and ZnO [5]. Our approach is to use the difference in thermal expansion coefficients to get a self separation of layer and substrate during cooldown. With our self fabricated MOVPE templates we create weak interlayers which define a breaking point for the separation at a predetermined position. In the last years our institute has developed a standardized procedure to create suitable templates [6].

Unfortunately overgrowing these templates in HVPE seldom leads to wholly intact 2" self separated layers. While the separation layer seems to work very well in the center of the wafer, we still get small pieces of separated material at the wafer edges. The origin of

this effect can be found in the nucleation of GaN on the wafer side. Growth on the wafer sidewall results in a clamping of the top layer (Fig. 1) which prevents the top layer to separate from the substrate. The adhesion of the surplus material seems to be greater than the layer stability, leading to a burst of the separating layer.

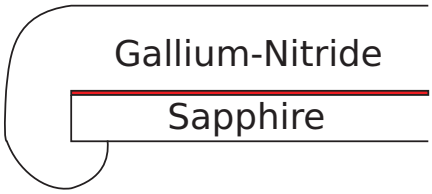

Fig. 1: Clamping top layer.

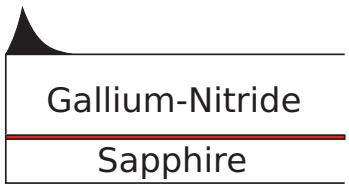

Fig. 2: Polycrystalline edge.

Another unwanted growth effect occurs alongside the wafer edge because of the horizontal design of our reactor. With the ammonia feed horizontally and GaCl being provided by a showerhead we get very high V-III ratios at the upstream wafer edge. GaN formed in long growth runs in this special zone possesses inferior properties such as many hexagonal pits and crystallites (Fig. 2). This effect reduces the usable area of the resulting pseudo substrate.

By simply covering the wafer edge with a metallic ring, the nucleation on the wafer sidewall can be prevented. From earlier experiments we know that molybdenum has the seldom ability to survive HVPE process conditions. Additionally some publications indicate that molybdenum could be able to bind ammonia by turning to molybdenum-nitride [7] thus lowering the V-III ratio in its vicinity. Therefore we studied the possibility of reducing parasitic edge effects by applying a molybdenum ring during growth.

2. Application of a Massive Molybdenum Ring to Prevent Growth on the Wafer Sidewalls

In the first attempt we used a wide ring of molybdenum which covers the whole rotation disc around the wafer (Fig. 3). By this approach the rotation disc is also protected against degradation due to parasitic nucleations on the disc, levering out pieces of quartz during cooldown after long growth runs.

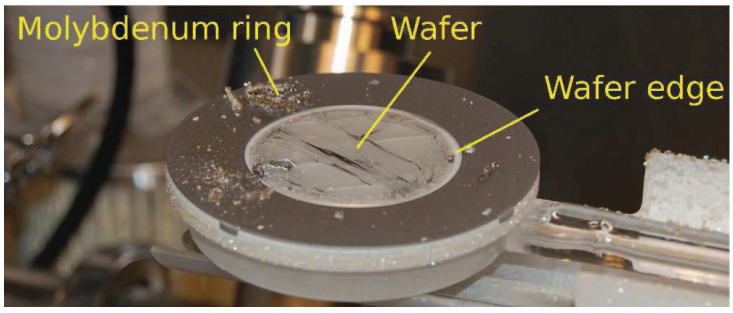

Fig. 3: First try with a completely covered rotation disc.

This first try already had the desired effect of preventing nucleation on the wafer side. Additionally no growth took place in a 1 mm broad ring at the wafer edge. As a third effect the wafer cracked during growth and the cracks filled with metallic gallium. This usually happens when the V-III ratio is extremely low. As the recipe has not been altered compared to previous growth runs, these facts indicate that the large molybdenum surface has taken ammonia from the process, a lot more than originally intended.

To decrease this effect we started using smaller molybdenum rings. We tried rings with a width of 4 mm and 2.5 mm. The latter one is the smallest considered to be mechanically stable in our HVPE process. With these smaller rings we were able to grow 300 µm thick, crackfree samples, which is the largest thickness being stable at room temperature. These samples still have a growth-free ring along the edge and thus are guaranteed to prevent clamping. However, growth with no clamping and covering the full 2" wafer would be preferred. This can be achieved by increasing the ammonia flow by 50 %. Unfortunately this change in the flow pattern increases the current thickness inhomogeniety compared to our standard process (Fig. 5). To prevent this, further optimization will be necessary.

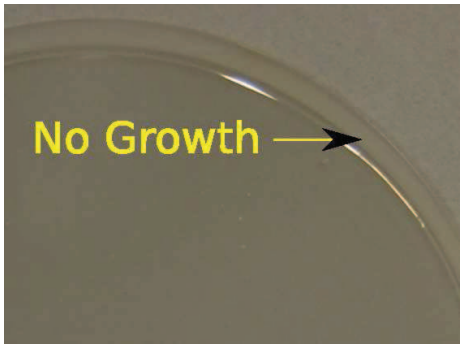

Fig. 4: Standard sample with Mo ring.

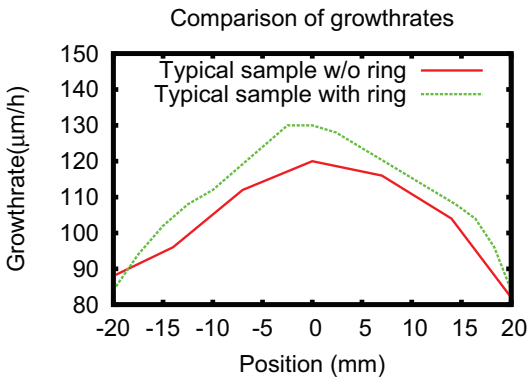

Fig. 5: Standard growth without and growth with mo-ring and additional ammonia.

Next we applied this new growth process to our self separation templates. Unfortunately the self separation didn't work with the molybdenum being applied already from the start of the HVPE growth. The ring seems to alter the growth conditions in a way that the weakened interlayer isn't able to develop properly which normally happens in the first few micrometers of HVPE growth. As a consequence we started HVPE growth without the molybdenum ring and applied the ring in a second, longer growth step resulting in the intended wafer thickness. This procedure however requires cooling down after the first growth step and a reconditioning of the reactor. This two step process makes the HVPE growth long and complicated.

Figs. 6 and 7 show a comparison of two self separation samples, one grown with and one without help of a molybdenum ring. Both samples have been grown on the same type of template. In both cases the growth has been designed as two-step growth with reactor reconditioning for a better comparison. The only difference in the recipe is the higher ammonia flow in the growth with molybdenum ring to compensate the effect of the ring on the V-III ratio. Although thickness homogeniety of the sample grown with

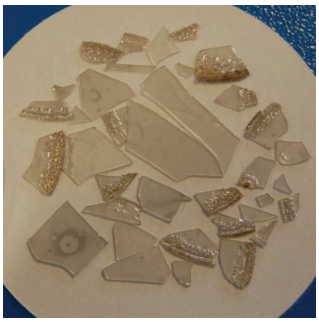

Fig. 6: Separated layer without ring.

Fig. 7: Separated layer with ring.

ring is worse than of the sample grown without molybdenum ring, the sample with ring has broken into considerably fewer pieces. Especially the size of the parts belonging to the layer edge is significantly larger. Thus the molybdenum ring is a great improvement towards separating whole 2" wafers. It can also be noticed that no mis-shaped material has grown along the wafer edge.

3. Application of a Sputtered Molybdenum Ring to Prevent Growth on the Wafer Edge

As seen in chapter 2, a massive molybdenum ring stable enough to withstand HVPE process conditions has some negative effects on GaN growth in general. To gain better control of the effect, we sputtered a thin layer of molybdenum on top of the MOVPE template and structured it by means of optical lithography and lift-off so that only a very small ring along the wafer edge was left (Fig. 8). The thickness of the sputtered molybdenum amounts to 150 nm in the first experiments.

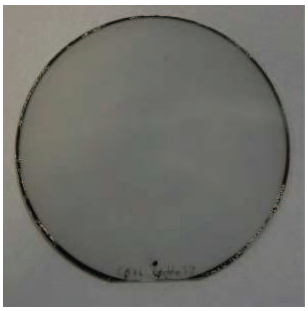

Fig. 8: MOVPE template with sputtered molybdenum ring.

Such templates have been overgrown with 80 µm and 200 µm GaN in HVPE, respectively. For the sample overgrown with 80 µm of HVPE GaN, a distance of about 600 µm width free of GaN can be seen in the SEM picture (Fig. 9, left sample). Growth on the sapphire side however doesn't seem to be affected by the topside ring of molybdenum. For the 200 µm thick sample this distance is covered with polycrystalline material (Fig. 9, right sample). We think that this is caused by a consumption of the sputtered molybdenum

during growth. Molybdenum is converted to molybdenum nitride which is barely stable at process temperatures and thus dissolves or evaporates and is carried to the exhaust by the gas stream.

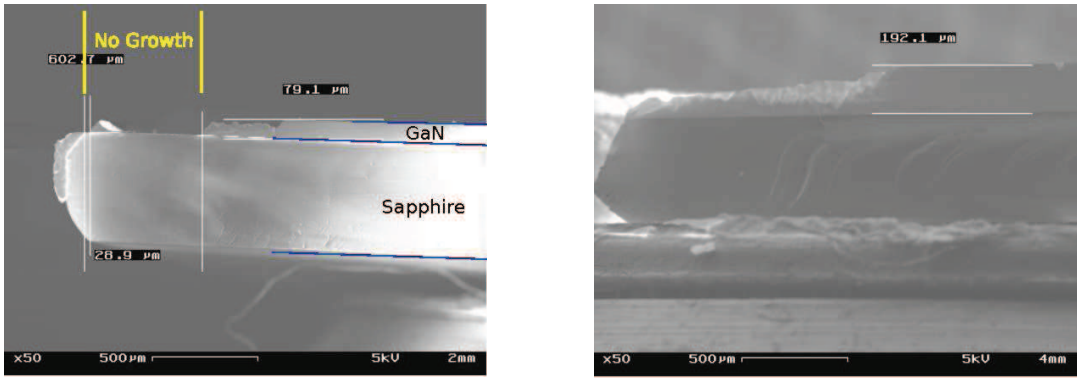

Fig. 9: SEM cross section, 80 µm and 200 µm GaN growth with sputtered molybdenum ring.

The formation of polycrystalline growth can even be seen macroscopically for self separated GaN layers. For most separated pieces this polycrystalline ring has broken off before removal of the sample from the machine, thus posing no obstacle in the separation process. However it still reduces the usable surface of the separated sample. Additionally the effect of the sputtered molybdenum in its present state is not strong enough to prevent the mis-shaped growth along the wafer edge. Next we want to try to deposit thicker molybdenum layers, the problem herein lies in the long deposition times and the poor adhesion of molybdenum to the wafer during lift-off.

4. Conclusion and Outlook

We have shown that molybdenum is most likely influencing the local V-III ratio in ammonia based epitaxy by drawing ammonia from the process. We have used this effect to improve the properties of our self separed GaN layers. However using solid molybdenum rings in combination with our method to produce weakened interlayers result in the necessity to split growth into two steps, making the process quite complex and time-consuming.

When using a thin, sputtered Mo layer instead of a solid Mo ring, no two-step growth is needed and all process parameters can be taken from the standard growth without molybdenum applied. However with the molybdenum being consumed, this method is not as effective as applying a solid Mo ring, in particular for thick layers to be grown. Some area of the 2" wafer is lost to bad growth.

For future investigations one should use solid molibdenum that is only partly exposed to the process environment to take advantage of a stable molybdenum source and having good control over the effect intensity. A possible setup to achieve this would be a modified rotation disc for the HVPE system that can hold a sapphire wafer in a defined position on top of a molybdenum plate or ring.

Acknowledgment

I want to thank I. Argut for preparing the separation templates and doing all lithography connected with the sputtered molybdenum experiments. The help in preparing the solid molybdenum parts by R. Rösch is also gratefully acknowledged. Thanks also go to D. Maier from the Institute of Electron Devices and Circuits for doing the sputtering. This work was financially supported by Freiberger Compound Materials GmbH, Freiberg.

References

[1] R. Dwilinski, R. Doradzinski, J. Garczynski, L. Sierzputowski, R. Kucharski, M. Zajac, M. Rudzinski, R. Kudrawiec, J. Serafinczuk, and W. Strupinski, "Recent achievements in AMMONO-bulk method", *J. Cryst. Growth*, vol. 312, pp. 2499–2502, 2009.

[2] C.R. Miskys, M.K. Kelly, O. Ambacher, and M. Stutzmann, "Freestanding GaN substrates and devices", *Phys. Status Solidi C*, vol. 0, pp. 1627–1650, 2003.

[3] S. Nakamura, M. Senoh, S. Nagahama, N. Iwasa, T. Yamada, T. Matsushita, H. Kiyoku, Y. Sugimoto, T. Kozaki, H. Umemoto, M. Sano, and K. Chocho, "InGaN/GaN/AlGaN-based laser diodes with cleaved facets grown on GaN substrates", *Appl. Phys. Lett.*, vol. 73, pp. 832–834, 1998.

[4] K. Motoki, T. Okahisa, N. Matsumoto, M. Matsushima, H. Kimura, H. Kasai, K. Takemoto, K. Uematsu, T. Hirano, M. Nakayama, S. Nakahata, M. Ueno, D. Hara, Y. Kumagai, A. Koukitu, and H. Seki, "Preparation of large freestanding GaN substrates by hydride vapor phase epitaxy using GaAs as a starting substrate", *Jpn. J. Appl. Phys.*, vol. 40, pp. L140–L143, 2001.

[5] F. Lipski, S.B. Thapa, J. Hertkorn, T. Wunderer, S. Schwaiger, F. Scholz, M. Feneberg, M. Wiedenmann, K. Thonke, H. Hochmuth, M. Lorenz, and M. Grundmann, "Studies towards freestanding GaN in hydride vapor phase epitaxy by in-situ etching of a sacrificial ZnO buffer layer", *Phys. Status Solidi C*, vol. 6, pp. 352–355, 2009.

[6] F. Lipski, T. Wunderer, S. Schwaiger, and F. Scholz "Fabrication of freestanding 2"-GaN wafers by hydride vapour phase epitaxy and self-separation during cooldown", *Phys. Status Solidi A*, vol. 207, pp. 1287–1291, 2010.

[7] P. Ettmayer, "Das System Molybdän-Stickstoff", *Monatshefte für Chemie*, vol. 101, pp. 127–140, 1970.

Wafer Bow of Freestanding GaN Substrates Grown by Hydride Vapor Phase Epitaxy

Frank Lipski and Ferdinand Scholz

Free-standing GaN wafers grown by hydride vapor phase epitaxy are typically concavely bowed. In situ *and* ex situ *curvature measurements indicate that some strain developing at the very beginning of the epitaxial process or even in the template grown by metalorganic vapor phase epitaxy may be the origin of this bow. It can be only partly released by etching the defective back-side of the samples indicating that the strong dislocation density gradient is not the only reason for strain in free-standing GaN.*

1. Introduction

GaN-based light emitting diodes are flooding the consumer market as they recently have reached excellent efficiencies [1]. For such LEDs, still foreign substrates like sapphire are the substrate of choice owing to their cheap price and their excellent availability in large amounts and best quality, although high threading dislocation densities in the range of at least $10^8\,\mathrm{cm}^{-2}$ must be accepted as a consequence of the substantial lattice mismatch between GaN layer and substrate. However, such huge defect densities are not acceptable for GaN based laser diodes, causing short lifetimes of these devices driven at comparably large current densities. For lower defect densities, GaN substrates are required which enable a homo-epitaxial solution. Due to the high melting point and huge equilibrium vapor pressure of GaN, it cannot be grown easily as a bulk substrate.

Therefore, different approaches have been developed over the recent years to realize low-defect-density GaN wafers. The simplest and most successful approach makes use of hydride vapor phase epitaxy (HVPE), where growth rates of several $100\,\mu\mathrm{m/h}$ and hence layers of several mm thickness can be obtained. This process also starts on foreign substrates causing several problems which are not yet solved completely. Fortunately, the above mentioned high dislocation density incorporated into these wafers at the beginning of growth is reduced to values below $10^6\,\mathrm{cm}^{-2}$ at the final surface due to dislocation annihilation processes [2], which is well acceptable for laser diodes. However, the large difference of the thermal expansion coefficients leads to a huge strain during cool-down of the wafer after epitaxy, which for several hundred micrometer thick layers cannot be accommodated elastically and typically causes cracking of the GaN layer into many small pieces. By a careful process optimization, the strain can be used to trigger a self-separation process resulting in free-standing GaN wafers (see, e.g. [3]).

After the substrate removal, the thick GaN wafers are expected to be stress-free. However, surprisingly such free-standing wafers typically are significantly bowed (c.f. [4]) making

further device epitaxy and processing difficult. Although commercially available wafers are typically polished to provide a flat surface, the bowing is still visible by a radially varying inclination of the lattice planes with respect to the flat surface. This will mask procedures where a slight mis-orientation of the wafer leads to optimized epitaxial results.

In order to understand this bow and eventually get inherently flat free-standing GaN layers with unbowed crystal planes, we have investigated the curvature and strain of HVPE grown GaN layers in a wide thickness range, its development during the epitaxial process and possible methods which might influence the wafer bow afterwards.

2. Experimental

The HVPE-growth was performed on templates grown in an Aixtron 200/4 RF-S metal organic vapor phase epitaxy (MOVPE) system on (0001) sapphire with a miscut of 0.3 ° towards the a-plane, a thickness of 430 µm and a diameter of 2". For defect-reduction an *in situ* SiN_x-layer was deposited during the growth of the GaN-buffer [5]. On these templates, a SiN_x layer was deposited *ex situ* by plasma-enhanced chemical vapor deposition (PE-CVD) and processed into a honeycomb-like mask structure by conventional lithography and dry etching in order to facilitate self-separation of the thick GaN layers grown later on these structures by HVPE [3]. Then, the samples were put back into the MOVPE system to initiate lateral growth starting from the open trenches in the mask partly covering the masked area. Although this step could also be done in the later HVPE growth, we preferred to include this extra MOVPE growth which provided a more reliable high quality overgrowth of the masked samples. Then, the samples were loaded into our HVPE reactor, a commercial Aixtron single-wafer HVPE system with a horizontal quartz reactor heated by a five zones furnace. Here, we applied our standard growth conditions as described earlier [3, 6] using ammonia and GaCl, formed *in situ* by streaming HCl gas over a liquid elemental Ga source, as N and Ga precursors, respectively. We adjusted the growth rates to be about 100 µm/h at 1050 °C. Thin layers remained connected to the sapphire wafer, whereas GaN layers with thicknesses above about 500 µm cracked off the substrate along the structured SiN_x mask layer resulting in free-standing GaN samples. The resulting GaN layers showed excellent properties with very sharp spectral lines in high resolution x-ray diffraction, low temperature photoluminescence (donor-bound excitonic line below 500 µeV) and low dislocation densities (below $10^6\,cm^{-2}$ for the mm-thick layers) [3].

For *in situ* measurements of the curvature, a LayTec EpiCurve sensor was adapted to our HVPE system where much higher bowing of the wafers is expected as compared to MOVPE reactors. Unfortunately, such *in situ* measurements could only be performed up to GaN thicknesses of 50–80 µm, because the surface of HVPE layers typically get increasingly bumpy degrading the quality of the reflected laser beams of the curvature sensor and eventually preventing the determination of their distance. The curvature of the layers was also measured *ex situ* after growth by comparing the x-ray diffraction peak angles of several slightly different positions on the samples. Hence the bowing of the crystal planes could be directly determined irrespective of any thickness variations which might disturb optical curvature measurements. The strain in the samples at the final

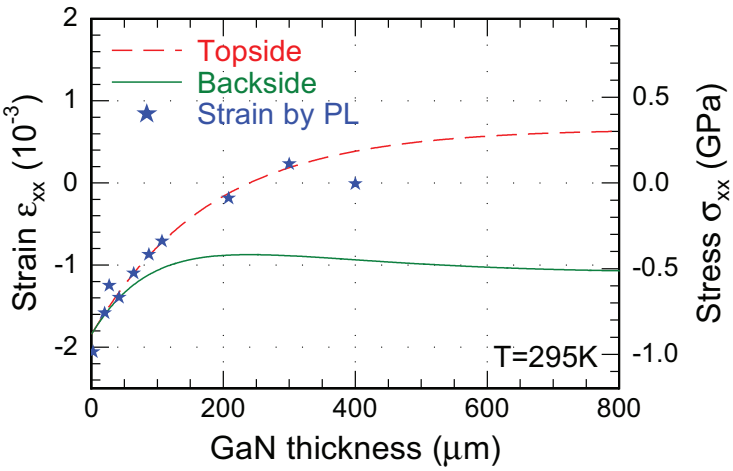

Fig. 1: Room temperature calculated in-plane strain (left axis) and stress (right axis) of GaN layers of various thicknesses grown on a 430 µm thick sapphire wafer at the GaN surface (broken red line) and at the layer-substrate interface (full green line) as compared to data measured by low temperature PL (blue stars).

surface could additionally be determined from the position of the donor-bound excitonic line measured by low-temperature photoluminescence (PL; $T \approx 15$ K) following the data published by Fu et al. [7]. The *ex situ* measurements have been typically performed on small pieces of the 2" wafers comparable in size and shape which we assumed to be spherically bowed, whereas the curvature of strongly bowed wafers may be influenced by the wafer size for larger areas. For the *in situ* measurements this can be neglected because of the only small curvature values obtained under these conditions.

3. Strain and Bow of Grown Layers

Owing to the difference in the thermal expansion coefficients between GaN and sapphire and the resulting stress, GaN layers still connected to a 430 µm thick sapphire wafer show a strong convex bowing at room temperature. Starting with the simplest assumption that they are flat during growth, we have determined the expected strain and bow at room temperature following an approach published by Etzkorn and Clarke [8]. The elastic coefficients needed in these calculations have been taken from [9], whereas the thermal expansion coefficients were taken from [10].

Figure 1 shows the in-plane strain (left axis) and stress (right axis) at the layer surface as well as at the substrate-layer interface expected at room temperature in such bowed samples. Data measured by PL on GaN layers still connected to the sapphire substrate coincide quite well to the surface values.

The curvature expected under those assumptions is plotted as a function of the layer thickness in Fig. 2. However, the curvature measured at room temperature by x-ray diffraction on the same samples deviates significantly from these data. In order to solve this problem, we have measured the curvature of such samples and its development *in*

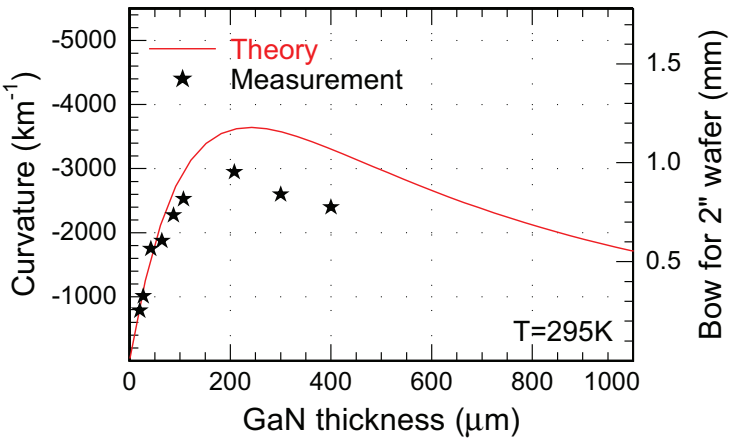

Fig. 2: Wafer bow at room temperature (full red line) determined from the calculated strain data (Fig. 1) as compared to data measured by x-ray diffraction (black stars).

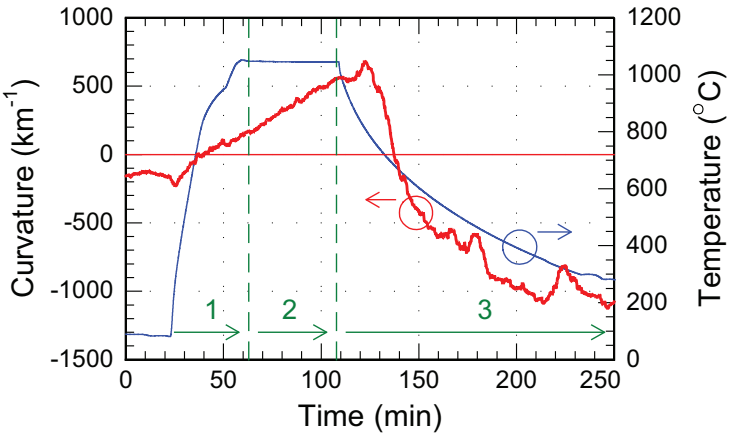

Fig. 3: Development of curvature measured *in situ* during the HVPE run (red line). The blue line shows the temperature profile during the growth process: Phase 1: Heatup; Phase 2: Growth; Phase 3: Cool-down.

situ during the HVPE growth (Fig. 3). For the beginning of the growth process where such measurements can be obtained (see section 2.), we typically find a linear increase of the curvature with a slope of about $6.8\,\mathrm{km}^{-1}/\mu\mathrm{m}$, i.e. the wafer does not stay flat during growth. As shown in Fig. 4, the *in situ* measured curvature (green squares) fits well to the difference of the *ex situ* measured curvature to the expected values depicted in Fig. 2 (brown circles). It can be explained by an in-plane strain of about $5 \cdot 10^{-4}$ (full blue line), already being present during growth. Obviously, it is then frozen in the samples and hence determines the curvature of the GaN layer after separation from the sapphire wafer.

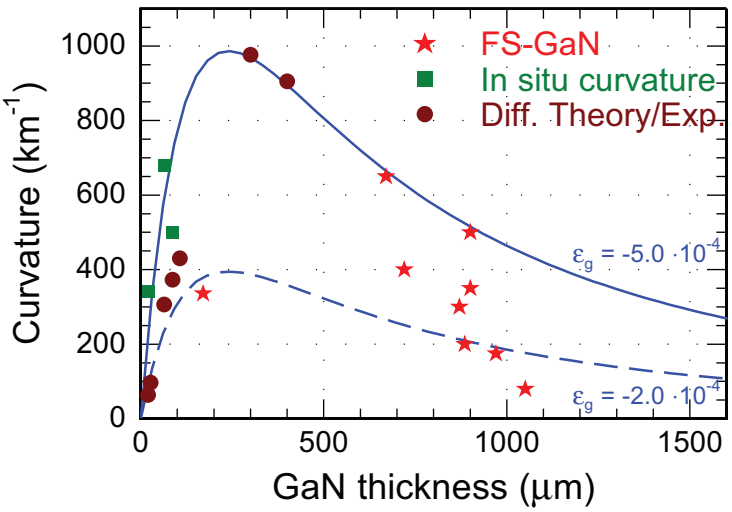

Fig. 4: Curvature of GaN layers measured *in situ* during HVPE growth (green squares) and difference of the *ex situ* measured curvature to the expected values depicted in Fig. 2 (brown circles) versus layer thickness. The full and broken blue lines show the curvatures which are expected for a tensile in-plane strain of about $5 \cdot 10^{-4}$ and $2 \cdot 10^{-4}$ of the GaN layer, respectively. The red stars show *ex situ* measured curvature data of free-standing wafers.

4. Bow of Free-Standing GaN

Normally, such strain results from different lattice constants on the top and the back side of the sample, which in many cases is caused by different thermal expansion coefficients of the two materials of a bi-layer system as discussed above. However, it is not clear what could make such differences in free-standing GaN which is expected to be fairly homogeneous through-out. Indeed, we found that the curvature, once established, does not change between room temperature and 1000 °C (Fig. 5) ruling out any gradients of the thermal expansion coefficient over the wafer thickness. Moreover, it shows that the wafer bow and the responsible strain cannot be easily annealed even after the sapphire wafer is removed which is regarded as the primary cause of any built-in strain.

What else could be responsible for this built-in strain? Free-standing GaN grown by HVPE typically contains a strong gradient of defect density. At the beginning of growth, the layer starts with a dislocation density in the range of at least $10^8\,\mathrm{cm}^{-2}$ to $10^9\,\mathrm{cm}^{-2}$ as a consequence of the hetero-epitaxy on sapphire. As already mentioned, this number decreases steadily during growth by defect annihilation [2] ending somewhere below $10^6\,\mathrm{cm}^{-2}$ for mm-thick layers [3]. In order to study the influence of this dislocation density gradient on the strain and bow of our free-standing GaN samples, we have removed the back-side by etching with molten KOH at 360 °C. This etchant only attacks the N-face, hence the back-side of the GaN layers, whereas the front Ga-face remains fairly unetched. This chemical etching should not have any direct influence on the bowing in contrast to mechanical polishing. Indeed, the curvature can be decreased by this procedure (Fig. 6, left). We found a linear behaviour between the change in curvature and the removed layer thickness. However, even when extrapolating these lines to the complete removal of the

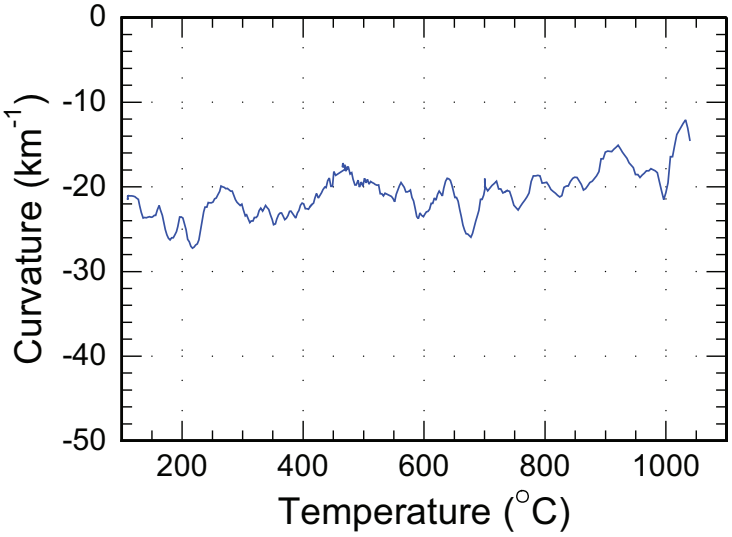

Fig. 5: Curvature of a free-standing GaN sample versus temperature. Notice that the curvature value is quite low because we have polished flat the surface of this particular sample to apply our optical *in situ* curvature measurement.

layers, still a significant bowing remains. Surprisingly, we find for many different samples that about 60 % of the bowing survives for such a complete etching (Fig. 6, right), although the absolute values fluctuate in some range (c.f. Fig. 4). Similarly, Chen et al. [11] found a linear decrease of the curvature after inductively plasma etching of free-standing GaN samples from initially 670 km^{-1} to zero and eventually to convex bowing. We currently can only speculate why their results are quite different to ours taking into consideration the differences in the details of the epitaxial processes and/or the influence of the dry-etch procedure on the wafer bow.

These results indicate that the dislocation density gradient is only partly responsible for the wafer bow of free-standing GaN. We should, however, notice, that the defect density declines inversely proportional to the thickness [2], whereas we found a proportional decrease of the curvature. Moreover, the different curvature values of the unetched samples (see Fig. 6, left) need to be explained. This fact may be related to different strain situations initiated in the very beginning of the growth or even in the MOVPE template. As reported by several groups, in many cases, MOVPE grown layers are fairly weakly strained at room temperature which translates into a significant tensile strain at growth temperature. Such tensile strain is explained to be caused by the coalescence of crystalline islands during nucleation [12] and depends on the details of the nucleation process (see, e.g., [5, 13]). More studies of the correlations between the MOVPE template strain and the curvature of free-standing HVPE-grown layers are currently underway in our labs and will be reported elsewhere.

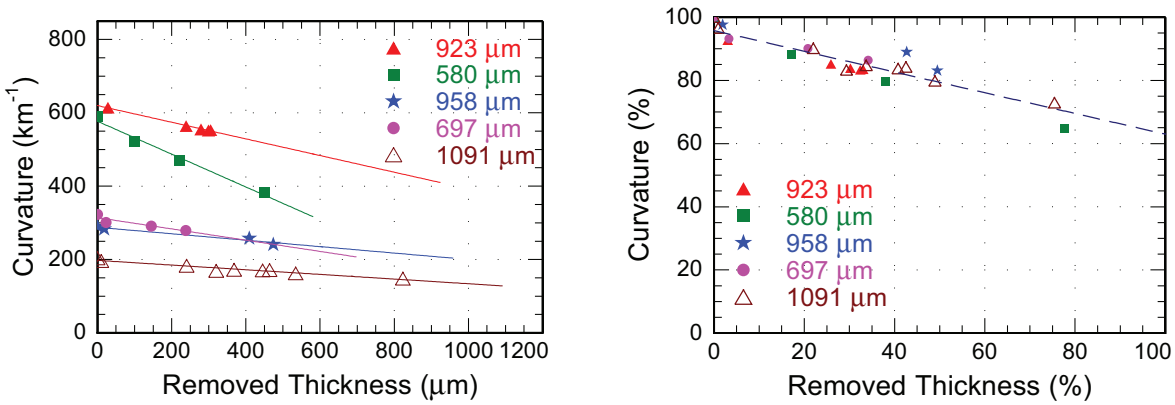

Fig. 6: Left: Curvature of free-standing GaN samples with various thicknesses as indicated in the legend measured by x-ray diffraction after several steps of KOH etching. Right: Same data with thickness axis normalized to the total original thickness of each sample and curvature axis normalized to the value of the unetched samples.

5. Summary

Thick GaN layers grown by HVPE typically are considerably bowed concavely. By comparing *in situ* curvature measurements to *ex situ* curvature and strain evaluations, we could show that this bow is already present during growth and then frozen in the layers, although the different thermal expansion coefficients of GaN and sapphire may lead to strong intermediate convex bow during cool-down of the samples. Some inherent strain developing in the very beginning of the epitaxial growth or even in the MOVPE-grown template may be responsible for it. However, we could not yet determine a cause for the strain still being present in the GaN layers after removal of the sapphire substrate. The dislocation density gradient from the back to the front side can only partly explain our observations.

Acknowledgment

The assistance of Martin Klein, Xiang Yao, (Inst. of Optoelectronics), Joachim Wiest, Benjamin Neuschl, Klaus Thonke (Inst. of Quantum Matter, Semiconductor Physics Group, Ulm University) and K. Koyama et al. (Namiki Precision Jewel Co. Ltd., Japan) is gratefully acknowledged. This work has been financially supported by the Bundesministerium für Bildung und Forschung (BMBF) and by Freiberger Compound Materials GmbH, Freiberg, Germany.

References

[1] Y. Narukawa, M. Ichikawa, D. Sanga, M. Sano, and T. Mukai, "White light emitting diodes with super-high luminous efficacy", *J. Phys. D: Appl. Phys.*, vol. 43, pp. 354002-1–6, 2010.

[2] D. Hanser, L. Liu, E.A. Preble, D. Thomas, and M. Williams, "Growth and Fabrication of 2 inch Free-standing GaN substrates via the boule growth method", *Mat. Res. Soc. Symp. Proc.*, vol. 798, p. Y2.1.1, 2004.

[3] F. Lipski, T. Wunderer, S. Schwaiger, and F. Scholz, "Fabrication of freestanding 2"-GaN wafers by hydride vapour phase epitaxy and self-separation during cooldown", *Phys. Status Solidi A*, vol. 207, pp. 1287–1291, 2010.

[4] K. Fujito, S. Kubo, and I. Fujimura, "Development of bulk GaN crystals and nonpolar/semipolar substrates by HVPE", *MRS Bulletin*, vol. 34, pp. 313–317, 2009.

[5] J. Hertkorn, F. Lipski, P. Brückner, T. Wunderer, S.B. Thapa, F. Scholz, A. Chuvilin, U. Kaiser, M. Beer, and J. Zweck, "Process optimization for the effective reduction of threading dislocations in MOVPE grown GaN using in situ deposited SiN_x masks", *J. Cryst. Growth*, vol. 310, pp. 4867–4870, 2008.

[6] P. Brückner, F. Habel, and F. Scholz, "HVPE growth of high quality GaN layers", *Phys. Status Solidi C*, vol. 3, pp. 1471–1474, 2006.

[7] D. Fu, R. Zhang, B. Wang, Z. Zhang, B. Liu, Z. Xie, X. Xiu, H. Lu, Y. Zheng, and G. Edwards, "Modification of the valence band structures of polar and nonpolar plane wurtzite-GaN by anisotropic strain", *J. Appl. Phys.*, vol. 106, pp. 023714-1–8, 2009.

[8] E.V. Etzkorn and D.R. Clarke, "Cracking of GaN films", *J. Appl. Phys.*, vol. 89, pp. 1025–1034, 2001.

[9] A. Polian, M. Grimsditch, and I. Grzegory, "Elastic constants of gallium nitride", *J. Appl. Phys.*, vol. 79, pp. 3343–3344, 1996.

[10] C. Roder, S. Einfeldt, S. Figge, and D. Hommel, "Temperature dependence of the thermal expansion of GaN", *Phys. Rev. B*, vol. 72, pp. 085218-1–6, 2005.

[11] K.M. Chen, Y.H. Yeh, Y.H. Wu, C.H. Chiang, D.R. Yang, C.L. Chao, T.W. Chi, Y.H. Fang, J.D. Tsay, and W.I. Lee, "Method for modulating the wafer bow of freestanding GaN substrates via inductively coupled plasma etching", *J. Cryst. Growth*, vol. 312, pp. 3574–3578, 2010.

[12] W.D. Nix and B.M. Clemens, "Crystalline coalescence: A mechanism for intrinsic tensile stresses in thin films", *J. Mater. Res.*, vol. 14, pp. 3467–3473, 1999.

[13] J. Napierala, D. Martin, N. Grandjean, and M. Ilegems, "Stress control in GaN/sapphire templates for the fabrication of crack-free thick layers", *J. Cryst. Growth*, vol. 289, pp. 445–449, 2006.

3D GaInN/GaN-based Green Light Emitters

Junjun Wang

The GaInN/GaN-based quantum wells (QWs) on one of the naturally stable semipolar facets (the $\{11\bar{2}2\}$ *facet) have inferior properties than those on the other (the* $\{10\bar{1}1\}$ *facet). By optimizing the epitaxial growth conditions, the evolution of the* $\{11\bar{2}2\}$ *facets of GaN inverse pyramids were successfully suppressed achieving a 50% higher photoluminescence (PL) intensity with even about 10 nm longer emission wavelength. The formation of structures with pure* $\{10\bar{1}1\}$ *facets could be enhanced by lower temperature, higher V/III ratio and lower filling factor of the* SiO_2 *selective growth mask. Complete light emitting diode (LED) structures were fabricated by using 3D GaN templates with GaInN/GaN-based QWs on the semipolar facets. A large leakage current occurring at the apex of the 3D structure was overcome by increasing the p-GaN growth time with 'pulse doping' which pushes the growth more vertically. The respective I-V curves show typical diode behavior.*

1. Introduction

Selective area growth (SAG) of group III nitrides allows the epitaxy of 3D GaN structures of high crystal quality with semipolar facets based on 2-inch sapphire substrates. The heavily reduced piezoelectric field on those semipolar facets compared to that on the c-plane promises a better device performance. A detailed description of the formation of the 3D structures can be found elsewhere [1].

The GaInN/GaN-based QW is a promising candidate for green light emitters which can be achieved as either an optically-pumped light converter [2] or an electrically-pumped conventional LED. The former has the great advantages of a better QW excitation homogeneity and a simpler structure without any doping or the AlGaN electron blocking layer (EBL). However, it requires a more complicated processing produre to integrate the conversion structures with excitation UV/blue LEDs compared to the conventional LEDs. In order to realize highly efficient green light emitting structures with both approaches mentioned above, we have investigated the epitaxial growth of inverse pyramid structures containing semipolar GaInN quantum wells on their side facets. Moreover, complete LED structures were fabricated by using 3D GaN templates with GaInN/GaN-based QWs on semipolar facets. During the overgrowth of p-(Al)GaN layers on the semipolar QWs, Mg-doping induces lateral growth. This results in a thin p-(Al)GaN layer on the apex of the n-GaN template causing a large leakage current. In order to overcome this problem, we increased the growth time when the vertical p-GaN growth is enhanced.

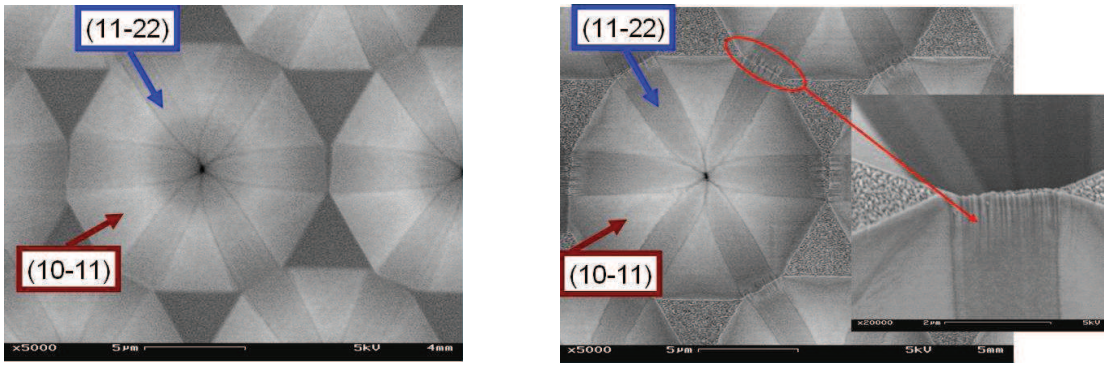

Fig. 1: Top view of the structure with both types of facets $\{10\bar{1}1\}$ and $\{11\bar{2}2\}$ before (left) and after (right) the growth of 5 GaInN/GaN QWs. The area close to the apex on the $\{11\bar{2}2\}$ facet is enlarged in the insert in the right-hand figure.

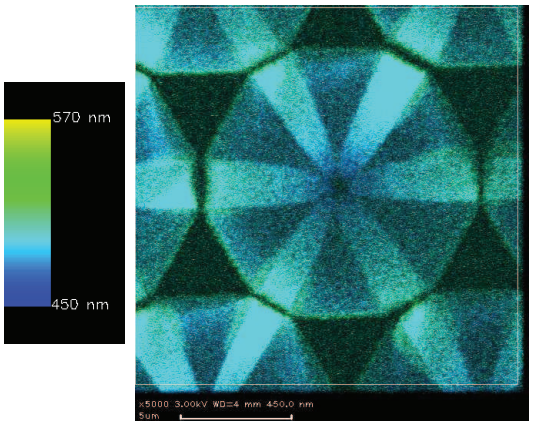

Fig. 2: Overlay of several CL mappings of the structure with both types of facets $\{10\bar{1}1\}$ and $\{11\bar{2}2\}$ after the GaInN/GaN QWs growth. The colors refer to the respective dominant wavelength.

2. Facet Control of GaN Inverse Pyramids

The crystal planes $\{10\bar{1}1\}$ and $\{11\bar{2}2\}$ are naturally stable semipolar facets for GaN inverse pyramids. When both types of crystal planes coexist, there are 12 facets on the surface. Such structures develop when reasonable growth conditions are applied (Fig. 1). According to the cathodoluminescence (CL) mapping for the structure with 5 GaInN/GaN QWs (Fig. 2), the emission wavelength is longer from the QWs on the $\{11\bar{2}2\}$ facet than from those on the other facet, different from our earlier studies [3]. This opposite behaviour may depend on different growth conditions. For such long wavelength quantum wells, we typically observe the formation of some mini-stripes near the apex of the $\{11\bar{2}2\}$ facets (see insert in Fig. 1, right). We measured locally resolved spectra on such a $\{11\bar{2}2\}$ facet within 8 excitation windows from top to bottom by CL (Fig. 3). The emission from the topmost excitation window – where we observe the mini-stripes – is relatively week and broad. From the second to the lowest excitation window, the emission is fairly strong and narrow with slightly decreasing intensity and a blue-shifting wavelength from top to bottom. Obviously, the mini-stripes developing during the GaInN/GaN MQW growth

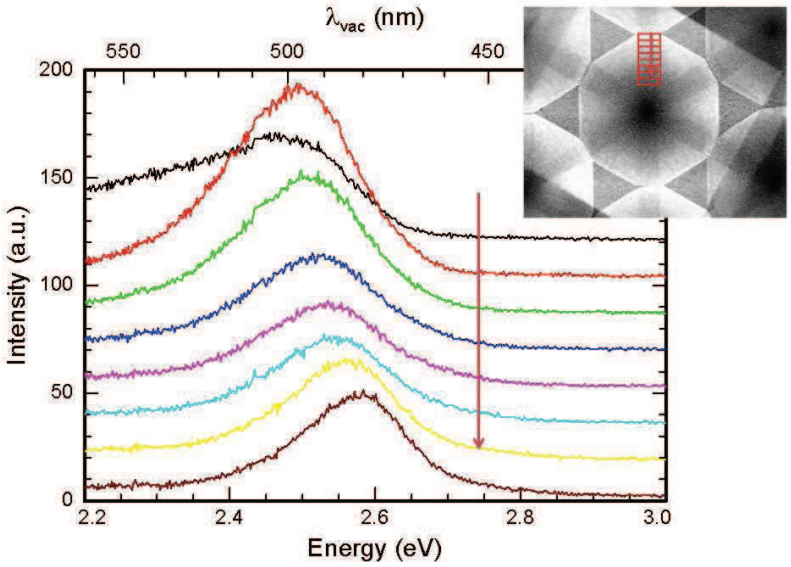

Fig. 3: CL linescan on the $\{11\bar{2}2\}$ facet from top to bottom. The insert shows a SEM top view on the investigated facets with the respective fields marked, in which the spectra have been measured.

degraded the QW quality causing a weak and broad emission. Therefore, our goal is to suppress the $\{11\bar{2}2\}$ facet on the GaN inverse pyramids due to the inferior properties of the mini-stripes.

Three parameters were varied during the growth of the GaN inverse pyramids to check their influence on the $\{11\bar{2}2\}$ facet suppression: The temperature, the V/III ratio, and the mask filling factor (the area ratio of the mask over the total surface) for the SiO_2 growth mask.

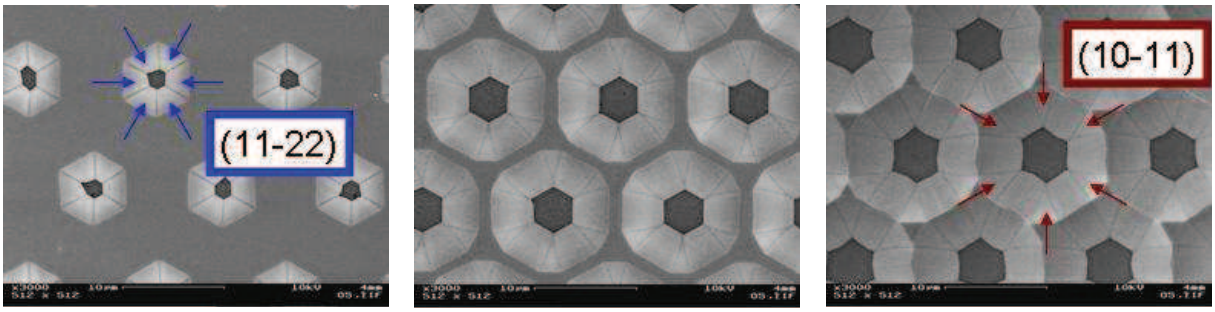

Fig. 4: Top view of GaN inverse pyramids grown at a temperature of 1120 °C (left), 1060 °C (middle) and 950 °C (right).

When decreasing the growth temperature from 1120 °C to 950 °C, we observed a steady transition from pure $\{11\bar{2}2\}$ facets to the increased appearance of $\{10\bar{1}1\}$ facets (Fig. 4). Similarly, the GaN inverse pyramidal surface is dominated by the $\{11\bar{2}2\}$ facet for a small V/III ratio of 200, getting gradually suppressed with increasing V/III ratio (Fig. 5). Finally, the $\{11\bar{2}2\}$ facet disappeared when the mask filling factor was reduced from 59 % to 25 % (Fig. 6).

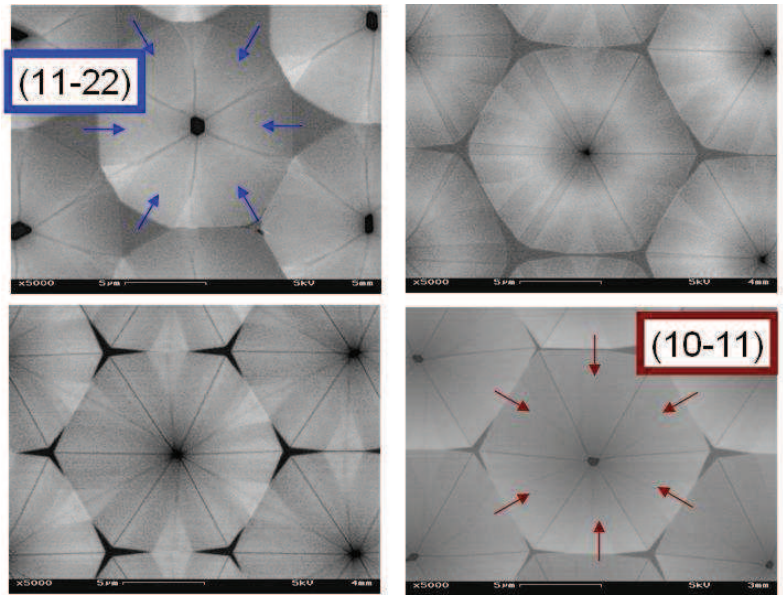

Fig. 5: Top view of GaN inverse pyramids grown with a V/III ratio of 200, 400, 500 and 700.

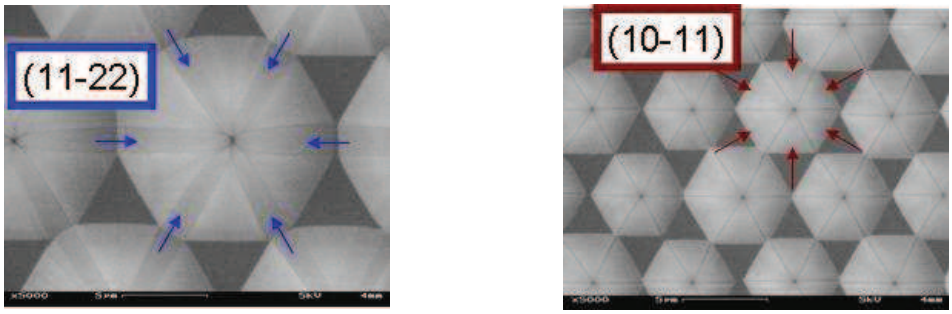

Fig. 6: Top view of GaN inverse pyramids with a mask filling factor of 59 % (left) and 25 % (right).

By applying the optimal values of the 3 parameters discussed above, the $\{11\bar{2}2\}$ facet was totally suppressed for a pure GaN structure without QWs (Fig. 7 (left)). Again, spectra were obtained from 8 excitation windows from top to bottom in CL (Fig. 8) for this optimized structure with 5 GaInN/GaN QWs (Fig. 7 (right)). The emission shows the trend of continuously decreasing intensity and blue-shifted wavelength from top to bottom without exceptions. The area within the first excitation window contributes to the strongest emission without suffering from the mini-stripes. The integrated photoluminescence of these structures peaking at 505 nm is about 50 % more intense as compared to the structure with the mini-stripes peaking at 494 nm.

In the top view of a structure without the $\{11\bar{2}2\}$ facet, but still grown with fairly low V/III ratio, three parts (one triangle and two symmetric neighboring parts as marked in Fig. 7) are observed within any of the 6 equivalent surface areas after the growth of the GaN layer below the quantum wells. The central triangle part is attributed to the facet $\{10\bar{1}1\}$ since its upper edge is parallel to the crystal direction $\langle 11\bar{2}0\rangle$ indicated by the growth mask alignment. The neighboring part could be either one single facet

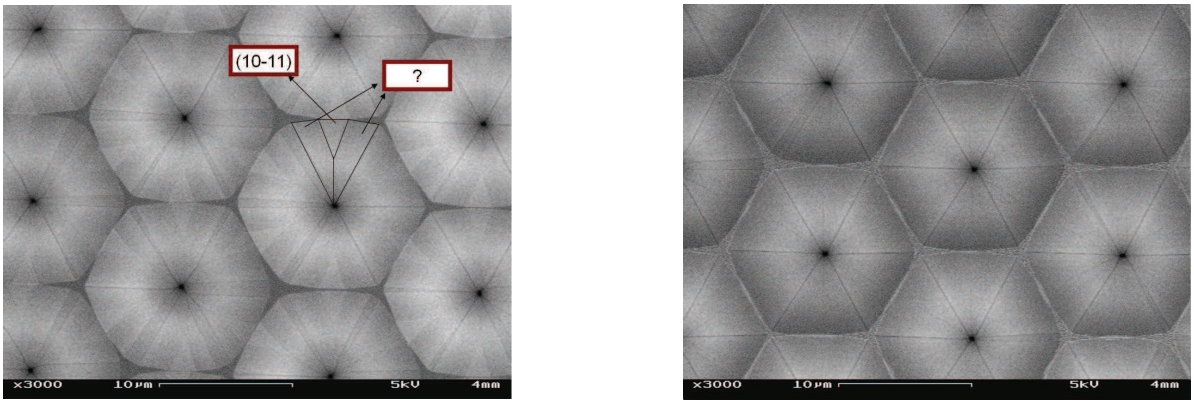

Fig. 7: Top view of the structure without the $\{11\bar{2}2\}$ facets before (left) and after (right) the GaInN/GaN QWs growth. The three parts in any of the 6 equivalent surface areas are marked. The central triangular part is attributed to the $\{10\bar{1}1\}$ facet. The other parts are attributed to unknown high-index facets very close to $\{10\bar{1}1\}$.

rotated by a slight angle with respect to the $\{10\bar{1}1\}$ facet or several small facets with tiny misorientations among them. However, seemingly only one pure $\{10\bar{1}1\}$ facet remains after the deposition of the 5 GaInN/GaN QWs. In spatially resolved CL mapping (Fig. 9) of the same structure with the 5 GaInN/GaN QWs, the 3 sub-facets are clearly resolved with longer emission wavelength from the two sub-facets as compared to the central triangle part. This may be explained by different In incorporation as a result of different surface orientations [4] needing more detailed studies. By increasing the V/III ratio to 700, the two neighboring parts are suppressed and GaN inverse pyramids with exclusively $\{10\bar{1}1\}$ facets have been achieved (Fig. 10).

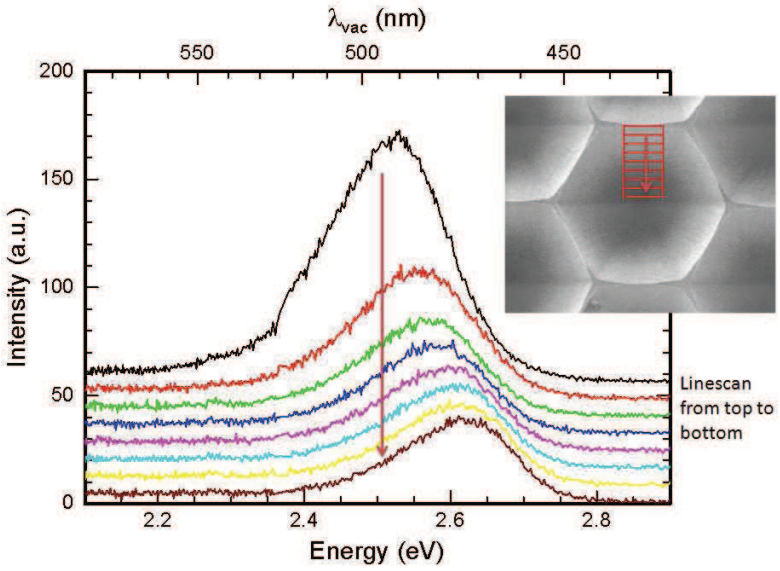

Fig. 8: CL linescan on the $\{10\bar{1}1\}$ facet from top to bottom. Insert shows again the areas in which the spectra have been acquired.

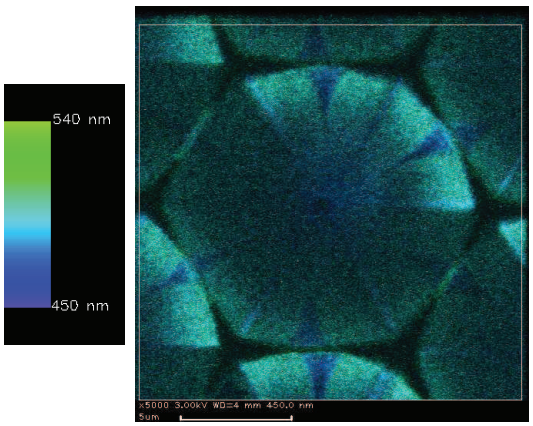

Fig. 9: CL mapping of the structure without the $\{11\bar{2}2\}$ facet after the GaInN/GaN QWs growth.

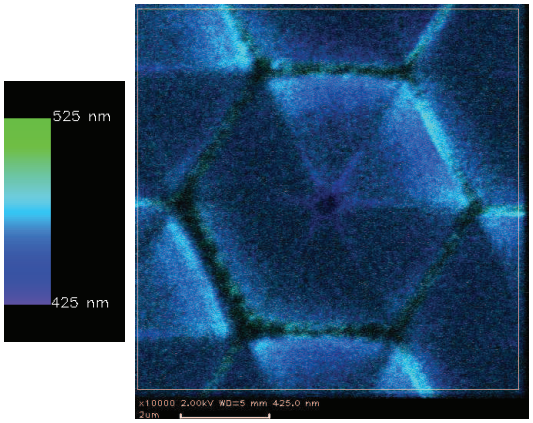

Fig. 10: CL mapping of the structure with exclusively $\{10\bar{1}1\}$ facets after the GaInN/GaN QW growth.

3. 3D μm-sized Light Emitting Diodes

For the fabrication of 3D-LEDs with semipolar quantum wells, the above-mentioned structures need to be overgrown by a p-doped GaN cap layer. The bottom part is now made of Si-doped GaN which normally forms a sharp apex. Mg doping induces lateral growth resulting in a plateau on the p-GaN surface with the sharp n-GaN apex underneath (Fig. 11 (left)). Therefore, the n-GaN apex might be either not covered by p-GaN at all or just overgrown by a very thin p-GaN layer. Hence, a too thin p-GaN layer causes large leakage currents in a LED device. A 'pulse doping' technique (the metalorganics and NH_3 are supplied alternatively in loops [5].) is helpful to push the p-GaN growth vertically. The total p-GaN layer was grown partly by normal epitaxy and partly by using the 'pulse doping'. This procedure was further optimized on striped LEDs since it is easier to check the p-GaN layer thickness by scanning electron microscopy than that of inverse pyramid LEDs. Indeed, the first stripe LED whose p-GaN was grown with the same parameters as the inverse pyramid LED suffered from such short-circuits in EL. The p-GaN on the n-GaN tip is only 57 nm thick. Therefore, we have doubled and tripled the growth time of

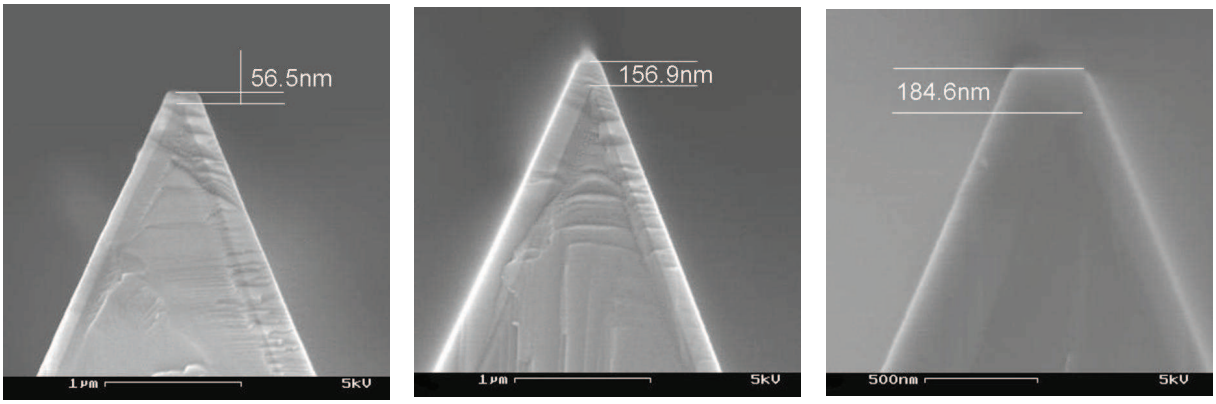

Fig. 11: Cross section view for the stripe LEDs with single, doubled and tripled pulse-doping p-GaN growth time, respectively (from left to right).

the pulse doped p-GaN. Now, the n-GaN tip is well isolated with at least 157 nm p-GaN on top (Fig. 11 (middle)). The current-voltage curves of the two latter structures show typical diode behavior (Fig. 12), although the light emission is still comparably weak requiring more optimization.

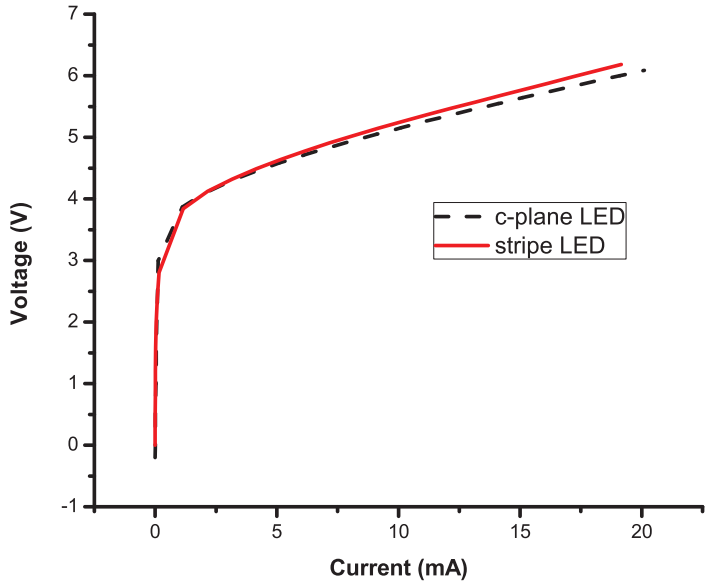

Fig. 12: I-V curve for the stripe LED with doubled pulse-doping p-GaN growth time.

4. Conclusion and Outlook

Luminescence conversion structures containing semipolar GaInN quantum wells are investigated on the basis of inverted pyramidal structures grown by selective area MOVPE. The formation of structures with pure $\{10\bar{1}1\}$ facets could be enforced by lower temperature, higher V/III ratio and lower mask filling factor. The formation of higher index

facets close to $\{10\bar{1}1\}$ showing a better In incorporation needs more detailed studies. In order to optimize in particular the electrical characteristics of stripe LEDs, we have varied the thickness of the top p-layer which helped to suppress otherwise observed leakage currents. More optimization is necessary to enhance the output power of the stripe LEDs in EL, for example the GaN spacer thickness between the QWs and the p-AlGaN EBL, the Mg-doping profile and so on. We need to transfer the knowledge from stripe LED optimization to the inverse pyramidal structure as well.

Acknowledgment

I gratefully acknowledge the scientific and technical support from R. Leute, I. Tischer, I. Argut, D. Zhang. CL measurements have been performed by I. Tischer and M. Hocker from the Inst. of Quantum Matter, Ulm University. This work was financially supported by the German Federal Ministry of Education and Research (BMBF).

References

[1] T. Wunderer, F. Lipski, J. Hertkorn, S. Schwaiger, and F. Scholz, "Fabrication of 3D InGaN/GaN structures providing semipolar GaN planes for efficient green light emission", *Phys. Status Solidi C*, vol. 6, pp. S490–S493, 2009.

[2] B. Galler, M. Sabathil, A. Laubsch, T. Meyer, L. Hoeppel, G. Kraeuter, H. Lugauer, M. Strassburg, M. Peter, A. Biebersdorf, U. Steegmueller, and B. Hahn, "Green high-power light sources using InGaN multi-quantum-well structures for full conversion", *Phys. Status Solidi C*, vol. 8, pp. 2369–2371, 2011.

[3] T. Wunderer, *Dreidimensionale Licht emittierende GaInN/GaN-Strukturen mit reduziertem piezoelektrischen Feld*. Ph.D. thesis, Ulm University, Ulm, Germany, 2010.

[4] P. Perlin, G. Franssen, J. Szeszko, R. Czernecki, G. Targowski, M. Kryśko, S. Grzanka, G. Nowak, E. Litwin-Staszewska, R. Piotrzkowski, M. Leszczyński, B. Łucznik, I. Grzegory, R. Jakieła, M. Albrecht, and T. Suski, "Nitride-based quantum structures and devices on modified GaN substrates", *Phys. Status Solidi A*, vol. 206, pp. 1130–1134, 2009.

[5] T. Wunderer, P. Brückner, B. Neubert, F. Scholz, M. Feneberg, F. Lipski, M. Schirra, and K. Thonke, "Bright semipolar GaInN/GaN blue light emitting diode on side facets of selectively grown GaN stripes", *Appl. Phys. Lett.*, vol. 89, pp. 041121-1–3, 2006.

Sub-μm Patterning for Semipolar GaN Based Light Emitters

Robert A.R. Leute and Dominik Heinz

We present patterning of GaN layers by laser interference lithography to create three-dimensional structures on a submicrometer scale. These structures exhibit surfaces comprised of semipolar crystal facets with reduced piezoelectric fields. The small dimensions of these 3D structures allow embedding. The resulting planarized surfaces considerably ease subsequent device processing. Structural characterization is shown and a first working light emitting device based on embedded submicrometer structures is presented.

1. Introduction

Interest in semipolar GaN crystal planes for efficient green light emitters is not waivering [1]. While the crest is constituted by efforts on free-standing GaN templates for homoepitaxy [2], selective area epitaxy of 3D structures remains suasive [3]. The latter employs relatively cheap 2-inch substrates and growth in c-direction which produces high crystal quality despite heteroepitaxy [4]. For device processing, however, plane surfaces are highly favorable because conventional structuring methods for contacts, resonator formation etc. could be applied. Therefore we seek a method to employ selective area growth for three-dimensional structures with semipolar surfaces only within the active region of our aspired device. The requirement is that the resulting elevation can be planarized easily. Consequently all dimension must be restricted to some hundred nanometers, thus leaving the realms of conventional optical lithography.

2. Subwavelength Lithography: Using Interference Patterns

Laser interference lithography creates periodic patterns with sub wavelength periodicity [5]. The premise is based on the well known Lloyd's mirror interference experiment [6] and given in Fig. 1. The laser beam of a HeCd UV laser ($\lambda = 325\,\mathrm{nm}$) is focused onto a pinhole thereby spread and spatially filtered. Half of the spread beam is directed onto the sample whereas the other half is reflected by a mirror and then directed onto the sample. Thus the two beam halves interfere on the sample surface resulting in a stripe pattern, the periodicity of which depends on the wavelength (λ) of the light source and the angle (2θ) between both incident light beams.

$$P = \frac{\lambda}{2 \cdot \sin\theta} \tag{1}$$

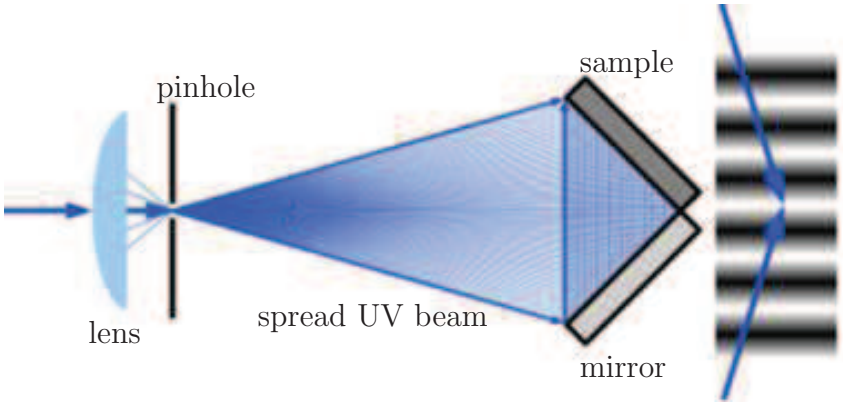

Fig. 1: Schematic drawing of the laser interference lithography setup.

2.1 Submicrometer resist patterns – 1D and 2D

Using a highly sensitive resist AZ MiR 701, diluted with ethyl lactate to get a very thin coating, exposure of a resist layer on GaN with the interference pattern results in a periodic arrangement of stripes, as shown in Fig. 2. We achieved periodicities between 230 nm and 280 nm, the height of the resist stripes is about 80 nm. If exposure time is halved and a second exposure is done with the sample rotated by 90 ° or 60 ° the result is a square or hexagonal arrangement of resist colums with 80 nm diameter. These 2D patterns are highly interesting for selective epitaxy of 3D structures like pyramids and inverse pyramids on a sub-µm scale.

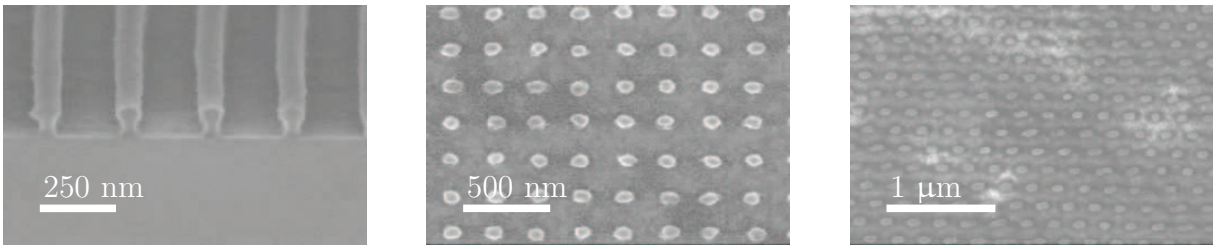

Fig. 2: 1D and 2D resist patterns. The square resist dot arrangement was achieved by a two-time exposure rotated by 90 °, the hexagonal arrangement by a two-time exposure with 60 ° tilt.

3. Selective Epitaxy on a Submicrometer Scale

Pattern transfer to a suitable growth mask for subsequent epitaxy is crucial. A thin layer (15 nm) of titanium is deposited on GaN templates with structured resist. After lift-off the pattern is transfered as an inverted image (see Fig. 3). The templates are then cleaned and transfered into the MOVPE reactor where the Ti mask is nitridized in a hot ammonia atmosphere. Afterwards, the second growth step is carried out. The MOVPE reactor used is an Aixtron-200/4RF-S HT with standard precursors TMGa, TMIn and high purity ammonia. Silane and CP_2Mg are used for doping with Pd diffused hydrogen

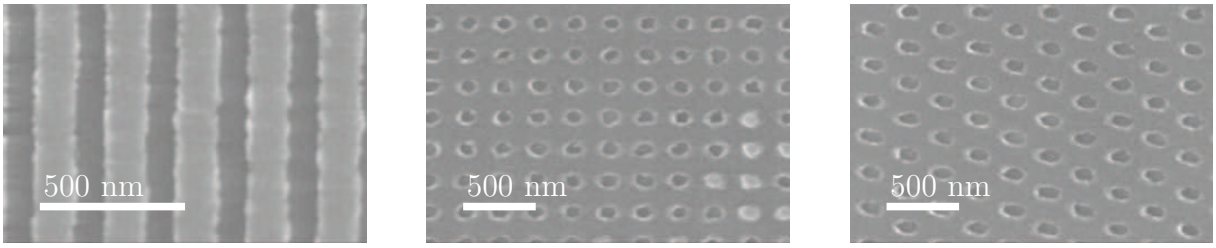

Fig. 3: 1D and 2D mask patterns. 15 nm titanium was evaporated on the resist patterns described above resulting in a negative pattern.

and high purity nitrogen as carrier gases. Growth parameters were chosen based on 3D GaN growth on a supermicrometer scale [7]. For stripes aligned parallel to the *a*-direction stable growth conditions were obtained, resulting in a homogeneous distribution of stripes over a large area. For 2D patterned masks resulting in nano-pyramids and inverse pyramids the fluctuation of the size distribution observed over the whole wafer was substantial. The overgrowth of 2D patterns seems very sensitive to small deviations of mask and growth parameters. The detailed parameters for all growth modes are given in table 1.

Table 1: Growth parameters for sub-μm sized 3D GaN.

	stripes ∥ *a*	pyramids	inverse pyramids
temperature/°C	970	950	950
pressure/ mbar	150	150	150
V/III ratio	260	310	260
growth time /min	2:00	2:00	3:00

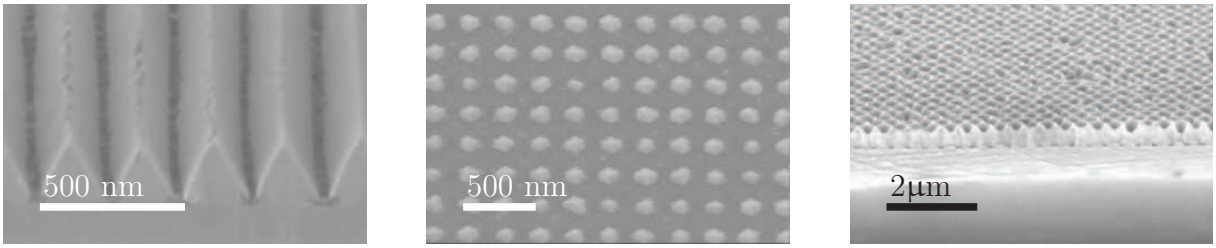

Fig. 4: Depending on mask pattern and growth conditions, several 3D structures can be realized. From left to right: stripes with triangular cross section and $\{10\bar{1}1\}$ side facets, pyramids and inverse pyramids.

4. LED

For stripes with triangular cross section aligned parallel to the *a*-direction with $\{10\bar{1}1\}$ side facets, homogeneous growth over large areas was established, allowing subsequent embedding. In order to facilitate contact evaporation as well as prevent short circuits, a

smooth flat surface is required. Based on the samples shown in the previous section, the second growth run is elongated to include a p-doped capping layer.

4.1 Embedding experiments

The presence of magnesium is favorable for lateral growth thus facilitating the planarization of the device. However, previous experiments [8] have shown the relative difficulty to planarize stripes with $\{10\bar{1}1\}$ side facets which are very stable. It can be seen in Fig. 5 that sufficient thickness is needed for planarization. Total coverage and a smooth surface was achieved for a growth time equivalent to 250 nm planar growth. Best results were obtained with a high temperature growth step. Further optimization is ongoing.

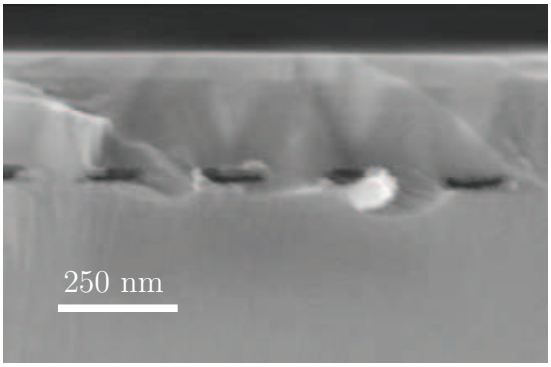

(a): SEM cross section view, non optimized planarization.

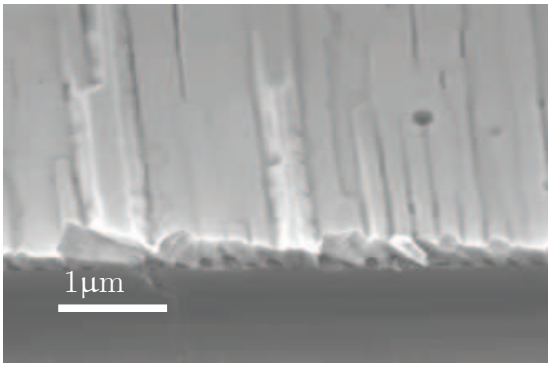

(b): SEM bird view, non optimized planarization results in rough surface.

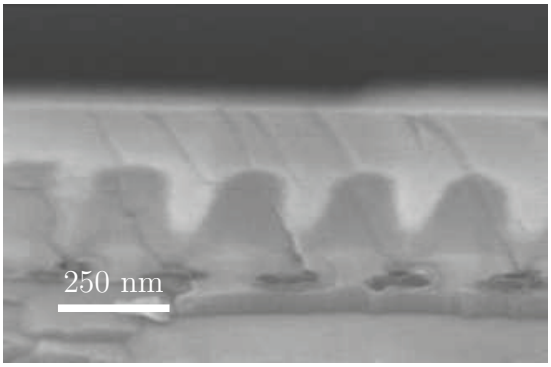

(c): SEM cross section view, the thicker overgrowth leads to a smooth surface.

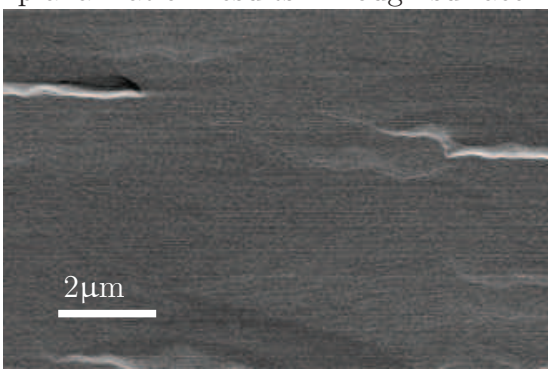

(d): SEM top view, after thicker overgrowth the surface is smooth with no remnants of the stripes visible.

Fig. 5: Planarization of LED structure before (a), (b) and after (c), (d) optimization.

4.2 Electrical characterization

Circular indium contacts were evaporated on the p-side of the LED. The contacts had diameters ranging vom 70 µm to 140 µm and were 1 µm thick. The n-region was contacted from the top, by creating a trench by mechanical force and filling it with indium. Figure

6 shows voltage and optical output power of the device versus current. The device was stable over a large current range, up to 200 mA. The peak wavelength was 460 nm with a FWHM of 32 nm (spectrum not shown).

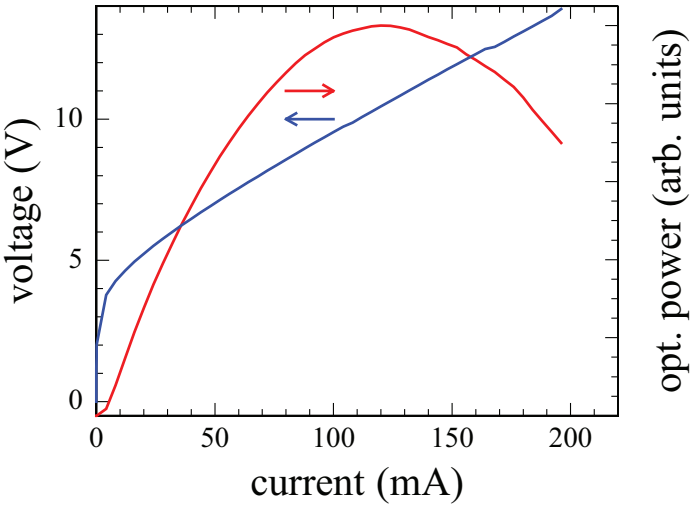

Fig. 6: PIV characteristics obtained for a LED structure via on-wafer testing with circular indium contacts.

5. Conclusion

Laser interference lithography with a Lloyd's mirror geometry was used to pattern GaN on a scale of a few hundred nanometers. The patterned area comprises several cm^2. Employing in-situ nitridized titanium, selective epitaxy of stripes, nanopyramids and inverse pyramids was achieved. Stripes aligned along the GaN *a*-direction with InGaN quantum wells on the semipolar $\{10\bar{1}1\}$ side facets were embedded and planarized with Mg doped GaN. On wafer testing produced fair electroluminescence stable up to 200 mA.

Acknowledgment

Technical and scientific support by I. Argut, R. Blood, F. Lipski, K. Forghani, J. Wang, T. Meisch, M. Dickel and K. Thonke is gratefully acknowledged.

References

[1] J.S. Speck, "Progress in nonpolar and semipolar GaN materials and devices", *Semiconductor Device Research Symposium (ISDRS), 2011 International 7–9 Dec. 2011*, 2011.

[2] R.M. Farrell, E.C. Young, F. Wu, S.P. Denbaars, and J.S. Speck, "Materials and growth issues for high-performance nonpolar and semipolar light-emitting devices", *Semicond. Sci. Technol.*, vol. 27, pp. 024001-1–14, 2012.

[3] F. Scholz, "Semipolar GaN grown on foreign substrates: a review", *Semicond. Sci. Technol.*, vol. 27, pp. 024002-1–15, 2012.

[4] T. Wunderer, M. Feneberg, F. Lipski, J. Wang, R.A.R. Leute, S. Schwaiger, K. Thonke, A. Chuvilin, U. Kaiser, S. Metzner, F. Bertram, J. Christen, G.J. Beirne, M. Jetter, P. Michler, L. Schade, G. Vierheilig, U.T. Schwarz, A.D. Dräger, A. Hangleiter, and F. Scholz, "Three-dimensional GaN for semipolar light emitters", *Phys. Status Solidi B*, vol. 248, pp. 549–560, 2010.

[5] X. Mai, R. Moshrefzadeh, U.J. Gibson, G.I. Stegeman, and C.T. Seaton, "Simple versatile method for fabricating guided-wave gratings", *Appl. Opt.*, vol. 24, pp. 3155–3161, 1985.

[6] Proceedings of the Royal Irish Academy, 1836–1837, Part I, p. 6.

[7] T. Wunderer, *Dreidimensionale Licht emittierende GaInN/GaN-Strukturen mit reduziertem piezoelektrischen Feld*. Ph.D. Thesis, Ulm University, Ulm, Germany, 2010.

[8] R.A.R. Leute, "Laser structures with semipolar quantum wells grown by selective area epitaxy", *Annual Report 2010*, pp. 95–102. Ulm University, Institute of Optoelectronics.

Heat-induced Transformations of Adsorbed Hydrocarbon Residues on Graphene

Benedikt Westenfelder

We describe new phenomena of structural reorganization of carbon adsorbates as revealed by in situ *atomic-resolution transmission electron microscopy (TEM) performed on specimens at extreme temperatures. In our investigations, a graphene sheet serves as both a quasi-transparent substrate for TEM and as an* in situ *heater. The melting of gold nanoislands deposited on the substrate surface is used to evaluate the local temperature. At annealing temperatures around 1000 K we observe the transformation of physisorbed hydrocarbon adsorbates into amorphous carbon monolayers and the initiation of crystallization. At temperatures exceeding 2000 K the transformation terminates in the formation of a completely polycrystalline graphene state. The resulting layers are bounded by free edges primarily in the armchair configuration.*

1. Introduction

The recent past has witnessed tremendous gains in the capabilities of transmission electron microscopy (TEM) for exploring the atomic configuration of materials, largely because of dramatic improvements in the correction of lens aberrations. It is now possible to obtain atomic-resolution images even of light-element materials, with a reduction in radiation damage effected by the utilization of reduced acceleration voltages (for more background info see ref. [1]). Our understanding of carbon systems, such as graphene or carbon nanotubes, has significantly benefitted from these instrumental developments. When a TEM is exploited as a platform for *in situ* experimentation, dynamic phenomena can be studied under direct observation of the atomic structure [2], but, owing to practical limitations, such investigations have been limited so far to temperatures below about 1500 K [3–5]. Our recent investigations enabled observations of heat-induced transformations of carbon adsorbates on a graphene substrate raised to temperatures in excess of 2000 K.

2. Experiment

In our experiments, a graphene sheet serves as both a quasi-transparent substrate for transmission electron microscopy and as an *in situ* heater that can withstand unprecedented temperatures [6] owing to its high mechanical [7, 8], thermal [6] and chemical stability. As reference points for the local temperature, we used the melting of gold particles (diameter dependent), the transition from amorphous to crystalline silicon nitride (1600 K) and the evaporation of SiN (2000 K) [9]. The experimental concept and thermal

calibration have been described in greater detail previously [9]. In brief, a graphene sheet is transferred onto a Si/SiN membrane platform prestructured with windows and gold contacts, resulting in a TEM-compatible geometry providing an electrically contacted graphene substrate with a freestanding region for transmission of the electron beam Fig. (1). The graphene layer was studied by aberration-corrected high-resolution transmission electron microscopy (AC-HRTEM) performed by a TITAN (80-300) FEI microscope equipped with a Fischione 2510 biasing TEM holder and operated at an accelerating voltage of 80 kV. Electrical current was passed through graphene specimens by applying a voltage between the gold contacts of the sample platform, achieving a typical current density on the order of 2×10^7 A/cm^2 (assuming a graphene thickness of 0.34 nm per layer) at an applied bias of 2 V. The heat-induced transformations of gold nanoislands deposited on graphene by thermal evaporation reveal the local temperature of the substrate. In this letter we focus on the initial scientific results yielded by this experimental approach.

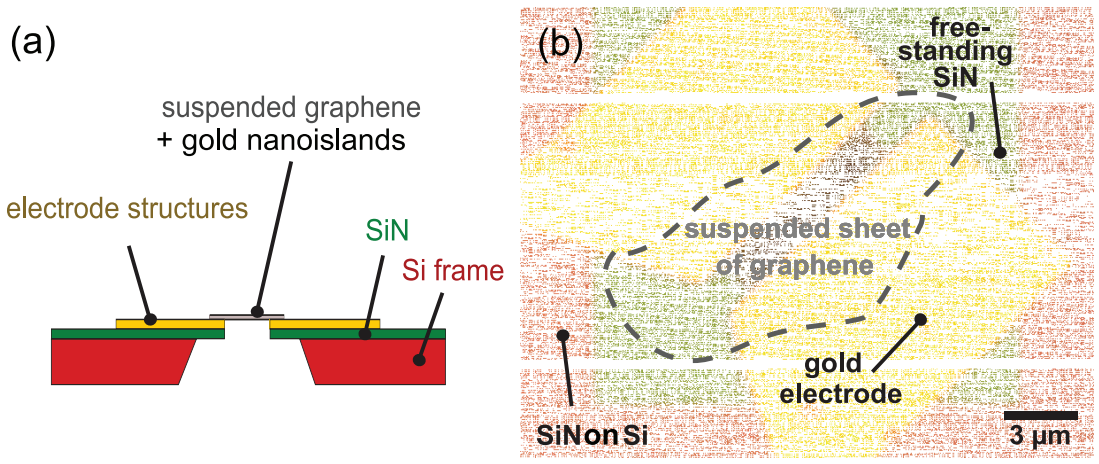

Fig. 1: (a) Cross-sectional schematic illustration of the sample carrier design. (b) Optical micrograph of the electrode support structure upon which a graphene sheet is suspended.

2.1 Temperature estimation during mild heating

Observations made during mild heating conditions help in the estimation of the temperature for our sample geometry [1, 9]. It is well known that the diffusion of Au adatoms on the surface of gold nanoparticles is significant even at room temperature (RT) [10, 11], leading to continuous shape changes of the particles upon heating [12]. In the case of gold nanoislands deposited on graphene, we were able to correlate a decrease in the particle surface area-to-volume ratio with an increase in temperature [1]. Above a certain temperature, the first particles form liquid drops and begin to evaporate [9, 13]. According to theoretical predictions and experimental findings, the melting temperature depends strongly on the particle size, with gold particles ranging in diameter from 3 to 20 nm expected to melt between 800 and 1300 K [14].

3. Observations in the Level of Individual Atoms

We now turn our attention to structural observations extending down to the level of individual atoms. Adsorbed hydrocarbon residues originating from the sample preparation undergo remarkable transformations at the atomic level when exposed to high temperatures. The use of a graphene substrate allows us to observe the precise atomic configuration of the carbon adsorbates. Moreover, graphene enables locally high temperatures to be reached while simultaneously providing a stable supporting surface that does not interact strongly with the adsorbates.

3.1 Hydrocarbon deposits at room temperature

A typical hydrocarbon deposit on an as-prepared graphene sample at 300 K is shown in Fig. 2a. Under electron irradiation at 80 kV, mobile hydrocarbon deposits are converted to amorphous carbon, while hydrogen atoms are knocked out by electron impacts.

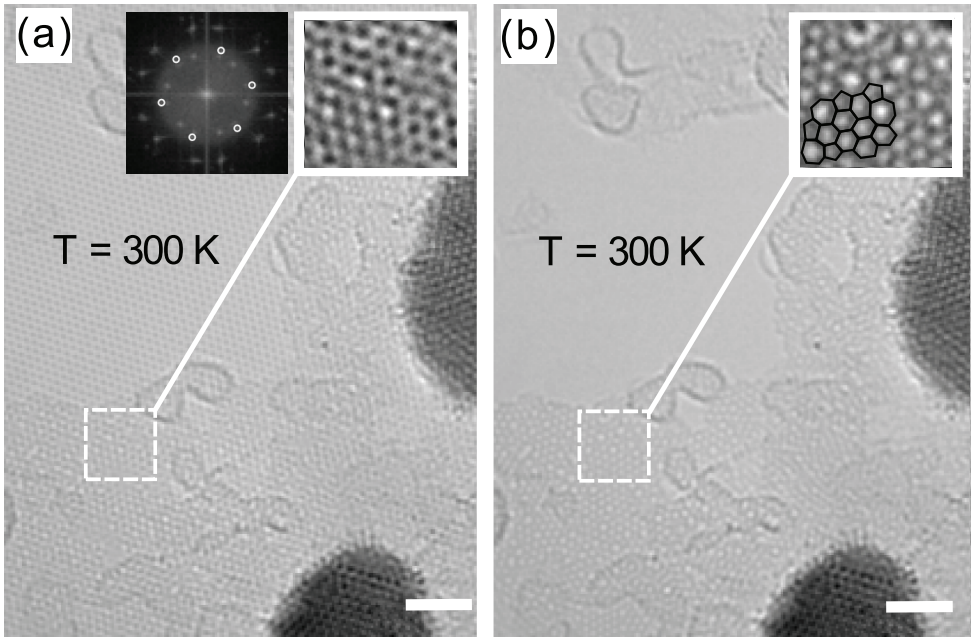

Fig. 2: AC-HRTEM images of carbon and hydrocarbon adsorbates (and gold nanoparticles) on graphene (scale bars = 2 nm). (a) Unfiltered image of carbon contamination and gold particles on a bilayer graphene substrate prior to heat treatment. The upper left inset shows an FFT of the entire image, containing diffraction peaks arising from the substrate (circled in white) and from gold. (b) Same image as in (a) after Fourier filtering of the graphene substrate. This procedure reveals the atomic structure of the amorphous carbon adsorbates, which is clearly resolved in the thinnest areas. The inset shows the region in the dashed box at higher magnification and contrast. The arrangement of atoms in the adsorbate can be interpreted as a random combination of carbon pentagons, hexagons and heptagons. The shape of the gold nanoislands (dark contrast at lower left and right) and their absence of encapsulating carbon shells indicate that the sample had not yet seen temperatures in excess of about 425 °C.

The resulting amorphous carbon adsorbates are comparably stable under further electron-beam irradiation, and they do not easily desorb at high temperatures. In the thinnest regions, we can even resolve the atomic structure of the adsorbates (Fig. 2b), which appears to be amorphous, consisting of a seemingly random arrangement of carbon pentagons, hexagons, heptagons and other (less-frequently observed) carbon polygons.

3.2 Transformations at moderate temperatures (≈1000 K)

The situation changes, however, when we apply temperatures of ≈ 1000 K (indicated by partial melting of the gold particles) at a heating current of 2×10^7 A/cm^2. First, the adsorbates reorganize into structures characterized by large areas consisting of single-layer amorphous carbon containing some crystallized domains (Fig. 3). Second, gold atoms originating from the surrounding nanoislands are incorporated into the carbon matrix, as marked by the arrows in Fig. 3b. Our AC-HRTEM images taken at 1000 K appear to be similar to those obtained by Turchanin et al. [15] from annealed samples characterized at RT—i.e., both crystalline and amorphous domains are observed.

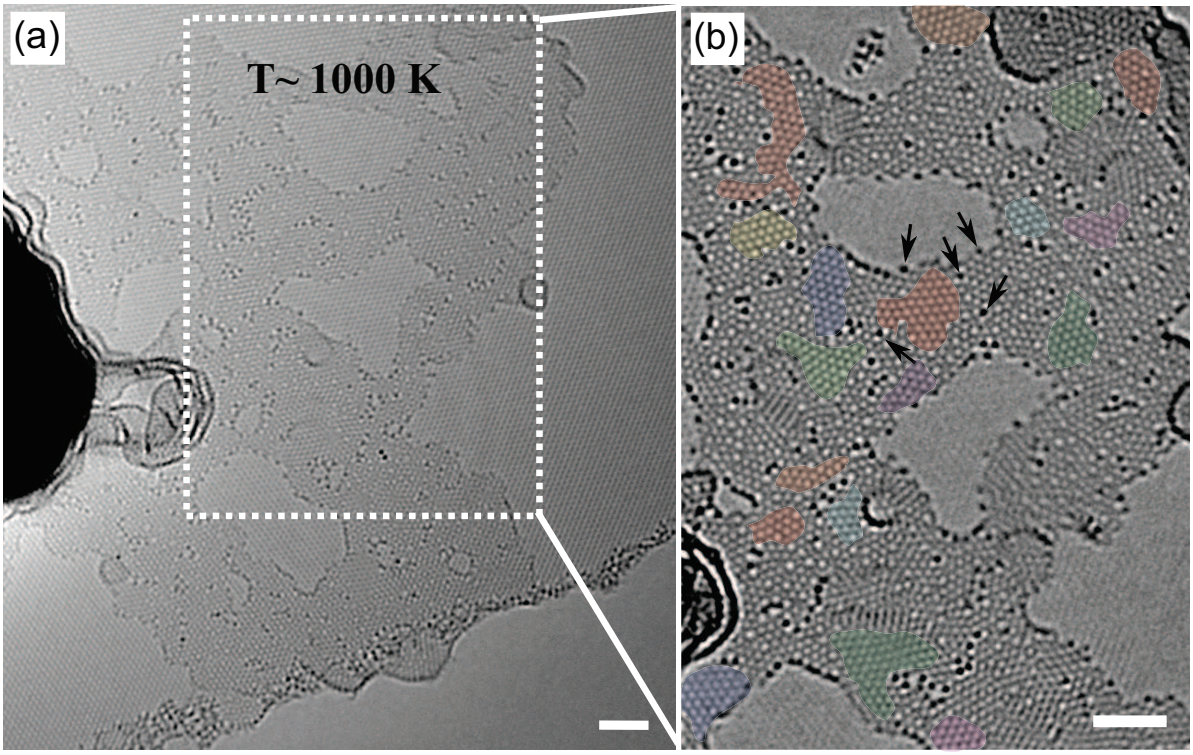

Fig. 3: (a) AC-HRTEM image of single-layer carbon adsorbates on a graphene substrate at 1000 K. (b) Fourier-filtered and magnified region from (a): here, crystalline domains (shaded in color) are evident in some regions, whereas others are still amorphous. Many edge sites and vacancies are occupied by individual gold atoms (black spots, several indicated by arrows). Scale bars are 2 nm in length.

3.3 Transformations at extreme temperatures ($\approx 2000\,\mathrm{K}$)

When we raise the temperature to approximately 2000 K (the heating current is now increased by a factor of two, and silicon nitride close to the imaged region begins to sublimate), the adsorbate transformation ends in fully crystallized graphene domains separated only by atomically sharp boundaries (Fig. 4a). In other words, the amorphous carbon contamination has been transformed almost completely into a polycrystalline graphene layer situated on top of the existing graphene substrate. Image pairs 1 to 3 in Fig. 4b illustrate various dynamic rearrangements of carbon bonds that occur at the grain boundaries, leading to greater crystallinity. The thermally induced healing of defect-like vacancies inside a crystalline grain is captured in image pair 4 of Fig. 4b. We observe a polycrystalline graphene sheet having a domain size of 1 to 3 nm lying on top of a defect-free crystalline graphene substrate (Fig. 4a). Some of the adsorbate grains are aligned with the underlying graphene lattice; however, other crystalline domains appear to be randomly oriented. Owing to the small domain size, we obtain a large number of grain boundaries within the field of view of the AC-HRTEM image. In agreement with previous studies by other authors [16, 17], we find that the grain boundaries consist of carbon pentagons and heptagons arranged in such a manner as to connect adjacent domains of differing orientation without dangling bonds.

Since the polycrystalline adsorbate layer does not completely cover the underlying substrate, we are able to observe a large number of "free edges" of individual grains. In contrast to previous room-temperature HRTEM observations of beam-induced holes in graphene [18,19], these edges are formed and observed under high-temperature annealing. Most strikingly, most of the annealed edges exhibit an armchair-type configuration (Fig. 4c). The contrast at the edges is in agreement with the presence of carbon atoms; the slightly stronger contrast of the edge atoms compared to the lattice in Fig. 4 is a result of the contrast transfer function (CTF) of the microscope at the present conditions. In a statistical analysis of the edge configurations (see Ref. [1]), 58 % of all visible edges could be assigned clearly to one of the geometries calculated in Ref. [20]. Among the classified edges, a dominant fraction —83 %— exhibits the armchair conformation, 14 % manifest the 5–7 reconstructed zigzag edge structure, and only 3 % are found in the unreconstructed zigzag geometry.

These observations are in excellent agreement with expectations from theory (Table 1 in Ref. [20]): The unreconstructed armchair edge and the 5–7 reconstructed zigzag are the two lowest-energy edge configurations. In light of these calculations, it is surprising that AC-HRTEM characterizations of freestanding graphene samples at room temperature [18, 19] observed a slight preponderance of the unreconstructed zigzag configuration, especially since the energy of the latter is $0.33\,\mathrm{eV/Å}$ (or 1.1 eV per atom) higher than that of the armchair edge [20]. It has been speculated previously that this finding arises from the unreconstructed zigzag edges being less sensitive to radiation damage [18]. In the case of high-temperature annealing, however, the thermodynamically preferred armchair configuration appears to be most stable, as observed not only in our measurements but also in recent investigations performed by Song et al. [22].

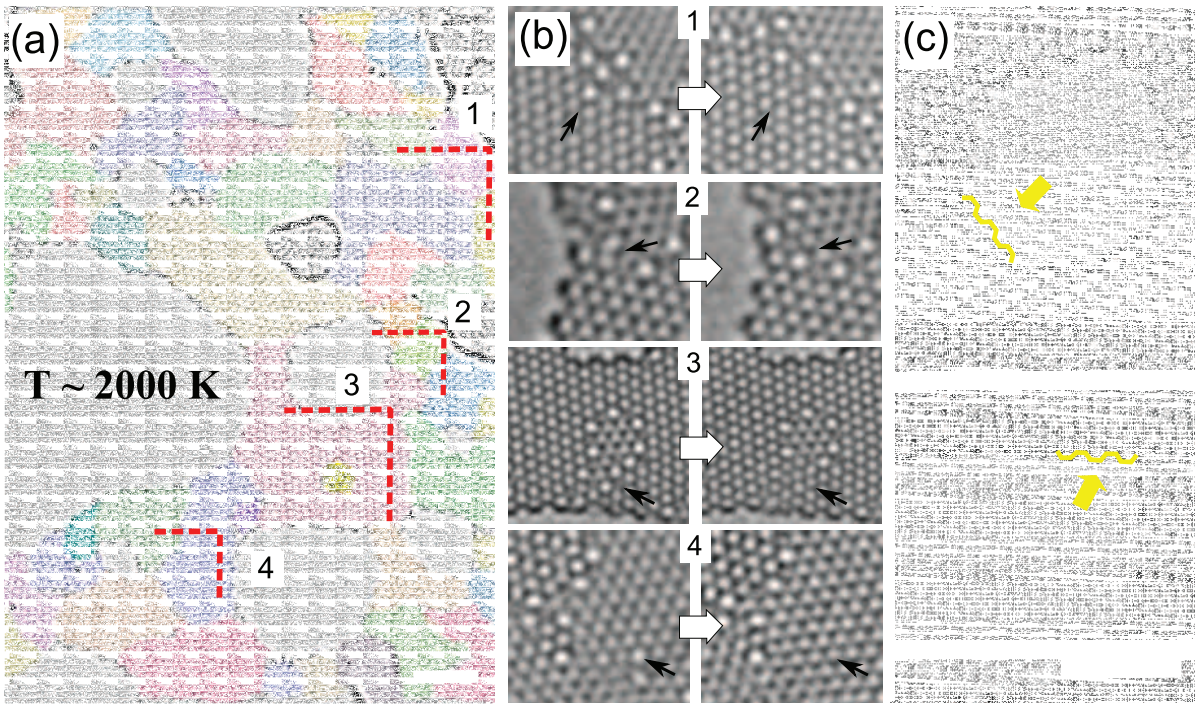

Fig. 4: (a) Fourier-filtered micrograph showing fully developed grains (shaded in color) of graphene. The filtering procedure worked perfectly only in the central part of the image. This micrograph was recorded during extreme heat treatment above 2000 K, as estimated from the behavior of freestanding SiN located close to the sample (amorphous SiN is known to crystallize at 1600 K [21] and to begin decomposing around 2000 K [9]). (b) Numbered image pairs capturing dynamic rearrangements of carbon bonds during constant heating (left image = starting configuration; right image = after 100 s). (c) Markers indicate armchair-type atomic configurations at the free edges of adsorbate layers. Scale bars are 2 nm in length.

4. Conclusions

In summary, we have presented atomically resolved *in situ* TEM studies of the heat-induced evolution of hydrocarbons on graphene. Temperature profiles with maxima up to $\approx$ 2000 K were obtained by passing an electrical current through a freestanding graphene substrate. We found that extreme heat activates a transformation of adsorbed hydrocarbons on top of graphene into atomic monolayers of amorphous carbon, followed by crystallization. The resulting polycrystalline layers consist of free edges showing predominantly armchair configuration.

Acknowledgment

We thank our technicians Ilona Argut, Susanne Menzel, Rudolf Rösch, Rainer Blood and Yakiv Men for their technical support. A special thank goes to Prof. Dr. Jannik C. Meyer for his collaboration with respect to scientific questions and the microscope operation.

References

[1] B. Westenfelder, J.C. Meyer, J. Biskupek, S. Kurasch, F. Scholz, C.E. Krill, and U. Kaiser, "Transformations of carbon adsorbates on graphene substrates under extreme heat", *Nano Lett.*, vol. 11, pp. 5123–5127, 2011.

[2] F.M. Ross, "In situ transmission electron microscopy", in *Science of Microscopy*, P.W. Hawkes and J.C.H. Spence (Eds.), pp. 445–534, Springer New York, 2007.

[3] T. Kamino, T.Y. Takahiro Sato, and T. Hashimoto, "Development of a technique for high resolution electron microscopic observation of nano-materials at elevated temperatures", *J. Electron Microsc.*, vol. 54, pp. 505–508, 2005.

[4] P.L. Gai and E.D. Boyes, "A very high temperature (2000 °C) stage for atomic resolution *in situ* ETEM", in *EMC 2008 14th European Microscopy Congress 1–5 September 2008, Aachen, Germany*, M. Luysberg, K. Tillmann, and T. Weirich (Eds.), pp. 481–482, Springer Berlin Heidelberg, 2008.

[5] A. Mayoral, L.F. Allard, D. Ferrer, R. Esparza, and M. Jose-Yacaman, "On the behavior of Ag nanowires under high temperature: in situ characterization by aberration-corrected STEM", *J. Mater. Chem.*, vol. 21, pp. 893–898, 2011.

[6] K. Kim, W. Regan, B. Geng, B. Alemán, B.M. Kessler, F. Wang, M.F. Crommie, and A. Zettl, "High-temperature stability of suspended single-layer graphene", *Phys. Status Solidi (RRL)*, vol. 4, pp. 302–304, 2010.

[7] C. Lee, X. Wei, J.W. Kysar, and J. Hone, "Measurement of the elastic properties and intrinsic strength of monolayer graphene", *Science*, vol. 321, pp. 385–388, 2008.

[8] T.J. Booth, P. Blake, R.R. Nair, D. Jiang, E.W. Hill, U. Bangert, A. Bleloch, M. Gass, K.S. Novoselov, M.I. Katsnelson, and A.K. Geim, "Macroscopic graphene membranes and their extraordinary stiffness", *Nano Lett.*, vol. 8, pp. 2442–2446, 2008.

[9] B. Westenfelder, J.C. Meyer, J. Biskupek, G. Algara-Siller, L.G. Lechner, J. Kusterer, U. Kaiser, C.E. Krill III, E. Kohn, and F. Scholz, "Graphene-based sample supports for in situ high-resolution TEM electrical investigations", *J. Phys. D: Appl. Phys.*, vol. 44, pp. 055502-1–7, 2011.

[10] J.O. Bovin, R. Wallenberg, and D.J. Smith, "Imaging of atomic clouds outside the surfaces of gold crystals by electron microscopy", *Nature*, vol. 17, pp. 47–49, 1985.

[11] S. Iijima and T. Ichihashi, "Motion of surface atoms on small gold particles revealed by HREM with real-time VTR system", *Jpn. J. Appl. Phys.*, vol. 24, pp. L125–L128, 1985.

[12] E. Sutter, P. Sutter, and Y. Zhu, "Assembly and interaction of Au/C core-shell nanostructures: in situ observation in the transmission electron microscope", *Nano Lett.*, vol. 5, pp. 2092–2096, 2005.

[13] A.S. Barnard, N.P. Young, A.I. Kirkland, M.A. van Huis, and H. Xu, "Nanogold: a quantitative phase map", *ACS Nano*, vol. 3, pp. 1431–1436, 2009.

[14] P. Buffat and J.P. Borel, "Size effect on the melting temperature of gold particles", *Phys. Rev. A*, vol. 13, pp. 2287–2298, 2000.

[15] A. Turchanin, D. Weber, M. Büenfeld, C. Kisielowski, M.V. Fistul, K.B. Efetov, T. Weimann, R. Stosch, J. Mayer, and A. Gölzhäuser, "Conversion of self-assembled monolayers into nanocrystalline graphene: structure and electric transport", *ACS Nano*, vol. 5, pp. 3896–3904, 2011.

[16] P.Y. Huang, C.S. Ruiz-Vargas, A.M. van der Zande, W.S. Whitney, M.P. Levendorf, J.W. Kevek, S. Garg, J.S.A.C.J. Hustedt, Y. Zhu, J. Park, P.L. McEuen, and D.A. Muller, "Grains and grain boundaries in single-layer graphene atomic patchwork quilts", *Nature*, vol. 469, pp. 389–392, 2011.

[17] O.V. Yazyev and S.G. Louie, "From graphene constrictions to single carbon chains", *Nature Materials*, vol. 9, pp. 806–809, 2010.

[18] C.O. Girit, J.C. Meyer, R. Erni, M.D. Rossell, C. Kisielowski, L. Yang, C.H. Park, M.F. Crommie, M.L. Cohen, S.G. Louie, and A. Zettl, "Graphene at the edge: stability and dynamics", *Science*, vol. 323, pp. 1705–1708, 2009.

[19] A. Chuvilin, J.C. Meyer, G. Algara-Siller, and U. Kaiser, "From graphene constrictions to single carbon chains", *New J. Phys.*, vol. 11, pp. 083019-1–10, 2009.

[20] P. Koskinen, S. Malola, and H. Häkkinen, "Self-passivating edge reconstructions of graphene", *Phys. Rev. Lett.*, vol. 101, pp. 115502-1–4, 2008.

[21] Y. Li, Y. Liang, F. Zheng, X. Shong, and Z. Hu, "Phase transition and particulate growth of laser synthesized ultrafine amorphous silicon nitride powders", *J. Mater. Sci. Lett.*, vol. 13, pp. 1588–1590, 1994.

[22] B. Song, G.F. Schneider, Q. Xu, G. Pandraud, C. Dekker, and H. Zandbergen, "Atomic-scale electron-beam sculpting of near-defect-free graphene nanostructures", *Nano Lett.*, vol. 11, pp. 2247–2250, 2011.

MOVPE Growth of Semipolar GaN on Patterned Sapphire Wafers: Influence of Substrate Miscut

Tobias Meisch

We describe epitaxial methods for two different semipolar GaN orientations on patterned sapphire substrates: With $(10\bar{1}2)$ *(r-plane) sapphire substrates we achieve planar* $(11\bar{2}2)$ *GaN layers with smooth surfaces on a large scale. In the case of* $(11\bar{2}3)$ *(n-plane) patterned wafers the growth of* $(10\bar{1}1)$ *GaN is possible. We optimized the growth conditions for* $(11\bar{2}2)$ *GaN (especially the growth temperature) yielding a coalesced, planar semipolar surface. Thereafter we transferred the knowledge from* $(11\bar{2}2)$ *oriented growth to* $(10\bar{1}1)$ *oriented growth and investigated the general influence of substrate miscuts on surface and crystal qualities, respectively. Due to the fact that the angle between* $(10\bar{1}1)$ *and* (0001) *in the case of GaN and the angle between* $(11\bar{2}3)$ *and* (0001) *in the case of sapphire are slightly different, we detected an imperfect surface. Choosing the right substrate miscut angle the crystal and / or the surface quality of GaN could be improved. The third important point is the non-homogeneous defect density distribution in the crystal. The right miscut could help to push the growth of the areas with less defects over the areas with a high defect density to improve the total crystal quality.*

1. Introduction

At present, optoelectronic devices like LEDs or laser diodes based on GaInN - GaN heterostructures are usually grown in c-direction. Due to the crystal geometry of GaN, strong piezoelectric fields are present within such heterostructures. These internal electric fields bend the energy levels leading to a charge carrier separation in the quantum wells. The reduced overlap of the wavefunctions of electrons and holes leads to a reduced recombination probability - the efficiency of a LED (e.g.) decreases. In addition, a red shifted emission wavelength as a result of a reduced effective bandgap is observable, known as "Quantum Confined Stark Effect" (QCSE).

One promising way to reduce the negative effect of QCSE on the efficiency is to grow GaN in non-c-direction. A growth direction with a vanishing QCSE is called non-polar - in the case of a reduced QCSE semi-polar, respectively. The growth in non-polar directions is typically affected by a very high defect density [1, 2]. To avoid this problem, a balance between a reduced QCSE and an acceptable crystal quality needs to be found by growing on semipolar surfaces.

Okada et al. [3] presented a possible method to grow GaN in the well known c direction obtaining yet a semipolar surface: They patterned r-plane sapphire substrates by etching trenches with c-like side facets into the wafer. With the help of selective epitaxy, crystal

growth just on the c-facets is possible. At the beginning, GaN forms triangular shapes which coalesce to a planar semipolar surface (cf. Fig. 1) after a suitable growth time.

Our main ambition is to grow $(10\bar{1}1)$ GaN on n-plane sapphire substrates. The general influence of miscut in the crystal quality has to be investigated. A slight misorientation between $(11\bar{2}3)$ sapphire and $(10\bar{1}1)$ GaN can be observed. The different crystal structures of the two materials are responsible for the different angles between $(10\bar{1}1)$ and (0001) in the case of GaN (61.95 °) and $(11\bar{2}3)$ and (0001) in the case of sapphire (61.22 °), respectively [4]. Based on this fact, slightly tilted triangular shapes (around 0.7 °) which build a rough surface are expected. On the other hand, previous investigations of Schwaiger et al. [5] showed that the -c-wing exhibits a higher defect density than the +c-wing. Therefore, one possibility to improve the total crystal quality is to overgrow the -c- by the +c-wing by choosing a vanishing miscut. So a compromise between crystal and surface quality has to be found, which means finding the most promising substrate miscut.

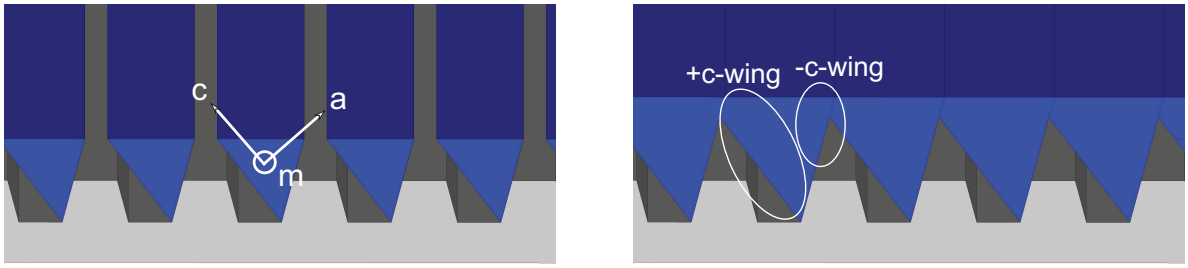

Fig. 1: Growth of GaN stripes (blue) with triangular shapes on a patterned substrate (grey). The triangular shapes (left) coalesce after a right growth time to a planar surface (right).

2. Experimental

The first step for obtaining semipolar GaN is to pattern the sapphire substrate with trenches having a c-plane-like side facet. At first a 200 nm thick layer of SiO_2 which later acts as a mask for selective area growth is deposited. It is followed by an about 500 nm thick nickel layer structured via lithography with a stripe mask (3 µm opening, 6 µm period). With reactive ion etching (RIE), the pattern is transferred into the sapphire - the resulting grooves have a width at the bottom of about 1.5 µm, a depth of about 1.2 µm and possess a c-plane-like facet.

All samples investigated in this study were grown in a low-pressure horizontal MOVPE reactor (Aixtron) with the precursors trimethylgallium (TMGa), trimethylaluminium (TMAl) and high purity ammonia.

The growth starts with an oxygen doped AlN nucleation layer at low temperature, followed by the GaN layer. The reactor pressure was set to 150 mbar and the V/III ratio was 650.

The crystal quality of the GaN layer was investigated by high resolution X-ray diffraction (HRXRD). With the help of a scanning electron microscope (SEM) we were able to determine the surface morphology. Surface roughness was measured via atomic force microscopy (AFM).

To investigate the influence of the substrate miscut on the growth of GaN it is important to know the crystal orientation angles as exactly as possible. A sample holder for the HRXRD machine was developed to measure the miscut angle with an accuracy of about 0.05 °. Using a conventional laser pointer, the sample alignment in the X-ray machine is easy to perform: While rotating the sample, the laser beam reflected on the surface produces a rotating point on a screen. Two micrometer screws allow to tilt the sample until the reflected beam describes a nearly constant point. Now the sample is perfectly aligned in the X-ray machine and the misalignment of the crystal structure within the substrate is measurable.

3. $(11\bar{2}2)$ GaN on $(10\bar{1}2)$ Sapphire

As mentioned above, our main target is to grow semipolar $(10\bar{1}1)$ GaN on $(11\bar{2}3)$ sapphire. S. Schwaiger already started some investigations in $(10\bar{1}1)$ GaN growth during his PhD thesis. Due to the changing of growth conditions over a large time range a rough adaptation of the most important parameters (e.g. temperature) is necessary. An additional problem is the limited number of n-plane wafers available for our institute. Therefore, we started our experiments with $(11\bar{2}2)$ GaN on $(10\bar{1}2)$ (r-plane) sapphire. After optimization, we can transfer the obtained knowledge to $(10\bar{1}1)$ GaN on $(11\bar{2}3)$ sapphire.

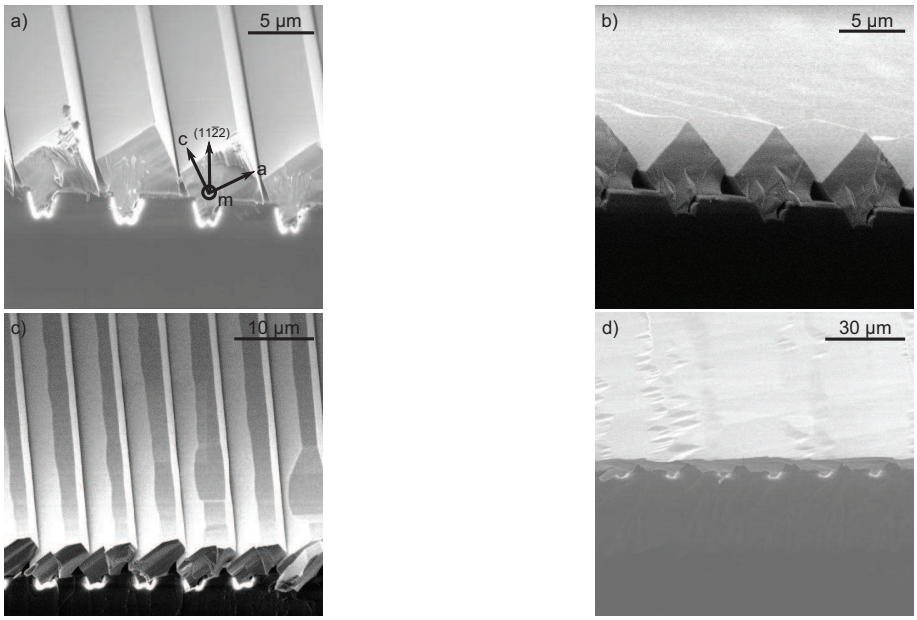

Fig. 2: Growth of $(11\bar{2}2)$ GaN on patterned $(10\bar{1}2)$ sapphire at different growth temperatures: a) 1130 °C, b) 1110 °C, c) 1070 °C and d) 1040 °C.

As shown in Fig. 2, at high growth temperatures (part a) (1130 °C) and b) (1110 °C)) the growth rate in a- is approximately the same as in c-direction. For closed layers, the growth rate in c-direction has to be increased by decreasing the temperature. In part c) (1070 °C) one can see very first beginnings of coalesced stripes and a closed planar surface. By a further reduction of the growth temperature to 1040 °C a coalesced and planar surface in $(11\bar{2}2)$ direction was obtained.

4. $(10\bar{1}1)$ GaN on $(11\bar{2}3)$ Sapphire

In the case of $(11\bar{2}2)$ GaN we were able to grow stripes with the right shape to form a coalesced semipolar layer with a reasonable surface. We just transferred the growth recipe to achieve $(10\bar{1}1)$ GaN.

As already explained, for this crystal orientation we want to investigate the influence of substrate miscut on crystal and surface quality. $(11\bar{2}3)$ sapphire substrates (20 mm x 20 mm) with miscuts of 0 °, 0.5 °, 1.0 °, 1.5 ° and 2.0 ° towards c-direction were available. We systematically investigated the growth of GaN on these substrates with unaltered growth conditions for each growth run.

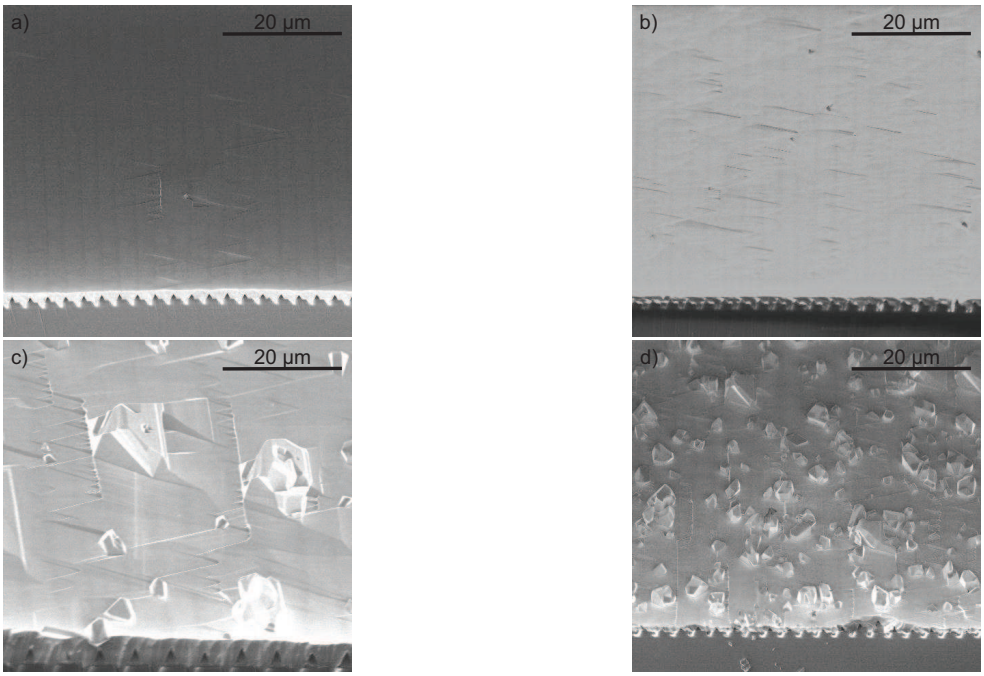

Fig. 3: SEM picture of semipolar $(10\bar{1}1)$ GaN on $(11\bar{2}3)$ sapphire with different miscut angles to c-direction: a) 0 °, b) 0.5 °, c) 1.0 ° and d) 1.5 °. A higher miscut angle shows a lower surface quality. In the case of 2 ° miscut, growth of an approximately planar surface was not possible.

As shown in Fig. 3, the higher the miscut, the lower the surface quality. In the case of 0 °, we achieved a very smooth surface over a large area with a RMS roughness of 2.5 nm in an area of 10 µm x 10 µm (cf. Fig. 5). One possible reason for the decreasing surface quality at higher miscuts could be the decreasing width of the trenches. SEM measurements show clearly the trend to small but deep grooves in the sapphire (cf. Fig. 4). In the case of substrates with a 2 ° miscut, the trenches were just 530 nm wide (instead of about 1.5 µm in the case of no miscut) - growth of a planar surface was not possible at these conditions.

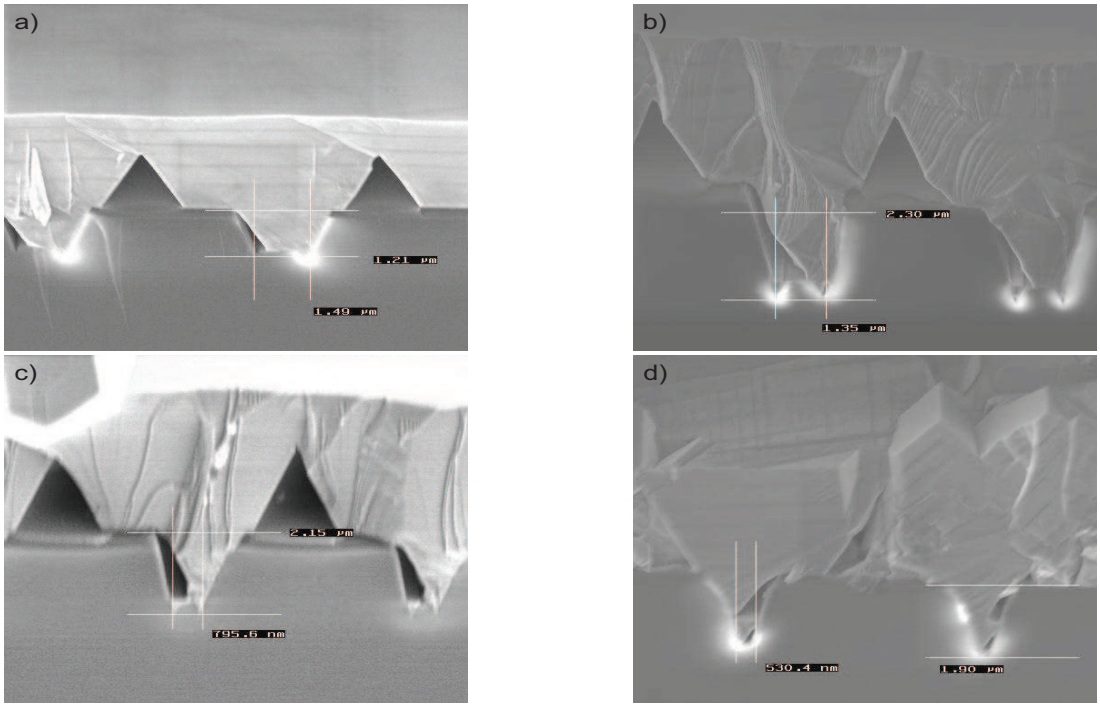

Fig. 4: SEM picture of semipolar $(10\bar{1}1)$ GaN on $(11\bar{2}3)$ sapphire with different miscut angles to c-direction: a) 0 °, b) 0.5 °, c) 1.5 ° and d) 2 °. The higher the miscut, the smaller the trenches.

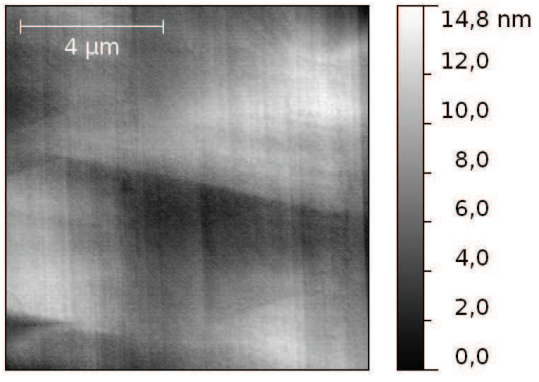

Fig. 5: AFM measurement on a planar $(10\bar{1}1)$ GaN surface on a sapphire substrate with 0 ° miscut with a RMS roughness of 2.5 nm.

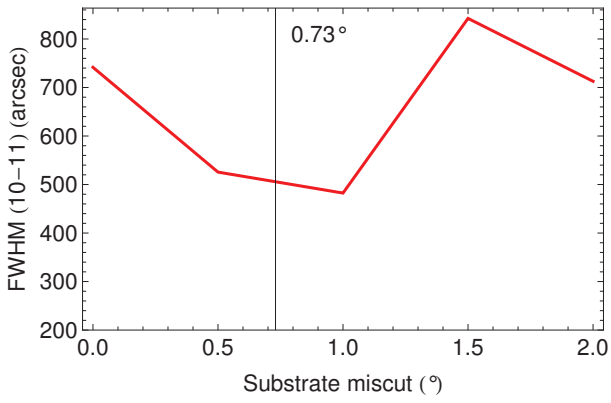

Fig. 6: FWHM of $(10\bar{1}1)$ rocking curve measurements over miscut angle. 0.73 ° is the misalignment between GaN layer and sapphire substrate.

Independently, we found (cf. Fig. 6) that the highest crystal quality with a FWHM of around 478 arcsec of $(10\bar{1}1)$ rocking curve is achieved with a substrate miscut of 1°. As already explained in the introduction, $(10\bar{1}1)$ GaN has a misorientation of about 0.73° to the $(11\bar{2}3)$ sapphire surface. Hence, we expected a maximum of crystal quality around this miscut angle. These investigations confirm our assumption.

5. Conclusion

With patterned $(10\bar{1}2)$ sapphire we developed a process to grow $(11\bar{2}2)$ oriented GaN with a smooth surface on large areas. The successful knowledge transfer to $(10\bar{1}1)$ GaN gives us the possibility to investigate the influence of substrate miscut in surface and crystal qualities, respectively. We could show that a misorientation of 1° to c-direction results in the best crystal quality. We reached a FWHM for $(10\bar{1}1)$ rocking curve measurements of around 478 arcsec. However, the disadvantage of the miscuts unequal zero is the decreasing surface quality. Obviously, the etching results depend on the substrate miscut. One possibility to solve this problem is to increase the trench dimension - which means using a larger mask for lithography.

Acknowledgment

I thank Ilona Argut, Rudolf Rösch, and Rainer Blood for the sample preparation and the technical support and I gratefully acknowledge the fruitful discussions with Robert Leute, Frank Lipski, Kamran Forghani, and Junjun Wang.

References

[1] B. Imer, F. Wu, M.D. Craven, J.S. Speck, and S.P. DenBaars, "Stability of (1-100) m-plane GaN films grown by metalorganic chemical vapor deposition", *Jpn. J. Appl. Phys.*, vol. 45, pp. 8644–8647, 2006.

[2] M.D. Craven, S.H. Lim, F. Wu, J.S. Speck, and S.P. DenBaars, "Structural characterization of nonpolar (11-20) a-plane GaN thin films grown on (1-102) r-plane sapphire", *Appl. Phys. Lett.*, vol. 81, pp. 469–471, 2002.

[3] N. Okada, A. Kurisu, K. Murakami, and K. Tadatomo, "Growth of semipolar (11-22) GaN layer by controlling anisotropic growth rates in r-plane patterned sapphire substrate", *Appl. Phys. Express*, vol. 2, pp. 091001-1–3, 2009.

[4] J. Däubler, *Wachstum und Charakterisierung von semipolarem GaN auf vorstrukturierten Saphirsubstraten*. Diploma Thesis, Ulm University, Ulm, Germany, 2010.

[5] S. Schwaiger, S. Metzner, T. Wunderer, I. Argut, J. Thalmair, F. Lipski, M. Wieneke, J. Bläsing, F. Bertram, J. Zweck, A. Krost, J. Christen, and F. Scholz, "Growth and coalescence behavior of semipolar (11-22) GaN on pre-structured r-plane sapphire substrates", *Phys. Status Solidi B*, vol. 248, pp. 588–593, 2011.

Band Structure Measurements and Calculations of Epitaxially Grown GaN Based Photonic Crystal Slabs with Semipolar Quantum Wells

Dominik Heinz

We report on the large area realization of GaN photonic crystal slabs with semipolar InGaN quantum wells (QWs) using laser interference lithography and selective area metalorganic vapour phase epitaxy (MOVPE). Directional extraction of guided modes was observed in angle-resolved photoluminescence spectroscopy (ARPL), and the photonic crystal slab dispersion relation was measured. A comparison of the observed band structure to theory was made using the finite difference time domain method (FDTD).

1. Introduction

Currently available GaN based green light emitting diodes (LEDs) and laser diodes (LDs) still suffer from a reduced device performance due to strong internal electrical fields. These fields especially appear in *c*-direction of the hexagonal wurtzite crystal, inducing a tilt in the band structure [1]. A separation of the electron and hole wave functions occurs, leading to a reduced overlap integral and, finally, causing a lowered radiative recombination rate. In contrast, devices grown in semipolar crystal directions reveal a reduced piezoelectric field and hence promise a more efficient way of light generation [2].

Today lots of efforts are made in order to overcome the so-called "green gap", with many groups working on semipolar GaN based optoelectronics. Nevertheless light extraction still plays an important role in device fabrication [3]. Due to high contrast in index of refraction most of the emitted light is typically trapped in the crystal by total internal reflection [3,4]. Only light emitted within a narrow light cone can directly escape into space, whereas most light gives rise to guided modes propagating in the high index dielectric similarly like in a waveguide [4, 5].

Extraction of guided modes can be done by integrating photonic crystals in a dielectric slab. Photonic crystals are periodically modulated dielectric structures with a periodicity comparable to the considered wavelength regime [6]. This periodicity introduces so-called Bloch modes which can be folded into the light cone by a photonic crystal reciprocal lattice vector $\vec{G}$, and thus couple to radiative modes. So-called photonic crystal LEDs [7] and LDs [8] have already been realized providing efficient and directional guided mode extraction without using additional optics [5]. Furthermore beam profile engineering becomes possible [9–12] using theoretical calculations of photonic crystal band structures.

In this work photonic crystal structures have been realized which combine both features, offering a directional light extraction and using semipolar QWs for highly efficient light

generation. Far field measurements of extracted Bloch modes have been performed using angle-resolved photoluminescence spectroscopy (ARPL). Subsequently the dispersion relation was determined and a comparison to simulation was made with the finite difference time domain method (FDTD) [13], using the freely available software package MEEP [14].

2. Fabrication Procedure

Realizing photonic crystals for the visible spectrum of light requires sub-µm-patterning. Here laser interference lithography, using a Lloyd's mirror [15–18], and conventional e-beam lithography have been used to structure periodically resist stripe and point structures on GaN templates, grown on sapphire substrates. These structures were subsequently transfered to epitaxial masks using a lift-off technique. Selective area overgrowth in MOVPE was applied to realize three-dimensional GaN-structures with semipolar side facets including InGaN-QWs (see annual report R.A.R. Leute).

3. Optical Characteristics

As described by E. Matioli and C. Weisbuch [19], directional light extraction of a GaN photonic crystal slab can be explained by considering guided modes as a finite sum of plane waves

$$\vec{E}^n(\vec{r}) = \vec{E}_0^n \mathrm{e}^{i\vec{k}_n \cdot \vec{r}}, \tag{1}$$

where each mode has been labeled by its own index n. For planar symmetry, wave vectors $\vec{k}_n$ can be separated into components parallel ($\vec{k}_{\parallel,n}$) and perpendicular ($\vec{k}_{z,n}$) to the waveguide

$$\vec{k}_n = \vec{k}_{\parallel,n} + \vec{k}_{z,n}. \tag{2}$$

The parallel component of a guided mode propagating in a dielectric slab can now be written as

$$k_{\parallel,n} = \frac{2\pi}{\lambda} n_{\mathrm{GaN}} \sin(\theta_n) \tag{3}$$

with propagation angle θ_n and index of refraction n_{GaN} for GaN [7]. Introducing a photonic crystal with reciprocal lattice vector $\vec{G}$, the parallel component of the wavevector can be changed following the equation

$$\vec{k}_{\parallel,m} = \vec{k}_{\parallel} + \vec{G} = \vec{k}_{\parallel} + m\vec{G}_0, \tag{4}$$

with scattered wavevector $\vec{k}_{\parallel,m}$, and new Bloch index m (index n was neglected for simplification) [19, 21]. For a 1D-photonic crystal the fundamental reciprocal lattice vector with lattice constant a can be considered as $G_0 \equiv \left|\vec{G}_0\right| = 2\pi/a$ [7]. The infinite sum of harmonics now introduces one Bloch mode [19, 22] described by

$$\vec{E}(\vec{r}) = \sum_m \vec{E}_m \mathrm{e}^{i(\vec{k}_{\parallel,m} \cdot \vec{r}_{\parallel} + k_z z)}. \tag{5}$$

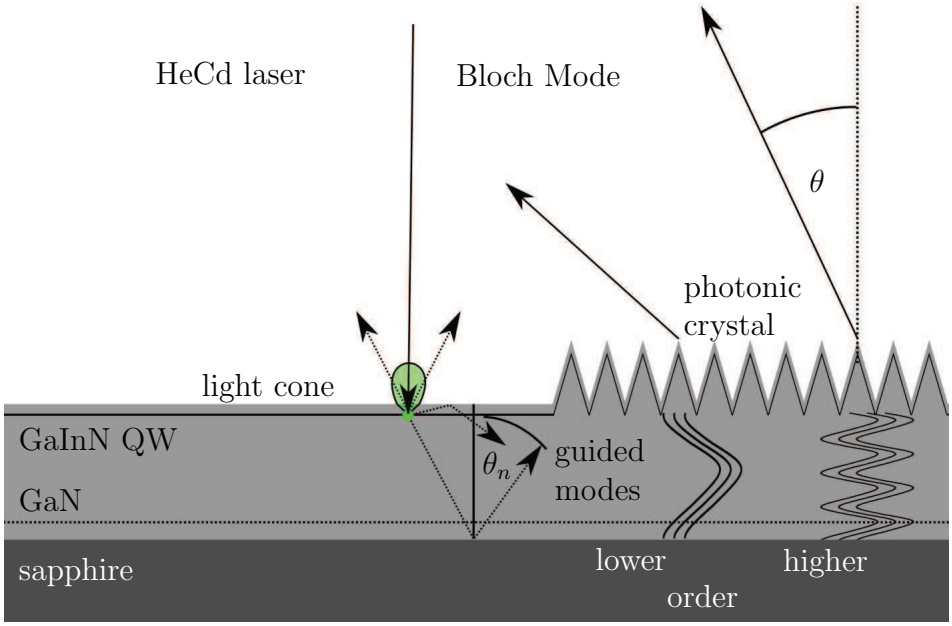

Fig. 1: Extraction of guided modes in a GaN slab by a photonic crystal made of Ga(In)N stripes. Excitation can be arranged by moving the focus point into or out of the structured area for investigation of semipolar or polar QWs, respectively [20, 23].

Bloch modes are periodic in $\vec{G}_0$ (see Eqn. 4 and 5) and by modifying $\vec{k}_{\parallel}$ total internal reflection can be avoided. Guided modes n with $\left|\vec{k}_{\parallel,m}\right| < k_0$ lie within the light cone and can couple to radiative modes [19]. Propagation and outcoupling of guided modes is schematically indicated in Fig. 1. Extracted guided modes are typically referred to as leaky modes and can be observed in angle-resolved photoluminescence spectroscopy. Excitation of semipolar and polar QWs could be achieved by moving the focus point of the HeCd-laser beam into or out of the structured area, respectively.

First one-dimensional photonic crystal stripe structures with period $a \approx 240\,\text{nm}$ have been investigated. The emission spectrum $I(\lambda)$ for TM modes was spectrally and directionally resolved with varying emission angle θ and presented in a colour map (Fig. 2). At $\lambda \approx 480\,\text{nm}$, semipolar QW emission could be observed, while longer wavelength contributions can be explained by yellow defect luminescence.

In addition, two folded GaN Bloch modes could be observed, corresponding to $m = \pm 1$ reciprocal lattice vectors $\vec{G}_0$, intersecting with each other. Both Bloch modes consist of several lines, each corresponding to a higher order guided mode in the GaN layer (order increases from top to bottom). At the intersection point of higher order guided modes (coming from left) with the QW emission, an increased light extraction was observed, while lower order modes (coming from right) show reduced light extraction. Compared to lower order modes, higher order guided modes in GaN have a higher overlap with the photonic crystal in longitudinal direction (compare Fig. 1 and [19]), hence show an improved light extraction.

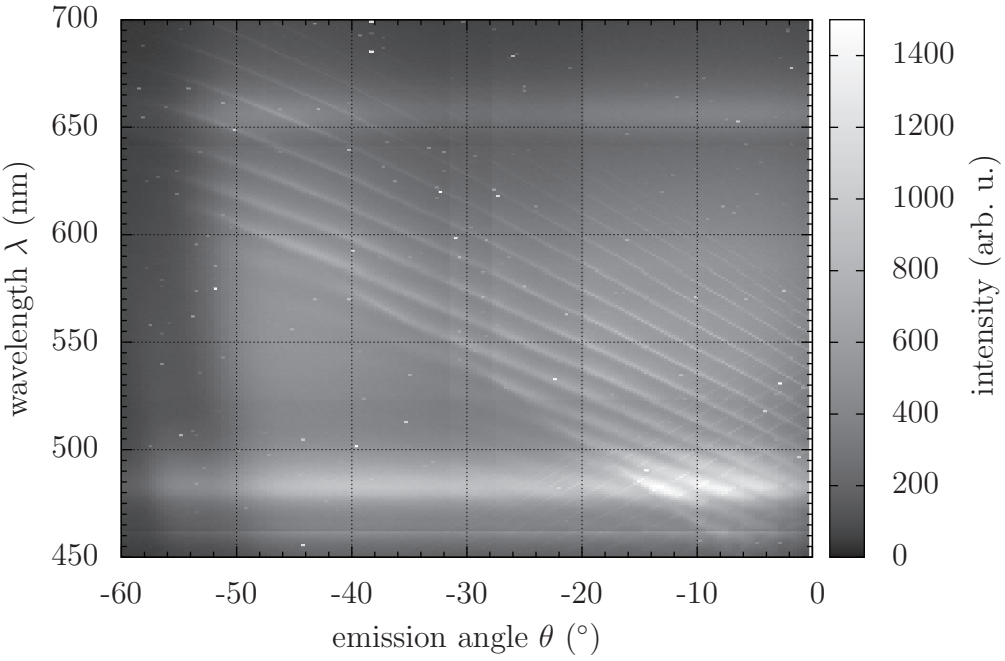

Fig. 2: Angle-resolved photoluminescence spectrum of a Ga(In)N stripe sample for TM modes (polarization set perpendicular to the stripes). Beside QW emission at $\lambda \approx 480\,\mathrm{nm}$, guided mode extraction was observed for the longer wavelength regime, excited by yellow defect luminescence. Both Bloch modes (corresponding to $m = \pm 1$ reciprocal lattice vectors $\vec{G}_0$) intersect in the QW region, showing an improved light extraction.

4. Dispersion Relation of a Photonic Crystal Slab

By performing an axis transformation from (λ, θ) to $\left(\frac{a}{\lambda}, \frac{a}{\lambda}\sin(\theta)\right)$ [20], the dispersion relation of a stripe photonic crystal slab could be derived (Fig. 3). Only the first Brillouin zone was plotted, and both axes are scaled using the photonic crystal period $a = 240\,\mathrm{nm}$ (Fig. 3). Additional lines have been plotted using the corresponding index of refraction for air ($n \approx 1$), GaN ($n \approx 2.45$) and sapphire ($n \approx 1.75$) using the relation

$$n \equiv \frac{k_{\parallel}}{k_0} = \frac{a\left(\frac{2\pi}{\lambda}\sin(\theta)\right)}{a\frac{2\pi}{\lambda}} \tag{6}$$

and folding them at the zone edges [19].

Bloch modes can only be observed inside the light cone, which is indicated by the light line in Fig. 3, and are limited to the region between the sapphire- and GaN-line. Regarding their slope, observed modes can clearly be correlated to guided modes in GaN. For a more detailed description, we calculated the dispersion relation and photonic band structure using the finite difference time domain [13] and filter diagonalization method [24] for an estimated thickness of the GaN layer of $d \approx 2.5\,\mu\mathrm{m}$. A broad Gauss-pulse was assumed for excitation with center frequency at $\frac{a}{\lambda} = 0.488$ and spectral width $\Delta = 0.3$. Simulated values are indicated in the overlay of Fig. 3 as points, with the field amplitude shown in grayscale. Calculated modes are in very good agreement with experiment, while some

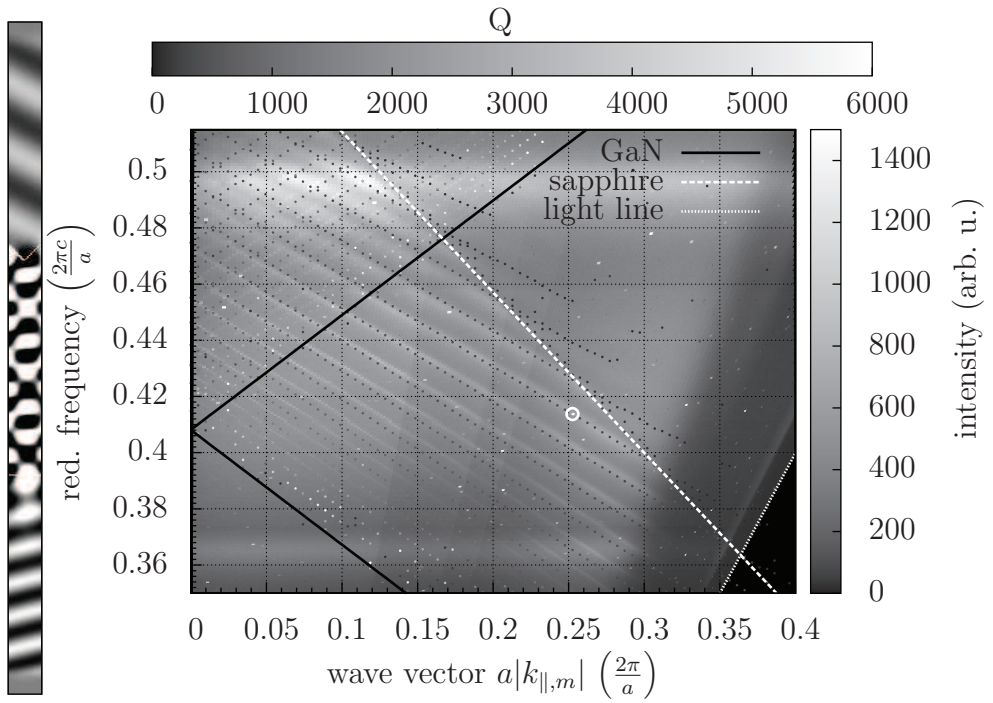

Fig. 3: Measured dispersion relation of a stripe (1D-)photonic crystal slab with corresponding intensity in gray scale (right). FDTD simulation is presented in the overlay with quality factor Q in gray scale (top). Extracted modes were folded into the light cone between GaN and sapphire line. Calculated field distribution for a certain leaky mode in the dispersion relation (white circle) can be seen on the left hand side with indicated unit cell. Observed modes clearly correspond to higher order guided modes in GaN (middle), which radiate to air (top) and sapphire (bottom).

minor discrepancy can be explained by the neglected material dispersion in this model. Calculations of the quality factor show highest Q values for lower order modes, which corresponds to the experimentally observed linewidth. Due to the reduced overlap with the photonic crystal, lower order modes stay longer confined in the crystal. This longer confinement corresponds to a smaller line width observed in the spectrum, because more stripes interfere. The higher order modes are coupled out faster (their extraction length is shorter), what results in broader linewidth of these modes.

Using a pulse with small spectral width and defined $|k_{\parallel,m}|$, corresponding field distributions have been calculated. On the left hand side of Fig. 3, the unit cell for calculation is presented (cross section) with the overlayed field distribution for an arbitrarily chosen frequency and wavevector (see corresponding white circle in dispersion relation). The investigated guided mode is obviously confined into the GaN-layer (middle) and radiates to air (top) and sapphire (bottom) directionally. Its order can be estimated to approximately 14 by counting the number of nodes.

If "forbidden" points above the sapphire and below the GaN-line are chosen, no total internal reflection at the interface GaN/sapphire occurs. Hence no extracted guided modes can be observed in this region.

5. Conclusion

In this work photonic crystal slabs with semipolar QWs have been realized. This approach based on selective area overgrowth allows structuring without using etching methods and could provide very high crystal quality. Directional extraction of Bloch modes could be observed in angle-resolved photoluminescence spectroscopy, as a characteristic feature of photonic crystals. Measurements of the dispersion relation show very good agreement with theoretical calculations done by FDTD method. Similar structures shall be applied in photonic crystal LEDs providing efficient and directional light extraction.

Acknowledgment

Photonic crystal slab fabrication using e-beam lithography was done by T. Wunderer and Y. Men. Scientific and technical support by K. Thonke from Institute of Quantum Matter / Semiconductor physics group (Ulm University) and R.A.R. Leute is gratefully acknowledged.

References

[1] F. Scholz and U. Schwarz, "Polarization-field control in nitride light emitters", *Phys. Status Solidi B*, vol. 248, pp. 547–548, 2011.

[2] T. Wunderer, M. Feneberg, F. Lipski, J. Wang, R.A.R. Leute, S. Schwaiger, K. Thonke, A. Chuvilin, U. Kaiser, S. Metzner, F. Bertram, J. Christen, G.J. Beirne, M. Jetter, P. Michler, L. Schade, C. Vierheilig, U.T. Schwarz, A.D. Dräger, A. Hangleiter, and F. Scholz, "Three-dimensional GaN for semipolar light emitters", *Phys. Status Solidi B*, vol. 248, pp. 549–560, 2011.

[3] C. Wiesmann, K. Bergenek, N. Linder, and U. Schwarz, "Photonic crystal LEDs - designing light extraction", *Laser & Photonics Reviews*, vol. 3, pp. 262–286, 2009.

[4] A. David, T. Fujii, R. Sharma, K. McGroddy, S. Nakamura, S.P. DenBaars, E.L. Hu, C. Weisbuch, and H. Benisty, "Photonic-crystal GaN light-emitting diodes with tailored guided modes distribution", *Appl. Phys. Lett.*, vol. 88, pp. 061124-1–3, 2006.

[5] E. Matioli, E. Rangel, M. Iza, B. Fleury, N. Pfaff, J. Speck, E. Hu, and C. Weisbuch, "High extraction efficiency light-emitting diodes based on embedded air-gap photonic-crystals", *Appl. Phys. Lett.*, vol. 96, pp. 031108-1–3, 2010.

[6] J.D. Joannopoulos, S.G. Johnson, J.N. Winn, and R.D. Meade, *Photonic Crystals - Molding the Flow of Light* (2nd ed.). Princeton, NJ: Princeton University Press, 2008.

[7] J.J. Wierer, A. David, and M.M. Megens, "III-nitride photonic-crystal light-emitting diodes with high extraction efficiency", *Nature Photonics*, vol. 3, pp. 163–169, 2009.

[8] H. Matsubara, S. Yoshimoto, H. Saito, Y. Jianglin, Y. Tanaka, and S. Noda, "GaN photonic-crystal surface-emitting laser at blue-violet wavelengths", *Science*, vol. 319, pp. 445–447, 2008.

[9] A. David, T. Fujii, E. Matioli, R. Sharma, S. Nakamura, S.P. DenBaars, C. Weisbuch, and H. Benisty, "GaN light-emitting diodes with Archimedean lattice photonic crystals", *Appl. Phys. Lett.*, vol. 88, pp. 073510-1–3, 2006.

[10] K. McGroddy, A. David, E. Matioli, M. Iza, S. Nakamura, S. DenBaars, J.S. Speck, C. Weisbuch, and E.L. Hu, "Directional emission control and increased light extraction in GaN photonic crystal light emitting diodes", *Appl. Phys. Lett.*, vol. 93, pp. 103502-1–3, 2008.

[11] C.F. Lai, C.H. Chao, H.C. Kuo, H.H. Yen, C.E. Lee, and W.Y. Yeh, "Directional light extraction enhancement from GaN-based film-transferred photonic crystal light-emitting diodes", *Appl. Phys. Lett.*, vol. 94, pp. 123106-1–3, 2009.

[12] E. Rangel, E. Matioli, Y.S. Choi, C. Weisbuch, J.S. Speck, and E.L. Hu, "Directionality control through selective excitation of low-order guided modes in thin-film InGaN photonic crystal light-emitting diodes", *Appl. Phys. Lett.*, vol. 98, pp. 081104-1–3, 2011.

[13] A. Taflove and S.C. Hagness, *Computational Electrodynamics: The Finite-Difference Time-Domain Method* (2nd ed.). Norwood, MA: Artech, 2000.

[14] A.F. Oskooi, D. Roundy, M. Ibanescu, P. Bermel, J.D. Joannopoulos, and S.G. Johnson, "MEEP: A flexible free-software package for electromagnetic simulations by the FDTD method", *Computer Physics Communications*, vol. 181, pp. 687–702, 2010.

[15] C.J.M. van Rijn, W. Nijdam, S. Kuiper, G.J. Veldhuis, H. van Wolferen, and M. Elwenspoek, "Microsieves made with laser interference lithography for micro-filtration applications", *Journal of Micromechanics and Microengineering*, vol. 9, pp. 170–172, 1999.

[16] S. Kuiper, H. van Wolferen, C. van Rijn, W. Nijdam, G. Krijnen, and M. Elwenspoek, "Fabrication of microsieves with sub-micron pore size by laser interference lithography", *Journal of Micromechanics and Microengineering*, vol. 11, pp. 33–37, 2001.

[17] I. Byun and J. Kim, "Cost-effective laser interference lithography using a 405 nm AlInGaN semiconductor laser", *Journal of Micromechanics and Microengineering*, vol. 20, pp. 055024-1–6, 2010.

[18] C.P. Fucetola, H. Korre, and K.K. Berggren, "Low-cost interference lithography", *J. Vac. Sci. Technol. B*, vol. 27, pp. 2958–2961, 2009.

[19] E. Matioli and C. Weisbuch, "Impact of photonic crystals on LED light extraction efficiency: approaches and limits to vertical structure designs", *J. Phys. D: Appl. Phys.*, vol. 43, pp. 354005-1–22, 2010.

[20] E. Matioli, B. Fleury, E. Rangel, E. Hu, J. Speck, and C. Weisbuch, "Measurement of extraction and absorption parameters in GaN-based photonic-crystal light-emitting diodes", *J. Appl. Phys.*, vol. 107, pp. 053114-1–6, 2010.

[21] E. Matioli, B. Fleury, E. Rangel, T. Melo, E. Hu, J. Speck, and C. Weisbuch, "High extraction efficiency GaN-based photonic-crystal light-emitting diodes: comparison of extraction lengths between surface and embedded photonic crystals", *Appl. Phys. Express*, vol. 3, pp. 032103-1–3, 2010.

[22] D.W. Prather, S. Shi, A. Sharkawy, J. Murakowski, and G.J. Schneider, *Photonic Crystals - Theory, Applications, and Fabrication*. Hoboken, NJ: John Wiley & Sons, Inc., 2009.

[23] A. David, H. Benisty, and C. Weisbuch, "Optimization of light-diffracting photonic-crystals for high extraction efficiency LEDs", *Journal of Display Technology*, vol. 3, pp. 133–148, 2007.

[24] V.A. Mandelshtam and H.S. Taylor, "Harmonic inversion of time signals and its applications", *The Journal of Chemical Physics*, vol. 107, pp. 6756–6769, 1997.

Design and Characterization of High-Power Optically Pumped Green-Emitting Semiconductor Disk Lasers Using Second-Harmonic Generation

Alexander Hein and Susanne Menzel

Frequency-doubled optically pumped VECSELs which are aimed for an emission wavelength of 520 nm are presented. Layer design as well as experimental results are discussed. Differential quantum and slope efficiencies in the fundamental regime as high as 75 % and 57 %, respectively, are demonstrated. An optical output power for the second harmonic of more than 7 W is achieved.

1. Introduction

Although green semiconductor lasers have been realized in the gallium nitride material system [1], the available output powers of these are rather small. On the other hand, semiconductor disk lasers also called Vertical-External-Cavity Surface-Emitting Lasers (VECSELs) with fundamental emission in the range of 1000–1100 nm can provide high output powers of several watts in the green spectral range [2, 3] when combined with intra-cavity second-harmonic generation. Even though the VECSEL may be considered a relatively large and bulky source in the semiconductor laser family, rather compact cavities with efficient green output slightly below the watt level were already demonstrated [4, 5].

2. Layer Design

Major elements in the layer design of the presented VECSELs are a dielectric anti-reflection (AR) coating, a Resonant Periodic Gain (RPG) structure, and a binary rear Distributed Bragg Reflector (DBR). Contrary to our previous work [6], we disclaimed to follow the double-band DBR approach since, for the target wavelength of 1040 nm, the overall layer thickness of such a structure could be well beyond 7 µm, thus, making defect-free growth more difficult. For the DBR, an alternating AlGaAs/AlAs stack of 56 layers in total was chosen, aimed for high reflectivity at 1040 nm. The RPG structure is composed of periodically arranged InGaAs quantum wells (QWs) with a thickness of 7 nm which are embedded into GaAs. Strain compensation of the QWs was realized by using two different compositions of GaAsP in the pump light absorbing barriers. The AR coating is a TiO_2 layer applied by ion-beam sputter deposition. The surface reflectivities of the pump and the emission wavelength are calculated as 4 % and 10 % for incident angles of 25 ° and 0 °, respectively. In order to tune the micro-cavity resonance, an AlGaAs confinement layer is placed between the gain structure and the dielectric coating.

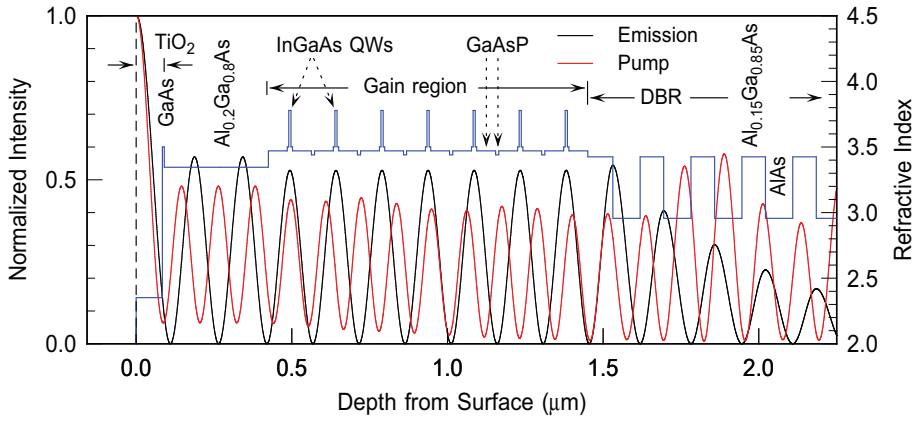

Fig. 1: Structure layout, indicated by the refractive index, and field intensities of the emission and the pump wavelength.

The structure layout is depicted in Fig. 1. Although the Bragg reflector mainly provides a high reflectivity for the emission wavelength, the structure enables a second resonance since the gold metalization at the end of the DBR acts as a reflector for the pump light.

3. Characterization

3.1 Structure quality

In a fast preliminary characterization by utilizing locally resolved photoluminescence (PL), the internal quality of the fabricated laser structures can be visualized. The samples are excited with the pump laser which is defocussed and illuminates the whole chip area as depicted in the center part of Fig. 2. Any structural defects arising from strain or processing errors are typically seen as dark lines in a cross-hatch pattern or simply appear as dark spots. According to the surface photograph (left) and the PL image (center) the laser structure shows no greater structural impairs. However, there are soldering imperfections and residues of the etch-stop layers. After extensive operation (right), these defects appear to have been intensified. This defect "growth" is attributed to "burn-ins" of the previously small defects/residues at high optical input of the pump. Any major detrimental impairs were not observed so far.

Fig. 2: Surface picture of a sample where substrate residues and solder imperfections are visible (left). Locally resolved photoluminescence images of a sample before (center) and after (right) laser operation. The sample was illuminated with the pump laser diode emitting at 804 nm.

3.2 Spectral characteristics

For further characterization of our structures, reflectivity and photoluminescence (PL) spectra are recorded as shown in Fig. 3. The Bragg reflector is centered around 1035 nm where highest reflectivity is provided. At the pump wavelength of around 804 nm, the reflectivity is strongly suppressed due to the AR coating. The excitonic absorption dip is located within the stop band around 1010–1020 nm. The PL peak from the QWs which is almost congruent with the excitonic absorption dip was designed to be around 1020 nm at room temperature corresponding to a detuning of 20 nm with respect to the micro-cavity resonance. The micro-cavity resonance is determined from PL spectra indicated in the right part of Fig. 3, where the temperature is varied between 0 °–90 °C. From the distinct peak evolving around 1049–1057 nm, the optical resonance is estimated to be around 1055 nm when accounted for a resonable temperature rise during operation. The red-shift happens at a rate of 0.09 nm/K. The determined value results in a 15 nm upward offset

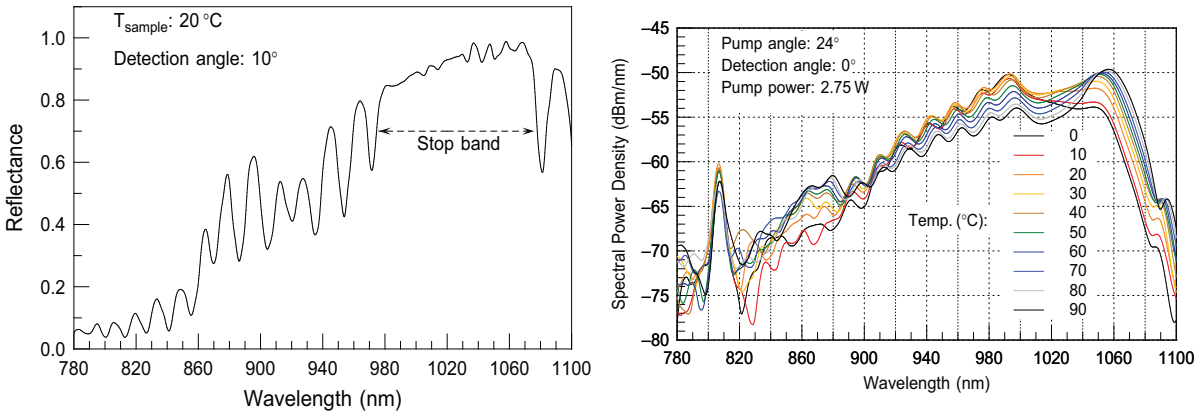

Fig. 3: Reflectivity spectrum (left) and the corresponding photoluminescence (right). The resonance at normal incidence is determined from the evolving peak in the optical spectra of the PL measurements. The pump radiation is visible as a distinct peak at around 804 nm.

to the target of 1040 nm. Reasons herefore are flux deviations during the growth process, insufficient incorporation of phophorous in the barrier layers, and thickness deviations of the AR coating. This detuning of approximately 35–40 nm can be considered large but would allow laser operation at elevated temperatures.

4. Fundamental Output

To effectively remove the heat from the devices during operation, these were soldered onto 300 µm thick diamond heatspreaders which in turn were soldered to either copper heatsinks or water cooled microchannel mounts. The output and absorptance characteristics of a microchannel mounted device are presented in Fig. 4 for various sizes of the pump spot. The microchannel mounts were not temperature controlled or stabilized. The cooling water temperature was set to 6 °C, while the ambient temperature was 20 °C. As the external mirror for the cavity an output coupler with a radius of curvature of 150 mm and a specified reflectivity of 98 % at a wavelength of 1035 nm was used. The pump radiation

was incident at an angle of 24° to normal. In case of the microchannel mount, a maximum output power of 14.1 W was achieved in the free running mode. The degree of absorptance for the pump ranged from 95–96 %. The spectral emission of the devices is rather broad, especially at high excitation. The peak wavelength shift over the absorbed optical power range was approximately 20 nm starting at around 1041 nm at threshold and increased to 1060 nm at the highest excitation. Due to the gradient on our wafers, the large pump spot, and the temperature gradient within, the spectral emission is broadend. Structures

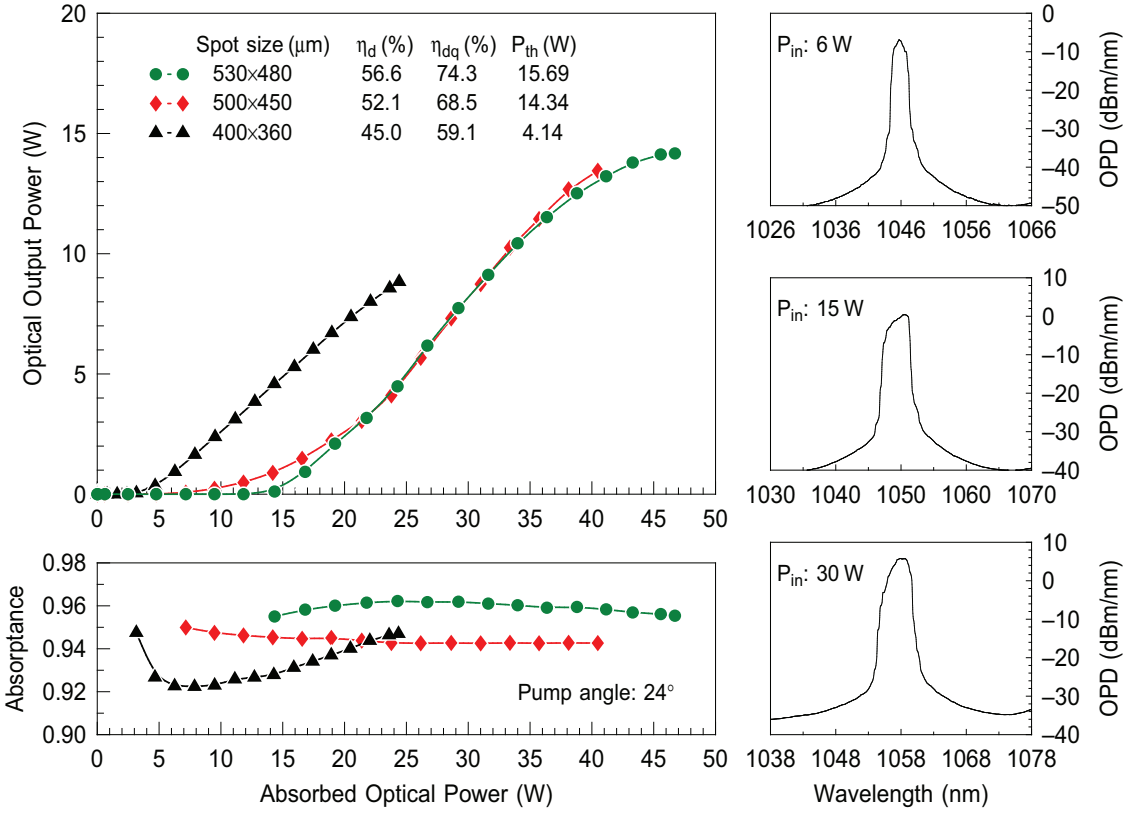

Fig. 4: Left: fundamental output and absorptance characteristics for different pump spot sizes. Slope η_d, differential quantum efficiency η_{dq}, and threshold power are calcultaed from fits. The measurements were performed with an outcoupling reflectivity of 98 % at 1035 nm. Right: optical spectra at different pump excitation levels with the increasing spectral width and red-shift.

that were soldered to copper heatsinks were temperature controlled and stabilized with a thermoelectric peltier cooler. The heatsink temperature was set to 16 °C in all presented measurements. Lower temperatures could not be sustained by the capacity of the cooling system during high power laser operation. The device was operated with two different outcoupling reflectivities, namely 98 % and 97 %. Because of thickness variations of the applied AR coating, the device was pumped at a slightly smaller angle of 20° where the surface reflectivity for the pump was smallest. The characteristics are given in Fig. 5. The maximum achieved output power was 18 W and 12.7 W, respectively. However, the pump spot was smaller when the device was operated with the lower outcoupling reflectivity. The absorptance was nearly identical to the previous device ranging between 94–96 %. For the higher outcoupling reflectivity and the larger pump spot we observed what may

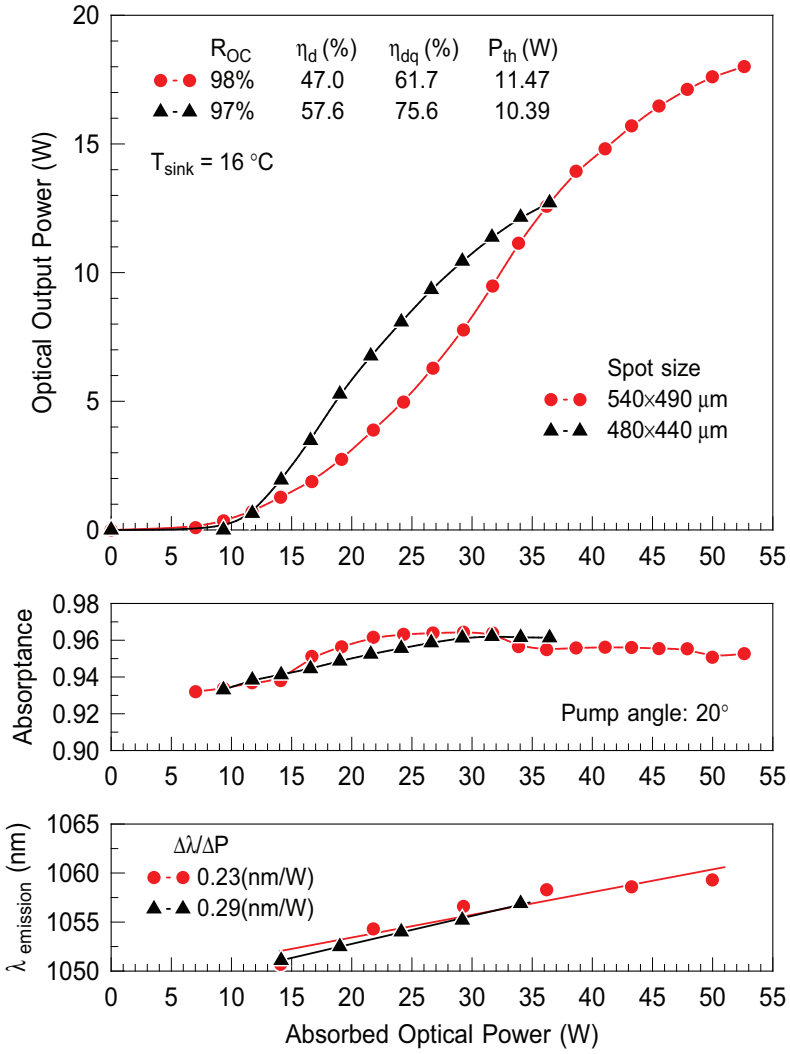

Fig. 5: Fundamental output of a temperature-controlled device. Absorptance and the spectral shift of the peak wavelength are shown in the lower parts of the figure. The spectral shift is indicated as a rate per unit of absorbed pump power and is determined from a linear fit.

be called "nonlinear behaviour" of the optical ouput. It seems that due to the larger than intended detuning between peak gain and micro-cavity resonance, the slope above threshold gradually increases until an optimum condition is reached around 25 W of absorbed power where the overlap of gain and micro-cavity resonance is best. The slope remains constant until approximately 37 W. Beyond that point thermal rollover gradually starts to set in. Accounting for this particular interval of the output curve, a slope efficiency higher than 65 % is achieved and would correspond to a differential quantum efficiency of more than 85 %. A higher efficiency in VECSELs was only achieved in an in-well pumped structure [7] where a tunable titanium-sapphire laser was used as the pump source. When considering an average slope of the output curve, the efficiency drops to 47 % with a corresponding differential quantum efficiency of 61 %. For the smaller spot size and higher outcoupling transmittance, the slope and differential quantum efficiency are above 57 % and 75 %, respectively, in the linear regime. The rate of the spectral shift per unit of

dissipated heat is with 0.44 nm/W and 0.60 nm/W, respectively, indicating better heat dissipation for the bigger spot size. However, better values as low as 0.1 nm/W can be obtained [8], but this rate also strongly depends on the detuning.

5. Second-Harmonic Output

The general cavity configuration for frequency doubling is illustrated in Fig. 6 and is similar to the one in our privious work [6]. Polarization and wavelength were controlled via a 4 mm thick birefringent quartz filter (BRF) located in the longer cavity arm. The BRF was set at the Brewster angle in order to suppress the σ-polarization (TE). The folding angle of the cavity was set to 30 ° corresponding to 15 ° of incidence with respect to beam propagation. The nonlinear crystals were placed in close proximity of the plane mirror due to the location of the second beam waist where the intensity is highest and the conversion most efficient. The nonlinear crystals were not temperature controlled or stabilized. The output was generated in a compact, folded, V-shaped cavity with foot prints of 89 mm for the longer and 32–33 mm for the shorter arm, depending on the crystal length and crystal material. The crystal facest are AR coated for the fundamental and the second harmonic in order to suppress etalon effects. The heat sink temperature was kept at 0 °C facilitating

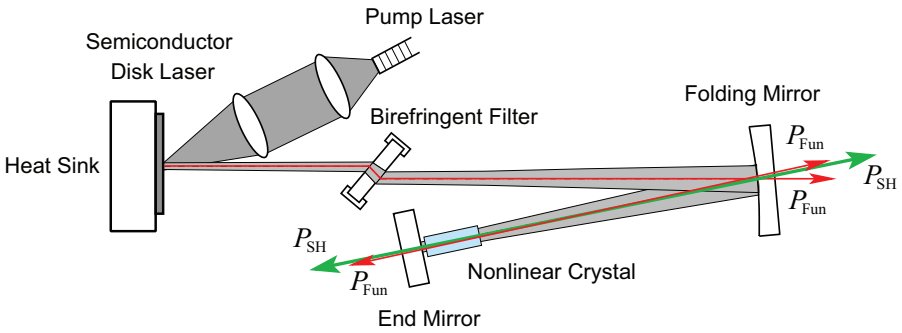

Fig. 6: Folded cavity with wavelength and polarization control via the BRF, and the nonlinear crystal for second-harmonic generation.

emission at a wavelength explicitly shorter than the favored micro resonance. Output characteristics of the second-harmonic regime are shown in Fig. 7 for different nonlinear crystals. Best performance was achieved with an 11 mm lithium triborate (LBO) crystal at wavelengths of 1046.7 nm and 523.4 nm, respectively. The recorded second-harmonic power is a sum of the two outputs as indicated in the figure. The ratio between these two was nearly unity. In fact the deviation of the two beams can be well placed within a band of 2.5 % as depicted in Fig. 7. The residual fundamental output was only a few milliwatts. The output power could be increased in a cavity configuration with larger footprints 190 mm for the longer arm and 65 mm for the shorter arm. The output characteristics are shown in Fig. 8. Here, a larger volume could be pumped compared to the compact cavity configuration due to a bigger pump spot. The highest extracted output power was 7.2 W with a spectrally clean emission locked to 523.6 nm. The spectral width at a 20 dB clip level was determined as 0.6 nm. We observed a higher output power although for the corresponding fundamental wavelength of 1047.3 nm, there is a larger offset to the target

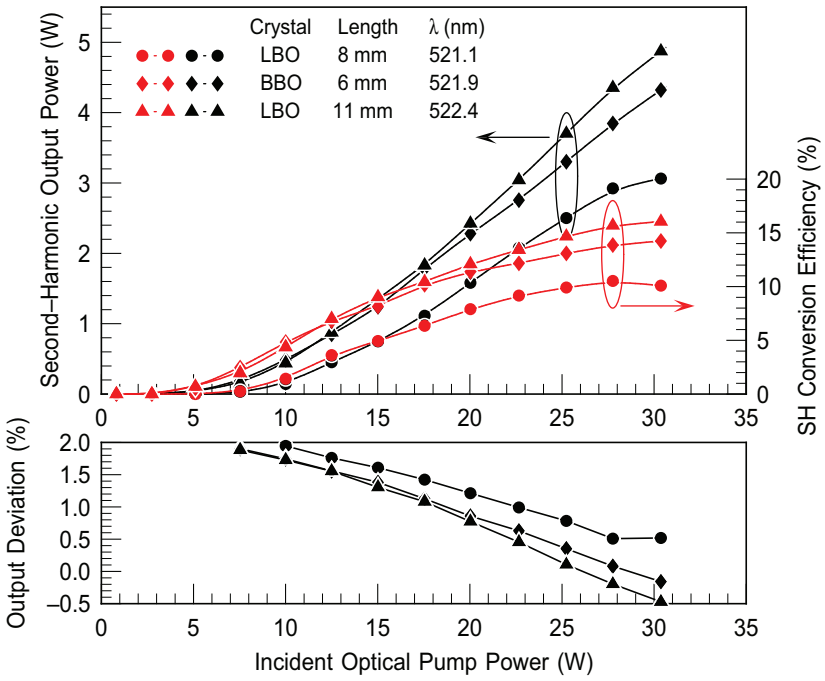

Fig. 7: Top: second-harmonic output characteristics for different materials and lengths of nonlinear crystals in a compact cavity setup. The outputs refer to a locked wavelength provided in the diagram. Bottom: relative power deviation of the two output beams.

wavelegth of 1040 nm. Since the fundamental ouput is higher at longer wavelengths than 1040 nm and the crystals still effectually convert at slightly longer or shorter wavelengths than 520 nm when the angle is changed the frequency conversion was more efficient. The best overall optical-to-optical conversion for this device was roughly 20 %. The maximum

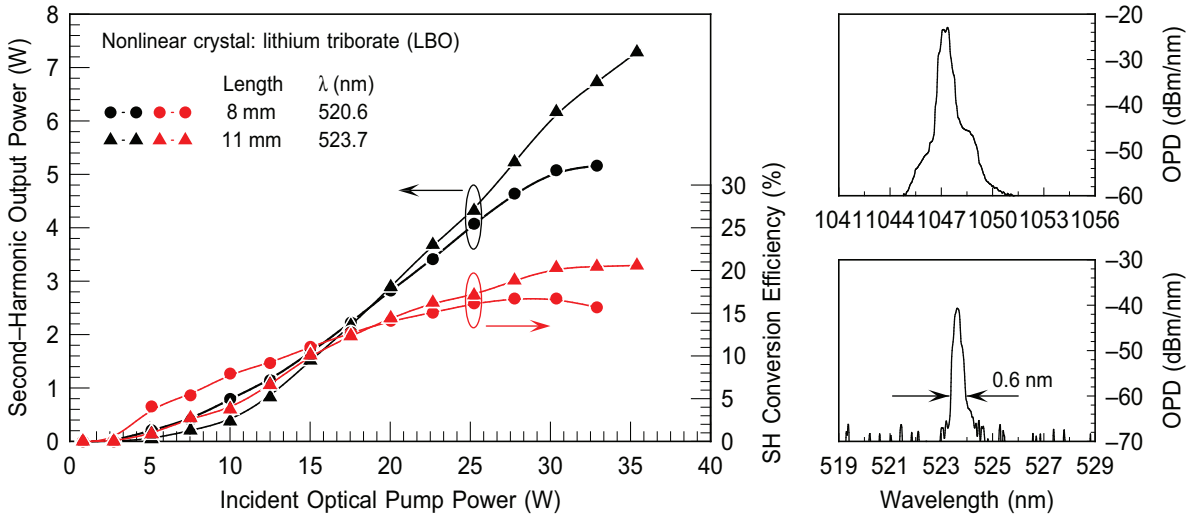

Fig. 8: Second-harmonic output power and optical-to-optical effeciency for different crystal lengths in a larger cavity with the respective wavelengths (left). Optical spectra of the fundamental and second-harmonic regime for the case of an 11 mm long LBO crystal (right).

second-harmonic output and also the conversion efficiency are believed to be limited by the mentioned detuning between the free running wavelength of the laser (1055–1060 nm) and the optimum wavelength for the nonlinear crystals (1040 nm).

6. Conclusion and Outlook

We presented a high-power optically pumped green-emitting VECSEL using intra-cavity second-harmonic generation. Disregarding the insufficient match for the wavelength, a bright multi-watt green laser emission has been demonstrated. With a more precise control of the micro-cavity resonance and subsequently a better match in the emission wavelength, the extraction of output powers of 10 W and more at even better efficiencies seem likely.

References

[1] T. Miyoshi, S. Masui, T. Okada, T. Yanamoto, T. Kozaki, S. Nagahama, and T. Mukai, "510–515 nm InGaN-based green laser diodes on c-plane GaN substrate", *Appl. Phys. Expr.*, vol. 2, pp. 062201-1–3, 2009.

[2] J. Lee, S. Lee, T. Kim, and Y. Park, "7 W high-efficiency continuous-wave green light generation by intracavity frequency doubling of an end-pumped vertical external-cavity surface-emitting semiconductor laser", *Appl. Phys. Lett.*, vol. 89, pp. 241107-1–3, 2006.

[3] J. Chilla, Q. Shu, H. Zhou, E. Weiss, M. Reed, and L. Spinelli, "Recent advances in optically pumped semiconductor lasers", Proc. SPIE 6451, 645109-1–10, 2007

[4] S. Cho, G.B. Kim, J.-Y. Kim, K.-S. Kim, S.-M. Lee, J. Yoo, T. Kim, and Y. Park, "Compact and efficient green VECSEL based on novel optical end-pumping scheme", *IEEE Photon. Technol. Lett.*, vol. 19, pp. 1325–1327, 2007.

[5] R. Hartke, E. Heumann, G. Huber, M. Kühnelt, and U. Steegmüller, "Efficient green generation by intracavity frequency doubling of an optically pumped semiconductor disk laser", *Appl. Phys. B*, vol. 87, pp. 95–99, 2007.

[6] A. Hein, F. Demaria, A. Kern, S. Menzel, F. Rinaldi, R. Rösch, and P. Unger, "Efficient 460-nm second-harmonic generation with optically pumped semiconductor disk lasers", *IEEE Photon. Technol. Lett.*, vol. 23, pp. 179–181, 2011.

[7] S. Beyertt, U. Brauch, F. Demaria, N. Dhidah, A. Giesen, T. Kübler, S. Lorch, F. Rinaldi, and P. Unger, "Efficient gallium-arsenide disk lasers", *IEEE J. Quantum Electron.*, vol. 43, pp. 869–875, 2007.

[8] T. Wang, Y. Kaneda, J.-M. Yarborough, J. Hader, J.V. Moloney, A. Chernikov, S. Chatterjee, S.W. Koch, B. Kunert, and W. Stolz, "High-power optically pumped semiconductor laser at 1040 nm", *IEEE Photon. Technol. Lett.*, vol. 22, pp. 661–663, 2010.

A New VCSEL Book

Rainer Michalzik

After about nine years of lean times, in the year 2012 there will be a new book on the market that is entirely devoted to vertical-cavity surface-emitting lasers (VCSELs). The present article briefly introduces the contents of this edited volume.

1. Introduction

Six books written in English with an exclusive focus on VCSELs have been published during the years 1995–2003 [1–6]. Enormous progress of VCSEL performance and applications has been achieved since then. In 2012 Springer-Verlag will thus publish a new VCSEL book [7] which will be a multi-author volume containing 18 chapters and about 550 pages. Figure 1 shows its tentative cover. Some of the chapters are state-of-the-art updates of chapters in previous VCSEL books. In addition, entirely new contributions are made to the fields of vectorial three-dimensional optical modeling, single-mode VCSELs,

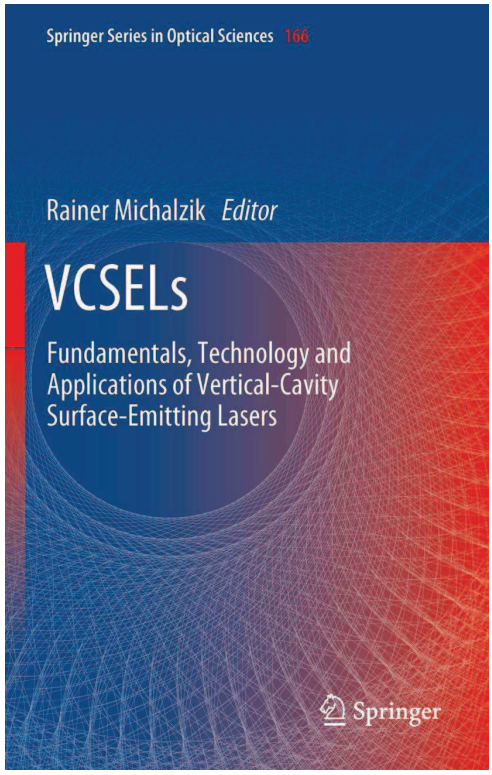

Fig. 1: Tentative cover design of the VCSEL book.

polarization control, polarization dynamics, very-high-speed design, high-power emission, use of high-contrast gratings, GaInNAsSb long-wavelength VCSELs, optical video links, VCSELs for optical mice and sensing, as well as VCSEL-based laser printing.

2. VCSEL Book Chapters

To give an overview of the contents of the book, in what follows we will introduce the individual book chapters in terms of their titles and abstracts with the authors and their affiliations inserted in square brackets.

1. **VCSELs: A Research Review** [R. Michalzik, Ulm University, Germany]: This chapter attempts to briefly review the research history of vertical-cavity surface-emitting lasers (VCSELs). Based on the contents of previous monographs on VCSELs written in English, we motivate the selection of topics in the present book and give an introduction to the individual chapters. Moreover, we mention some other research that is not covered in a dedicated chapter in order to provide the readers with even deeper insights into VCSEL research. Future directions and opportunities are also indicated.

2. **VCSEL Fundamentals** [R. Michalzik, Ulm University, Germany]: In this chapter we outline major principles of vertical-cavity surface-emitting laser (VCSEL) design and operation. Basic device properties and generally applicable cavity design rules are introduced. Characteristic parameters like threshold gain and current, differential quantum efficiency and power conversion efficiency, as well as thermal resistance are discussed. We describe the design of Bragg reflectors and explain the transfer matrix method as a convenient tool to compute VCSEL resonator properties in a one-dimensional approximation. Experimental results illustrate the emission characteristics of high-efficiency VCSELs that apply selective oxidation for current and photon confinement. Both the 850 and 980 nm wavelength regions are considered. The basic treatment of laser dynamics and noise behavior is presented in terms of the small-signal modulation response as well as the relative intensity noise. Finally we give some examples of VCSEL applications in fiber-based optical interconnects, i.e., optical data transmission over short distances.

3. **Three-Dimensional Modeling of VCSELs** [P. Debernardi, IEIIT-CNR, Torino, Italy]: VCSELs are complicated objects, also from a modeling point of view. In fact the computation of statical and dynamical operation implies the interaction of different physical phenomena: electrical, thermal and optical. All are strongly coupled and rule device operation. In this chapter the relevant effects and corresponding mutual interactions will be reviewed and possible ways to numerically address them discussed. Particular attention will be devoted to the optical solver, which is the core of any VCSEL simulation tool. In fact the optical characteristics determine the final device performance.

4. **Single-Mode VCSELs** [A. Larsson, J.S. Gustavsson, Chalmers University of Technology, Sweden]: The only active transverse mode in a truly single-mode VCSEL

is the fundamental mode with a near Gaussian field distribution. A single-mode VCSEL produces a light beam of higher spectral purity, higher degree of coherence and lower divergence than a multimode VCSEL and the beam can be more precisely shaped and focused to a smaller spot. Such beam properties are required in many applications. In this chapter, after discussing applications of single-mode VCSELs, we introduce the basics of fields and modes in VCSELs and review designs implemented for single-mode emission from VCSELs in different materials and at different wavelengths. This includes VCSELs that are inherently single-mode as well as inherently multimode VCSELs where higher-order modes are suppressed by mode selective gain or loss. In each case we present the current state-of-the-art and discuss pros and cons. At the end, a specific example with experimental results is provided and, as a summary, the most promising designs based on current technologies are identified.

5. **Polarization Control of VCSELs** [J.M. Ostermann, R. Michalzik, Ulm University, Germany]: In most types of VCSELs, the light output polarization is inherently unstable. While, in case of single-mode oscillation, the emitted light is mainly linearly polarized, its orientation is not well defined. This is because both the resonator and the gain medium are quasi isotropic in the plane of the active layers. Since a stable polarization is required for almost all sensing and some datacom applications, extensive and in-depth investigations have been undertaken during the last twenty years in order to stabilize the polarization of VCSELs without affecting their favorable operation parameters. Polarization control of VCSELs can be achieved by introducing a polarization-dependent gain, an asymmetric resonator, or mirrors with a polarization-dependent reflectivity. It has turned out that the last approach is most promising. It can be realized by incorporating a shallow surface grating in the upper mirror of a top-emitting VCSEL. Several million grating VCSELs are in reliable operation meanwhile, mainly in optical computer mice.

6. **Polarization Dynamics of VCSELs** [K. Panajotov, Vrije Universiteit Brussel, Belgium, F. Prati, Università dell'Insubria, Italy]: In this chapter we wrap up the experimental and theoretical results on polarization dynamics of solitary vertical-cavity surface-emitting lasers. Experiments have shown that VCSELs emit a linearly polarized fundamental transverse mode either along the [110] or [1$\bar{1}$0] crystallographic direction. Polarization switching between these modes can occur when the injection current is increased, showing either a frequency shift from the higher to the lower frequency mode (type I) or the reverse (type II). The two modes of linear polarization are strongly anti-correlated. The switching can happen through a region of mode hopping, with a dwell time scaling over eight orders of magnitude with the switching current, or through a region of hysteresis. Thermal (carrier) effects influence the polarization behavior of VCSELs through a red (blue) shift of the gain maximum. Also, in-plane anisotropic strain can strongly modify the polarization behavior of VCSELs. All these experimental results call for explanations, as there is no a priori intrinsic polarization selection mechanism in VCSELs. We present different gain equalization models to explain type I, type II or double polarization switching. Alternatively, the spin-flip model can explain both types polarization

switching by involving a microscopic spin-flip relaxation mechanism. Its predictive power has been experimentally established as, e.g., polarization switching through elliptically polarized states and dynamical instabilities. Finally, we highlight some perspective applications using polarization dynamics of VCSELs.

7. **Design and Performance of High-Speed VCSELs** [Y.-C. Chang, L.A. Coldren, University of California, Santa Barbara, USA]: Over the past several years, high-speed vertical-cavity surface-emitting lasers (VCSELs) have been the subject of intensive worldwide research due to their applications in optical interconnects and optical data networks. The performance of VCSELs, especially with respect to their high-speed characteristics, has made significant progress. In this chapter, we first present the basic theory for current-modulated VCSELs using rate equations and small-signal analysis. Factors that affect the modulation bandwidth, including the intrinsic laser responses and extrinsic parasitics, are identified. Once these limitations are known, we discuss various designs that have been implemented in VCSELs to specifically address them, followed by a review of the current high-speed VCSEL performance based on these designs at several different wavelengths, including 850 nm, 980 nm, 1.1 μm, and 1.3–1.6 μm. Finally, we consider new modulation schemes based on loss modulation in coupled-cavity VCSELs, which has the potential to reach even higher speeds.

8. **High-Power VCSEL Arrays** [J.-F. P. Seurin, Princeton Optronics, USA]: We review recent developments on high-power, high-efficiency two-dimensional vertical-cavity surface-emitting laser (VCSEL) arrays emitting around 808 and 980 nm. Selectively oxidized, bottom-emitting single VCSEL emitters with 50 % power conversion efficiency were developed as the basic building block of these arrays. More than 230 W of continuous-wave (CW) power is demonstrated from a 5 mm × 5 mm array chip. In quasi-CW mode, smaller array chips exhibit 100 W output power, corresponding to more than 3.5 kW/cm^2 of power-density. High-brightness VCSEL pumps have been developed, delivering a fiber output power of 40 W, corresponding to a brightness close to 50 kW/(cm^2 sr). High-energy VCSEL arrays in the milli-Joule range have also been developed. Many of the advantages of low-power single VCSEL devices such as reliability, wavelength stability, low-divergence circular beam, and low-cost manufacturing are preserved for these high-power arrays. VCSELs thus offer an attractive alternative to the dominant edge-emitter technology for many applications requiring compact high-power laser sources.

9. **High-Contrast Grating VCSELs** [C.J. Chang-Hasnain, University of California, Berkeley, USA]: We review a recent invention of single-layer one-dimensional high-index contrast subwavelength grating (HCG) and its incorporation into a VCSEL structure. The HCG is approximately 50 times thinner than a conventional distributed Bragg reflector (DBR), but offers higher reflectivity with a much broader spectral width. It provides lithographically defined control of polarization, transverse mode and emission wavelength. Using this ultrathin reflector, the tunable mirror in a micromechanical HCG-VCSELs are fabricated with a 10^4 times volume reduction and more than two orders of magnitude improved tuning speed.

10. **Long-Wavelength VCSELs With Buried Tunnel Junction** [M. Ortsiefer, VERTILAS, Germany, W. Hofmann, Technische Universität Berlin, Germany, J. Rosskopf, VERTILAS, Germany, M.-C. Amann, Technische Universität München, Germany]: Despite the earliest work on VCSELs in the late 1970s on InP-based materials, the further realization of VCSELs beyond 1.3 µm emission wavelength has been significantly delayed for many years with respect to their short-wavelength counterparts on GaAs substrates. This chapter covers the specific challenges, solutions and application prospects of VCSELs in non-GaAs-based material systems which are suitable for achieving significantly extended wavelength ranges. By using highly advanced device concepts, since the late 1990s it became possible to overcome the fundamental technological drawbacks related with long-wavelength VCSELs such as inferior thermal properties and to realize lasers with remarkable device performance. In particular and with respect to huge application opportunities in optical communications, this chapter presents InP-based VCSELs with single-mode output powers of several milliwatts at room temperature and well beyond 1 mW at 85°C, as well as modulation frequencies far above 10 GHz in conjunction with ultra-small power consumption. While the InP-based VCSEL technology is limited to maximum emission wavelengths around 2.3 µm, even longer emission up to the mid-infrared wavelength range can be achieved with VCSELs based on GaSb. With their inherent and, compared to other laser types, superior properties like enhanced tuning characteristics, long-wavelength VCSELs are regarded as key components for applications in optical sensing.

11. **GaInNAs(Sb) Long-Wavelength VCSELs** [J.S. Harris, H. Bae, T. Sarmiento, Stanford University, USA]: The push to provide high-speed optical network access directly to the end user is creating both significant pressure for the development of low-cost, high-speed access terminals as well as opportunities for development of entirely new technological approaches compared to those now used in the optical backbone networks. One of the most challenging is that of providing low-cost, long wavelength, single mode lasers that can be directly modulated at 10 Gbit/s, operate un-cooled in ambient environments and are easily packaged and coupled to fiber. Long wavelength vertical cavity surface emitting lasers (VCSELs) on GaAs certainly have the potential to meet these challenges. The development of MBE growth of GaInNAsSb on GaAs, issues of VCSEL design and successful demonstration of low threshold edge emitting lasers and the first 1530 nm monolithic VCSELs in GaInNAsSb on GaAs are described.

12. **Red Emitting VCSEL** [M. Jetter, R. Roßbach, P. Michler, Universität Stuttgart, Germany]: This chapter describes the progress in development of vertical-cavity surface-emitting lasers (VCSEL) emitting in the red spectral region around 650 nm for data transmission over polymer optical fibers (POF). First, growth issues of red VCSEL using two different material systems, namely AlGaAs and AlGaInP, are introduced. In particular, the optical and electrical state-of-the-art characteristics as low threshold currents (1 mA) and high output powers (several mW) are presented with a special focus on emission wavelength. Also the thermal budget and heat removal in the devices are pointed out with regard to the geometry of the VCSEL.

Small-signal modulation response in terms of maximum resonance frequency in dependance on temperature behavior are discussed. Applications of these devices in optical interconnects are described and digital data transmission at data rates up to 2.1 Gbit/s over step-index POF is reported. These properties make red emitting VCSEL perfectly suited for high-speed low power consuming light sources for optical data communication via POF. By introducing InP quantum dots as gain material in red emitting VCSEL nearly temperature independent record low threshold current densities of around 10 A/cm^2 could be observed.

13. **GaN-Based VCSELs** [S.-C. Wang, T.-C. Lu, H.-C. Kuo, J.-R. Chen, National Chiao Tung University, Taiwan]: This chapter first briefly reviews the background of the development of GaN-based edge-emitting lasers and key technical issues and approaches. Then we present the design considerations and fabrication technology for the development of GaN-based vertical-cavity surface-emitting lasers (VCSELs). The technical issues and approaches for fabricating high-quality and high-reflectivity GaN distributed Bragg reflectors (DBRs) are discussed. The trade-offs among the three kinds of GaN microcavity structures are compared. Fabrication processes and key performance characteristics of hybrid and double dielectric microcavities for optically pumped GaN VCSELs are presented. The key approaches to achieve electrically pumped GaN VCSELs are analyzed and recent developments in electrically pumped GaN VCSELs are described. The future prospects of enhancing the GaN VCSEL performance and operation temperature are discussed. Finally the emerging applications for nitride-based VCSELs are briefly described.

14. **VCSEL-Based Transceivers for Data Communications** [K.P. Jackson, Emcore, USA, C.L. Schow, IBM, USA]: The data communications (datacom) transceiver market has experienced tremendous growth over the last fifteen years due in large part to the use of vertical-cavity surface-emitting lasers (VCSELs) and multimode optical fibers. This chapter reviews the evolution of 850 nm laser-based datacom transceivers beginning with the early use of AlGaAs edge-emitters to the adoption of VCSELs where their unique attributes have enabled significant performance enhancements and cost reductions in transceiver designs.

15. **Low-Cost Optical Video Links Based on VCSELs** [H.-K. Shin, OPTICIS, Korea]: The history of introduction and current status of VCSEL based optical video link modules which have emerged as one of the main applications of VCSELs are described. The structure and characteristics of VCSELs in optical video links are summarized. The technical issues of the next generation optical video links for the mass market are discussed.

16. **Progress in VCSEL-Based Parallel Links** [D.M. Kuchta, IBM, USA]: This chapter covers most aspects of VCSEL-based parallel optical links during the period of 2000–2010, a period of tremendous advancement in this field both in research and in commercial deployment. Section 16.1 introduces the topic. Commercial activities are covered in Sect. 16.2. Section 16.3 covers research activities in this field. Deployment of these technologies in large systems, supercomputers and test

beds is discussed in Sect. 16.4. Advances in multi-fiber, multicore fiber and multi-fiber connectors for parallel links is the topic of Sect. 16.5. Section 16.6 discusses reliability for parallel links and its application to large systems. Finally, Sect. 16.7 concludes the chapter with future applications for VCSEL-based parallel links.

17. **VCSELs for Optical Mice and Sensing** [M. Grabherr, Philips Technologie GmbH U-L-M Photonics, Germany, H. Moench, Philips Research Laboratories, Germany, A. Pruijmboom, Philips Laser Lighting Systems, The Netherlands]: A real mass application for VCSELs is their use in optical mice and sensing. As illumination source for sensing applications VCSELs offer a better performance than LEDs. The even more advanced approach of laser self-mixing interference sensors allows a next step in integration, accuracy and new application fields. This chapter summarizes the major requirements towards VCSELs in illumination for sensing applications and gives typical specifications. A detailed description of the production process and the achieved reproducibility makes clear that these VCSELs are ideally suited for production in large quantities. In the second half of the chapter the self-mixing interference method is described in more detail and a highly integrated two axes laser Doppler interferometer is shown. This product is designed for a laser mouse but offers a number of other sensing applications.

18. **VCSEL-Based Laser Printing System** [N. Ueki, N. Mukoyama, FUJI XEROX, Japan]: There is an endless demand for improved image quality and higher speed in printer applications. To meet market requirements, in 2003 we launched DocuColor 1256GA, the world's first VCSEL-based electrophotographic printer utilizing a 780 nm single-mode 8×4 VCSEL array. The printer features 2400 dots per inch (dpi) resolution, which is still the highest level in the industry, and a speed of 12.5 pages per minute (ppm). A two-dimensional VCSEL array makes it much easier to increase the pixel density and printing speed by simultaneously scanning the 32 beams on the photoconductor in the light exposure system. Adopting VCSELs as a light source also contributes to reduced power consumption, because the operating current of VCSELs is extremely small and the wall-plug efficiency is very high. In this chapter, we explain the key technologies of VCSELs in light exposure system of laser printer, as well as their required characteristics to assure high image quality.

3. Conclusion

The time was ripe for a new VCSEL book. With this volume we hope to have closed the gap — at least for a little while.

References

[1] T.E. Sale, *Vertical Cavity Surface Emitting Lasers*. Taunton, Somerset: Research Studies Press, Ltd., 1995.

[2] T.P. Lee (Ed.), *Current Trends in Vertical Cavity Surface Emitting Lasers*. Singapore: World Scientific Publishing, 1995.

[3] C. Wilmsen, H. Temkin, and L.A. Coldren (Eds.), *Vertical-Cavity Surface-Emitting Lasers*. Cambridge: Cambridge University Press, 1999.

[4] J. Cheng and N.K. Dutta (Eds.), *Vertical-Cavity Surface-Emitting Lasers: Technology and Applications*. Amsterdam: Gordon and Breach Publishing, 2000.

[5] S.F. Yu, *Analysis and Design of Vertical Cavity Surface Emitting Lasers*. Hoboken: John Wiley & Sons, Inc., 2003.

[6] H. Li and K. Iga (Eds.), *Vertical-Cavity Surface-Emitting Laser Devices*. Berlin: Springer-Verlag, 2003.

[7] R. Michalzik (Ed.), *VCSELs — Fundamentals, Technology and Applications of Vertical-Cavity Surface-Emitting Lasers*, Springer Series in Optical Sciences, vol. 166, ISBN 978-3-642-24985-3. Berlin: Springer-Verlag, 2012, in press.

VCSELs with Two-Sided Beam Emission for Sensing Applications

Andreas Strodl and Rainer Michalzik

For use in optical sensors, vertical-cavity surface-emitting lasers (VCSELs) have been designed to provide simultaneous light emission from both facets. The VCSELs are based on active InGaAs quantum wells for laser output close to 960 nm wavelength where the GaAs substrate is transparent. Here we describe the laser fabrication and some static operation characteristics.

1. Introduction

VCSELs with two-sided emission have been presented in the literature long times ago (see, e.g., [1]). In the common AlGaAs material system on GaAs substrates, this is most easily achieved with the use of compressively strained InGaAs quantum wells (QWs) which have a reduced bandgap energy and with current supply through a top ring contact and a bottom ring contact at the back side of the substrate. For photon energies exceeding approximately 920 nm, the GaAs substrate is essentially transparent. For VCSELs based on GaAs QWs with emission in the 850 nm wavelength range, substrate removal or substrate replacement with, e.g., a glass wafer are alternative options. As for most cases in optical sensing, the optical pressure sensor application described in [2] requires single-mode, single-polarization emission with a high side-mode suppression ratio. In the sections to follow we first describe the chosen device structure for emission close to 960 nm wavelength and its processing and mounting and then present the experimental results for static operation. It turns out that a high-quality anti-reflection (AR) coating at the substrate side is a necessity for proper laser output.

2. VCSEL Processing and Mounting

Figure 1 shows a schematic of the selected oxide-confined VCSEL design providing simultaneous top and bottom emission. The layer structure is grown by molecular beam epitaxy on an n-type GaAs substrate. The silicon n-doped bottom distributed Bragg reflector (DBR) consists of 27.5 AlGaAs layer pairs with the Al content varying between 0 and 90 %. The one material wavelength thick active region contains three InGaAs QWs with a thickness of about 8 nm and 15 % In content. The carbon p-type doped top DBR has 24 AlGaAs layer pairs with the same composition as the n-DBR. An about 30 nm thick AlGaAs layer with almost 100 % Al content is inserted above the active region to provide current and mode confinement after selective oxidation.

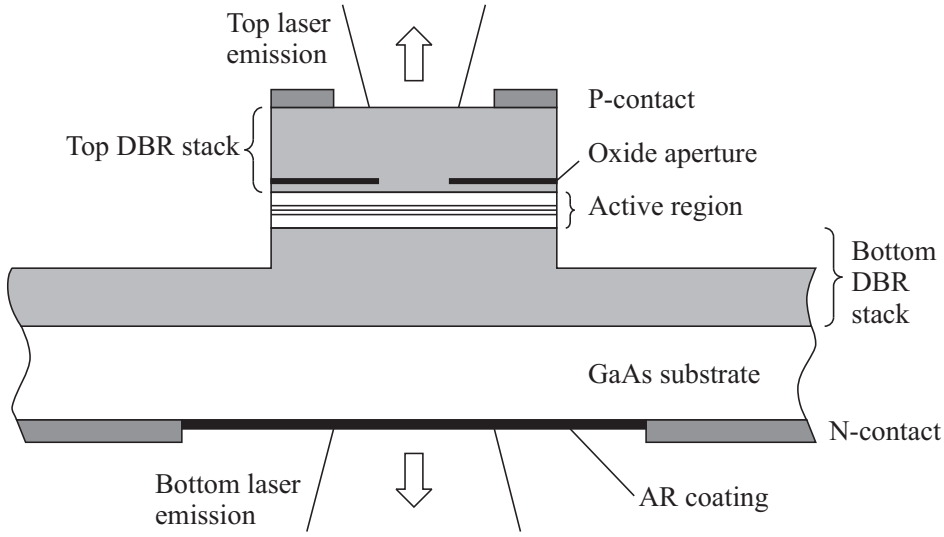

Fig. 1: Schematic cross-section of the VCSEL with two-sided emission.

VCSEL processing starts with mesa formation by wet-chemical etching, followed by selective oxidation (in a hot water vapor atmosphere) of the current aperture which defines the active diameter of the laser. The ohmic TiPtAu p-contact ring is structured with a photolithographic lift-off process. A polyimide passivation layer is then applied, onto which a NiAuTiPtAu bondpad metalization is deposited and shaped with another lift-off step. The GaAs substrate is thinned to about 180 µm to facilitate the cleaving of individual laser dies. In an annealed GeAuNiAu n-type ohmic contact at the back side of the substrate, 100 µm diameter openings centered to the active area are fabricated by lift-off for bottom light output. Finally, with another lift-off step, the openings are filled with a dielectric AR coating. The left part of Fig. 2 shows the top side view of one of the processed VCSELs. The bondpad has a width (horizontal direction) of 150 µm. The laser pitch on the sample is 250 µm.

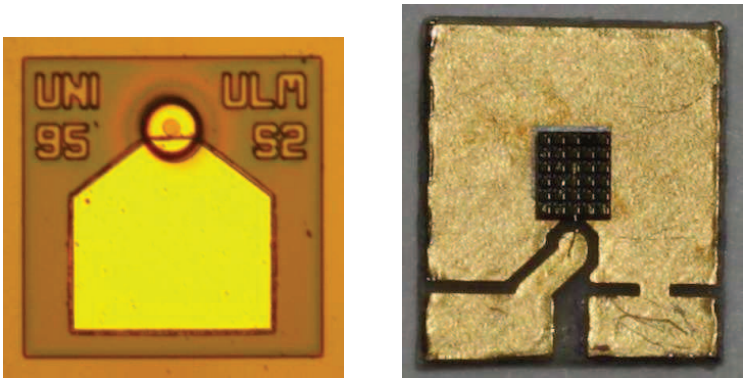

Fig. 2: Photographs of a processed VCSEL (left, top view) and of a printed-circuit board onto which a VCSEL die with 5×6 lasers has been mounted (right). The center VCSEL in the third row from the bottom is wire-bonded to the fanout track at the bottom left side of the board.

The experimental data reported in Sect. 3 were taken at wafer level by individual device probing with a contact needle. After this step, for more convenient handling, the processed sample was cleaved into individual dies of $1.25 \times 1.5\,\mathrm{mm}^2$ size containing 30 VCSELs. According to the right part of Fig. 2, such a die is soldered with indium substrate-side

down onto a small printed-circuit board from FR4 material. The large metal area on the board thus serves as the macroscopic n-contact, whereas the small metal area is connected with a bond wire to the p-bondpad of a single VCSEL in the center of the board. Underneath that VCSEL is a 400 µm diameter hole to allow bottom emission.

3. VCSEL Characterization

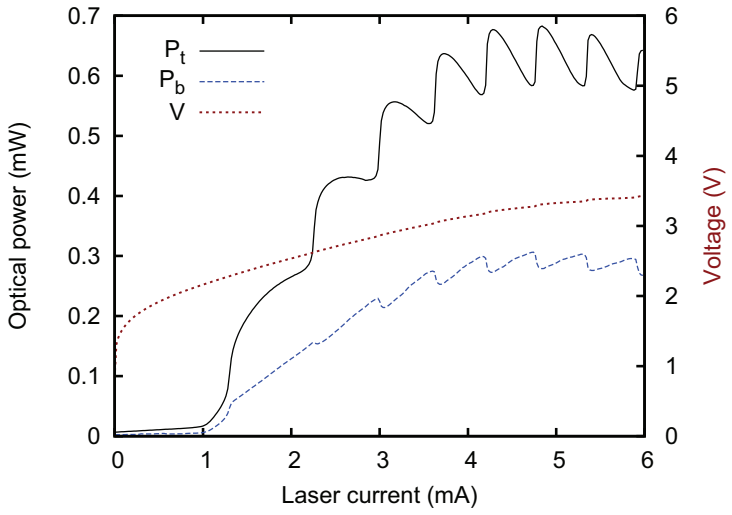

Fig. 3: LIV curves (top-emitted optical output power P_t, bottom-emitted power P_b, and voltage V versus laser current I) of a single-mode VCSEL from the first processing run.

Figure 3 shows the light–current–voltage (LIV) curves of a single-mode VCSEL with an active diameter of about 3 µm. The threshold current is a little below 1 mA. Strong ripples are seen in the LI curve for top-side emission. The ripples are less pronounced for the bottom side, and moreover the curves are anti-correlated in the sense that — at least close to thermal roll-over — local power maxima for top emission correspond to local minima for bottom emission. This VCSEL has a single quarter-wave Al_2O_3 AR coating which reduces the reflectivity of the GaAs–air interface to nominally 1.6 %. Without coating, the facet reflectivity is about 25 %, which led to even stronger power oscillations with a depth of up to 100 %.

These oscillations are caused by beam divergence and interference in the parasitic Fabry–Pérot resonator established in the GaAs substrate. Transitions between constructive and destructive interference occur due to the red-shift of the emission wavelength with increasing current at a rate of approximately 1 nm/mA. This explanation is supported by the fact that the top-side emission has a quasi-Gaussian shape over the entire current range. These VCSELs from the first processing run according to Fig. 3 were entirely unsuited for the intended application.

Obviously the reflectivity of the GaAs–air interface had to be reduced below the previous level. We have estimated a maximum tolerable reflectivity R (power reflection coefficient) of 0.1 % for proper laser operation. Experimental improvements were attempted with a dual-layer TiO_2–SiO_2 AR coating. Figure 4 illustrates the theoretical reflectivity spectrum $R(\lambda)$ of a GaAs–TiO_2–SiO_2–air layer sequence calculated for one-dimensional wave propagation. The layer thicknesses are 70 nm for TiO_2 (refractive index $n = 2.36$) and

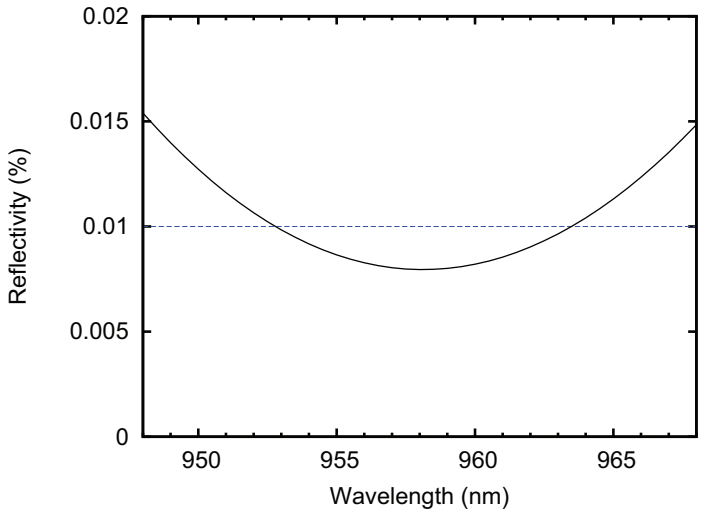

Fig. 4: Calculated reflectivity spectrum of a TiO_2–SiO_2 anti-reflection coating at the back side of the GaAs substrate.

114 nm for SiO_2 ($n = 1.49$). Close to 960 nm and over a spectral width of more than 10 nm we obtain $R < 0.01\,\%$, which is an order of magnitude lower than the target value.

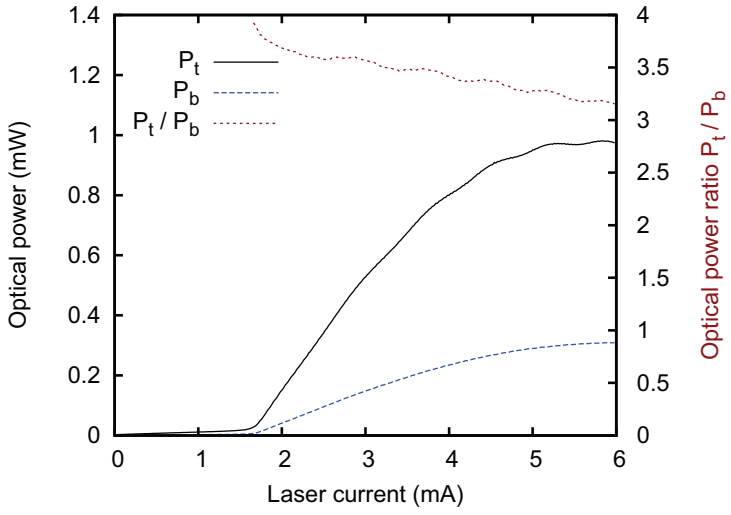

Fig. 5: Light–current characteristics $P_\mathrm{t}(I)$ and $P_\mathrm{b}(I)$ as well as the power ratio $P_\mathrm{t}(I)/P_\mathrm{b}(I)$ of a single-mode VCSEL from a second processing run with improved AR coating.

VCSEL processing was repeated for a second run, ending with the deposition of an improved dual-layer AR coating according to Fig. 4. The resulting laser output curves of a device with an active diameter of about 4 µm are displayed in Fig. 5. Compared to the laser in Fig. 3, both the threshold current and the maximum output power now have increased to about 1.7 mA and almost 1 mW, respectively. Most importantly, the power ripples have virtually vanished with some remnants remaining only in the top emission. The power outcoupling ratio is ≈ 4 at threshold and decreases to ≈ 3.2 at thermal roll-over, which might be caused by asymmetric heating of the top and bottom DBRs. A smaller power ratio would require a higher reflectivity of the top DBR, which could be achieved by deposition of dielectric material. However, this would only be a workaround involving increased processing effort. Ideally, a new VCSEL wafer with a larger number of top mirror pairs should be grown.

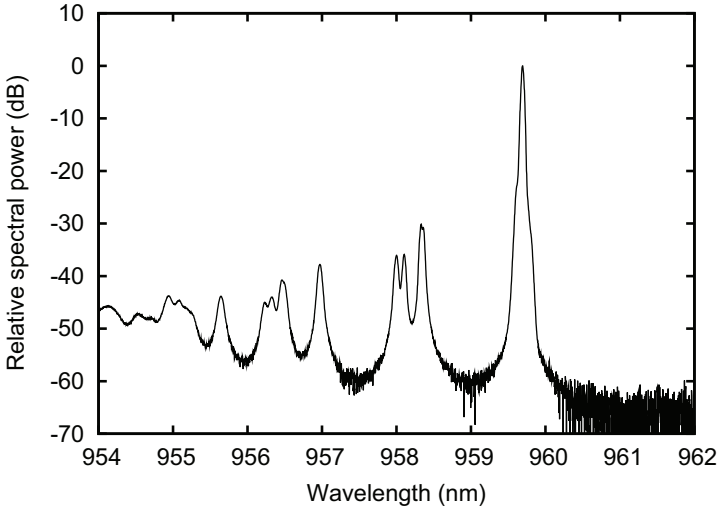

Fig. 6: Emission spectrum of the VCSEL from Fig. 5 at 5 mA current.

Figure 6 shows the emission spectrum of the laser from Fig. 5 at a current of 5 mA. It has a dominating peak at 959.7 nm wavelength which corresponds to the fundamental mode with nearly Gaussian field profile. Various higher-order transverse modes are separated by at least 1.4 nm on the short-wavelength side of the main peak. The side-mode suppression ratio is about 30 dB. Owing to the short cavity length and the associated longitudinal mode spacing in the order of 100 nm, only one longitudinal mode is able to oscillate. In other words, all transverse modes have the same longitudinal mode order. The device in Fig. 6 clearly deserves the name *single-mode VCSEL*.

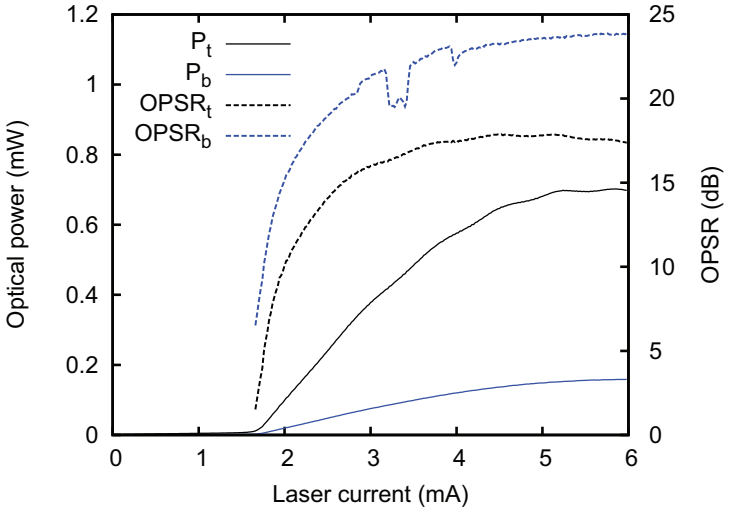

Fig. 7: LI curves repeated from Fig. 5 and corresponding OPSRs for top and bottom emission.

Since single-polarization in addition to single-mode emission is another requirement for the VCSEL sensor, the polarization properties of the lasers had also to be investigated. To reduce the processing complexity, in this initial study we did not attempt to control the light output polarization of the VCSELs, which can most favorably be done with a surface grating etched into the top DBR [3]. It is well known that standard VCSELs can show polarization switches with varying current [4]. We have taken the polarization-resolved LI curves of the VCSELs for two orthogonal directions of a polarizer inserted

in the free-space collimated beam path between the VCSEL and the photodetector. One direction coincides with the preferred polarization orientation of the device. The ratio of the two powers is called the orthogonal polarization suppression ratio (OPSR), which is usually expressed in units of decibel (dB). The top- and bottom-side OPSR curves of the VCSEL from Fig. 5 are depicted in Fig. 7 for operating currents above threshold. The laser is polarization-stable over the entire current range with a higher amount of suppression for bottom emission despite the smaller power level. Maximum OPSRs are 18 and 24 dB for top and bottom emission, respectively. The discontinuities in the curve $\mathrm{OPSR_b}(I)$ are noise artifacts at the very low power levels. It should be noted that in the literature often the peak spectral intensities are compared. This leads to larger suppression ratios because during power measurements, unpolarized spontaneous emission is added according to the large optical bandwidth of the photodetector. It must be emphasized that for a commercial low-cost use, the selection of polarization-stable devices is no option but the use of surface gratings is strongly recommended.

Acknowledgments

The authors would like to thank Rudolf Rösch and Anna Bergmann for metal deposition and substrate thinning and for various hints regarding device processing, respectively.

References

[1] G. Reiner, E. Zeeb, B. Möller, M. Ries, and K.J. Ebeling, "Optimization of planar Be-doped InGaAs VCSEL's with two-sided output", *IEEE Photon. Technol. Lett.*, vol. 7, no. 7, pp. 730–732, 1995.

[2] B. Fischer, A. Strodl, A. Hein, E. Wintner, and R. Michalzik, "VCSELs with two-sided beam emission for pressure sensor applications", in *Semiconductor Lasers and Laser Dynamics V*, K.P. Panayotov, M. Sciamanna, A.A. Valle, R. Michalzik (Eds.), Proc. SPIE 8432, paper 8432-05, 12 pages, 2012, in press.

[3] R. Michalzik, J.M. Ostermann, and P. Debernardi, "Polarization-stable monolithic VCSELs", in *Vertical-Cavity Surface-Emitting Lasers XII*, C. Lei, J.K. Guenter (Eds.), Proc. SPIE 6908, pp. 69080A-1–16, 2008.

[4] J.M. Ostermann and R. Michalzik, "Polarization Control of VCSELs", Chap. 5 in *VCSELs — Fundamentals, Technology and Applications of Vertical-Cavity Surface-Emitting Lasers*, R. Michalzik (Ed.), Springer Series in Optical Sciences, vol. 166, 33 pages. Berlin: Springer-Verlag, 2012, in press.

Inverted Grating Relief Atomic Clock VCSELs

Ahmed Al-Samaneh

Vertical-cavity surface-emitting lasers (VCSELs) with single-mode and single-polarization emission at a wavelength of 894.6 nm have become attractive light sources for miniaturized Cs-based atomic clocks. So far, VCSELs used for these applications are single-mode because of small active diameters which has the drawbacks of increased ohmic resistance and reduced lifetime. Employing surface grating reliefs, enhanced fundamental-mode emission as well as polarization-stable laser oscillation are achieved. VCSELs with 5 µm active diameter show side-mode suppression ratios of 20 dB even at currents close to thermal roll-over with orthogonal polarization suppression ratios better than 20 dB at elevated ambient temperatures up to 100° C.

1. Introduction

Over the last few years, microscale atomic clocks have emerged as a new application field of VCSELs. Owing to their enhanced accuracy and low power consumption compared to thermally stabilized quartz-based oscillators, such clocks are key elements in a wide range of systems and applications such as global positioning, synchronization of communication networks, or undersea exploration. The first demonstrations of microscale atomic clocks based on coherent population trapping (CPT) spectroscopy [1] and microelectromechanical system (MEMS) fabrication techniques were done separately at the National Institute of Standards and Technology (NIST) [2] and at Symmetricom [3], both in the USA in the year 2004. Such frequency sources have recently become commercially available [4]. VCSELs used in those clocks must feature single-mode, single-polarization, low noise, and narrow linewidth emission under harmonic modulation at about 4.6 GHz with a center wavelength of about 894.6 nm to employ the CPT effect of the cesium D1 line. VCSELs of this kind have already been developed [5–8]. Our own research [6–8] has targeted the use in the first European microscale atomic clock demonstrators [9]. The polarization and dynamic properties of the lasers are reported in [7]. For polarization control, a semiconducting surface grating is etched in the top Bragg mirror. In particular, so-called inverted grating VCSELs have been employed where the grating is etched in an extra topmost GaAs quarter-wave antiphase layer [10]. These VCSELs are single-mode because of a small active diameter, e.g., 3 to 4 µm, which is achieved by wet-chemical oxidation of a thin AlAs layer grown above the active region. However, VCSELs with small active diameters have the drawbacks of increased ohmic resistances and reduced lifetimes owing to higher current densities and possibly increased internal temperatures resulting from higher thermal and electrical resistances. Oxide-confined VCSELs with larger active diameter showing single transverse mode oscillation can be realized by, e.g., etching a

shallow surface relief in the top Bragg mirror of a regular VCSEL structure [11] (alternative approaches are summarized in [12]). An annular etch of the laser outcoupling facet lowers the effective mirror reflectivity particularly for higher-order modes, which show higher optical intensities outside the device center. The resulting differences in threshold gains strongly favor the fundamental mode. A more advanced approach is to etch the surface relief in an extra topmost GaAs quarter-wave antiphase layer, leading to the so-called inverted relief VCSELs. Here, the antiphase layer is removed only in the center of the outcoupling facet, and consequently the threshold gain for the fundamental mode is most strongly decreased. This approach requires a less precise etch depth control and has been successfully demonstrated in [13] with maximum single-mode output powers of up to 6.3 mW. So-called inverted grating relief VCSELs combine a surface grating and a surface relief in an extra topmost antiphase layer. Such a combination results simultaneously in a favorable single-mode and polarization-stable laser emission [14]. In this article, the design, fabrication, characterization, and preliminary reliability test results of inverted grating relief VCSELs are presented.

2. VCSEL Design and Fabrication

The VCSELs are grown by solid-source molecular beam epitaxy on n-doped (100)-oriented GaAs substrates. The layer structure of the VCSELs is similar to the one described in [7]. There is a highly n-doped GaAs contact layer above the GaAs substrate to allow n-contacting. The active region contains three compressively strained InGaAs quantum wells with 4 % indium content and is positioned in an optical cavity between doped distributed Bragg reflectors (DBRs). The n- and p-type DBRs consist of 38.5 Si-doped $Al_{0.2}Ga_{0.8}As/Al_{0.9}Ga_{0.1}As$ layer pairs and 25 C-doped layer pairs with identical composition, respectively. The DBRs are graded in composition and doping concentration to minimize the free-carrier absorption and decrease the electrical resistance. A 30 nm thick AlAs layer is grown above the active region. It is wet-chemically oxidized to achieve current confinement and optical index guiding. To maximize compactness in the clock microsystem, flip-chip-bondable VCSEL chips have been realized, similar to the ones described in [6, 7]. The structure has an extra topmost quarter-wave thick GaAs layer to achieve an antiphase reflection for all modes. By etching a circular area of 3 to 4 µm diameter in the center of this layer, the reflectivity is increased particularly for the fundamental mode. If instead a grating with the same extension is etched into the topmost layer (see Fig. 1), this additionally leads to different reflectivities for the two polarizations of the fundamental mode. Inverted grating reliefs with quarter-wave etch depth, sub-emission-wavelength grating periods (specifically 0.6 µm), and 50 % duty cycle have been employed. The grating grooves are etched along the [011] crystal axis.

3. Operation Characteristics and Spectra

The VCSELs to be incorporated in miniaturized atomic clock microsystems will experience high ambient temperatures (e.g., $T = 65 \ldots 80\,^{\circ}\mathrm{C}$). The polarization-resolved light–current–voltage (PR-LIV) characteristics of a grating relief VCSEL with 4.5 µm active

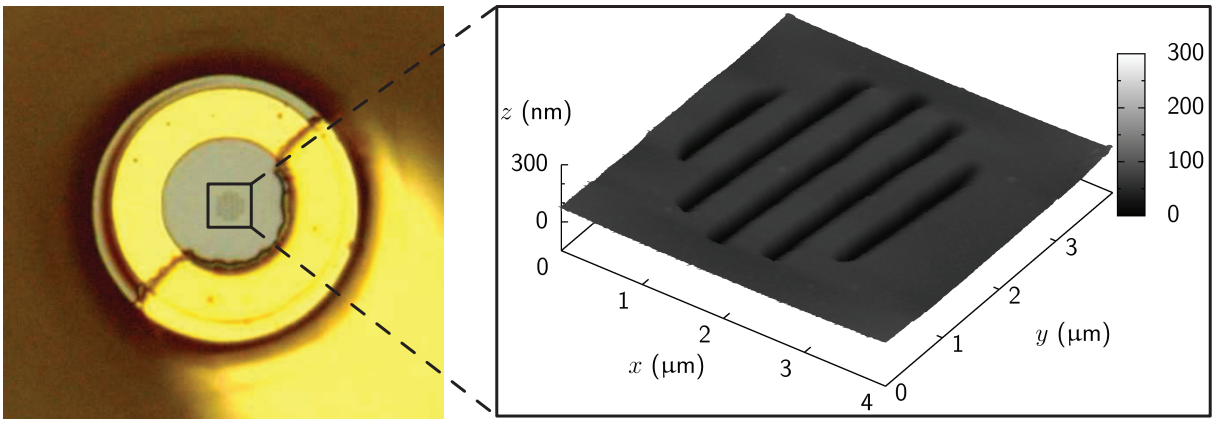

Fig. 1: Optical micrograph of a fully processed VCSEL with an inverted grating relief (left) and its surface profile measured with an atomic force microscope (right). The grating relief has a diameter of 3 µm, a grating period of 0.6 µm, and an etch depth of 70 nm.

diameter at 80 °C substrate temperature are shown in Fig. 2 (left). The dashed and dash-dotted lines indicate the optical powers P_{orth} and P_{par} measured behind a Glan–Thompson polarizer whose transmission direction is oriented orthogonal and parallel to the grating lines, respectively. The device remains polarization-stable up to thermal roll-over with a maximum magnitude of the orthogonal polarization suppression ratio (OPSR) as high as 19.5 dB, where OPSR $= 10\log(P_{\mathrm{par}}/P_{\mathrm{orth}})$. Figure 2 (right) depicts polarization-resolved spectra at 80 °C. The target wavelength is reached at a current of 3.8 mA with both a side-mode suppression ratio (SMSR) and a peak-to-peak difference between the dominant and the suppressed polarization modes of almost 27 dB, which well exceed the target values of 20 dB.

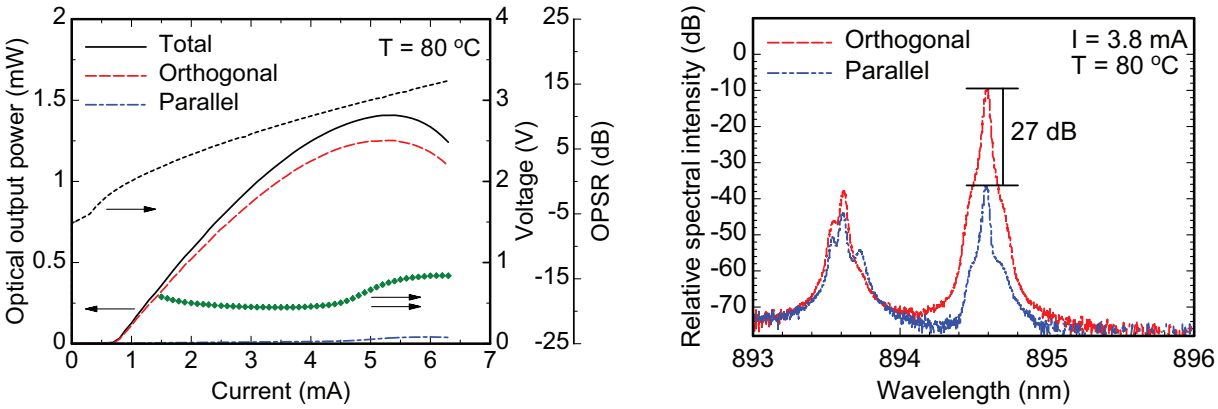

Fig. 2: Polarization-resolved operation characteristics of a grating relief VCSEL with 4.5 µm active diameter at 80 °C substrate temperature (left). Polarization-resolved spectra of the same VCSEL at 3.8 mA bias current (right). The grating relief has a diameter of 3.3 µm.

The polarization control induced by the grating relief has also been investigated for different ambient temperatures. Figure 3 depicts PR-LIV characteristics of a grating relief VCSEL with 5 µm active diameter for substrate temperatures varied between 20 and

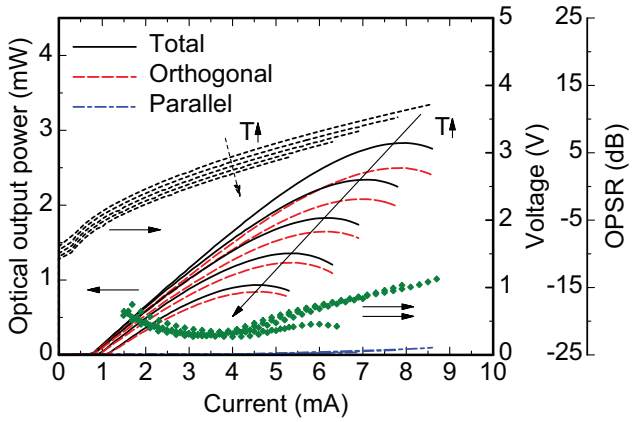

Fig. 3: Polarization-resolved operation characteristics of a grating relief VCSEL with 5 µm active diameter at substrate temperatures from 20 to 100 °C in steps of 20 °C. The grating relief has a diameter of 4 µm.

100 °C in steps of 20 °C. As can be seen, the VCSEL remains polarization-stable even well above thermal roll-over. The magnitudes of the OPSR for $T = 80$ and 100 °C are increased in comparison with lower temperatures as the current exceeds 4.5 mA.

For investigating the enhancement of fundamental-mode emission, standard reference devices were fabricated on the same wafer adjacent to the grating relief VCSELs for comparison purposes. For the reference VCSELs, the topmost GaAs quarter-wave antiphase layer is etched over the whole outcoupling facet. This means that in-phase reflection is achieved for all modes. The reference VCSELs can thus be considered as standard VCSELs. Figure 4 displays the PR-LI characteristics of a reference device with an oxide

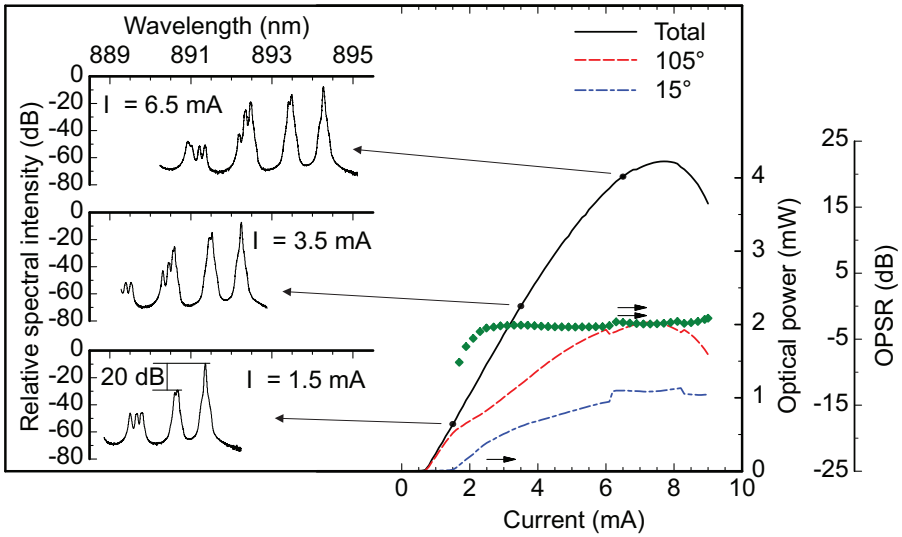

Fig. 4: Polarization-resolved operation characteristics of a reference VCSEL with 5 µm active diameter at 80 °C substrate temperature. The emission spectra in the insets show higher-order lasing modes. The polarization directions of the two orthogonal, linearly polarized fundamental modes are rotated by 15 ° towards the $[0\bar{1}1]$ axis.

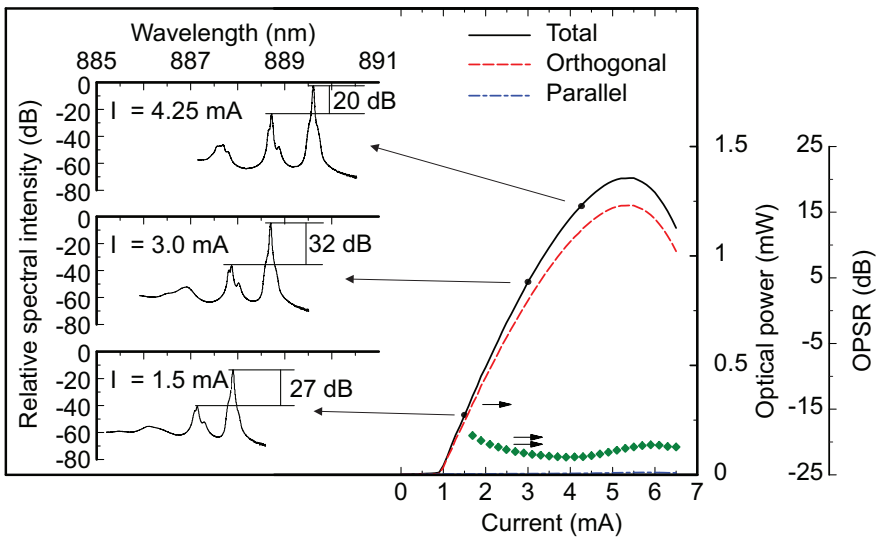

Fig. 5: Polarization-resolved operation characteristics of the grating relief VCSEL from Fig. 3 at 80 °C substrate temperature. The emission spectra in the insets show SMSRs of at least 20 dB.

aperture of about 5 µm at 80 °C substrate temperature and its optical spectra at different driving currents. The laser has a threshold current of 0.7 mA and a maximum output power of 4.2 mW. At 1.5 mA drive current it shows single-mode operation with an SMSR of 20 dB. However, the spectrum gets highly multimode for higher currents. Having no surface grating, the reference VCSEL shows a weak polarization control with an average OPSR of −4.1 dB. The OPSR is calculated for data points in steps of 0.1 mA and then averaged over the current range yielding 10 % to 100 % of the maximum output power. Due to built-in strain forces, the two orthogonal, linearly polarized fundamental modes are not aligned parallel and orthogonal to the usually preferred [011] crystal axis. Instead, they are rotated by 15 ° towards the $[0\bar{1}1]$ axis because of the elasto-optic effect [15]. Figure 5 depicts the same measurements for a nearby laser (same as Fig. 3) on the same sample, which is nominally identical except for a surface grating relief with a diameter of 4 µm. The grating relief device shows an increased threshold current of 0.9 mA due to the effectively decreased mirror reflectivity. The optical spectra confirm SMSRs exceeding 20 dB up to 4.25 mA at which the laser delivers a maximum single-mode output power of 1.2 mW. This current is just 1.25 mA below the thermal roll-over point. Owing to the grating, the VCSEL is polarization-stable well above thermal roll-over with an average OPSR of −21 dB.

4. Reliability Test

For preliminary reliability testing, a sample containing several grating relief VCSELs was introduced in a setup in which six individual lasers with 5.5 (2 devices), 5.0, 4.4, 3.8 and 3.7 µm active diameter are operated at a constant current of 3 mA and 80 °C ambient temperature. The optical output power of each device is measured separately (while the other devices are switched off) using a 1 mm^2 area Si photodiode. The optical power was recorded every half hour for about 2500 hours. Figure 6 shows the output power versus

time for all devices. Obviously such a small number of devices is not sufficient to obtain reliable lifetime estimations. Nevertheless, this preliminary test shows that all lasers kept to be functional with slower degradation of the devices with active diameters $\geq 5\,\mu m$.

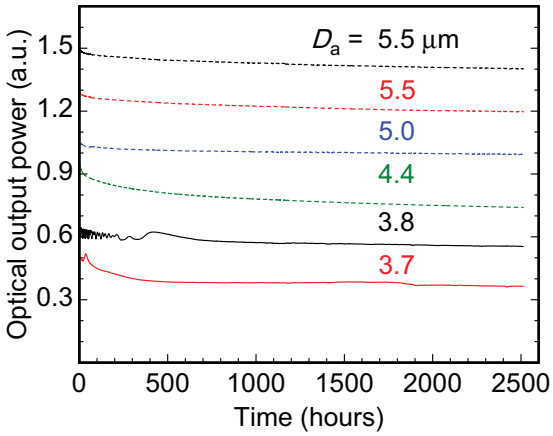

Fig. 6: Output power evolution in a long-term test of grating relief VCSELs with different active diameter D_a at 80 °C and 3 mA constant current.

Figure 7 depicts the LIV characteristics of two VCSELs from Fig. 6 with 3.8 µm and 5 µm active diameter. Both lasers were measured at 80 °C after 0, 100, 200, 500 and 2500 hours. The VCSEL with 3.8 µm active diameter suffers from an increase in threshold current from 0.6 to 0.87 mA (i.e., by 45 %) with almost no change in the slope efficiency of about 0.48 W/A after 2500 hours of lifetime test. On the other hand, for the second VCSEL with 5 µm active diameter, the threshold current increases only from 0.84 to 0.91 mA (i.e., by 4.5 %). Its slope efficiency decreases from 0.43 to 0.39 W/A after the same test time, where the change occurs mainly during the first 100 hours of operation. It can thus be expected that lasers with 5 µm active diameter provide greater potential for increased lifetime in comparison with standard small-aperture single-mode devices with 3 to 4 µm

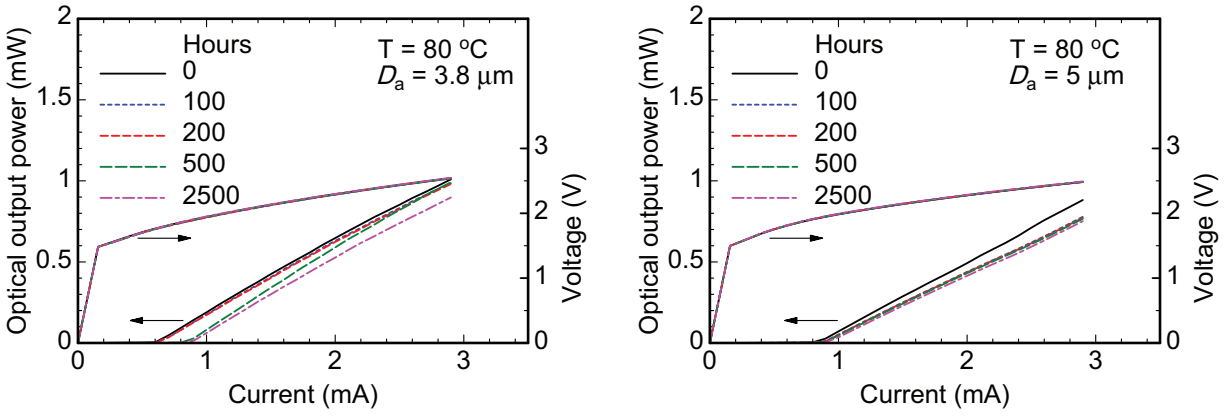

Fig. 7: Operation characteristics of the VCSEL with 3.8 µm active diameter (left) and of the VCSEL with 5 µm diameter from Fig. 6 measured at 80 °C during the reliability test at 0, 100, 200, 500 and 2500 hours.

active diameters. For both lasers the voltage characteristics remain almost unchanged during the degradation test time.

5. Conclusion

In summary, inverted grating relief VCSELs emitting at 894.6 nm wavelength have been fabricated for Cs-based miniature atomic clocks. Their emission is stable on the fundamental mode with a fixed linear polarization. VCSELs with 5 µm active diameter show side-mode suppression ratios of 20 dB even at currents close to thermal roll-over with orthogonal polarization suppression ratios better than 20 dB at elevated ambient temperatures up to 100 °C. Preliminary lifetime tests confirm a better reliability of these VCSELs compared to those which are single-mode due to small oxide apertures.

Acknowledgments

The author would like to cordially thank Y. Men for performing the electron-beam lithography step for grating fabrication. He wishes to thank W. Schwarz and A. Hein for their technical assistance with lifetime measurements. This work is funded by the EC within FP7 (grant agreement number 224132, www.mac-tfc.eu).

References

[1] N. Cyr, M. Têtu, and M. Breton, "All-optical microwave frequency standard: a proposal", *IEEE Transactions on Instrumentation and Measurement*, vol. 42, no. 2, pp. 640–649, 1993.

[2] S. Knappe, V. Shah, P. Schwindt, L. Hollberg, J. Kitching, L.A. Liew, and J. Moreland, "A microfabricated atomic clock", *Appl. Phys. Lett.*, vol. 85, no. 9, pp. 1460–1462, 2004.

[3] R. Lutwak, J. Deng, W. Riley, M. Varghese, J. Leblanc, G. Tepolt, M. Mescher, D.K. Serkland, K.M. Geib, and G.M. Peake, "The chip-scale atomic clock – low-power physics package", in Proc. *36th Annual Precise Time and Time Interval (PTTI) Meeting*, pp. 339–354. Washington, DC, USA, Dec. 2004.

[4] W.D. Jones, "Chip-scale atomic clock", *IEEE Spectrum*, Mar. 2011. Web page: http://spectrum.ieee.org/semiconductors/devices/chipscale-atomic-clock, last visited Apr. 2012.

[5] D.K. Serkland, K.M. Geib, G.M. Peake, R. Lutwak, A. Rashed, M. Varghese, G. Tepolt, and M. Prouty, "VCSELs for atomic sensors", in *Proc. SPIE*, vol. 6484, pp. 648406-1–10, 2007.

[6] A. Al-Samaneh, S. Renz, A. Strodl, W. Schwarz, D. Wahl, and R. Michalzik, "Polarization-stable single-mode VCSELs for Cs-based MEMS atomic clock applications", in *Semiconductor Lasers and Laser Dynamics IV*, Proc. SPIE 7720, pp. 772006-1–14, 2010.

[7] A. Al-Samaneh, M. Bou Sanayeh, S. Renz, D. Wahl, and R. Michalzik, "Polarization control and dynamic properties of VCSELs for MEMS atomic clock applications", *IEEE Photon. Technol. Lett.*, vol. 23, no. 15, pp. 1049–1051, 2011.

[8] A. Al-Samaneh, M.T. Haidar, D. Wahl, and R. Michalzik, "Polarization-stable single-mode VCSELs for Cs-based miniature atomic clocks", in Online Digest *Conf. on Lasers and Electro-Optics Europe, CLEO/Europe 2011*, paper CB.P.23, one page. Munich, Germany, May 2011.

[9] C. Gorecki, M. Hasegawa, N. Passilly, R.K. Chutani, P. Dziuban , S. Gailliou, and V. Giordano, "Towards the realization of the first European MEMS atomic clock", in Proc. *2009 IEEE/LEOS International Conference on Optical MEMS and Nanophotonics*, pp. 47–48. Clearwater, FL, USA, Aug. 2009.

[10] J.M. Ostermann, P. Debernardi, and R. Michalzik, "Optimized integrated surface grating design for polarization-stable VCSELs", *IEEE J. Quantum Electron.*, vol. 42, no. 7, pp. 690–698, 2006.

[11] H.J. Unold, S.W.Z. Mahmoud, R. Jäger, M. Grabherr, R. Michalzik, and K.J. Ebeling, "Large-area single-mode VCSELs and the self-aligned surface relief", *IEEE J. Select. Topics Quantum Electron.*, vol. 7, no. 2, pp. 386–392, 2001.

[12] A. Larsson and J.S. Gustavsson, "Single-Mode VCSELs", Chap. 4 in *VCSELs — Fundamentals, Technology and Applications of Vertical-Cavity Surface-Emitting Lasers*, R. Michalzik (Ed.), Springer Series in Optical Sciences, vol. 166, 26 pages. Berlin: Springer-Verlag, 2012, in press.

[13] A. Kroner, F. Rinaldi, J.M. Ostermann, and R. Michalzik, "High-performance single fundamental mode AlGaAs VCSELs with mode-selective mirror reflectivities", *Optics Commun.*, vol. 270, pp. 332–335, 2007.

[14] J.M. Ostermann, F. Rinaldi, P. Debernardi, and R. Michalzik, "VCSELs with enhanced single-mode power and stabilized polarization", *IEEE Photon. Technol. Lett.*, vol. 17, no. 11, pp. 2256–2258, 2005.

[15] M. Peeters, K. Panajotov, G. Verschaffelt, B. Nagler, J. Albert, H. Thienpont, I. Veretennicoff, and J. Danckaert, "Polarisation behavior of vertical-cavity surface-emitting lasers under the influence of in-plane anisotropic strain", in *Vertical-Cavity Surface-Emitting Lasers VI*, Proc. SPIE 4649, pp. 281–291, 2002.

10 Gbit/s Bidirectional Data Transmission with Monolithic VCSEL–PIN Transceiver Chips

Alexander Kern and Dietmar Wahl

We report the monolithic integration, fabrication, and electro-optical properties of AlGaAs–GaAs-based transceiver (TRx) chips for 850 nm wavelength optical links with data rates of multiple Gbit/s. Avoiding the use of external fiber coupling optics and using a single butt-coupled multimode fiber (MMF) with 50 or 62.5 µm core diameter, low-cost bidirectional communication in half- and even full-duplex mode is demonstrated. Based on a vertical-cavity surface-emitting laser (VCSEL) and a monolithically integrated p-doped–intrinsic–n-doped (PIN) photodiode (PD), such TRx chips are capable of high-speed bidirectional data transmission with MMFs over distances of a few hundred meters. Standard MMF networks can thus be upgraded using monolithic VCSEL–PIN transceiver chips which can handle data rates of up to 10 Gbit/s.

1. Introduction

The demand for increasingly compact and low-priced high-speed optical links in local-area networks, the industrial and home environments but also in mobile systems requires novel approaches. One of them is bidirectional interconnection over a single multimode fiber with a vertical-cavity surface-emitting laser (VCSEL) acting as an efficient light source and a resonant-cavity-enhanced photodetector [1]. Half-duplex operation at 1.25 Gbit/s data rate over a 50 µm core diameter MMF with 500 m length was achieved with such a dual-purpose transceiver. Full-duplex operation is inherently not possible. Additionally, the resonant detection requires temperature control at both fiber ends, increasing the cost of such a link. Only non-resonant devices with separate epitaxial layers for photodiode and VCSEL can operate in full-duplex mode and without temperature control.

In previous work [2] we have demonstrated full-duplex data transmission at 1 Gbit/s over a 500 m long 50 µm core diameter MMF using monolithically integrated transceiver chips containing VCSELs and size-mismatched 110 µm diameter metal–semiconductor–metal detectors. In order to reduce the inevitable optical crosstalk in such full-duplex links on one hand and to increase the responsivity of rather small photodetector areas on the other hand, PIN PDs are used in miniaturized VCSEL-based 850 nm wavelength range transceivers [3]. In Fig. 1, the top view of such a TRx chip can be seen in which the VCSEL is positioned off-center with respect to the photodetector in order to maximize the effective photodetecting area of the transceiver. The monolithic integration of both components as well as a design enabling data transmission via a single, two-side butt-coupled standard MMF — avoiding the use of external optics as shown in Fig. 4 (top) — saves space, weight, and module cost.

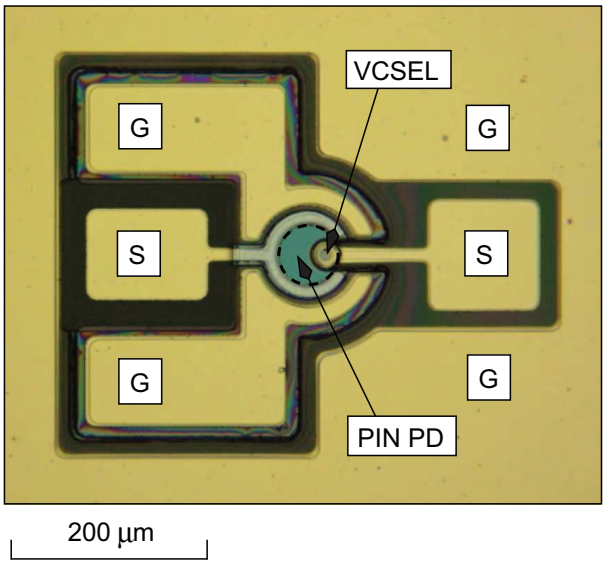

Fig. 1: Photograph of a transceiver chip consisting of a VCSEL and a PIN photodiode, each with indicated ground–signal–ground (GSG) microwave probe contacts. The dashed circle indicates the alignment of a MMF with 50 µm core diameter (from [4]).

2. Transceiver Layer Design and Fabrication

For the full-monolithic chip design, the layers for the VCSEL are grown using molecular beam epitaxy on a GaAs substrate, followed by the layers for the PIN photodiode. Epitaxially separated by a 150 nm thick etch stop layer, as can be seen in Fig. 2, both, the detector layers as well as the etch stop layer can be selectively removed from the VCSEL by a combination of two reactive-ion etching (RIE) and two wet-etching processes [6–8]. The intrinsic $Al_{0.9}Ga_{0.1}As$ between both devices also partially acts as an insulator for capacitive decoupling. Apart from the etching of the VCSEL mesa, which separates both devices spatially, another dry-etching process is required due to the vertical displacement of the PIN PD contacts. With an appropriate $SF_6/SiCl_4$ gas ratio for the RIE process, high etching selectivity between GaAs and $Al_{0.3}Ga_{0.7}As$ can be achieved [6,7]. Thus the n- and p-doped PD contact layers not only act as spectral window layers for the wavelengths of interest at around 850 nm, but likewise as an etch stop layer. Minimizing the bandgap discontinuities between the absorption and contact layers by linearly graded $Al_xGa_{1-x}As$ ($x = 0 \rightarrow 0.3$), an easier escape of the photocarriers from the undoped GaAs is ensured. Both devices are protected from oxidation of the subjacent aluminum-containing layers by n- or p-doped GaAs cap layers.

Current confinement of the VCSEL is achieved by selective oxidation of the p-doped AlAs, positioned in a node of the standing-wave pattern just above the inner cavity. Owing to the stacked layer structure of the transceiver chip, the incident light passes the PD twice after being reflected by the subjacent VCSEL layers. With an Al_2O_3 quarter-wave antireflection (AR) layer sputtered on the PIN PD, the responsivity of a transceiver PD with 3 µm thick GaAs absorption layer reaches 0.61 A/W, corresponding to a quantum efficiency of nearly 88 % [9]. The AR coating reduces the reflectivity of the semiconductor

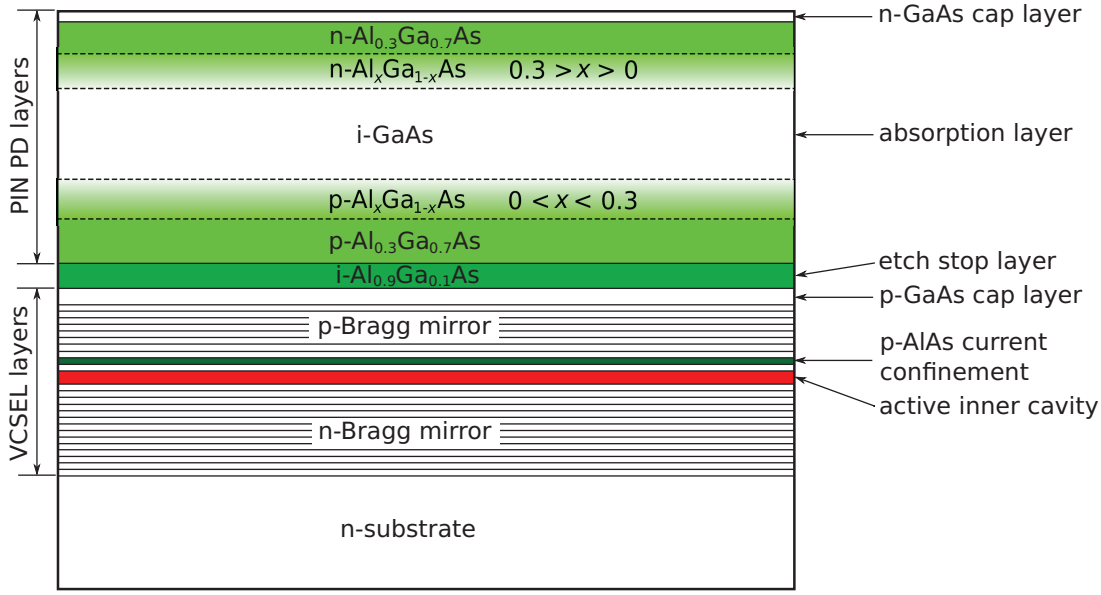

Fig. 2: Schematic layer structure design of the monolithically integrated transceiver chip (from [5]).

surface from initially 30 % down to 1.3 % over a spectral width of nearly 50 nm [3].

3. Experimental Results

3.1 Small-signal operation characteristics

For high-speed measurements, both, VCSEL and PIN PD can be on-wafer tested by two coplanar microwave probes, as seen from the GSG configurations in Fig. 1. A typical small-signal frequency response of an integrated VCSEL with about 8 µm oxide aperture and 25 µm mesa diameter is shown in the left graph of Fig. 3. A maximum 3-dB bandwidth of 11.5 GHz is observed for an operating current of 10 mA, giving a suitable flat frequency characteristic for large-signal experiments. Unintentional cavity detuning has led to optical emission at around 810 nm, a rather high threshold current of 2.3 mA, and a relatively low maximum output power of 2.8 mW and gives much room for further optimization.

The bandwidth of the adjacent 3 µm thick and 60 µm diameter photodetector can be sufficiently improved by increasing its reverse bias voltage to −8 V, as shown in the right graph of Fig. 3. Whereas the frequency response of the VCSEL typically decays strongly for frequencies beyond the resonance peak, the rather slow small-signal decay of the 1st order low-pass of the PIN PD gives a 3-dB frequency in the range of 4.5 to 6 GHz. Nevertheless, the resistor–capacitor (RC) low-pass and drift time bandwidths are expected to be at 14 and 15 GHz, respectively for $R = 50\,\Omega$ and if bondpad capacitances are neglected. The much smaller experimental values as well as the corrugations of the frequency responses can probably be attributed to the non-negligible parasitic coupling with the highly doped VCSEL layers.

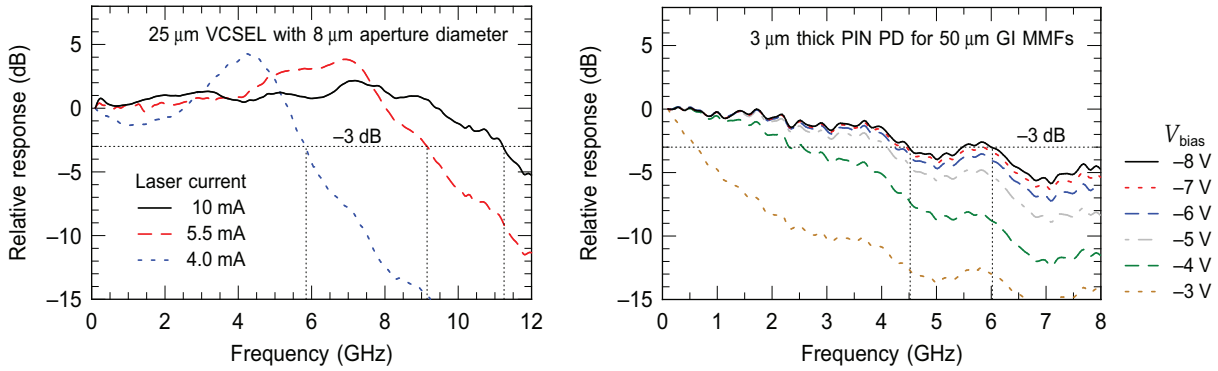

Fig. 3: Small-signal frequency responses (from [5]) of a TRx VCSEL (left) and an integrated PIN PD (right).

3.2 Digital data transmission

According to the results in Fig. 3, the lower small-signal bandwidths of the PIN PDs compared to those of the VCSELs are expected to limit the maximum achievable data rate of the transceivers. For evaluation purposes, two different transceiver chips with 2 and 3 µm thick PIN PDs were used in the experiments. The thinner PD with an increased capacitance has a smaller 3-dB bandwidth of approximately 4.2 GHz. For digital data transmission experiments, a 500 m long 50 µm core diameter OM3-type graded-index (GI) MMF with a bandwidth–distance product ($B \times L$) of ~ 2 GHz × km was butt-coupled (about 30 µm distance) to each chip, as depicted in Fig. 4 (top).

First, data transmission in half-duplex mode was performed in order to avoid the influence of optical and electrical crosstalk in the system. The optical eye diagram in Fig. 4 (bottom left) shows error-free operation with the 2 µm thick PIN PD at 7 Gbit/s, thus fully utilizing the $B \times L$ of the MMF. Here, the maximum data rate is additionally limited by the rising and falling edges caused by RC parasitics. For the opposite channel with a 3 µm thick PIN PD in Fig. 4 (bottom center), an error-free eye with slightly smaller peak-to-peak modulation voltage due to the smaller on–off ratio of the VCSEL on TRx chip 2 can be seen. The RC limit for the 3 µm thick PD is less pronounced. The signals detected by the PDs on the transmitter side correspond to optical crosstalk, which mainly originates from the reflections on each fiber end and the opposite TRx chip. Its contribution is sufficiently smaller than the trace widths of the operating channel, which are predominantly due to the non-ideal frequency responses as well as thermal and amplifier noise. Thus, quasi error-free full-duplex data transmission could be achieved at 6 Gbit/s, shown in Fig. 4 (bottom right). The trade-off of 1 Gbit/s compared to the half-duplex mode operation is attributed to the higher noise level arising from the optical crosstalk. Compared to previous results [2], the full-duplex data rate has been increased by a factor of six and is to our knowledge the highest reported so far.

Additional data transmission experiments were performed in back-to-back (BTB) mode in order to avoid mode dispersion and optical crosstalk effects of the glass fiber and thus to obtain the maximum achievable data rate of the transceivers. The laser beam is focused via free-space optics on the transceiver PIN PD, as shown in Fig. 5 (top). Here, 3 µm

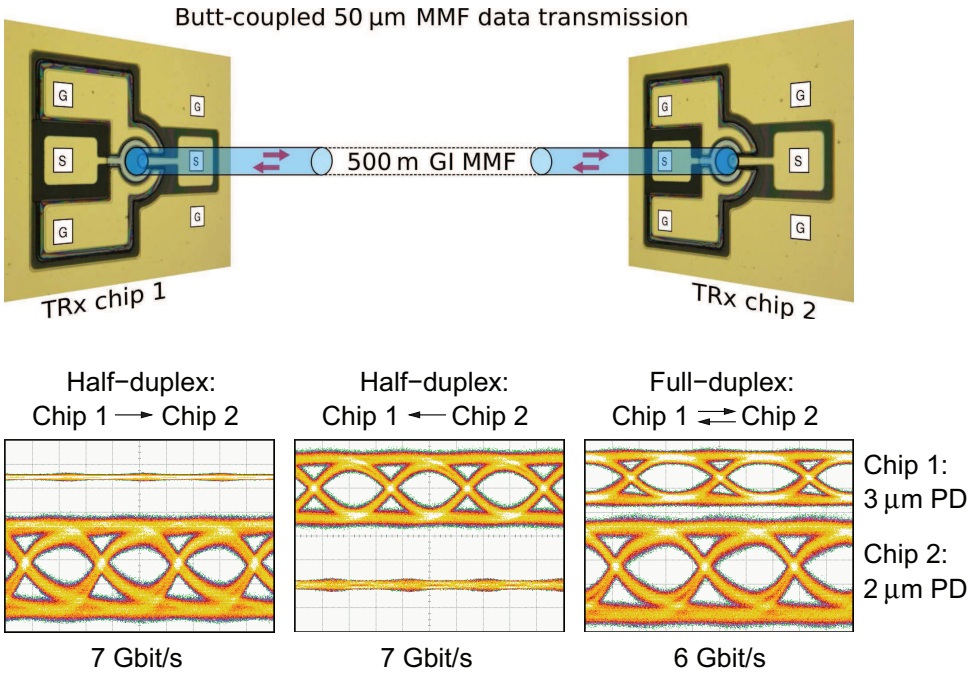

Fig. 4: Optical eye diagrams (from [10]) for error-free half-duplex $2^{15}-1$ word length non-return-to-zero (NRZ) pseudorandom bit sequence (PRBS) data transmission at 7 Gbit/s (bottom left and center), as well as 6 Gbit/s error-free full-duplex operation (bottom right), all over 500 m graded-index (GI) MMF, as indicated in the schematic setup (top).

thick PIN PDs were used in both TRx chips. As can be seen in Fig. 5 (bottom center), quasi error-free data transmission in half-duplex mode was possible at 10 Gbit/s for one channel. Owing to lower optical crosstalk contributions in BTB mode as observed in the eye diagrams for half-duplex transmission (bottom left and center), error-free full-duplex operation could be achieved at 7 Gbit/s for both channels (bottom right). Keeping the data rate for the transmission direction between chip 1 and chip 2 fixed at 7 Gbit/s, we could even demonstrate full-duplex error-free operation at 10 Gbit/s for the channel chip 2 → chip 1. In such free-space communication, there is no limit of the maximum data rate by the $B \times L$ of the fiber, as was the case in the previous subsection. Thus, a 10 Gbit/s optical link employing a 500 m long OM4-type fiber with $B \times L \geq 4.7\,\text{GHz} \times \text{km}$ is feasible.

In Fig. 6, bit error ratios (BERs) are shown for different data rates in both, half- and full-duplex mode. For simplicity, only one transmission direction (here from chip 2 to 1) is presented. On average, there is 0.5 dB power penalty for full-duplex compared to half-duplex transmission at the same data rate. At a relatively high optical power of approximately –1.5 dBm, even 10 Gbit/s could be transmitted quasi error-free in full-duplex mode.

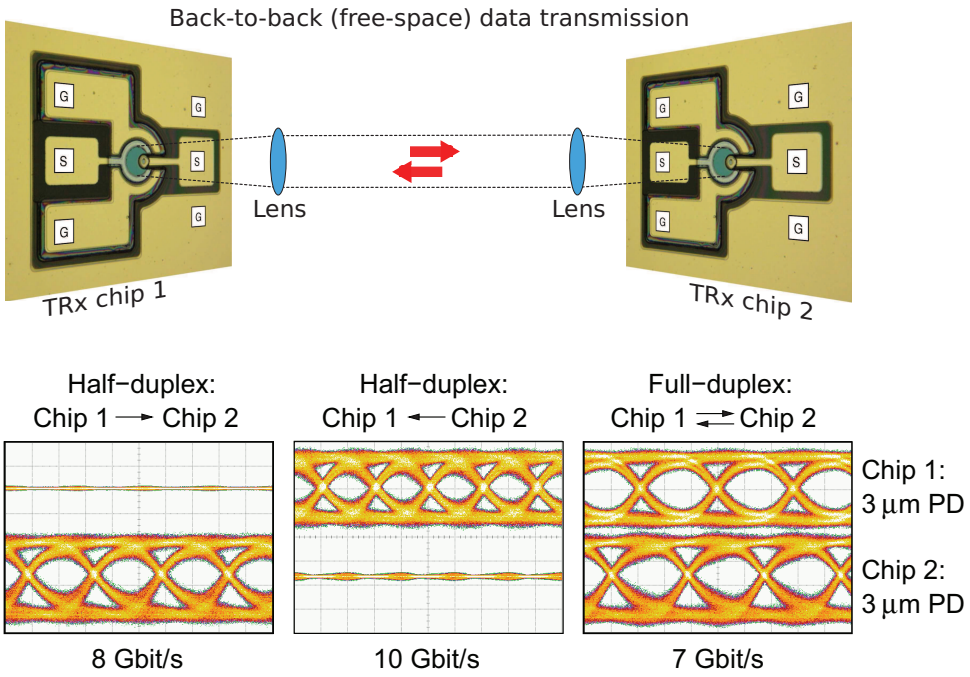

Fig. 5: Optical eye diagrams (bottom) for back-to-back (top) error-free half-duplex $2^{15} - 1$ word length NRZ PRBS data transmission at 8 Gbit/s (left) and 10 Gbit/s (center), as well as 7 Gbit/s error-free full-duplex operation (right).

4. Conclusion

In summary, we have presented the current achievements on the fabrication and properties of monolithically integrated 850 nm wavelength transceiver chips for bidirectional data transmission over a single butt-coupled multimode fiber. The VCSEL–PIN transceiver chips were miniaturized in order to match with standard MMFs of 50 and 62.5 µm core diameters. The main challenge in chip processing was the sophisticated combination of selective dry- and wet-etching techniques for various mesa formations. PIN PDs with maximum bandwidths of 4.5 to 6 GHz and VCSELs with 11.5 GHz can handle data rates of up to 10 Gbit/s in BTB half- and full-duplex data transmission. Over a 500 m long butt-coupled OM3 MMF, data rates of 7 Gbit/s in half-duplex and 6 Gbit/s in full-duplex mode could be demonstrated — mainly limited by the relatively low bandwidth–distance product of the fiber. With optimized epitaxial TRx chip design and the use of an OM4-type MMF, even further improvements in bidirectional single-fiber data transmission reaching 10 Gbit/s are realistic.

Acknowledgment

The authors would like to thank R. Rösch, R. Blood, and A. Hein for their support with chip processing. They also thank W. Schwarz for his technical assistance with device measurements and S. Paul for his work on current generation VCSEL–PIN PD chips. Ulm University gratefully acknowledges partial funding of this work by the German Research Foundation (DFG).

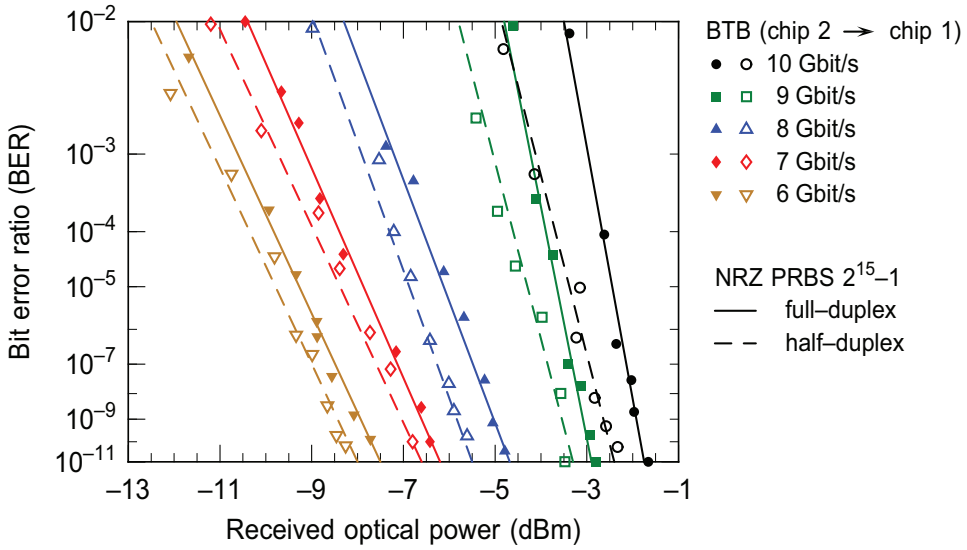

Fig. 6: BER characteristics for back-to-back half- and full-duplex $2^{15} - 1$ word length NRZ PRBS data transmission.

References

[1] J.D. Ingham, R.V. Penty, and I.H. White, "Bidirectional multimode-fiber communication links using dual-purpose vertical-cavity devices", *J. Lightwave Technol.*, vol. 24, pp. 1283–1294, 2006.

[2] M. Stach, F. Rinaldi, D. Wahl, D. Rimpf, S. Lorch, and R. Michalzik, "1 Gbit/s full-duplex bidirectional optical data transmission over 500 m of 50 µm-core graded-index multimode fiber with novel monolithically integrated transceiver chips", in Proc. *33rd Europ. Conf. on Opt. Commun., ECOC 2007*, vol. 5, pp. 127–128. Berlin, Germany, Sept. 2007.

[3] R. Michalzik, A. Kern, M. Stach, F. Rinaldi, and D. Wahl, "True bidirectional optical interconnects over multimode fiber", in *Optoelectronic Interconnects and Component Integration IX*, A.L. Glebov, R.T. Chen (Eds.), Proc. SPIE 7607, pp. 76070B-1–17, 2010.

[4] A. Kern, D. Wahl, S. Paul, M.T. Haidar, R. Blood, W. Schwarz, and R. Michalzik, "Up to 9 Gbit/s data transmission with monolithically integrated VCSELs and PIN photodiodes", in Online Digest *Conf. on Lasers and Electro-Optics Europe, CLEO/Europe 2011*, paper CB1.4, one page. Munich, Germany, May 2011.

[5] A. Kern, S. Paul, D. Wahl, A. Hein, R. Rösch, W. Schwarz, and R. Michalzik, "6 Gbit/s full-duplex multimode fiber link with monolithic VCSEL–PIN transceiver chips", in Proc. *37th Europ. Conf. on Opt. Commun., ECOC 2011*, paper We.9.LeSaleve.2, three pages. Geneva, Switzerland, Sept. 2011.

[6] A. Kern, S. Paul, D. Wahl, A. Al-Samaneh, and R. Michalzik, "Single-fiber bidirectional optical data links with monolithic transceiver chips" (invited), *Advances in*

Optical Technologies, Special Issue on *Recent Advances in Semiconductor Surface-Emitting Lasers*, Article ID 729731, 8 pages, 2012.

[7] S. Salimian and C.B. Cooper, III, "Selective dry etching of GaAs over AlGaAs in $SF_6/SiCl_4$ mixtures", *J. Vac. Sci. Technol. B*, vol. 6, pp. 1641–1644, 1988.

[8] J.H. Kim, D.H. Lim, and G.M. Yang, "Selective etching of AlGaAs/GaAs structures using the solutions of citric acid/H_2O_2 and de-ionized H_2O/buffered oxide etch", *J. Vac. Sci. Technol. B*, vol. 16, pp. 558–560, 1998.

[9] A. Kern, S. Paul, D. Wahl, R. Blood, W. Schwarz, and R. Michalzik, "Bidirectional multimode fiber interconnection at Gb/s data rates with monolithically integrated VCSEL–PIN transceiver chips", *IEEE Photon. Technol. Lett.*, vol. 23, pp. 1058–1060, 2011.

[10] A. Kern, S. Paul, D. Wahl, and R. Michalzik, "Bidirectional optical data transmission over a single multimode fiber", SPIE Newsroom, Oct. 6, 2011, DOI: 10.1117/2.1201109.003825.

Miniaturized Optical Particle Manipulation with Integrated VCSEL Arrays

Anna Bergmann

In recent years, optical manipulation has gained increasing interest, especially in combination with microfluidics. The contamination-free handling of micrometer-sized particles without any mechanical contact is an attractive tool for biology and medicine. VCSELs (vertical-cavity surface-emitting lasers) are an excellent choice for the trapping lasers, offering the opportunity of miniaturization by means of integration, and of parallel particle manipulation by using two-dimensional VCSEL arrays.

In this report, we present a novel concept for the realization of the so-called integrated optical trap. For this purpose, AlGaAs–GaAs-based VCSEL arrays with a very small device pitch were fabricated. We show the realization of integration-ready particle manipulation devices.

1. Introduction

The fact that the radiation pressure exerted by a laser beam is able to accelerate particles was first reported by Arthur Ashkin in 1970 [1]. This pressure is commonly called scattering force. Additionally, he discovered a second, unexpected force, pulling particles towards the center of the laser beam. This effect can be explained considering the momentum transfer from the incident laser beam to transparent particles, assuming a laser beam with a transverse intensity gradient, as shown in Fig. 1. The beam rays incident to the particle are refracted at the particle surface, resulting in a force oriented orthogonal to the beam propagation direction. For two exemplary rays A and B, with A closer to the beam center and thus having a higher intensity than B, the force F_{A} caused by ray A is larger than the force F_{B}, giving rise to a net force pulling the particle towards the intensity maximum, or towards the beam center. As this force is based on the transverse intensity gradient, it is commonly called transverse gradient force. It is exploited in so-called optical traps or optical tweezers, of which the latter was discovered in 1986 by Arthur Ashkin [2]. Here, a strong focusing of the laser beam is needed. The focusing provides an additional intensity gradient in longitudinal direction, pulling particles to the focal point (Fig. 2). If the longitudinal gradient force exceeds the scattering force, stable three-dimensional trapping can be achieved. Optical manipulation covers an important area of research dealing with the handling and trapping of nanometer- to micrometer-sized particles. It is a field of interest mainly for biology and medicine offering the big advantage of handling biological material without contamination or mechanical damage [3].

The field of microfluidics has rapidly expanded since the development of the first microfluidic devices in the early 1990s [4]. Microfluidic channels enable the examination

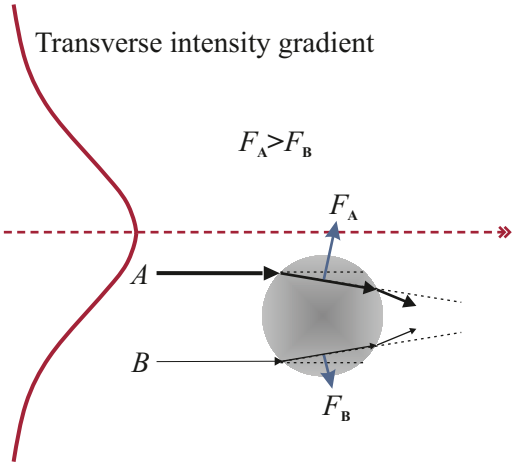

Fig. 1: Working principle of a two-dimensional optical trap. A laser beam with a transverse intensity gradient is refracted at the transparent, spherical particle, resulting in forces by momentum transfer. The net force points towards the intensity maximum.

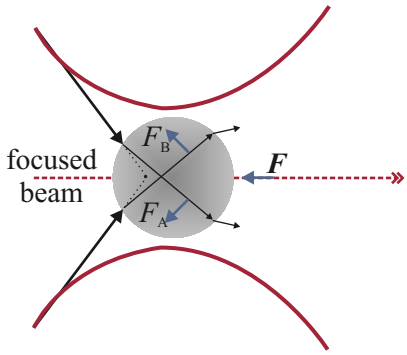

Fig. 2: Working principle of three-dimensional optical tweezers. Due to tight focusing, the laser beam has a longitudinal intensity gradient. If the longitudinal gradient force overcomes the scattering force, the particle is three-dimensionally trapped.

of biological samples with strongly reduced sample volumes, parallel cycling and exact timing [5, 6]. For the handling of particles inside the channels without additional tools like valves, electroosmotic or hydrodynamic setups, microfluidics and optical manipulation were successfully combined [7, 8]. With the driving force of miniaturization in almost all areas, the use of vertical-cavity surface-emitting lasers (VCSELs) as laser sources has gained increasing interest [8–13]. Their advantageous properties make them highly suitable for optical manipulation in microfluidics. One advantage of VCSELs is their emission in the near-infrared range. Since biological material has only little absorption at these wavelengths, the risk of thermal damage is minimized. Because of their vertical emission, which allows the comparatively easy fabrication of two-dimensional laser arrangements (arrays), patterns of multiple optical traps can be generated without the need for extensive beam splitting or steering setups. Besides the classical tweezers setup, even a drastically miniaturized setup can be envisioned. By directly integrating VCSEL arrays and microfluidic channels, a portable, low-cost particle manipulation device is feasible, whereas one can hardly imagine the realization of similar integrated modules with other laser sources.

2. VCSEL Arrays as Laser Sources for Optical Manipulation in Microfluidics

The schematic structure of a top-emitting VCSEL is depicted in the left part of Fig. 3. It is grown in the AlGaAs material system using molecular beam epitaxy, with a structure designed for an emission wavelength of around 850 nm. The laser resonator is built by distributed Bragg reflector (DBR) mirrors. Both the bottom DBR and the GaAs substrate

underneath are n-doped to enable back side contacting. The top DBR is p-doped and has a reduced number of mirror pairs compared to the n-type DBR. As this is the light outcoupling side of the VCSEL, the top p-contact is structured as a ring on top of the mesa. The active region in the inner cavity consists of three 8 nm thick GaAs quantum wells, separated by 10 nm thick barriers.

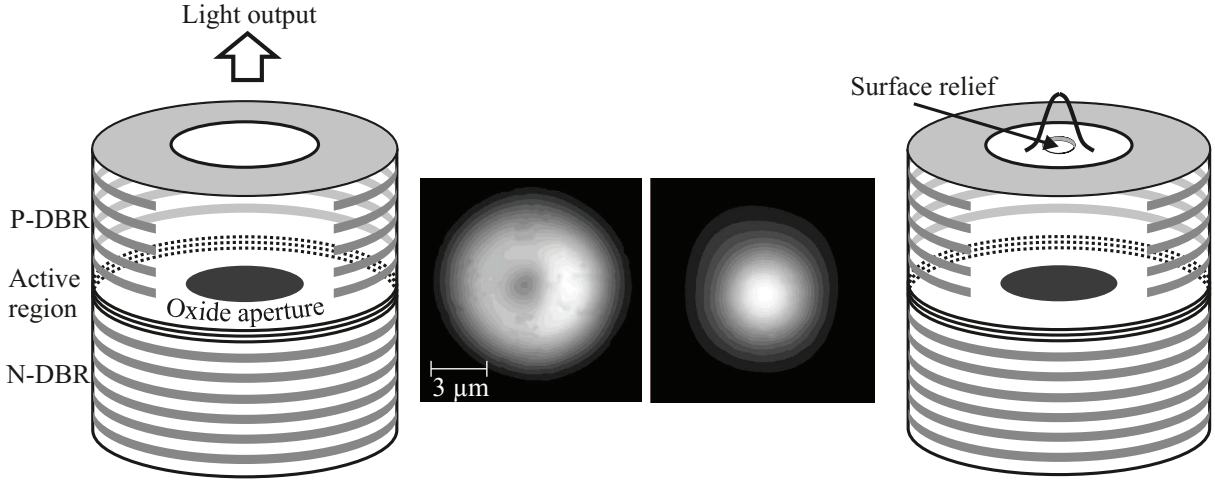

Fig. 3: Left: schematic of a standard VCSEL structure with a typical donut-like near-field intensity distribution. Right: schematic of a surface relief VCSEL with Gaussian-like intensity distribution.

An AlGaAs layer with a high aluminum content located above the active region is selectively oxidized after mesa etching, thus providing current confinement on the p-doped side. The diameter of the remaining oxide aperture strongly influences the VCSEL behavior. With a small enough diameter, for instance, a Gaussian-like beam profile can be achieved. Unfortunately, by current apertures of only up to 4 µm, the output power is limited to about 3 mW. With larger apertures it is possible to get much higher output powers. However, large active diameters result in a larger beam divergence and in the emission of higher-order transverse modes with an often donut-shaped beam profile, as shown in Fig. 3. A donut- or ring-like intensity distribution is undesirable for the intended trapping scheme because it leads to an offset between beam and trapping center [14]. Furthermore, because of the lower beam quality, the beam diameter at the focal point is increased.

The right part of Fig. 3 shows one possibility to achieve Gaussian-like emission without being limited that strongly in the optical output power. On top of the p-doped DBR, an antiphase layer with a thickness of one quarter of the material wavelength is additionally grown. By reducing the top mirror reflectivity, the antiphase layer increases the threshold gain significantly. During the VCSEL fabrication process, the antiphase layer is selectively removed in the center of the laser facet. As a result, the threshold gain is reduced only in the center to favor a Gaussian-like beam profile. The corresponding intensity distribution of a laser with a so-called surface relief is shown in the inset in Fig. 3.

Because VCSELs offer the advantageous possibility of creating various two-dimensional arrays, it is very obvious to realize patterns of optical traps, so-called optical lattices. An ultra-dense spacing of the VCSELs is highly desirable for such optical lattices and

a challenging requirement. The typical device pitch for commercial VCSELs for data communication applications is 250 µm [15]. For interruption-free optical manipulation this value needs to be reduced by an order of magnitude. Such a drastic reduction requires not only a minimized distance between adjacent mesas of about 2 µm, but also mesa diameters reduced to around 25 µm. For an exact alignment between surface relief and active aperture, a multiple-resist self-aligned fabrication process is used, which is shown in Fig. 4.

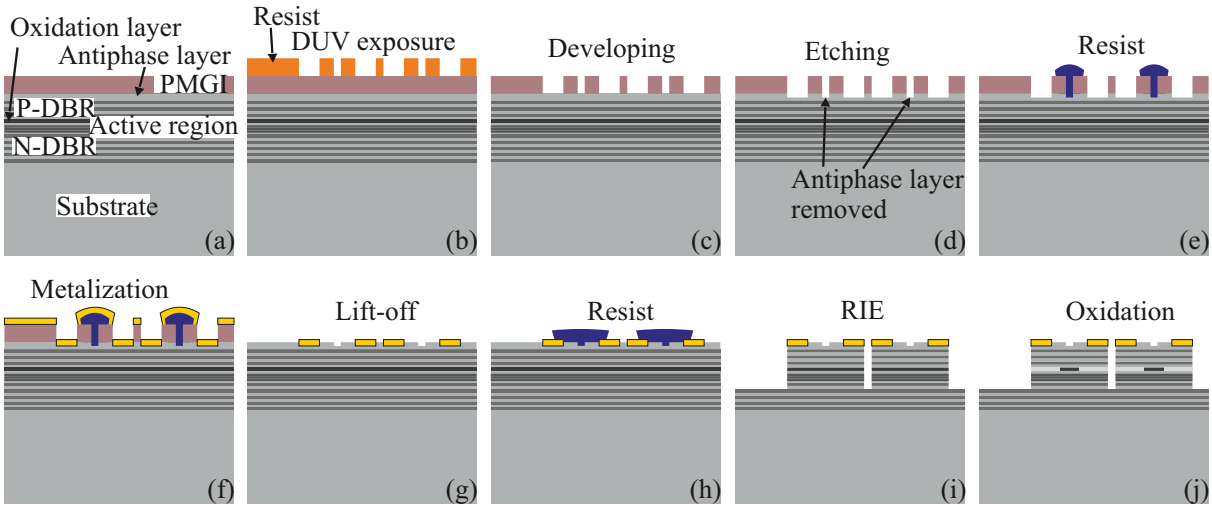

Fig. 4: Processing steps for the fabrication of densely packed VCSEL arrays. By means of a multi-layer resist self-alignment process, surface relief and oxide aperture are exactly aligned to each other. Reactive-ion etching provides for the needed vertical side walls for close spacing.

In the first step, relief and p-ring contact are defined at the same time in a PMGI (polymethylglutarimide) resist (a). Contrary to other photoresists, PMGI requires an exposure to light in the deep-ultraviolet regime. As there is no possibility to implement a photomask in the DUV exposure setup, a structured, novolak-based resist serves as the exposure mask here (b). Due to its unique properties, the PMGI is not affected by the second resist layer. After DUV exposure and developing, the upper resist can be easily removed without damaging the PMGI underneath (c). In the second step, the surface relief is structured by wet-chemical etching (d), and the relief as well as the area surrounding the lasers are covered with another resist (e) for the subsequent metalization (f) and lift-off process (g) of the p-ring contact. For the etching of the mesas, the facets are covered with yet another novolak-based resist (h). For the desired dense packing of the lasers, wet-chemical etching of the mesas is not an option. Reactive-ion etching with carefully chosen parameters provides vertical side walls for close packing (i). As the p-ring metalization serves as etch mask, the mesa and thus the active aperture are automatically aligned exactly to p-ring and surface relief. Afterwards, the protective resist is removed and the oxidation layer is selectively oxidized by wet oxidation (j).

In a classical tweezers setup with several lenses for beam forming [16], continuous deflection of flowing particles was achieved by means of tilted linear VCSEL arrays. Continuous deflection is enabled by the following principle [17, 18]: a particle is passing the optical

lattice, created by the linear laser array. The particle is not retained but deflected at each trap if the trapping force is in the same range as the fluidic drag force. Due to the deflection at each trap, the particle follows the tilt of the array and is thus deflected orthogonal to its initial flow direction and, in our case, directed into the upper branch of the Y-junction without any mechanical or electrical intervention. The calculated x- and y-displacements for exemplary particles with diameters of 10 µm and 15 µm are presented in [16].

3. Drastic Miniaturization by a Novel Integration Concept

The so-called integrated optical trap represents a strongly miniaturized version of the classical tweezers setup. The bulky setup, containing several lenses for beam collimation and focusing [16], is to be replaced by one fully integrated component. For an efficient operation of the integrated optical trap, the distance between microfluidic channel and trapping lasers must be minimized to prevent strong beam expansion. The realization of electrical contacts at the p- and n-side of the laser chip turns out to be the main challenge.

An earlier approach for the integrated optical VCSEL trap is depicted in Fig. 5. It envisioned flip-chip bonding of the laser chip to the microfluidic chip using several micrometers thick indium for both mechanical and electrical connection. On the laser side, the indium bumps for soldering are placed on bondpads, simultaneously connecting several lasers. On the microfluidic side, on the lower surface of the sealing glass, the indium bumps are connected to a metal fan-out, enabling electrical contacting of the lasers.

The major disadvantage of this integration approach lies in the insufficient heat dissipation and thus an increase in the thermal resistance due to the absence of a heat sink. Figure 6 shows the output characteristics of an array of six VCSELs, comparing the behavior on wafer (left) and in the integrated module according to the earlier approach (right). Even with permanent cooling by nitrogen purging, the maximum output power was reduced by a factor of two after integration. The temperature problem could also be seen in the

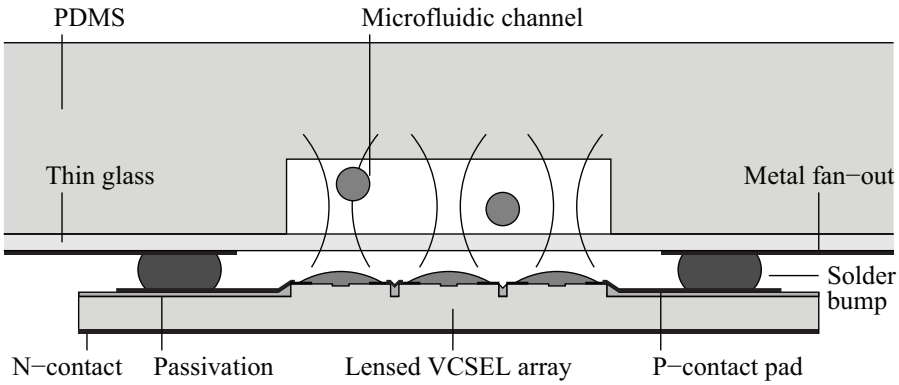

Fig. 5: Schematic of an earlier approach for the integrated optical trap array module. By indium solder bumps, the laser chip is connected both mechanically and electrically to the microfluidic chip. The VCSEL output beams are shaped by microlenses, generating weakly focused beams for particle manipulation in the microfluidic channel (from [16]).

formation and movement of bubbles in the microfluidic channel during laser operation (see inset in the right part of Fig. 6).

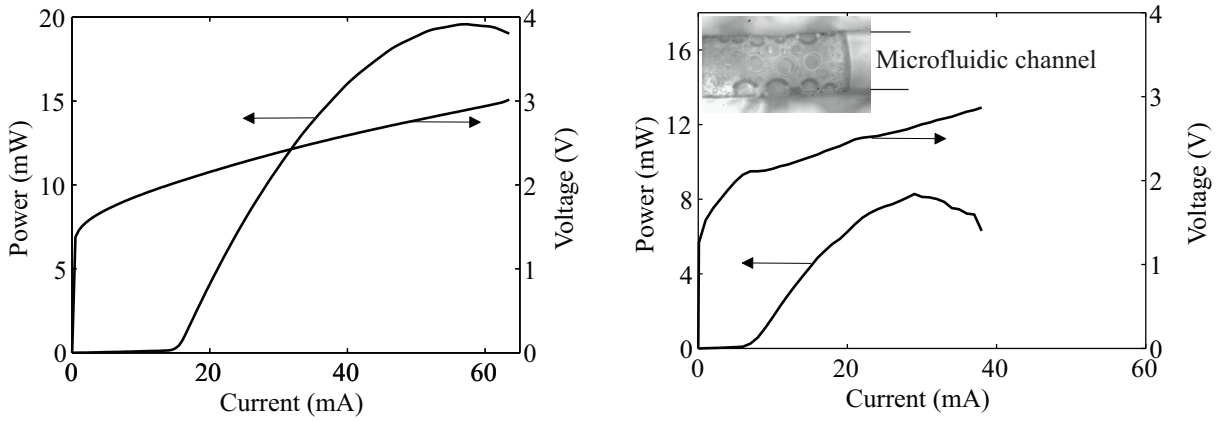

Fig. 6: Optical output power and voltage versus current of an array of six emitting VCSELs with active diameters of 6.5 µm, before (left) and after (right) integration with the microfluidic chip. Due to insufficient heat dissipation, the maximum output power is reduced by a factor of two. The inset in the right graph shows the formation of bubbles in the microfluidic channel due to the elevated temperature during laser operation.

Nonetheless, we were able to show particle deflection with a device integrated according to Fig. 5. With four emitting VCSELs, we deflected a flowing particle with 15 µm diameter. Figure 7 shows snapshots of this experiment. We expect that with higher VCSEL output powers, continuous deflection would be possible at much higher flow velocities.

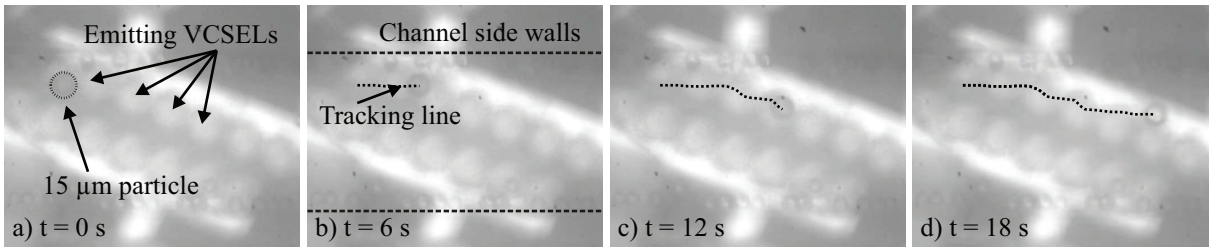

Fig. 7: Snapshots of a deflection experiment with an integrated optical trap module, realized according to the described earlier integration approach. The flowing particle is deflected by each of the emitting VCSELs (after [19]).

As mentioned above, the successful miniaturization of the VCSEL-based optical trap with avoidance of any external optics requires a minimized distance between laser facets and the microfluidic channel. However, the necessity of accessing the laser p- and n-side for electrical contacting remains. Our novel integration approach is shown in Fig. 8. It envisions to place the bondpad in a deeply etched groove in the substrate, which allows for contacting by means of bond wires. After processing, the laser chips are separated and soldered to structured heat sinks, containing several fanout tracks. The bondpads are then wire-bonded to these tracks. Microlenses on the laser facets provide slight beam shaping.

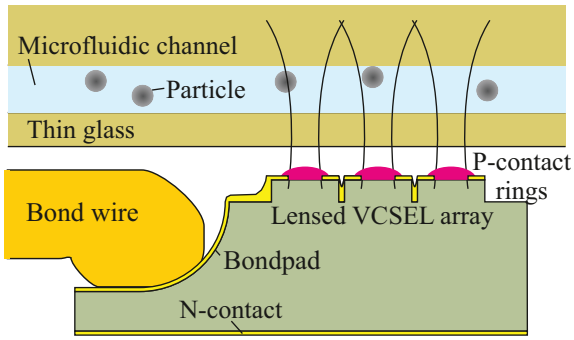

Fig. 8: Schematic of the novel integrated optical trap module. The p-contact metal is recessed, thus giving space for a thin bond wire. The back of the laser chip is accessible for n-contacting. Integrated microlenses on the laser facets achieve a weak focusing of the beams.

Earlier work [19] has shown that there is no dependence of the individual laser threshold current on the number of lasers addressed in parallel. Accordingly, we are able to connect a comparatively large number of VCSELs in parallel, in our case up to 21 per linear array. The mesa diameters range from 22 µm to 26 µm, with active diameters between 6 µm and 10 µm and device pitches ranging from 24 µm to 28 µm.

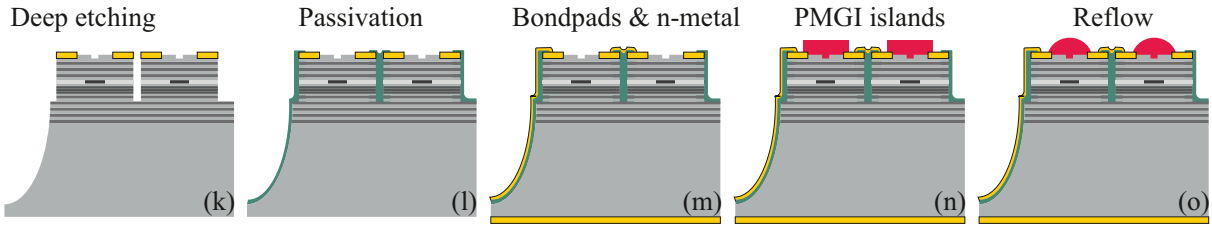

Fig. 9: Processing steps for integration-ready densely packed VCSEL arrays. After very deep etching, the side walls are passivated, then covered with metal for the bondpads. With a PMGI resist-based reflow process, microlenses are structured on the laser facets.

Figure 9 shows a schematic of the additional fabrication steps, building on the processing steps presented in Fig. 4. First, the laser arrays and the surrounding area are protected, and the bonding grooves are structured by wet-chemical etching with depths of several tens of micrometers (k). To allow the subsequent process steps, the formation of a strong undercut during groove etching has to be avoided.

As a next step, the side walls are protected with a passivation layer to prevent a short circuit between p- and n-doped layers (l). On top of the passivation, large-area bondpads are structured in the bonding grooves (m). The lithographical step for defining the bondpad metalization is difficult, especially because of the extreme topology after deep etching. During evaporation of the bondpad metalization, the samples are tilted with respect to the evaporation direction and constantly rotated. This method ensures that not only the flat surfaces but also the inclined side walls are metalized. A scanning electron microscope picture of processed VCSEL arrays with recessed bondpads is depicted in Fig. 10.

For a weak beam focusing, microlenses are structured directly on top of the laser facets. For this purpose, cylindrical islands of PMGI photoresist are structured (n), which melt

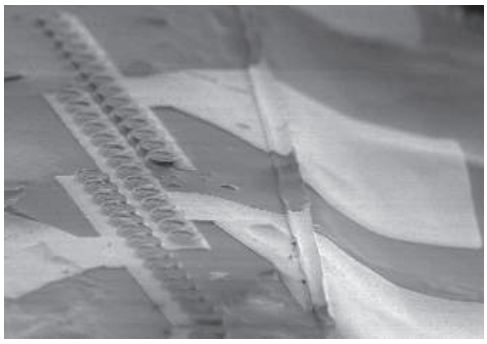

Fig. 10: Scanning electron micrograph of VCSEL arrays, fabricated according to the novel process. The bondpads can be seen in the deeply etched grooves. The length of each of the three linear 14-elements VCSEL arrays is about 390 µm.

to microlenses in the subsequent reflow process (o). With these lenses, it is possible to achieve a point of delayed divergence [19].

The output characteristics of a laser array with 16 emitting VCSELs of approximately 8 µm active diameter is depicted in Fig. 11. Voltage and optical output power are plotted against the driving current. From the graph, a threshold current of 38 mA and a maximum optical output power of 56 mW can be obtained. The insets in Fig. 11 show the near-field intensity distributions of one laser in the array for three different operating currents. Dominance of the fundamental mode can be clearly seen.

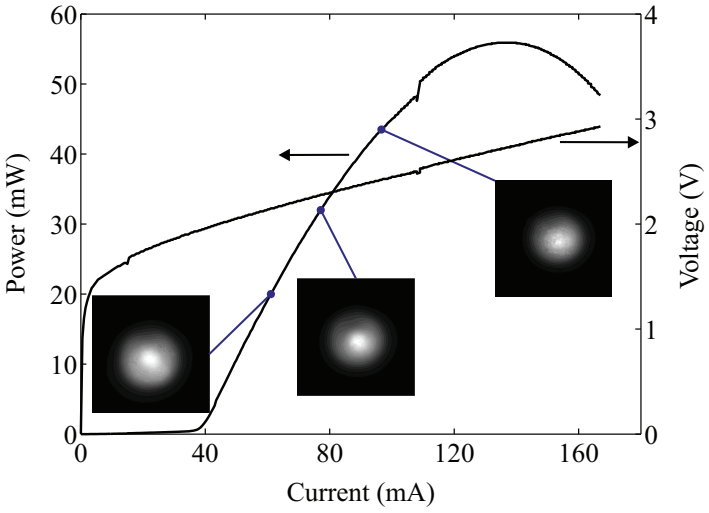

Fig. 11: Light–current–voltage characteristics of an array with 16 emitting VCSELs with 8 µm individual active diameter. The insets show the near-field intensity distributions at three different operating currents, with a clear dominance of the fundamental mode.

4. Conclusion

In this report, we summarized the evolving progress on VCSEL arrays serving as laser sources for optical manipulation in microfluidic channels. VCSELs are excellent light sources for this purpose, thanks to their circular, high-quality beam profiles, to their low power consumption, and to their possibility of being arranged in dense two-dimensional arrays. VCSEL-based optical trapping enables compact, contamination-free particle manipulation. In classical tweezers setups, various manipulation experiments have been presented so far with solitary VCSELs or VCSEL arrays.

Our aim is the drastic miniaturization of the setup, including the development of a novel VCSEL fabrication process to achieve densely packed VCSEL arrays, with the special

feature of direct integration with the microfluidic component. The novel integration concept provides for the integration of microlenses on the laser facets for beam focusing, as well as for the possibility of electrical contacting without increased distance between lasers and microfluidics and thus loss in device performance. With the latest results, portable and inexpensive devices for VCSEL-based biological cell manipulation in microfluidics become feasible.

Acknowledgment

We thank Alexander Hein, Niazul Islam Khan, Jose Antonio Martos Calahorro, Susanne Menzel, Rudolf Rösch, Wolfgang Schwarz, and Dietmar Wahl for their support. This project was financed by the Baden-Württemberg Stiftung gGmbH.

References

[1] A. Ashkin, "Acceleration and trapping of particles by radiation pressure", *Phys. Rev. Lett.*, vol. 24, pp. 156–159, 1970.

[2] A. Ashkin, J.M. Dziedzic, J.E. Bjorkholm, and S. Chu, "Observation of a single-beam gradient force optical trap for

dielectric particles", *Opt. Lett.*, vol. 11, pp. 288–290, 1986.

[3] K. Dholakia, P. Reece, and M. Gu, "Optical manipulation", *Chem. Soc. Rev.*, vol. 37, pp. 42–55, 2008.

[4] D.J. Harrison, A. Manz, Z. Fan, H. Lüdi, and H.M. Widmer, "Capillary electrophoresis and sample injection systems integrated on a planar glass chip", *Anal. Chem.*, vol. 64, no. 17, pp. 1926–1932, 1992.

[5] J.C. McDonald and G.M. Whitesides, "Poly(dimethylsiloxane) as a material for fabricating microfluidic devices", *Acc. Chem. Res.*, vol. 35, pp. 491–499, 2002.

[6] N.-T. Nguyen, *Mikrofluidik*. Wiesbaden: Teubner Verlag, 2004.

[7] R.W. Applegate Jr., J. Squier, T. Vestad, J. Oakey, D.W.M. Matt, P. Bado, M.A. Dugan, and A.A. Said, "Microfluidic sorting system based on optical waveguide integration and diode laser bar trapping", *Lab Chip*, vol. 6, pp. 422–426, 2006.

[8] M. Wang, M. Ozkan, E. Ata, P. Wen, M. Sanchez, C. Ozkan, O. Kibar, and S. Esener, "Integration of optoelectronic array devices for cell transport and sorting", in *Optical Diagnostics of Living Cells*, D.L. Farkas, R.C. Leif (Eds.), Proc. SPIE 4260, pp. 68–73, 2001.

[9] A. Kroner, J.F. May, I. Kardosh, F. Rinaldi, H. Roscher, and R. Michalzik, "Novel concepts of vertical-cavity laser-based optical traps for biomedical applications", in *Biophotonics and New Therapy Frontiers*, R. Grzymala, O. Haeberlé (Eds.), Proc. SPIE 6191, pp. 619112-1–12, 2006.

[10] B. Shao, S. Zlatanovic, M. Ozkan, A.L. Birkbeck, and S.C. Esener, "Manipulation of microspheres and biological cells with multiple agile VCSEL traps", *Sensors and Actuators B*, vol. 113, pp. 866–874, 2006.

[11] F. Sumiyama, Y. Ogura, and J. Tanida, "Fabrication of three-dimensional microscopic structure by VCSEL array trapping", in *Optical Trapping and Optical Micromanipulation*, K. Dholakia, G.C. Spalding (Eds.), Proc. SPIE 5514, pp. 379–386, 2004.

[12] A.L. Birkbeck, R.A. Flynn, M. Ozkan, D. Song, M. Gross, and S.C. Esener, "VCSEL arrays as micromanipulators in chip-based biosystems", *Biomedical Microdevices*, vol. 5, pp. 47–54, 2003.

[13] Y. Ogura, T. Beppu, F. Sumiyama, and J. Tanida, "Toward photonic DNA computing: developing optical techniques for parallel manipulation of DNA", in *Photonics for Space Environments X*, E.W. Taylor (Ed.), Proc. SPIE 5897, pp. 34–43, 2005.

[14] A. Kroner, I. Kardosh, F. Rinaldi, and R. Michalzik, "Towards VCSEL-based integrated optical traps for biomedical applications", *Electron. Lett.*, vol. 42, pp. 93–94, 2006.

[15] H. Roscher, F. Rinaldi, and R. Michalzik, "Small-pitch flip-chip-bonded VCSEL arrays enabling transmitter redundancy and monitoring in 2-D 10-Gbit/s space-parallel fiber transmission", *IEEE J. Select. Topics Quantum Electron.*, vol. 13, pp. 1279–1289, 2007.

[16] A. Kroner, C. Schneck, F. Rinaldi, R. Rösch, and R. Michalzik, "Application of vertical-cavity laser-based optical tweezers for particle manipulation in microfluidic channels", in *Nanophotonics II*, D.L. Andrews, J.-M. Nunzi, A. Ostendorf (Eds.), Proc. SPIE 6988, pp. 69881R-1–12, 2008.

[17] M.P. MacDonald, G.C. Spalding, and K. Dholakia, "Microfluidic sorting in an optical lattice", *Nature*, vol. 426, pp. 421–424, 2003.

[18] K. Ladavac, K. Kasza, and D.G. Grier, "Sorting mesoscopic objects with periodic potential landscapes: optical fractionation", *Phys. Rev. E*, vol. 70, pp. 010901-1–4, 2004.

[19] R. Michalzik, A. Kroner, A. Bergmann, and F. Rinaldi, "VCSEL-based optical trapping for microparticle manipulation", in *Vertical-Cavity Surface-Emitting Lasers XIII*, K.D. Choquette, C. Lei (Eds.), Proc. SPIE 7229, pp. 722908-1–13, 2009.

Towards a Laser-Integrated Module for Marker-Free Sorting of Micrometer-Sized Particles in Microfluidic Channels

Wolfgang Schwarz

In recent years, microfluidic devices have become important tools for cell analysis in biology and medicine. They enable fast and inexpensive analysis with reduced consumption of analytes. However, for optical detection involving FACS (fluorescence-activated cell sorting), sample preparation by attaching an antibody-labeled fluorochrome to the cell is required. Cell tagging by fluorochromes is a mature technology but might affect cell viability and function. In this article we present a novel concept for marker-free detection and first realization steps. We show the integration of a microfluidic chip and an electrically pumped GaAs-based oxide-confined VECSEL (vertical-extended-cavity surface-emitting laser). Particles in the microchannel flow through the laser resonator and induce a change of the cavity resonance, thus allowing sensitive detection to trigger a subsequent sorting process.

1. Introduction

For gas sensing, locking a laser to an atomic transition line, or detecting biological samples, a single-pass scheme is most commonly used [1–3]. Here the optical field is absorbed or scattered during a single encounter with the sample under test.

The cross-section can be enhanced if the sample is part of an optical resonator, as demonstrated for THz spectroscopy [4] and for passive optical resonators [5,6]. Here, the emission from a remote optical source with a broad spectrum is filtered by the cavity and spectrally analyzed. The drawback of this configuration is the low power efficiency, since the major part of the optical excitation is dumped before being detected. An interesting approach with an active resonator was presented by Paul Gourley and dates back to more than a decade ago [7]. The optical cavity was formed by two planar distributed Bragg reflectors (DBRs). An optically pumped active region was embedded between the mirrors which provided optical gain. By injection of a cell into the intermediate microfluidic channel, the cavity's multiple transversal resonances were confined by the gradient refractive index profile of the cell. This scheme demonstrated the discrimination between astrocytoma tumor cells and astrocytes by analysis of the spatially distributed emission spectrum of the cavity.

In contrast, the presented sensor makes use of an electrically pumped active region, which has major benefits for practical applications: (i) the electrical interface allows for integration with other electronics and for instant operation without cumbersome alignment of

the pump laser spot, (ii) the potential of array fabrication with simultaneous operation of multiple active regions enables parallel sensing, and (iii) the direct access to the active region supports additional sensing features like online monitoring of the laser threshold and analysis of self-heterodyne beats giving information on the flow velocity in the microfluidic channel [8].

If a sample is introduced into the standing-wave pattern inside the extended cavity it affects the laser mode and changes of the beam shape and of the emission wavelength are induced. The detection of the beam shape can be realized by an image sensor. Image processing is done to extract the modal pattern. Signal processing algorithms like multidimensional fast Fourier transform (FFT) have a $O(N\log N)$ complexity [9], with N being the number of image points. In a typical image, N can exceed 10^5. Unlike the beam shape, the spectrum can be optically analyzed by a grating in a parallel fashion. The resulting signal can be captured by a single line of a charge-coupled device (CCD) with $N \approx 10^3$. Thus, evaluation is much faster, which is a favorable advantage in high-throughput applications with frame rates in excess of 1 kHz.

As shown in Fig. 1, the sensor consists of three functional elements: (i) the customized vertical-cavity surface-emitting laser (VCSEL) soldered to a structured heat sink, (ii) the concave surface of the external mirror which is coated with a dielectric distributed Bragg reflector (DBR), and (iii) a microfluidic channel carrying a suspension of the particles to be analyzed.

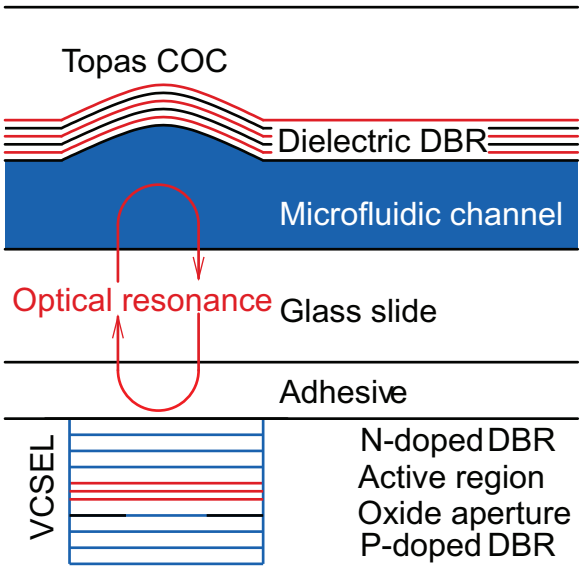

Fig. 1: Schematic drawing of the resonator structure. It comprises the VCSEL at the bottom, the microfluidic channel, and the concave-shaped Topas® COC channel wall, which is coated with a dielectric DBR to form the resonator mirror. Electrical contacts and the heat sink are omitted.

2. Fabrication Steps

This section describes the fabrication of the elements in detail. The requirement of a short extended resonator including a microfluidic channel puts tight constraints onto the fabrication procedure: Bond wires are too thick to interface the device electrically. Thus, flip-chip mounting including removal of the substrate is the only reasonable approach

allowing to shrink the cavity length. Since a multitude of fabrication and mounting techniques is employed and the used materials partially have contradictory thermal and mechanical requirements, the choice of materials and mounting sequence is challenging.

On the flip-chip mounted part, both cathode and anode are accessed from the epitaxial side of the wafer. Thus, n-contact and p-contact are structured and equipped with solder bumps for mounting. To prevent diffusion of the solder metal to the fan-out, all possible diffusion paths are blocked by a diffusion barrier.

2.1 VCSEL and heat sink

The VCSEL was grown by molecular beam epitaxy (MBE) on a [100]-oriented n-doped GaAs substrate. The n-doped and p-doped DBRs consist of 10 and 30 periods of AlGaAs, respectively, with an Al content varying between 0.2 and 0.9. After substrate removal, any aluminum-containing surfaces are prone to corrosion. Therefore the phase matching layer beneath the n-doped DBR is terminated by GaAs which is sufficiently chemically stable. However, this layer absorbs light with wavelengths shorter than 870 nm by a fraction of approximately $10^{-3}\,\mathrm{nm}^{-1}$, which is unreasonably high for being part of an optical resonator with an enhanced field at this layer. For this reason, the layer structure was designed for a laser emission wavelength from 940 nm to 980 nm, requiring strained indium-containing quantum wells in the active region. Strain compensation by phosphorus was applied in the barriers of the three $In_{0.16}Ga_{0.84}As/GaAs$ quantum wells.

The schematic cross-section is shown in Fig. 2a. After mesa etching (Fig. 2b), the n-contact was structured on the exposed n-doped DBR by GeAuNiAu evaporation (Fig. 2c) and lift-off. The current injection aperture was formed by selective wet oxidation (Fig. 2d) of an AlAs layer adjacent to the active region. During oxidation, the n-contact was annealed to achieve a low contact resistance. Afterwards, the p-contact (TiPtAu, Fig. 2e) was patterned on top of the mesa via evaporation and lift-off. The exposed surface next to the mesa was planarized with polyimide (Fig. 2f), and gold vias were electroplated to adapt the n-contact to the mesa level (Fig. 2g). A diffusion barrier of 30 nm thick tantalum and 30 nm gold was sputter-deposited on the planarized surface (Fig. 2h). For the subsequent reactive-ion etching (RIE) of the diffusion barrier by argon and tetrafluoromethane (CF_4), 500 nm thick gold was electroplated on mesas and vias as an etch mask (Fig. 2i,j). The processing of the VCSEL part was finalized by wafer thinning (Fig. 2k) and dicing.

The delivery of the electrical pump current to the fluidic VECSEL is crucial. A structured planar piece of silicon was selected to laterally extend the electrical contacts of the mounted VCSEL and to spread the dissipated power. Floating-zone silicon with high resistivity was chosen for the heat sinks because of its beneficial electrical and thermal conductivity. On top of a thin layer of aluminum oxide (Al_2O_3), 30 nm tantalum and 30 nm gold were sputter-deposited on the substrate. The metals served as a base layer for electroplating. The transmission lines were defined by electroplating of 1 µm thick gold. Afterwards, the plating base layer was etched by RIE to electrically separate the transmission lines, and the surface was planarized with polyimide. For good bondability and release of strain in the metallization, the wafer was thermally processed at 727 K for

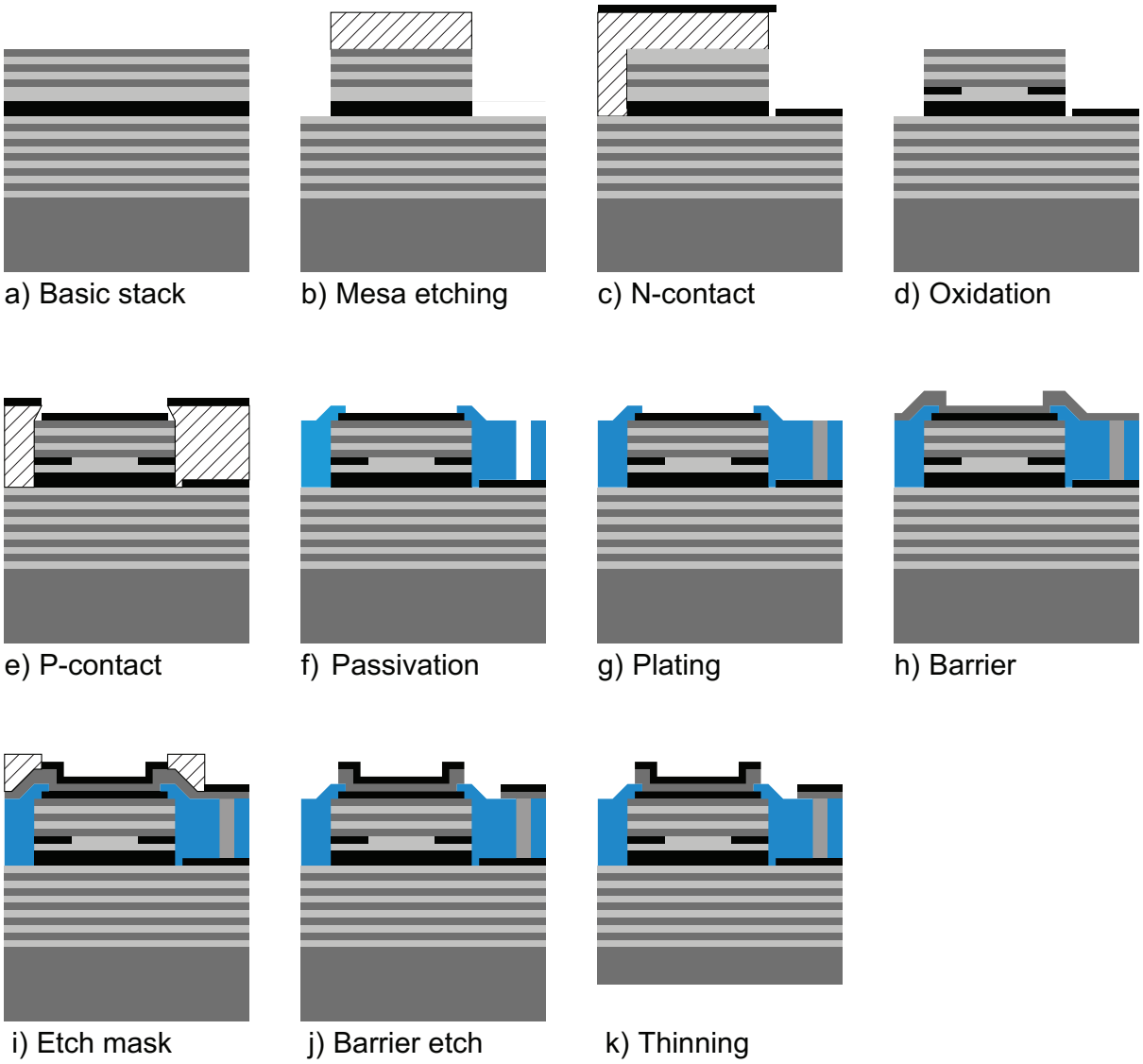

Fig. 2: Processing steps of VCSEL fabrication for flip-chip mounting. The processing of the photoresist (hatched) is simplified; steps like spin coating, photoexposure, development and resist removal are omitted.

10 minutes in nitrogen atmosphere. An insulation resistance reduced to about 80 kΩ was recorded after this step, still keeping leakage of the pump current below 30 µA. Finally, a diffusion barrier was patterned and 5 µm thick indium solder bumps were structured by evaporation and lift-off.

The diced VCSEL chips were mounted to the heat sinks by flip-chip soldering at a temperature of 538 K, under assistance of a pressure force of 5 N and formic acid for removal of the native oxides on the solder metal. Care was taken not to overheat the devices, which would result in insulation failures by creation of indium whiskers. The gold surfaces on the VCSELs and on the heat sinks form a soft intermetallic compound with the indium solder. This compound is not prone to embrittlement [10] and reduces the diffusion of solder metal to the gold pads. Due to its mechanical properties, it is well suited for the

mounting of fragile lasers, since it reduces stress originating in the different thermal expansion coefficients of laser substrate and heat sink. The GaAs substrate of the VCSEL was removed by spray etching with a solution of ammonium hydroxide (NH_4OH) and hydrogen peroxide (H_2O_2). When mixed to a pH value of 8.3, the GaAs etchant is highly selective with increasing aluminum content of AlGaAs, and the etching process stops after complete substrate removal at the AlAs layer which is grown prior to the VCSEL structure and serves as an etch stop layer. The remaining part of the n-doped VCSEL mirrors (Fig. 3) is literally brittle and stabilized during the substrate removal by carefully underfilling the gap between VCSEL chip and heat sink with Loctite® 3593™.

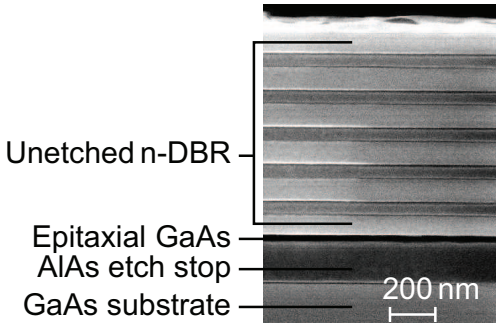

Fig. 3: Cross-section scanning electron micrograph of the remaining layer stack after mesa etching, containing the unetched part of the n-doped DBR, the etch stop layer and the substrate.

The mounted VCSELs are shown in Fig. 4. By means of 36 wire-bondable pads on the heat sinks, the same number of VCSELs on each chip is individually addressable with a processing yield of better than 95 %. The different mesa sizes on each chip allow to match the active diameter of the VCSEL to the radius of curvature of the microfluidic resonator mirror.

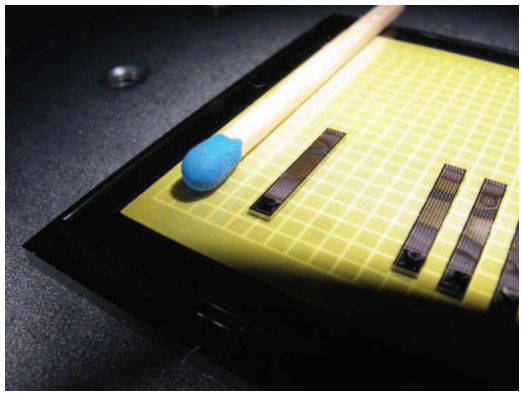

Fig. 4: Photograph of VCSEL chips soldered to the tips of structured heat sinks (approx. $1.88 \times 12.3\,\mathrm{mm}^2$). Each chip accommodates 36 individually addressable lasers with different active diameters.

2.2 External mirror and microfluidic channel

For the design of the external mirror, the radii of curvature in dependence of the distance from the laser were simulated for two different beam sizes assuming Gaussian beam propagation (Fig. 5). We assumed a plane beam front passing the p-DBR, neglecting thermal lensing and other guiding or anti-guiding effects in the VCSEL [11, 12]. The invisible pole at the position $z = 0\,\mu\mathrm{m}$ is in accordance with the assumed plane beam front at this

point. At the axial position of 20 µm, the air/glass boundary shifts the radius of curvature towards a larger radius. An opposite shift is introduced at the glass/channel boundary at $z = 50\,\mu m$. For a stable resonator, the concave extended mirror should match the radius of curvature of the beam front. The radii of curvature of the fabricated external mirrors range from about 160 µm to 290 µm and allow stable resonator modes for beam waists of 8 µm and 10 µm at the VCSEL part. The diameter of the mirror aperture was designed in such a way that less than 10^{-3} relative power of the fundamental mode is cut by the aperture.

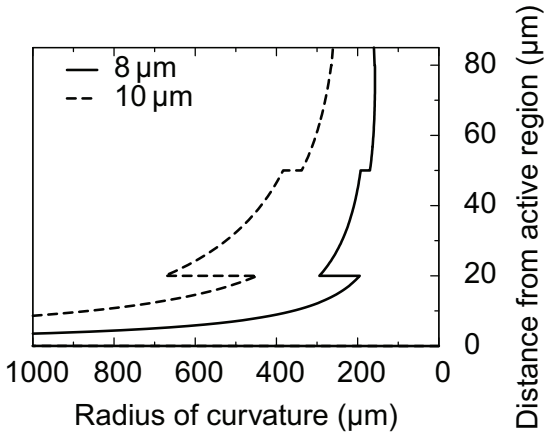

Fig. 5: Calculated radii of curvature of the wavefronts in the extended resonator for two different beam waist sizes. The beam propagates bottom up.

The external mirrors and the microfluidic channels were fabricated by hot embossing of the cyclo-olefin-copolymer Topas® COC 5013. From the existing micro-molding techniques, hot embossing enables the fabrication of high precision and high quality polymer micro-structures and is mainly used for optical applications where high accuracy in the geometrical dimensions and a very low surface roughness are required [13]. With this molding technique, a roughness $R_a < 15\,nm$ and a high contour accuracy could be achieved. Topas® COC material was chosen for its low birefringence and high transparency. Contrary to polymethylmethacrylate (PMMA), its low water absorption prevents swelling in water and it supports the deposition of stable dielectric mirrors with thicknesses up to a few micrometers, which is important for the present application. Figure 6 depicts the embossed channels. The channels are 30 µm high and have additional inputs for injection of a sheath fluid to center the particles with respect to the channel [14], which is important for a reproducible response of the sensor. In the region of the resonator mirrors, the channel walls are coated with a dielectric DBR via a shadow mask. Since the DBR is transparent for visible light, only the outer parts of the mirror coating with thinner layers and thus lower Bragg wavelength appear as a bright halo.

Optical layer systems as required for highly reflecting and partially transparent mirrors typically consist of several periods of high and low refracting dielectrics with an overall thickness of several micrometers. If such a system is deposited on a polymer substrate, the maximum layer thickness is limited by the adhesion of the dielectric to the substrate and by mechanical stress building up during deposition. The deposition of thick layer stacks on polymer substrates was rarely reported [15]. By reactive-ion-beam sputter-deposition of oxides of aluminum and tantalum, mirror reflectivities in excess of 98 % have been realized with good adhesion to Topas® COC and fair adhesion in case of a microfluidic ambience.

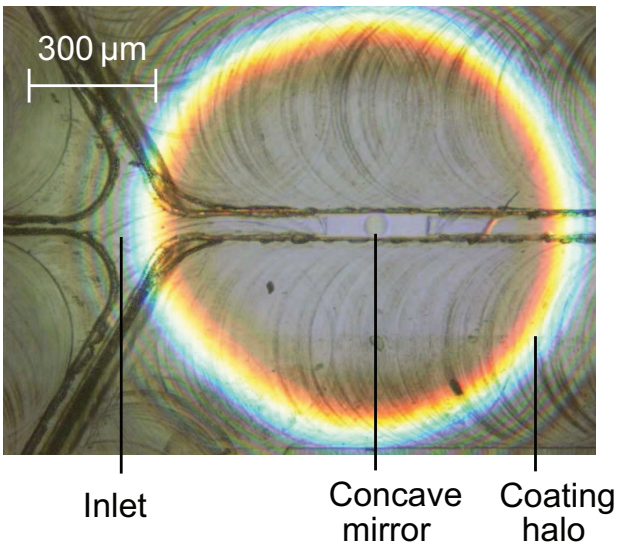

Fig. 6: Optical confocal microscope image of a molded fluidic channel with a concave resonator mirror, coated with a dielectric DBR.

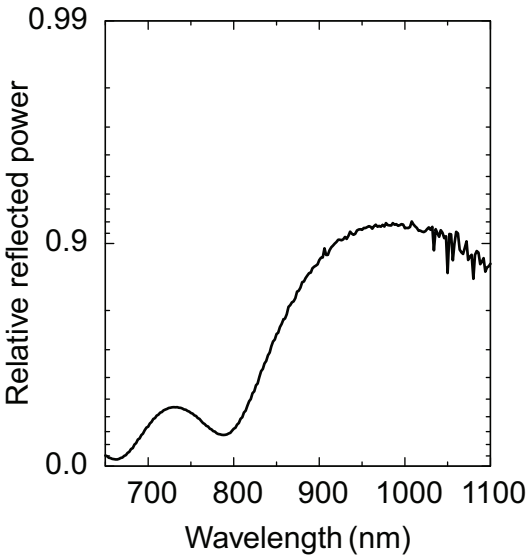

Fig. 7: Measured power reflectivity spectrum of a DBR with 5.5 periods of Ta_2O_5/SiO_2 for a reflectivity of 93 %. The measurement was done on a coated BK7 glass.

The reflectivity measurement in Fig. 7 was done on a coated BK7 glass as a reference sample. In the present case, the curved surface was coated with 5.5 periods of Ta_2O_5/SiO_2 to attain a reflectivity of 93 %. With proper surface preparation, this coating has proven to be extraordinary reliable even after weeks of operation in microfluidic ambience. After mirror deposition, the channel is closed vertically by a 30 µm thin glass slide which is fixed by a photocurable adhesive. As a last step, the VCSEL is forward biased, actively aligned to the concave-shaped mirror for laser operation and again fixed by a photocurable adhesive.

3. Operation Characteristics of the Microfluidic VECSEL

The light–current (LI) characteristics of an integrated microfluidic VECSEL with about 15 µm active diameter is shown in Fig. 8. The emission spectra at 7 mA and 10 mA driving current are depicted in Fig. 9. Between 7 mA and 10 mA, the output power is non-monotonic. This transition is accompanied by a hop of the longitudinal mode order with a longitudinal mode spacing of about 1.8 nm. Fundamental transverse operation below and above the hopping point is indicated by low M^2 factors, which where measured to be 1.28 and 1.21 at 7 mA and 10 mA driving current, respectively.

4. First Experiments With Microfluidic Flow

The microfluidic channel was supplied with a flow of 10 nl/s by a precision syringe pump. The emission spectra of the VECSEL were recorded by a linear CCD attached to a

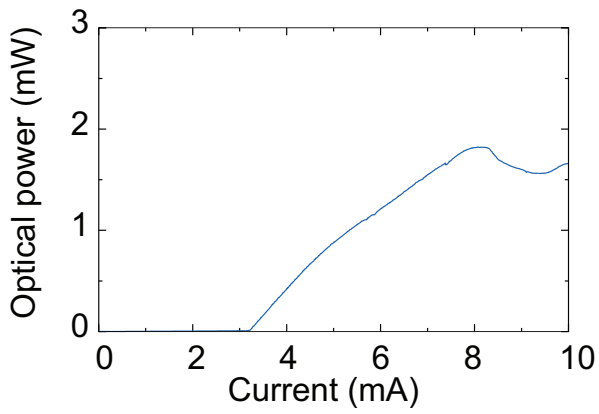

Fig. 8: LI characteristics of a fully functional microfluidic VECSEL.

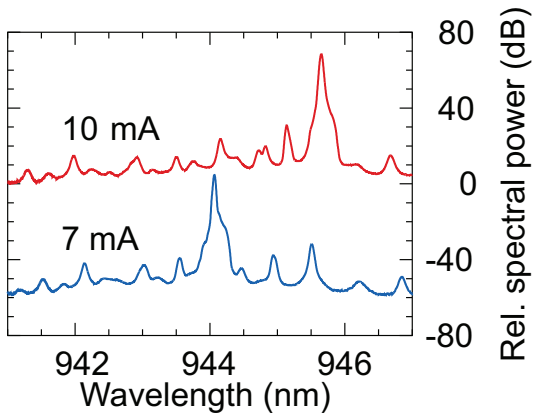

Fig. 9: Emission spectra of a the VECSEL from Fig. 8 at two different driving currents.

monochromator. The monochromator has a Czerny–Turner configuration and 1 m focal length.

For an emission wavelength of 940 nm to 950 nm, each element of the CCD corresponds to a spectral increment of 3 pm and almost resembles the resolving power of the monochromator. Figure 10 shows the change in the peak wavelength over the time. At the beginning of the recording, the dominant wavelength peaks periodically by about 300 pm relative to the baseline. When the syringe pump is stopped after 12 s, the flow stops as well as the periodic pattern in the emission wavelength. The following sudden steps in the emission wavelength are attributed to longitudinal mode flips induced by temperature changes of the channel. There is clear evidence that the periodic changes of the emission wavelength before stopping the pump are related to the pulsation of the syringe drive which changes the optical cavity length.

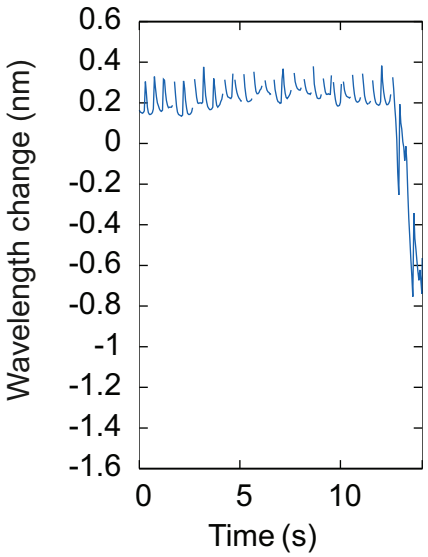

Fig. 10: Time-resolved change of the dominant emission wavelength of the VECSEL. After 12 s, the flow stops as well as the periodic pattern in the emission wavelength. The following discontinuities are attributed to longitudinal mode hops.

5. Conclusion

We demonstrated the concept of an integrated optical sensor. The working principle of the sensor is based on an extended vertical resonator through which the particles flow for detection. Particles passing the resonator are expected to induce a measurable change in the cavity resonance. Details of the fabrication process were presented as well as device characterization and first experiments with water flow inside the microfluidic channel.

The sensor is fully functional. Pulsation of the microfluidic flow could be resolved with a high update rate. Experiments with particle injection into the resonator are in progress and results will be reported in the near future.

Acknowledgment

We thank Antonio Jorge Márquez del Pino for device assembly and measurements, Dieter Rimpf for providing the microfluidic components, Susanne Menzel, Ilona Argut, and Rudolf Rösch for their help with microfabrication, Josef Theisz for fabricating many mechanical parts of the setup, as well as Patrick Herfurth and David Maier for advice on dry etching and flip-chip soldering. This project is financed by the Baden-Württemberg Stiftung gGmbH.

References

[1] A. Hangauer, A. Spitznas, J. Chen, R. Strzoda, H. Link, and M. Fleischer, "Laser spectroscopic oxygen sensor for real time combustion optimization", *Procieda Chemistry*, vol. 1, no. 1, pp. 955–958, 2009.

[2] S. Knappe, "MEMS Atomic Clocks", Chap. 3.18 in *Comprehensive Microsystems*, Y. Gianchandani, O. Tabata, and H. Zappe (Eds.), pp. 571–612. Amsterdam: Elsevier, 2008.

[3] P.K. Horan and L.L. Wheeless, Jr., "Quantitative single cell analysis and sorting", *Science*, vol. 198, no. 4313, pp. 149–157, 1977.

[4] R. Mendis, V. Astley, J. Liu, and D.M. Mittleman, "Terahertz microfluidic sensor based on a parallel-plate waveguide resonant cavity", *Appl. Phys. Lett.*, vol. 95, no. 17, pp. 171113-1–3, 2009.

[5] L.K. Chin, A.Q. Liu, C.S. Lim, X.M. Zhang, J.H. Ng, J.Z. Hao, and S. Takahashi, "Differential single living cell refractometry using grating resonant cavity with optical trap", *Appl. Phys. Lett.*, vol. 91, pp. 243901-1–3, 2007.

[6] H. Shao, W. Wang, S.E. Lana, and K.L. Lear, "Optofluidic intracavity spectroscopy of canine lymphoma and lymphocytes", *IEEE Photon. Tech. Lett.*, vol. 20, pp. 493–495, 2008.

[7] P.L. Gourley, "Biocavity laser for high-speed cell and tumour biology", *J. Phys. D: Appl. Phys.*, vol. 36, pp. R228–239, 2003.

[8] A.N. Serov, J. Nieland, S. Oosterbaan, F.F.M. de Mul, H. van Kranenburg, H.H.P.Th. Bekman, and W. Steenbergen, "Integrated optoelectronic probe including a vertical cavity surface emitting laser for laser doppler perfusion monitoring", *IEEE Trans. Biomed. Engineering*, vol. 53, pp. 2067–2074, 2006.

[9] M. Frigo and S.G. Johnson, "Design and implementation of FFTW3", *Proc. IEEE*, vol. 93, no. 2, pp. 216–231, 2005.

[10] G. Humpston and D.M. Jacobson, *Principles of Soldering*. Materials Park (Ohio): ASM International, 2004.

[11] G.A. Smolyakov and M. Osiński, "Analysis of ring-metal-aperture VCSELs for single-lateral-mode operation", *J. Lightwave Technol.*, vol. 23, pp. 4278–4286, 2005.

[12] L. Raddatz, I.H. White, H.D. Summers, K.H. Hahn, M.R. Tan, and S.-Y. Wang, "Measurement of guiding effects in vertical-cavity surface-emitting lasers", *IEEE Photon. Technol. Lett.*, vol. 8, pp. 743–746, 1996.

[13] M. Heckele, W. Bacher, K. D. Müller, "Hot embossing – The molding technique for plastic microstructures", *Microsystem Technologies*, vol. 4, pp. 122–124, 1998.

[14] M.L. Shuler, R. Aris, and H.M. Tsuchiya, "Hydrodynamic focusing and electronic cell-sizing techniques", *Applied Microbiology*, vol. 24, pp. 384–388, 1972.

[15] U. Schulz, U.B. Schallenberg, and N. Kaiser, "Antireflection coating design for plastic optics", *Appl. Optics.*, vol. 41, pp. 3107–3110, 2002.

Ph.D. Theses

1. Stephan Ulrich Schwaiger,
   Gasphasenepitaxie und Eigenschaften von nicht- und Semipolarem GaN,
   May 2011.

2. Ihab Kardosh,
   Verbesserung der Emissionseigenschaften
   substratseitig emittierender Vertikallaserdioden,
   June 2011.

Diploma and Master Theses

1. Mohammadreza Gharavipour,
   Doping Studies of AlGaN With High Al Content,
   Master Thesis, January 2011.

2. Bassem Arar,
   Design of Bragg gratings on SOI nano-rib waveguides,
   Master Thesis, July 2011.

3. Sujoy Paul,
   Monolithic Integration of VCSEL/PIN-detector for Bidirectional Optical Links: Fabrication, Characterization and Data Transmission,
   Master Thesis, August 2011.

4. Haoyuan Qi,
   Investigations on AlN Buffer Layer for AlGaN-Based Deep Ultraviolet LEDs,
   Master Thesis, September 2011.

5. Ren Zhe,
   Optimization of coaxial InGaN quantum wells around GaN nano tubes,
   Master Thesis, November 2011.

6. Marian Caliebe,
   Elektro-optische Untersuchungen an selektiv gewachsenen GaN-basierten semipolaren Laserstrukturen,
   Diploma Thesis, December 2011.

7. Frederic Demmerle,
   Leistungsbilanz und Emmissionseigenschaften von optisch gepumpten Halbleiterscheibenlasern,
   Diploma Thesis, December 2011.

8. Tony Amende,
   In-situ 4-point Measurements on Freestanding Graphene Structures for TEM Investigations,
   Master Thesis, December 2011.

Bachelor Theses

1. Hannes Stuhldreier,
   Untersuchungen zu Eigenschaften und Vergleich von optisch gepumpten Halbleiterscheibenlasern mittels Photolumineszenzspektroskopie,
   June 2010.

2. Yao Xiang,
   Investigations on the wafer bow of freestanding GaN substrates by wet chemical etching,
   June 2011.

Semester Project

1. Benedikt Schlecker,
   Design and Analysis of Optically Pumped Semiconductor Disk Lasers with Fully Homogeneous Excitation,
   December 2011.

Talks

[1] A. Al-Samaneh, M.T. Haidar, D. Wahl, and R. Michalzik, "Polarization-stable single-mode VCSELs for Cs-based miniature atomic clocks", *Conf. on Lasers and Electro-Optics Europe, CLEO/Europe 2011*, Munich, Germany, May 2011.

[2] A. Bergmann, A. Kroner, and R. Michalzik, "Towards VCSEL-based integrated microfluidic sorting systems", poster at *1st EOS Conference on Optofluidics, EOSOF 2011*, Munich, Germany, May 2011.

[3] A. Bergmann, D. Wahl, and R. Michalzik, "Integration of VCSEL-based optical traps with microfluidic channels", poster at *10th Int. Symposium on Scanning Probe Microscopy & Optical Tweezers in Life Sciences*, Berlin, Germany, Oct. 2011.

[4] M. Fikry, M. Madel, I. Tischer, K. Thonke, and F. Scholz, "Epitaxial GaN around ZnO nanopillars", *DPG Spring Meeting*, Dresden, Germany, March 2011.

[5] M. Fikry, M. Madel, I. Tischer, K. Thonke, and F. Scholz, "Position control and luminescence properties of coaxial GaN/InGaN/GaN heterostructures", poster at *XIV European Workshop on Metalorganic Vapor Phase Epitaxy*, Wroclaw, Poland, June 2011.

[6] K. Forghani, M. Gharavipour, F. Scholz, B. Neuschl, T. Meisch, I. Tischer, K. Thonke, O. Klein, and U. Kaiser, "Si doping studies in AlGaN", *DPG Spring Meeting*, Dresden, Germany, March 2011.

[7] K. Forghani, M. Gharavipour, F. Scholz, K. Thonke, O. Klein, U. Kaiser, I. Tischer, B. Neuschl, L. Kirste, and R. Gutt, "Detailed studies of Si-doped AlGaN films grown by MOVPE", poster at *9th International Conference on Nitride Semiconductors*, Glasgow, UK, July 2011.

[8] K. Forghani, M. Gharavipour, F. Scholz, B. Neuschl, T. Meisch, I. Tischer, and K. Thonke, "Studies on Si-doped AlGaN epilayers", *DPG Spring Meeting*, Dresden, Germany, March 2011.

[9] K. Forghani, M. Gharavipour, M. Klein, F. Scholz, B. Neuschl, T. Meisch, I. Tischer, K. Thonke, O. Klein, and U. Kaiser, "On the growth of AlGaN for UV LED applications: defect reduction and doping", *Heimbach Workshop*, Heldrungen, Germany, Sept. 2011.

[10] A. Hein, F. Demaria, and P. Unger,"Efficient optically pumped semiconductor disk lasers: layer design and characterization", poster at *CIOMPOSA International Summer Session "Lasers and Their Applications"*, Changchun, China, Aug. 2011.

[11] D. Heinz, R.A.R. Leute, K. Thonke, F. Lipski, T. Meisch, T. Wunderer, J. Wang, and F. Scholz, "Epitaktische Herstellung nitridischer photonischer Kristalle durch selektive MOVPE", *26th DGKK Workshop*, Stuttgart, Germany, Dec. 2011.

[12] A. Kern, D. Wahl, S. Paul, M.T. Haidar, R. Blood, W. Schwarz, and R. Michalzik, "7 Gbit/s data transmission over 500 m multimode fiber with monolithically integrated bidirectional VCSEL-based transceiver chips", *Conf. on Lasers and Electro-Optics, CLEO 2011*, Baltimore, MD, USA, May 2011.

[13] A. Kern, D. Wahl, S. Paul, M.T. Haidar, R. Blood, W. Schwarz, and R. Michalzik, "Up to 9 Gbit/s data transmission with monolithically integrated VCSELs and PIN photodiodes", *Conf. on Lasers and Electro-Optics Europe, CLEO/Europe 2011*, Munich, Germany, May 2011.

[14] A. Kern, S. Paul, D. Wahl, A. Hein, R. Rösch, W. Schwarz, and R. Michalzik, "6 Gbit/s full-duplex multimode fiber link with monolithic VCSEL–PIN transceiver chips", *37th Europ. Conf. on Opt. Commun., ECOC 2011*, Geneva, Switzerland, Sept. 2011.

[15] A. Kern, D. Wahl, and R. Michalzik, "Multi-Gbit/s full-duplex data transmission over standard multimode fiber with butt-coupled transceiver chips", poster at *European Semiconductor Laser Workshop*, Lausanne, Switzerland, Sept. 2011.

[16] M. Klein, F. Lipski, and F. Scholz, "The effect of MoN_x on the local V-III ratio in hydride vapor phase epitaxy", *26. DGKK Workshop*, Stuttgart, Germany, Dec. 2011.

[17] F. Lipski, X. Yao, M. Klein, and F. Scholz, "Reduction of the wafer bow of freestanding GaN substrates by wet chemical etching", *EMRS Spring Meeting*, Nice, France, May 2011.

[18] R.A.R. Leute, K. Forghani, F. Lipski, F. Scholz, I. Tischer, B. Neuschl, and K. Thonke, "Growth of AlGaN stripes with semipolar side facets as waveguide claddings for semipolar laser structures", *DPG Spring Meeting*, Dresden, Germany, March 2011.

[19] R.A.R. Leute, F. Lipski, K. Forghani, I. Tischer, K. Thonke, and F. Scholz, "Selective area growth of AlGaN for epitaxially realized waveguides of semipolar GaN based laser diodes", poster at *XIV European Workshop on Metalorganic Vapor Phase Epitaxy*, Wroclaw, Poland, June 2011.

[20] R.A.R. Leute, K. Forghani, F. Lipski, F. Scholz, I. Tischer, K. Thonke, and B. Witzigmann, "Selective epitaxy of 3 D AlGaN/GaN waveguides for semipolar laser structures", *EMRS Spring Meeting*, Nice, France, May 2011.

[21] R.A.R. Leute, D. Heinz, M. Dickel, K. Thonke, F. Lipski, T. Meisch, and F. Scholz, "Selektive Epitaxie von GaN-basierten Nanopyramiden mit semipolaren Quantenfilmen durch Laser-Interferenz-Lithographie und MOVPE", *26. DGKK Workshop*, Stuttgart, Germany, Dec. 2011.

[22] T. Meisch, K. Forghani, F. Lipski, B. Neuschl, M. Feneberg, U. Röder, F. Scholz, and K. Thonke, "Optical studies on the valence band structure of AlGaN", *9th International Conference on Nitride Semiconductors*, Glasgow, UK, July 2011.

[23] T. Meisch, F. Lipski, K. Forghani, B. Neuschl, M. Feneberg, F. Scholz, and K. Thonke, "Optical investigation on the valence band structure of AlGaN with low Al content", poster at *DPG Spring Meeting*, Dresden, Germany, March 2011.

[24] R. Michalzik, A. Kern, M. Stach, F. Rinaldi, and D. Wahl, "Bidirectional data transmission over multimode fiber using integrated transceiver chips" (invited), *SPIE Photonics West 2011, Optical Metro Networks and Short-Haul Systems III*, San Francisco, CA, USA, Jan. 2011.

[25] R. Michalzik, A. Kern, and D. Wahl, "VCSEL integration with high-speed photodiodes", *VCSEL Day 2011*, Toulouse, France, May 2011.

[26] R. Michalzik, P. Debernardi, and W. Schwarz, "Optical modes of an optofluidic microparticle VCSEL sensor", *European Semiconductor Laser Workshop*, Lausanne, Switzerland, Sept. 2011.

[27] F. Scholz, T. Wunderer, S. Schwaiger, and R.A.R. Leute, "Semipolar GaInN quantum well structures on large area substrates" (invited), *2011 German-Japanese-Spanish Joint Workshop on Frontier Photonic and Electronic Materials and Devices*, Granada, Spain, March 2011.

[28] F. Scholz, T. Wunderer, S. Schwaiger, and R.A.R. Leute, "Semipolar GaInN quantum well structures on large area substrates" (invited), *3rd International Symposium on Advanced Plasma Science and its Applications for Nitrides and Nanomaterials, ISPlasma2011*, Nagoya, Japan, March 2011.

[29] F. Scholz, "Nitride semiconductor research in Germany and Europe: Attempt of a short description" (invited), *10th Nitride Semiconductor Application Workshop, NSAW 2011*, Nagoya, Japan, March 2011.

[30] F. Scholz, S. Schwaiger, J. Däubler, I. Tischer, K. Thonke, S. Neugebauer, S. Metzner, F. Bertram, J. Christen, and R.A.R. Leute, "Semipolar GaInN quantum well structures on large area substrates", *9th International Conference on Nitride Semiconductors*, Glasgow, UK, July 2011.

[31] F. Scholz, F. Lipski, X.Yao, and M. Klein, "Studies about wafer bow of freestanding GaN substrates grown by hydride vapor phase epitaxy", *American Conference on Crystal Growth and Epitaxy*, Monterey, CA, USA, Aug. 2011.

[32] F. Scholz, S. Schwaiger, J. Däubler, I. Tischer, K. Thonke, S. Neugebauer, S. Metzner, F. Bertram, J. Christen, H. Lengner, J. Thalmair, and J. Zweck, "Semipolar GaInN quantum well structures on large area substrates", seminar talk, *PARC*, Palo Alto, CA, USA, July 2011.

[33] K. Forghani, M. Gharavipour, F. Scholz, B. Neuschl, T. Meisch, I. Tischer, K. Thonke, O. Klein, and U. Kaiser, "MOVPE of undoped and Si-doped AlGaN epilayers", seminar talk, *PARC*, Palo Alto, CA, USA, July 2011.

[34] F. Scholz, "Semipolare Nitrid-Strukturen: Effizientere Leuchtdioden?", seminar talk, *Hochschule Regensburg*, Regensburg, Germany, Oct. 2011.

[35] W. Schwarz, A.J. Márquez del Pino, D. Rimpf, F. Rinaldi, T. Mappes, and R. Michalzik, "Hybrid-integrated optofluidic microparticle sensor using a vertical-extended-cavity surface-emitting laser", *4th EOS Topical Meeting on Optical Microsystems (OμS'11)*, Capri, Italy, Sept. 2011.

[36] P. Unger, "Physics and technology of edge-emitting high-power semiconductor lasers"(invited), *CIOMPOSA International Summer Session "Lasers and Their Applications*", Changchun, China, Aug. 2011.

[37] P. Unger, "Vertical-cavity surface-emitting lasers (VCSELs) and semiconductor disk lasers" (invited), *CIOMPOSA International Summer Session "Lasers and Their Applications*", Changchun, China, Aug. 2011.

[38] P. Unger, "Semiconductor disk lasers", seminar talk, *Institut für Nanostrukturtechnologie und Analytik (INA)*, *Universität Kassel*, Kassel, Germany, Nov. 2011.

[39] D. Wahl, A. Kern, S. Paul, R. Rösch, and R. Michalzik, "Herstellung von VCSELn mit monolithisch integriertem PIN-Photodetektor", *Deutscher MBE-Workshop*, Berlin, Germany, Oct. 2011.

[40] J. Wang, R.A.R. Leute, T. Wunderer, and F. Scholz, "Doping studies of inverse-pyramidal semipolar GaInN/GaN LEDs", poster at *XIV European Workshop on Metalorganic Vapor Phase Epitaxy*, Wroclaw, Poland, June 2011.

[41] B. Westenfelder, J.C. Meyer, S. Kurasch, X. Lin, A. Gross, C.E. Krill, F. Scholz, and U. Kaiser, "Aberration-corrected in-situ TEM investigation under extreme heat: Atomically resolved adsorbates of gold and hydrocarbon on graphene", poster at *25th International Winterschool on Electronic Properties of Novel Materials, IWEPNM 2011*, Kirchberg, Austria, March 2011.

[42] B. Westenfelder, J.C. Meyer, X. Lin, A. Groß, C.E. Krill, F. Scholz, and U. Kaiser, "In-situ TEM investigation under extreme heat: Gold and hydrocarbon adsorbates on graphene", poster at *DPG Frühjahrstagung*, Dresden, Germany, March 2011.

[43] B. Westenfelder, J.C. Meyer, S. Kurasch, X. Lin, A. Gross, C.E. Krill, F. Scholz, and U. Kaiser, "Atomically resolved in-situ HRTEM study of high temperature-induced structural transformations on graphene substrates after Au deposition", *Microscopy Conference, MC2011*, Kiel, Germany, Sept. 2011.

[44] F. Gruet, L. Bimboes, D. Miletic, C. Affolderbach, G. Mileti, A. Al-Samaneh, D. Wahl, and R. Michalzik, "Spectral characterisation of VCSELs emitting at 894.6 nm for CPT-based miniature atomic clocks", poster at *Conf. on Lasers and Electro-Optics Europe, CLEO/Europe 2011*, Munich, Germany, May 2011.

[45] H. Jönen, U. Rossow, H. Bremers, S. Schwaiger, F. Scholz, A. Hangleiter, A. Kruse, J. Thalmair, J. Zweck, L. Hoffmann, and M. Brendel, "Indium incorporation in GaInN quantum wells on various surface orientations: A comparative study by X-ray diffraction and photoluminescence", *DPG Spring Meeting*, Dresden, Germany, March 2011.

[46] C. Karbaum, F. Bertram, S. Metzner, J. Christen, T. Wunderer, and F. Scholz, "Spectrally resolved cathodoluminescence microscopy of an InGaN SQW on hexagonally inverted GaN pyramids", *DPG Spring Meeting*, Dresden, Germany, March 2011.

[47] T. Langer, A. Kruse, M. Göthlich, H. Jönen, H. Bremers, U. Rossow, S. Schwaiger, F. Scholz, and A. Hangleiter, "Nonradiative recombination in long-wavelength polar, nonpolar, and semipolar GaInN/GaN quantum wells", *9th International Conference on Nitride Semiconductors*, Glasgow, UK, July 2011.

[48] M. Lohr, J. Thalmair, M. Jetter, F. Scholz, and J. Zweck, "Locally resolved imaging of internal electric fields in GaN/GaInN quantum wells by differential phase contrast microscopy", poster at *DPG Spring Meeting*, Dresden, Germany, March 2011.

[49] S. Metzner, F. Bertram, J. Christen, T. Wunderer, F. Lipski, S. Schwaiger, and F. Scholz, "Temperature dependent microscopic energy relaxation in semipolar InGaN SQW imaged by spatio-spectrally-time resolved cathodoluminescence", *DPG Spring Meeting*, Dresden, Germany, March 2011.

[50] S. Metzner, F. Bertram, J. Christen, H. Jönen, T. Langer, U. Rossow, A. Hangleiter, S. Schwaiger, and F. Scholz, "Spatially, spectrally and time-resolved cathodoluminescence study of polarization-reduced InGaN quantum wells for long wavelength emission", *9th International Conference on Nitride Semiconductors*, Glasgow, UK, July 2011.

[51] S. Neugebauer, S. Metzner, F. Bertram, T. Hempel, J. Christen, S. Schwaiger, and F. Scholz, "Highly spatially and spectrally resolved cathodoluminescence microscopy of planar semipolar InGaN/GaN MQWs grown on pre-patterned sapphire substrate", *DPG Spring Meeting*, Dresden, Germany, March 2011.

[52] I. Tischer, M. Fikry, M. Madel, F. Scholz, and K. Thonke, "GaN-ZnO-InGaN/GaN core shell nanorods", poster at *DPG Spring Meeting*, Dresden, Germany, March 2011.

Publications

[1] A. Al-Samaneh, M.T. Haidar, D. Wahl, and R. Michalzik, "Polarization-stable single-mode VCSELs for Cs-based miniature atomic clocks", in Online Digest *Conf. on Lasers and Electro-Optics Europe, CLEO/Europe 2011*, paper CB.P.23, one page. Munich, Germany, May 2011.

[2] A. Al-Samaneh, M. Bou Sanayeh, S. Renz, D. Wahl, and R. Michalzik, "Polarization control and dynamic properties of VCSELs for MEMS atomic clock applications", *IEEE Photon. Technol. Lett.*, vol. 23, pp. 1049–1051, 2011.

[3] A. Al-Samaneh, M. Bou Sanayeh, W. Schwarz, D. Wahl, and R. Michalzik, "Vertical-cavity lasers for miniaturized atomic clocks", *SPIE Newsroom*, Aug. 18, 2011, DOI: 10.1117/2.1201108.003824.

[4] A. Bergmann, A. Kroner, and R. Michalzik, "Towards VCSEL-based integrated microfluidic sorting systems", in Proc. (CD ROM) *1st EOS Conference on Optofluidics, EOSOF 2011*, paper 4285, two pages. Munich, Germany, May 2011.

[5] A. Bergmann, D. Wahl, and R. Michalzik, "Integration of VCSEL-based optical traps with microfluidic channels", in Digest *10th Int. Symposium on Scanning Probe Microscopy & Optical Tweezers in Life Sciences*, optical tweezers poster P4, two pages. Berlin, Germany, Oct. 2011.

[6] M. Fikry, M. Madel, I. Tischer, K. Thonke, and F. Scholz, "Luminescence properties of epitaxially grown GaN and InGaN layers around ZnO nanopillars", *Phys. Status Solidi A*, vol. 208, pp. 1582–1585, 2011.

[7] K. Forghani, M. Klein, F. Lipski, S. Schwaiger, J. Hertkorn, R.A.R. Leute, F. Scholz, M. Feneberg, B. Neuschl, K. Thonke, O. Klein, U. Kaiser, R. Gutt, and T. Passow, "High quality AlGaN epilayers grown on sapphire using SIN_x interlayers", *J. Cryst. Growth*, vol. 315, pp. 216–219, 2011.

[8] K. Forghani, M. Gharavipour, M. Klein, F. Scholz, O. Klein, U. Kaiser, M. Feneberg, B. Neuschl, and K. Thonke, "In-situ deposited SiN_x nanomask for crystal quality improvement in AlGaN", *Phys. Status Solidi C*, vol. 8, pp. 2063–2065, 2011.

[9] A. Gadallah and R. Michalzik, "High-output-power single-higher-order transverse mode VCSEL with shallow surface relief", *IEEE Photon. Technol. Lett.*, vol. 23, pp. 1040–1042, 2011.

[10] A. Kern, D. Wahl, S. Paul, M.T. Haidar, R. Blood, W. Schwarz, and R. Michalzik, "7 Gbit/s data transmission over 500 m multimode fiber with monolithically integrated bidirectional VCSEL-based transceiver chips", in Proc. (CD ROM) *Conf. on Lasers and Electro-Optics, CLEO 2011*, paper CFB3, two pages. Baltimore, MD, USA, May 2011.

[11] A. Kern, D. Wahl, S. Paul, M.T. Haidar, R. Blood, W. Schwarz, and R. Michalzik, "Up to 9 Gbit/s data transmission with monolithically integrated VCSELs and PIN photodiodes", in Online Digest *Conf. on Lasers and Electro-Optics Europe, CLEO/Europe 2011*, paper CB1.4, one page. Munich, Germany, May 2011.

[12] A. Kern, S. Paul, D. Wahl, R. Blood, W. Schwarz, and R. Michalzik, "Bidirectional multimode fiber interconnection at Gb/s data rates with monolithically integrated VCSEL–PIN transceiver chips", *IEEE Photon. Technol. Lett.*, vol. 23, pp. 1058–1060, 2011.

[13] A. Kern, S. Paul, D. Wahl, A. Hein, R. Rösch, W. Schwarz, and R. Michalzik, "6 Gbit/s full-duplex multimode fiber link with monolithic VCSEL–PIN transceiver chips", in Proc. (USB flash drive) *37th Europ. Conf. on Opt. Commun., ECOC'2011*, paper We.9.LeSaleve.2, three pages. Geneva, Switzerland, Sept. 2011.

[14] A. Kern, D. Wahl, and R. Michalzik, "Multi-Gbit/s full-duplex data transmission over standard multimode fiber with butt-coupled transceiver chips", in Proc. *European Semiconductor Laser Workshop*, pp. 53–54. Lausanne, Switzerland, Sept. 2011.

[15] A. Kern, S. Paul, D. Wahl, and R. Michalzik, "Bidirectional optical data transmission over a single multimode fiber", *SPIE Newsroom*, Oct. 6, 2011, DOI: 10.1117/2.1201109.003825.

[16] S. Schwaiger, S. Metzner, T. Wunderer, I. Argut, J. Thalmair, F. Lipski, M. Wieneke, J. Bläsing, F. Bertram, J. Zweck, A. Krost, J. Christen, and F. Scholz, "Growth and coalescence behavior of semipolar $(11\bar{2}2)$ GaN on pre-structured r-plane sapphire substrates", *Phys. Status Solidi B*, vol. 248, pp. 588–593, 2011.

[17] W. Schwarz, A.J. Márquez del Pino, D. Rimpf, F. Rinaldi, T. Mappes, and R. Michalzik, "Hybrid-integrated optofluidic microparticle sensor using a vertical-extended-cavity surface-emitting laser", in Proc. (CD ROM) *4th EOS Topical Meeting on Optical Microsystems (OμS'11)*, paper 4550, two pages. Capri, Italy, Sept. 2011.

[18] D. Wahl, A. Kern, M. Stach, F. Rinaldi, R. Rösch, and R. Michalzik, "VCSELs with monolithically integrated photodiodes for single-fiber bidirectional data transmission in the Gbit/s range", *J. Cryst. Growth*, vol. 323, pp. 438–441, 2011.

[19] B. Westenfelder, J.C. Meyer, J. Biskupek, G. Algara-Siller, L.G. Lechner, J. Kusterer, U. Kaiser, C.E. Krill III, E. Kohn, and F. Scholz, "Graphene-based sample supports for in situ high-resolution TEM electrical investigations", *J. Phys. D: Appl. Phys.*, vol. 44, pp. 055502-1–7, 2011.

[20] B. Westenfelder, J.C. Meyer, J. Biskupek, S. Kurasch, F. Scholz, C.E. Krill III, and U. Kaiser, "Transformations of carbon adsorbates on graphene substrates under extreme heat", *Nano Lett.*, vol. 11, pp. 5123–5127, 2011.

[21] T. Wunderer, M. Feneberg, F. Lipski, J. Wang, R.A.R. Leute, S. Schwaiger, K. Thonke, A. Chuvilin, U. Kaiser, S. Metzner, F. Bertram, J. Christen, G.J. Beirne, M. Jetter, P. Michler, L. Schade, C. Vierheilig, U.T. Schwarz, A.D. Dräger, A. Hangleiter, and F. Scholz, "Three-dimensional GaN for semipolar light emitters", *Phys. Status Solidi B*, vol. 248, pp. 549–560, 2011.

[22] M. Barchuk, V. Holý, D. Kriegner, J. Stangl, S. Schwaiger, and F. Scholz, "Diffuse x-ray scattering from stacking faults in a-plane GaN epitaxial layers", *Phys. Rev. B*, vol. 84, pp. 094113-1–8, 2011.

[23] P. Debernardi, W. Schwarz, and R. Michalzik, "Optical modes of an optofluidic microparticle VCSEL sensor", in Proc. *European Semiconductor Laser Workshop*, pp. 30–31. Lausanne, Switzerland, Sept. 2011.

[24] R. Gutt, T. Passow, W. Pletschen, M. Kunzer, L. Kirste, K. Forghani, F. Scholz, O. Klein, U. Kaiser, K. Köhler, and J. Wagner, "Efficient 350 nm LEDs on low edge threading dislocation density AlGaN buffer layers" in *Light-Emitting Diodes: Materials, Devices, and Applications for Solid State Lighting XV*, K.P. Streubel (Ed.), Proc. SPIE 7954, pp. 79540Q-1–8, 2011.

[25] F. Gruet, L. Bimboes, D. Miletic, C. Affolderbach, G. Mileti, A. Al-Samaneh, D. Wahl, and R. Michalzik, "Spectral characterisation of VCSELs emitting at 894.6 nm for CPT-based miniature atomic clocks", in Online Digest *Conf. on Lasers and Electro-Optics Europe, CLEO/Europe 2011*, paper CB.P.27, one page. Munich, Germany, May 2011.

[26] H. Jönen, U. Rossow, H. Bremers, L. Hoffmann, M. Brendel, A.D. Dräger, S. Schwaiger, F. Scholz, J. Thalmair, J. Zweck, and A. Hangleiter, "Highly efficient light emission from stacking faults intersecting nonpolar GaInN quantum wells", *Appl. Phys. Lett.*, vol. 99, pp. 011901-1–3, 2011.

[27] H. Jönen, U. Rossow, H. Bremers, L. Hoffmann, M. Brendel, A.D. Dräger, S. Metzner, F. Bertram, J. Christen, S. Schwaiger, F. Scholz, J. Thalmair, J. Zweck, and A. Hangleiter, "Indium incorporation in GaInN/GaN quantum well structures on polar and nonpolar surfaces", *Phys. Status Solidi B*, vol. 248, pp. 600–604, 2011.

[28] O. Klein, J. Biskupek, K. Forghani, F. Scholz, and U. Kaiser, "TEM investigations on growth interrupted samples for the correlation of the dislocation propagation and growth mode variations in AlGaN deposited on SiN_x interlayers", *J. Cryst. Growth*, vol. 324, pp. 63–72, 2011.

[29] M. Kunzer, R. Gutt, L. Kirste, T. Passow, K. Forghani, F. Scholz, K. Köhler, and J. Wagner, "Improved quantum efficiency of 350 nm LEDs grown on low dislocation density AlGaN buffer layers", *Phys. Status Solidi C*, vol. 8, pp. 2363–2365, 2011.

[30] S. Metzner, F. Bertram, C. Karbaum, T. Hempel, T. Wunderer, S. Schwaiger, F. Lipski, F. Scholz, C. Wächter, M. Jetter, P. Michler, and J. Christen, "Spectrally and time-resolved cathodoluminescence microscopy of semipolar InGaN SQW on $(11\bar{2}2)$ and $(10\bar{1}1)$ pyramid facets", *Phys. Status Solidi B*, vol. 248, pp. 632–637, 2011.

[31] U.T. Schwarz and F. Scholz,"Rosige Aussichten für grünes Licht", *Physik Journal*, vol. 10, pp. 21–26, 2011.

[32] I. Tischer, M. Feneberg, M. Schirra, H. Yacoub, R. Sauer, K. Thonke, T. Wunderer, F. Scholz, L. Dieterle, E. Müller, and D. Gerthsen, "I_2 basal plane stacking fault in GaN: origin of the 3.32 eV luminescence band", *Phys. Rev. B*, vol. 83, pp. 035314-1–6, 2011.

ulm university universität ulm

Ulm University
Institute of Optoelectronics
Albert-Einstein-Allee 45
89081 Ulm | Germany

Ulm University | Institute of Optoelectronics | Annual Report 2011